Studies on diversity and chloroplast reduction in *Paragymnodinium* (Dinophyceae)

(パラギムノディニウム属(渦鞭毛藻綱)における多様性と葉緑体の縮小進化の研究)

Koh Yokouchi

Department of Natural History Sciences, Graduate School of Science,

Hokkaido University

2022, March

CONTENTS

ABSTRACT

It is believed that chloroplasts arose through a primary endosymbiotic uptake of a photosynthetic prokaryote by a non-photosynthetic eukaryote, and have spread to a wide range of eukaryotic lineages via secondary endosymbioses. On the other hand, many eukaryotes are also known to have lost the photosynthetic function of their chloroplasts. It is known that in dinoflagellates, multiple losses of chloroplasts had taken place, resulting in the occurrence of large number of heterotrophic species in different lineages. However, the process of reductive evolution of chloroplasts within dinoflagellates is not well investigated. This study aims to understand the process of early stages of reductive evolution of chloroplasts by comparing dinoflagellate species within a single genus, *Paragymnodinium*, which exhibit varying degrees of dependence on their chloroplasts: mixotrophic species, mostly dependent on phagotrophy, as well as completely phototrophic species.

This thesis consists of four chapters. In chapter 1, an overview of chloroplast evolution, characteristics of dinoflagellates and research background relating to the chloroplast reduction are reviewed.

For the purpose of this study, I used species of the genus *Paragymnodinium*. The genus *Paragymnodinium* was established by Kang et al. (2010), based on a type species, *P. shiwhaense*, which was newly described from Korea and characterized by mixotrophic nutrition and possession of complex extrusomes, the nematocysts. In chapter 2, four new species of dinoflagellates belonging to the genus *Paragymnodinium* were described based on observations using light, scanning and transmission electron microscopy, together with molecular analysis. *Paragymnodinium stigmaticum* was 8.5–15.2 µm long and 6.3–12.4 µm wide and shared many features with *P. shiwhaense*, including the possession of nematocysts and ingestion of prey cells despite the possession of chloroplasts. However, it was distinguished from *P. shiwhaense* by its feeding mechanism, its chloroplast ultrastructure, the presence of an eyespot and a benthic lifestyle (*P. shiwhaense* is planktonic). *Paragymnodinium verecundum* was 9.4–17.1 µm long and 5.7–13.6 µm wide, and similar to *P. stigmaticum* in its shape, possession of an eyespot and nematocysts, ingestion of prey, and benthic lifestyle. On the other hand, *P. verecundum* showed

negative phototaxis and possessed a pusule, which were not observed in *P. stigmaticum*, indicating these two dinoflagellates were different species. *Paragymnodinium asymmetricum* was 7.9–12.6 μm long and 4.7–9.0 μm wide and did not show feeding behavior and were phototrophically maintainable. *Paragymnodinium asymmetricum* shared many features with *P. shiwhaense*, such as nematocysts, absence of eyespot and the planktonic lifestyle. However, *P. asymmetricum* was distinguished from *P. shiwhaense* by the asymmetric shape of hyposome and nutritional mode. *Paragymnodinium inerme* was 15.3–23.7 μm long and 10.9–19.6 μm wide and also did not show feeding behavior. *Paragymnodinium inerme* was similar to *P. shiwhaense* in its shape and planktonic lifestyle, but the nutritional mode was different. The presence of incomplete (partly collapsed) nematocysts was also a unique feature in *P. inerme*. A phylogenetic analysis inferred from concatenated 18S and 28S ribosomal DNA sequences recovered the four dinoflagellates along with *P. shiwhaense* in a robust clade that was included in the clade *Gymnodinium sensu stricto*. Therefore, together with the morphological similarities, it was concluded that all of these dinoflagellates should be regarded as new species in the genus *Paragymnodinium*. The fact that genus *Paragymnodinium* exhibits various nutritional strategies provides an excellent opportunity to investigate the evolution of the mode of nutrition and the function of the chloroplasts.

In chapter 3, I analyzed the growth, pigment composition, absorption spectra, variable chlorophyll *a* fluorescence, and photosynthetic carbon fixation capabilities of *Paragymnodinium stigmaticum*, *P. asymmetricum* and *P. inerme*. The autotrophic species *P. asymmetricum* and *P. inerme* without resorting to any nutrition from prey organisms displayed high photosystem II activity and carbon fixation rates. The pigment compositions of these two species were identical to those of other typical peridinin-containing type dinoflagellates. On the other hand, the phagotrophic species *P. stigmaticum* showed heterotrophic growth, i.e., addition of cryptomonad *Rhodomonas* sp. was required for its prey, and the variable chlorophyll *a* fluorescence properties and carbon fixation rates indicated significantly lower photosynthetic competence relative to those of the above two species. *Paragymnodinium stigmaticum* also contained peridinin, but pigment content ratios of peridinin, chlorophyll c_2 and β-carotene were significantly

different from those of other two species. The absorption spectrum analysis revealed a red-shift in the peak of the Q_y band of chlorophyll *a* in *P. stigmaticum*, presumably due to a change in chlorophyll-protein complexes. Such distinct differences in nutritional strategies between members of the genus *Paragymnodinium* would provide a platform for the hypothetical loss of photosynthetic function leading to colorless dinoflagellates.

In chapter 4, a comparative transcriptomic analysis within the photosynthetic and non-photosynthetic species in the genus *Paragymnodinium* (*P. asymmetricum*, *P. inerme* and *P. stigmaticum*) was conducted to evaluate differences of the chloroplast-related gene expression which were involved in heme, chlorophyll, isopentenyl diphosphate and carotenoids synthesis pathways, carbon fixation (Calvin cycle) and photosynthesis. *Paragymnodinium stigmaticum* showed a significant lack of mRNA expressions for photosystem II and its light harvesting complex, in spite of the other components for photosynthetic functions were expressed at the same level to the other phototrophic species. In addition, the transcription of *rbcL* gene was shown to be absent in *P. stigmaticum*, whereas the other species actively expressed it. Lacks of expression of a few genes in chlorophyll and carotenoid synthesis pathways were also observed in *P. stigmaticum*, whereas heme and isopentenyl diphosphate synthesis pathways showed a same level of expression within the three *Paragymnodinium* species. These results were consistent with the inactivated photosynthesis and carbon fixation in *P. stigmaticum*, and represented an example for the process of genetic changes during an early transitional stage of loss of photosynthetic capability.

ACKNOWLEDGEMENTS

I would like to express my greatest thanks to Professor Takeo Horiguchi for his guidance and suggestion on the study of dinoflagellates and critical reading of the manuscript. I also would like to thank Professor Kazuhiro Kogame and Dr. Hiroshi Kajihara for their advice on this study. My special thanks go to Dr. Kevin C. Wakeman for his scientific as well as technical advice as my advisory board member. I would like to show my great appreciation to Professor Koji Suzuki and his laboratory members, Dr. Yan Dong, Mr. Yudai Oshino and Ms. Yuri Fukai for permitting me to use analytical equipment and providing a lot of helpful technical advices. I wish to thank Professor Atsuko Sugimoto and Ms. Yumi Hoshino for their assistance in operating the isotope mass spectrometer. I am grateful to Dr. Ryo Onuma for providing *P. stigmaticum* (strain SD01), *Chroomonas* sp. (strain Ak01) and *Rhodomonas* sp. (strain Mr06), and technical advice and critical suggestions for transcriptomic analyses. My thanks also go to Dr. Kazuya Takahashi for providing *P. asymmetricum* (strain vnd299) and *P. inerme* (strain JGD), and Dr. Masakazu Aoki and Ms. Mana Yamamoto for providing a sample from Kitsunezaki. I express my thanks to Dr. Aika Yamaguchi for her technical advice. For SEM observations, critical point drying was performed at the Electron Microscope Laboratory, Research Faculty of Agriculture, Hokkaido University. For computation of RNA-seq data, *de novo* assembly and BLASTP were performed on the National Institute of Genetics (NIG) supercomputer at the Research Organization of Information and Systems of the NIG. This work was supported by Grant-in-Aid for JSPS Fellows Grant Number JP19J20893.

Chapter 1. General introduction

Overview of chloroplast evolution

A chloroplast is a representative form of plastid and is an essential organelle for creation of organic matter from inorganic carbon and for oxygen evolution by photosynthesis. It is generally believed that photosynthesis was firstly developed by a cyanobacteria-like prokaryote and chloroplasts arose through the endosymbiotic uptake of the photosynthetic prokaryote by a non-photosynthetic eukaryote (Howe et al. 2008a, Rockwell et al. 2014, Archibald 2015, Ponce-Toledo et al. 2017). The chloroplast established by this event (primary endosymbiosis) is termed primary chloroplast, and is inherited to members in the supergroup Archaeplastida including land plants, green algae, red algae, and glaucophyte algae (Howe et al. 2008a, Keeling 2013). It is now broadly accepted that the primary endosymbiosis by the ancestor of Archaeplastida has occurred only one time (Rockwell et al. 2014, Ponce-Toledo et al. 2017). After that, secondary endosymbioses occurred by uptake of the photosynthetic eukaryotes with the primary chloroplasts by other heterotrophic eukaryotes, arising secondary chloroplasts (Keeling 2013). Unlike the primary endosymbiosis, the secondary endosymbiosis is thought to have occurred in multiple eukaryotic lineages (Keeling 2013). The chloroplasts of the members of alveolates, stramenopiles, haptophytes and cryptomonads are originated from red algae, while those of euglenids and chlorarachniophytes are from green algae (Keeling 2013). The chloroplasts are used not only for photosynthesis and carbon fixation but also for synthesis and metabolism of various materials such as amino acids, nitrogen, sulfur, carotenoid, heme, chlorophyll, isopentenyl diphosphate (IPP), fatty acids and so on (Ruhlman and Daniell 2007). The integration of photosynthetic organisms to chloroplasts as organelle must be accompanied by an extensive genomic modification in both host and symbiont. A significant part of endosymbiont genes has been transferred into the host nucleus by a process known as endosymbiotic gene transfer (EGT) (Zimorski et al. 2014, Archibald 2015). A large number of nuclear-encoded proteins with transit peptides are consequently targeted to the chloroplast, achieved by a development of translocation machineries known as translocon of the outer and inner chloroplast membrane (TOC and

TIC, respectively) , and involved in various functions including gene expression, division, trafficking and metabolism (Martin et al. 1998, 2002, Archibald 2015).

On the other hand of the acquisition of chloroplasts explained above, the loss of chloroplasts is also known to have occurred in wide range of eukaryotic lineages, except for haptophytes, largely contributing to the diversification of species and their lifestyles (Hadariová et al. 2018, Maciszewski and Karnkowska 2019). Thus, it is worth unraveling the evolutionary process of loss of chloroplasts for further understanding the mechanism of biodiversity and organelle evolution. Recent genomic and transcriptomic investigations have revealed various patterns of potential functions and the status of remaining genes of colorless cryptic plastids in non-photosynthetic organisms (e.g., Wilson et al. 1996, Gockel and Hachtel 2000, Wicke et al. 2016, Kamikawa et al. 2017, Dorrell et al. 2019, Kayama et al. 2020, Tanifuji et al. 2020). One of the most representative examples of relict plastids is 'apicoplasts' observed in apicomplexan parasites, shown to retain a reduced genome and a part of metabolic functions (Wilson et al. 1996, Foth and McFadden 2003). The accumulated information by such studies gradually clarifies the general model for the process of loss of chloroplasts (Fig. 1.1) (Barrett et al. 2014, Graham et al. 2017, Hadariová et al. 2018, Maciszewski and Karnkowska 2019); the photosynthetic function and its genes seem to be lost in the early step of chloroplast reduction, together with the degradation of thylakoids, while the housekeeping proteins and the biosynthetic functions for secondary metabolites tend to be retained for a relatively long period. The plastid is consecutively thought to abandon its genome, exhibited by a few cases of genome-lacking plastids, e.g., the green alga *Polytomella* (Smith and Lee 2014) and the parasitic plant *Rafflesia lagascae* (Molina et al. 2014). Eventually the plastids disappear completely, which occurred only in some parasitic lineages in Apicomplexa and dinoflagellates (Gornik et al. 2015, Janouškovec et al. 2015).

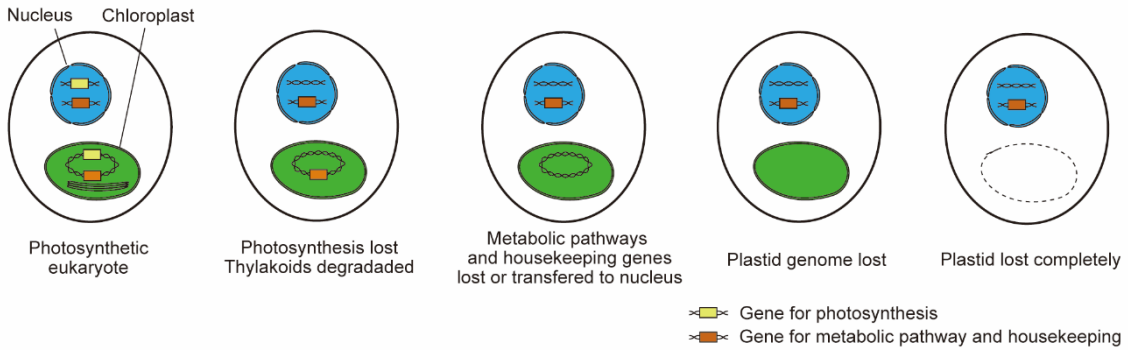

Fig. 1.1. Schematic representation of the stages of reductive evolution of chloroplast, based on the model by Maciszewski and Karnkowska (2019).

General characteristics of dinoflagellates

Dinoflagellates are unicellular microorganisms widely distributed in aquatic environments, belonging to Alveolata together with apicomplexans and ciliates (Adl et al. 2019). The number of known species is estimated to be approximately 2,400 (Janouškovec et al. 2017), including 1,555 free-living marine species (Gómez 2005), approximately 190 marine benthic species (Hoppenrath et al. 2014) and 350 freshwater species (Moestrup and Calado 2018). Typical dinoflagellates are characterized by possession of two flagella emerged from the ventral area of the cell; a transverse flagellum running leftward of the cell drawing a spiral, and a longitudinal flagellum running straightly to backward of the cell (Fig. 1.2A). Usually, each flagellum runs along two furrows, a cingulum for the former and a sulcus for the latter, and the sulcus defines the ventral side of the cell (Fig. 1.2A). The cell is divided by the cingulum into the anterior part (episome or epicone) and the posterior part (hyposome or hypocone) (Fig. 1.2A).

In addition to these fundamental characteristics, the dinoflagellates also share some unique characters. Amphiesmal vesicles lie beneath the plasma membrane and cover the cortex of whole cell (Fig. 1.2B). Dinoflagellates can be classified into thecate and athecate taxa, and the former species possess cellulosic thecal plates in the amphiesmal vesicles (Fig. 1.2B). The tabulation of thecal plates is species specific and regarded as one of the most important criteria for taxonomy (Hoppenrath 2017). The nucleus of dinoflagellates is called dinokaryon which is mainly characterized by the presence of permanently condensed chromosomes (Fig. 1.2B) (Dodge 1987). Although

the absence of typical histone and nucleosomes was previously regarded as one of the genetic characters of dinoflagellates, Lin et al. (2010) demonstrated the presence of the nucleosome components in the dinoflagellate genome. The nuclear genome is also remarkable in its large size, although it largely varies between species (Lin 2011, Wisecaver and Hackett 2011). A pusule seen in dinoflagellates is also a unique structure (Fig. 1.2B). It presumably works as an osmo-regulatory organelle, but its precise function is not yet known (Dodge 1972, 1987). Dinoflagellates may contain some kinds of extrusomes, such as trichocyst, mucocyst, nematocyst and taeniocyst (Fig. 1.2B) (Dodge 1987, Greuet 1987).

Some dinoflagellates possess an eyespot as a part of photoreceptor system (Fig. 1.2B). Not like other algal groups, the morphology of dinoflagellate eyespots shows a variety, with eight different types currently recognized (Hoppenrath 2017). The eyespot is located in the sulcal area close to the flagellar root, except for the types Ia and Ib *sensu* Hoppenrath (2017) located in the dorsal area of the cell. Most typical type-I (or type-A *sensu* Moestrup and Daugbjerg (2007)) eyespot is comprised of pigment globules located inside a chloroplast near the sulcus, and can be observed using light microscopy as a red stigma. In addition, a more complex photoreceptor called ocelloid consisting of a cornea, lens, iris, and retina is observed in the warnowiid dinoflagellates (Greuet 1987, Gavelis et al. 2015).

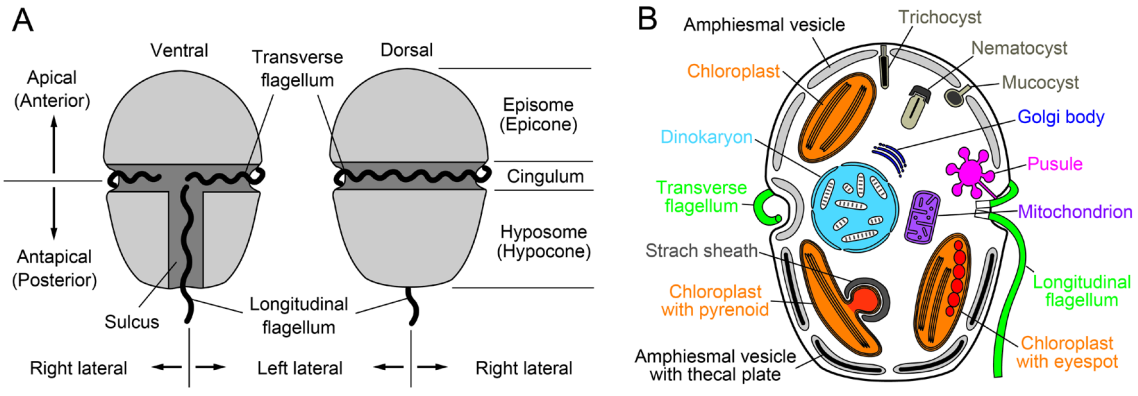

Fig. 1.2. (A) External morphology and its terminology of dinoflagellate cells. (B) Schematic drawing of a dinoflagellate cell showing internal ultrastructures, viewed from right lateral. Both were redrawn from Hoppenrath (2007).

Chloroplasts and nutritional strategies in dinoflagellates

In addition to the various unique features introduced above, chloroplasts and nutritional strategies in dinoflagellates also show many unusual characters. It is estimated that approximately half of described dinoflagellates are phototrophic and the other half are heterotrophic or parasitic (Moestrup and Daugbjerg 2007). The common ancestor of dinoflagellates and the sister group apicomplexans is presumed to have acquired a chloroplast by secondary endosymbiosis by engulfing a red alga, and many dinoflagellates have retained it (Moestrup and Daugbjerg 2007, Keeling 2013). This type of chloroplasts is called 'peridinin-type' or 'peridinin-containing type' because of their unique xanthophyll only detected in dinoflagellates. Peridinin-type chloroplasts are surrounded by triple membranes, contain triple-stacked thylakoid lamellae, and may contain pyrenoids (Dodge and Crawford 1971, Schnepf and Elbrächter 1999). The chloroplasts in dinoflagellates can also be characterized by possession of unique organellar genome. It is highly reduced in gene content and plasmid-like circular DNA in organization called minicircles, each of which contains mostly a single gene only (Zhang et al. 1999, Howe et al. 2008b, Barbrook et al. 2014, Mungpakdee et al. 2014).

As mentioned, about half of known dinoflagellates have no chloroplasts. Non-phototrophic dinoflagellates are thought to have lost their peridinin-type chloroplasts secondarily through a process that have presumably occurred multiple times among various lineages of dinoflagellates (Saldarriaga et al. 2001, Keeling 2013, Janouškovec et al. 2017, Waller and Kořený 2017). Heterotrophic dinoflagellates display various feeding mechanisms such as engulfment, pallium-feeding, and myzocytosis using a peduncle (Hansen 1991, Schnepf and Elbrächter 1992). Parasitic life styles are also recognized in several lineages of dinoflagellates (Coats 1999). Molecular studies on plastid-derived genes have suggested that some heterotrophic dinoflagellates, such as *Crypthecodinium* and *Oxyrrhis*, previously considered to lack plastids, still retain non-pigmented cryptic plastids (Sanchez-Puerta et al. 2007, Slamovits and Keeling 2008). The parasitic dinoflagellates *Hematodinium* and *Amoebophyra*, however, exhibit no evidence of retention of a plastid (Gornik et al. 2015, John et al. 2019).

Moreover, some dinoflagellates are known to have replaced their plastids after the loss of original plastids (Keeling 2013, Waller and Kořený 2017). As a result, other

than peridinin-type, additional seven types of chloroplasts (or kleptoplastids) are recognized today (Moestrup and Daugbjerg 2007). For example, all the species in the family Kareniaceae contain chloroplasts derived from haptophyte (Tengs et al. 2000), while those of the genus *Lepidodinium* were originated from a green alga (Watanabe et al. 1987, 1990, Matsumoto et al. 2011). These establishments of chloroplasts by heterotrophic (but originally-photosynthetic) organisms with other primary or secondary chloroplast-bearing eukaryotes are termed tertially endosymbiosis, which is recognized only in dinoflagellates (Keeling 2013).

Currently, many photosynthetic dinoflagellates are regarded as mixotrophic, that is, they have the capability to use both phototrophic and heterotrophic nutritional strategies (Gaines and Elbrächter 1987, Schnepf and Elbrächter 1992, Stoecker 1999, Hansen 2011). Many potentially mixotrophic dinoflagellates can grow only by photosynthesis and thus they were described as phototrophic species at first. Later, the capabilities of phagotrophy of these species have been revealed (Gaines and Elbrächter 1987, Stoecker 1999, Hansen 2011) and subsequently their mixotrophic nature was demonstrated. In addition, kleptoplastidic lifestyle (i.e., ingesting other photosynthetic protists and maintaining functional plastids for a limited period for photosynthesis) is recognized in some dinoflagellates as one form of mixotrophy (Schnepf and Elbrächter 1992, Takano et al. 2014, Mitra et al. 2016). Mixotrophic nutrition has also been described in other divergent eukaryotes such as ciliates, haptophytes, stramenopiles, rhizaria and euglenophytes (Stoecker 1998, Burkholder et al. 2008, Yamaguchi et al. 2012, Stoecker et al. 2017). The strategies for, and dependence on, nutrient acquisition through photosynthesis or ingestion in mixotrophic organisms are diverse (Stoecker 1999, Mitra et al. 2016, Stoecker et al. 2017). Although mixotrophic organisms are recognized as important components of aquatic ecosystems (Mitra et al. 2016, Stoecker et al. 2017, Wilken et al. 2019), information on mixotrophy remains limited.

The frequent losses and gains of photosynthetic function and the transition of nutritional strategies within dinoflagellates provide an excellent opportunity to explore the evolution of chloroplasts. Especially, previous studies on kleptoplastidic or tertiary-photosynthetic dinoflagellates have provided a lot of insights into the chloroplast acquisition by endosymbiosis (e.g., Onuma and Horiguchi 2015, Matsuo and Inagaki

2018). On the other hand, the processes of loss of photosynthesis have been less investigated in dinoflagellates, in spite of frequent multiple losses of chloroplasts in this group compared to the other eukaryotes. It is mainly caused by the lack of adequate species representing the early steps of loss of chloroplasts. Most part of heterotrophic dinoflagellates are unculturable, making execution of the investigations difficult too. In addition, the large size of dinoflagellate nucleus prevents genomic-scaled analyses (Lin 2011, Wisecaver and Hackett 2011).

Aims of this study

Recently, four novel strains of dinoflagellates belonging to the genus *Paragymnodinium* were established and maintained in the laboratory. This genus was established by Kang et al. (2010) based on a new species (type species), *P. shiwhaense*. This species feeds on other prey cells, despite the presence of plastids, showing mixotrophic growth (Yoo et al. 2010). Interestingly, however, the four novel dinoflagellates used in this study display a notable variety of nutritional strategies, i.e., two of the four species showed phototrophy, while the remaining two showed phagotrophy (= mixotrophy). The comparison of different functional traits displayed within a single genus provides an excellent opportunity to better understand the evolution of nutritional strategies within dinoflagellates as a whole. The aims of this study are:

(1) to describe these four novel species based on morphological observations with light, scanning and transmission electron microscopy (LM, SEM and TEM, respectively) and phylogenetic analyses with concatenated sequences of the small (SSU) and large subunit (LSU) ribosomal RNA genes (rDNA);

(2) to investigate the precise state of nutritional strategies and photosynthetic properties of each species, in terms of growth properties, pigment profiles, absorption spectrum patterns, variable chlorophyll *a* fluorescence, and carbon fixation capabilities;

(3) to compare the expression of chloroplast-related genes between the photosynthetic and non-photosynthetic species in the genus *Paragymnodinium* based on a transcriptomic analysis.

The results of this study demonstrated remarkable variations exist in nutritional strategies and also in the morphological, functional and genetic states of chloroplasts

within the genus *Paragymnodinium*, shedding a light on an early evolutionary step toward the loss of chloroplasts, which has been unclear so far in dinoflagellates.

Chapter 2. Systematics and taxonomy of four novel species within the genus *Paragymnodinium*

INTRODUCTION

Many athecate dinoflagellates traditionally comprised the order *Gymnodiniales* and most of species in this order have been assigned in the genus *Gymnodinium*. However, ultrastructural observations with transmission electron microscopy (TEM) and phylogenetic studies have revealed that this order is polyphyletic (Daugbjerg et al. 2000, Hoppenrath 2017). The monophyletic clade including the type species of the genus *Gymnodinium* is called *Gymnodinium sensu stricto* and the genus was redefined by Daugbjerg et al. (2000). The newly defined genus *Gymnodinium* is characterized by three morphological features; a horseshoe-shaped apical groove running on an episome in an anticlockwise direction, a nuclear envelope with vesicular chambers, and a fibrous connective that interconnects the longitudinal microtubular root R1 (LMR) of flagellar apparatus with the nucleus (Daugbjerg et al. 2000). Although these features are shared by many species within the clade *Gymnodinium sensu stricto*, some species do not conform these three features and these species were classified in genera other than *Gymnodinium* (Daugbjerg et al. 2000, Hoppenrath 2017). Therefore, now the clade *Gymnodinium sensu stricto* consists of multiple genera, such as *Gymnodinium*, *Paragymnodinium*, *Lepidodinium*, *Nusuttodinium*, *Polykrikos*, *Gyrodiniellum*, *Nematodinium*, *Spiniferodinium*, etc. (Hoppenrath 2017).

Kang et al. (2010) established the genus *Paragymnodinium* based on a new species, *P. shiwhaense* as a type, which was included in the clade *Gymnodinium sensu stricto*. *Paragymnodinium shiwhaense* lacks the three key characters for the genus *Gymnodinium*, horseshoe-shaped apical groove, nuclear envelope chambers and nuclear fibrous connective (Kang et al. 2010). Despite the presence of plastids, it feeds on other prey cells using a peduncle, thus showing mixotrophic growth (Yoo et al. 2010). Interestingly, this species requires both light and prey to grow and survive (Yoo et al. 2010). This obligate mixotrophic growth is rarely demonstrated among the non-kleptochloroplastidic dinoflagellates and thus far has been demonstrated in

Esoptrodinium sp. (Fawcett and Parrow 2014), *Polykrikos lebourae* (Kim et al. 2015) and *P. shiwhaense*. This species is also characterized by the possession of complex extrusomes, the 'nematocysts' (Kang et al. 2010). Such structures have been found only in some genera of polykrikoids and the warnowiids, as well as in the genus *Gyrodiniellum* (Marshall 1925, Westfall et al. 1983, Greuet 1987, Hoppenrath and Leander 2007a, b, Hoppenrath et al. 2009, 2010, Kang et al. 2011). These nematocyst-bearing species are restricted in the clade *Gymnodinium sensu stricto*, but the origin of nematocyst is unknown. Previous studies of *Polykrikos* and *Nematodinium* have shown that their nematocysts are used to capture prey cells for ingestion (Matsuoka et al. 2000, Gavelis et al. 2017). That of *Paragymnodinium* is presumed to function in the same way, although its utilization has not been observed directly (Jeong et al. 2017).

Recently, four novel culture strains of dinoflagellates were established. My study showed that these four dinoflagellates should represent new species in the genus *Paragymnodinium*. In this chapter, these four species are described based on light, scanning and transmission electron microscopies (LM, SEM and TEM, respectively) and phylogenetic analyses with concatenated sequences of the small (SSU) and large subunit (LSU) ribosomal RNA genes (rDNA). The characteristics and evolution of nutritional strategies, nematocyst, feeding behavior, chloroplast, flagellar apparatus and phototaxis are discussed. It should be noted that of the four species, *Paragymnodinium stigmaticum* has been published in 2018 (Yokouchi et al. 2018), *P. asymmetricum* and *P. inerme* have been described in 2020 (Yokouchi et al. 2020) and *P. verecundum* was published in 2021 (Yokouchi and Horiguchi 2021).

MATERIAL AND METHODS

Preparation of culture strains

Paragymnodinium stigmaticum (strain SD01) was isolated from sandy sediment samples taken from Sumiyoshi beach, Sado Island, Niigata Prefecture, Japan (38°04.40′N, 138°27.36′E) on 15 August, 2011 using a microcapillary pipette. *Paragymnodinium verecundum* (strain KZ04) was isolated from sandy sediment samples from −5 m depth of Kitsunezaki beach, Miyagi Prefecture, Japan (38°21.21′N, 141°25.26′E) on 26 March, 2018. *Paragymnodinium asymmetricum* (strain vnd299) was isolated from water samples from Nha Trang beach, Nha Trang, Vitenam (12°14.56′N, 109°11.49′E) on 26 April, 2014. *Paragymnodinium inerme* (strain JGD) was isolated from water samples from Jogashima, Kanagawa, Japan (35°08.02′N, 139°36.41′E) on 19 November, 2017. Isolated cells were kept in Daigo's IMK Medium for Marine Microalgae (Nihon Pharmaceutical Co., Tokyo, Japan). Cells of *Chroomonas* sp. (strain Ak01, Phycological Laboratory Culture Collections, Hokkaido University) (Cryptophyceae) were added as prey for *P. stigmaticum*, and cells of *Rhodomonas* sp. (strain Mr06, Phycological Laboratory Culture Collections, Hokkaido University) were added as prey for *P. verecundum*. The cultures of *P. asymmetricum* and *P. inerme* can be maintained without adding any prey. The established cultures of *P. stigmaticum*, *P. asymmetricum* and *P. inerme* were incubated at 20°C, while *P. verecundum* was maintained at 15°C with an illumination of 50 μmol photons m^{-2} s^{-1} under 16:8 h light:dark cycle.

Light microscopy

Cells were observed using differential interference contrast (DIC) optics with a Zeiss Axioskop 2 Plus microscope (Zeiss Japan, Tokyo, Japan), and images were taken using a Leica MC 120 HD digital camera (Leica Microsystems, Wetzlar, Germany) for *P. stigmaticum*, and Canon EOS Kiss X8i digital camera (Canon, Tokyo, Japan) for other strains. Feeding behavior and mechanism of *P. stigmaticum* were observed with a Nikon Diaphot inverted phase contrast microscope (Nikon, Tokyo, Japan), and images were taken using a Canon EOS 60D digital camera (Canon, Tokyo, Japan) with a camera adapter SA20 (Wraymer, Osaka, Japan). Chlorophyll autofluorescence was observed using a Zeiss Axioskop 2 Plus microscope with a No. 15 filter set. The nucleus of *P.*

asymmetricum and *P. inerme* was stained with 4', 6-diamidino-2-phenylindole (DAPI) after fixation in 2.5% glutaraldehyde (final concentration) and the fluorescence was observed using a Zeiss Axioskop 2 Plus microscope with a No. 49 filter set.

Negative phototactic behavior of *Paragymnodinium verecundum* was confirmed by observing the response of well-fed cells using a CKX41 inverted microscope (Olympus, Tokyo, Japan) to monodirectional light created by laterally illuminating a 24-well plate with a fiber optic light source (Nikon, Tokyo, Japan). The behavior was observed following changes in the light intensity over a range of 50–1000 μmol photons m^{-2} s^{-1}. The responses of cells to red and blue light were observed by illuminating them through LEE filters (Andover, UK); No. 106 for red and No. 079 for blue. The light intensity at which the cells responded was measured using a QMSW-SS quantum meter (Apogee instruments, Logan, USA). Cinematographic records of the response of cells to the various light parameters were made using a scopepad-500 camera (Gellex International, Tokyo, Japan). The observations were started at 9:30, 15:00, 18:00 and 21:00.

Scanning electron microscopy (SEM)

For SEM, cells of *Paragymnodinium stigmaticum*, *P. verecundum* and *P. inerme* were fixed for 1.5 h on ice with 2 or 3% (final concentration) OsO_4 in distilled water. Cells of *P. asymmetricum* were fixed for at least 0.5 h on ice with 1 or 2% (final concentration) OsO_4 in distilled water. The fixed cells of *P. stigmaticum* were attached to a glass plate coated with poly-L-lysine, and other strains were placed on the membrane filter (pore size = 5 μm) that was glued on the bottom of a short tube (cut-off proximal part of 1000 μl blue tip), using a pipette. The glass plate or membrane filter were washed three times, for 10 min each, with distilled water. Then, the cells were dehydrated in an ethanol series (30%, 50%, 70%, 80%, 90%, 95%) for 10 min at each concentration, with two subsequent submersions of 30 min each in 100% ethanol. Dehydrated cells were dried with CO_2 using a critical point drier (Hitachi HCP-2, Tokyo, Japan or Leica EM CPD300, Wetzlar, Germany), sputter coated with gold (Hitachi E-1045 sputter coater), and viewed with a Hitachi S-3000N SEM.

Transmission electron microscopy (TEM)

For TEM, cells were fixed using one of two protocols. In the first, cells were fixed in 2.5% glutaraldehyde (final concentrations) in seawater for 1 h, and washed twice in sea water. Cells were post fixed in 1% OsO_4 (final concentrations) for 1 h. In the second, cells were fixed in a mixture of 2% glutaraldehyde and 0.5% OsO_4 (final concentrations) in 0.1 M Na-cacodylate buffer, pH 7.4 for 15 or 30 min, and rinsed twice in 0.1 M Na-cacodylate buffer. The cells were post-fixed in 1% OsO_4 (final concentration) in 0.1 M Na-cacodylate buffer, pH 7.4 for 1 h. In both protocols, cells were first attached to the bottom of a polypropylene dish coated with poly-L-lysine. After fixation, cells of both protocols were dehydrated in an acetone series (30%, 50%, 80%, 90%, 95%) for 10 min at each concentration, and submersed twice, each time for 30 min, in 100% acetone. One hundred percent acetone and Agar Low Viscosity Resin (Agar Scientific, Essex, UK) were mixed in ratios of 3:1, 1:1, and 1:3 and the samples were introduced into each higher resin concentration sequentially for 15 min each. Finally, the cells were infiltrated in 100% resin for 30 min, after which they were polymerized at 65°C for 16 h. Samples were sectioned into 70 nm thick using a diamond knife on an EM-Ultracut S ultramicrotome (Leica Microsystems, Wetzlar, Germany). The sections were placed on formvar-coated one-slot grids and observed with a Hitachi H-7650 TEM.

Molecular analysis

For extraction of total DNA, cells of *Paragymnodinium stigmaticum* and *P. verecundum* were incubated in IMK medium without prey cells for 5 days to remove prey cell DNA from the dinoflagellate. Thereafter, several cells were isolated by capillary pipettes, rinsed several times in serial drops of sterilized culture medium and transferred into 10 µl of Quick Extract FFPE RNA Extraction Kit (Epicentre, Wisconsin, USA) to extract DNA according to manufacturer's protocol. We used the primers SR1, SR4, SR5TAK, SR6, SR8TAK, SR9, SR11, SR12b and 18SRF to amplify SSU rDNA sequences (Nakayama et al. 1996, Takano and Horiguchi 2004, Iritani et al. 2018), and D1RF1, 25R1, D3A and 28-1483R to amplify partial LSU rDNA (Scholin et al. 1994, Nunn et al. 1996, Kogame et al. 1999, Daugbjerg et al. 2000). To amplify SSU rDNA sequences, almost complete SSU rDNA sequences were obtained using the SR1 and SR12b primers in the first round

of PCR. In the second round of PCR, the first PCR products were used as DNA templates, and three pairs of primers (SR1-SR5TAK, SR4-SR9 and SR8TAK-SR12b) were used for *P. stigmaticum*, four pairs of primers (SR1-SR5TAK, SR4-SR9, SR6-SR11 and SR8TAK-SR12b) were used for *P. verecundum*, three pairs of primers (SR1-18SRF, SR4-SR12b and SR8TAK-SR12b) were used for *P. asymmetricum*, and three pairs of primers (SR1-18SRF, SR4-SR9 and SR8TAK-SR12b) were used for *P. inerme*. To obtain partial LSU rDNA sequences, D1RF1 and 28-1483R were applied in the first round of PCR. In the second round of PCR, two pairs of primers (D1RF1-25R1 and D3A-28-1483R) were used for LSU rDNA amplification for all strains. The PCR conditions for both rounds of amplification consisted of one initial cycle of denaturation at 94°C for 5 min, followed by 35 cycles (in the second round for LSU rDNA, 25 cycles) of denaturation at 94°C for 30 s, annealing at 55°C for 30 s, and extension at 72°C. The time of extension step was 30 s for all sequences of *P. stigmaticum*. For other strains, it was changed by the length of targeting sequences; 2 min for the first round, 1 min 40 s for the two pairs of primers, SR1-18SRF and SR4-SR12b, and 1 min for other pairs of primers. PCR was completed by a final extension cycle at 72°C for 7 min. Purified PCR products were used in a sequencing reaction with ABI BigDye Terminator (Applied Biosystems, Foster City, California, USA) and subsequently purified with ethanol. The products were eluted in 18 μL of Hi-Di Formamide (Applied Biosystems) and sequenced with 3130 genetic analyzer (Applied Biosystems).

Both SSU rDNA sequences and partial LSU rDNA sequences were aligned using MUSCLE (Edgar 2004) together with 44 taxa, including *Perkinsus andrewsi* as an outgroup, and the alignments were modified manually using MEGA7 (Kumar et al. 2016). The highly divergent D2 region of LSU rDNA sequences was deleted. Consequently, 1770 positions of SSU rDNA and 1107 positions of LSU rDNA were aligned. The two aligned sequences for all taxa were concatenated using Kakusan4 (Tanabe 2011). No significant nucleotide compositional heterogeneity was detected for the combined data set (P = 0.99849 using the chi-square test in Kakusan4). The appropriate models of substitution ratio for concatenated rDNA sequences were determined using Kakusan4, resulted in separate model for maximum likelihood (ML) analysis and proportional model for Bayesian analysis. The appropriate models of DNA evolution for each rDNA

sequences were determined by AIC for ML analysis and by BIC for Bayesian analysis using Kakusan4, and resulted in the selection of the GTR + Gamma model. The parameters in these analyses for SSU rDNA were: assumed nucleotide frequencies A = 0.264, C = 0.199, G = 0.262 and T = 0.275; substitution rate matrix with A <-> C = 1.209517, A <-> G = 3.106689, A <-> T = 1.357108, C <-> G = 0.426016, C <-> T = 8.194312 and G <-> T = 1.000000. The proportion of sites were assumed to follow a gamma distribution with the shape parameter = 0.285810. The parameters for LSU rDNA were: assumed nucleotide frequencies A = 0.285, C = 0.191, G = 0.285 and T = 0.239. The substitution rate matrix had A <-> C = 0.648716, A <-> G = 2.091448, A <-> T = 0.816149, C <-> G = 0.510800, C <-> T = 5.576418 and G <-> T = 1.000000. The proportion of sites were assumed to follow a gamma distribution with the shape parameter = 0.369383. The ML analysis was performed using the RAxML 8.0.0 (Stamatakis 2006). Bootstrap analysis for ML was calculated for 1000 pseudo-replicates. The Bayesian analysis was performed using MrBayes 3.2.6 (Huelsenbeck and Ronquist 2001). Markov chain Monte Carlo iterations were carried out until the average standard deviation of split frequency fell below 0.01 (3400000 generations were attained) and trees were sampled every 100 generations. The first 850000 generations were discarded as burn-in. Posterior probabilities were calculated from all post burn-in trees.

RESULTS

Paragymnodinium stigmaticum Yokouchi, Onuma et Horiguchi sp. nov.

Light and scanning electron microscopy: Cells were 8.5–15.2 μm (12.2 ± 1.6 μm, mean ± SD, n = 47) long and 6.3–12.4 μm (9.6 ± 1.6 μm, n = 47) wide. The episome and hyposome were almost equal in size (Fig. 2.1A, B). The episome was conical to hemispherical, while the hyposome was hemispherical (Fig. 2.1A, B). The cingulum was wide, well excavated and descended by a distance equal to one quarter to a half of its own width (Fig. 2.1A, B). The sulcus was straight and widened slightly before reaching the antapex (Fig. 2.1A). A red, rod-shaped eyespot with a hook-like anterior extension was located in the upper part of the sulcal area (Fig. 2.1A). A slightly curved sulcal extension-like furrow (SEF) ran from the right end of the cingulum toward the apex (Fig. 2.1A). The nucleus was located in the central or dorsal area of the episome (Fig. 2.1B). *Paragymnodinium stigmaticum* captured its prey cell by a peduncle-like structure and engulfed it through the antapical area (Fig. 2.1C, D). It took about 30 sec to engulf a whole *Chroomonas* sp. cell (Ak01). A cell of *P. stigmaticum* could engulf up to five prey cells in one event, and digest them in one day. The cell sometimes discharged trichocysts and nematocysts (Fig. 2.1E). Chloroplasts were small, elongated ovals, and yellowish brown (Fig. 2.1F). Chloroplast autofluorescence demonstrated 5–10 in each cell (Fig. 2.1G). Ingested prey cells in food vacuoles (Fig. 2.1H) were also autofluorescent (Fig. 2.1I), and they were clearly distinguished from chloroplasts of *P. stigmaticum* by intensity of fluorescence (chloroplasts of *P. stigmaticum* emit weaker fluorescence than that of their prey) and shape. The motile cell swam near the bottom of culture dish during most of the light period. Cells encysted and attached to the bottom during the dark period, whereas a well-fed cell which had ingested sufficient prey cells encysted even before it became dark. Cysts were 8.0–13.1 μm (10.4 ± 1.2 μm, n = 21) long, 6.0–11.1 μm (8.6 ± 1.3 μm, n = 21) wide. Cell division took place during the cyst stage (Fig. 2.1J). When *P. stigmaticum* was starved for about 4 days, it formed another type of cyst (Fig. 2.1K). This cyst was oval and 6.5–11.4 μm (8.8 ± 1.5 μm, n = 10) long, 5.9–11.0 μm (7.8 ± 1.6 μm, n = 10) wide (Fig. 2.1K). The conditions required for this to return to the motile form are unknown.

SEM observations showed cells were covered by small polygonal amphiesmal vesicles (AVs) (Fig. 2.1L–O). AVs were arranged in 16 lateral rows, i.e., eight rows on the episome, four rows in the cingulum, and four rows on the hyposome (Fig. 2.1L–O). The SEF was slightly depressed and consisted of some elongate AVs (Fig. 2.1P), but the boundary between AVs belonging to the SEF and others was not clear (Fig. 2.1L, N, P). It was also difficult to distinguish the sulcal AVs from others (Fig. 2.1L, O). Consequently, the numbers of AVs comprising the SEF and sulcus were not defined. Some cells possessed a peduncle-like structure at the ventral area (Fig. 2.1Q, R). This structure consisted of a rod-shaped portion and a bulb-shaped tip, which protruded from the cell near the upper border of the cingulum on the ventral side (Fig. 2.1Q, R). A cell at the point of ingesting a prey cell through the antapical area of the hyposome revealed no involvement of a peduncle-like structure (Fig. 2.1S). Rarely, some cells were found to possess double transverse and longitudinal flagella (Fig. 2.1T). This condition corresponds to a planozygote formed after sexual fusion, as reported for some dinoflagellates (e.g., Blackburn et al. 1989).

Transmission electron microscopy: Fig. 2.2B, C, E, F are cell fixed using the first fixation protocol, while others were fixed using the second protocol (see material and methods). A transverse section of a motile cell shows a dinokaryon, amphiesmal vesicles, mitochondria, chloroplasts, eyespot, nematocysts and trichocysts (Fig. 2.2A). The food vacuoles of some cells contained recognizable prey cells (Fig. 2.2B), but in most cases digestion was far advanced and the contents unidentifiable (Fig. 2.2B). Each chloroplast contained a thylakoid-free region in its central area, and was traversed by one or two thylakoid bands (Fig. 2.2C). The chloroplasts were surrounded by three membranes (Fig. 2.2D) and contained multiple thylakoids (Fig. 2.2E). Fourteen to twenty thylakoid bands were located in the peripheral area of each chloroplast, and these were separated from each other, not forming triple thylakoid lamellae (Fig. 2.2E). The distance between adjacent thylakoid bands was 6–9 nm. The eyespot was located in one of the chloroplasts near the sulcus and consisted of two rows of osmiophilic globules (Fig. 2.2F). The trichocysts were typical for dinoflagellates and were peripheral (Fig. 2.2G, H), widening towards their apical extremity (Fig. 2.2G). Cells were covered by a typical amphiesma (Fig. 2.2I), the vesicles of which had no thecal plates or other plate-like

structures (Fig. 2.2I). The nucleus was a typical dinokaryon with condensed chromosomes (Fig. 2.2J), and was central or on the dorsal side of the cell. The nuclear envelope possessed nuclear pores but lacked nuclear envelope chambers (Fig. 2.2K).

The cell contained several nematocysts (Fig. 2.3). Each nematocyst was composed of a pyriform posterior body (PB) and an anterior operculum (Op). The PB was covered by a capsule (Ca) and a posterior chamber (PC), and contained a fibrous strand (FS). The anterior region of the PB was occupied by an anterior chamber (AC), and an anteriorly-directed stylet (St) (terms after Westfall et al. 1983). The length and width of nematocysts were approximately 1.1 μm and 0.8 μm, respectively. Taeniocysts and posterior vacuoles were not observed.

A microtubular strand of a peduncle-like structure (MSP) ran from the right side of the flagellar apparatus (Figs 2.4, 6). The MSP consisted of over 15 microtubules (Figs 2.4, 6). There were some electron-opaque vesicles near the MSP (Figs 2.4, 6). The extruded peduncle-like structure contained a nematocyst in its bulb-shaped body (Fig. 2.4A–D). The nematocyst in this structure had discharged a fibrous strand from the anterior area (Fig. 2.4B).

The flagellar apparatus of *Paragymnodinium stigmaticum* was reconstructed (Fig. 2.5) from serial sections (Figs 2.6, 7). Terminology follows Moestrup (2000). The transverse basal body (TB) and the longitudinal basal body (LB) were connected by three basal body connectives (bbc1–3) at an oblique angle of about 150° to one another (Figs 2.6B–D, 7A, B, F–H). Root 1 (R1) consisted of 16 microtubules and was inserted on the dorsal side of LB (Figs 2.6, 7A–E, N). R1 and LB were linked by the two connectives C1 and C2 (Fiss 6A–C, F, 7A, C). A left ventral fiber (LVF) linked R1 and a membrane near the end of basal bodies (Fig. 2.6A). Root 3 (R3) was comprised of a transverse microtubular root (TMR) and a transverse microtubular root extension (TMRE) (Figs 2.6, 7D, J–L). TMR was a single microtubular root and inserted on the right side of TB (Figs 2.6A–E, 7D, J, K). The TMRE consisted of four microtubules nucleated by the TMR (Figs 2.6D–F, 7K, L). Root 4 (R4), comprising a transverse striated root (TSR) and TSR microtubule (TSRM), was inserted on the left side of the TB (Figs 2.6B–E, 7A–D, K–M). R1 and R4 were linked by a striated root connective (SRC) (Figs 2.6B–E, 7C, D, H, I).

Despite our observations of flagellar apparatuses from nine cells, root 2 and a nuclear fibrous connective were not observed.

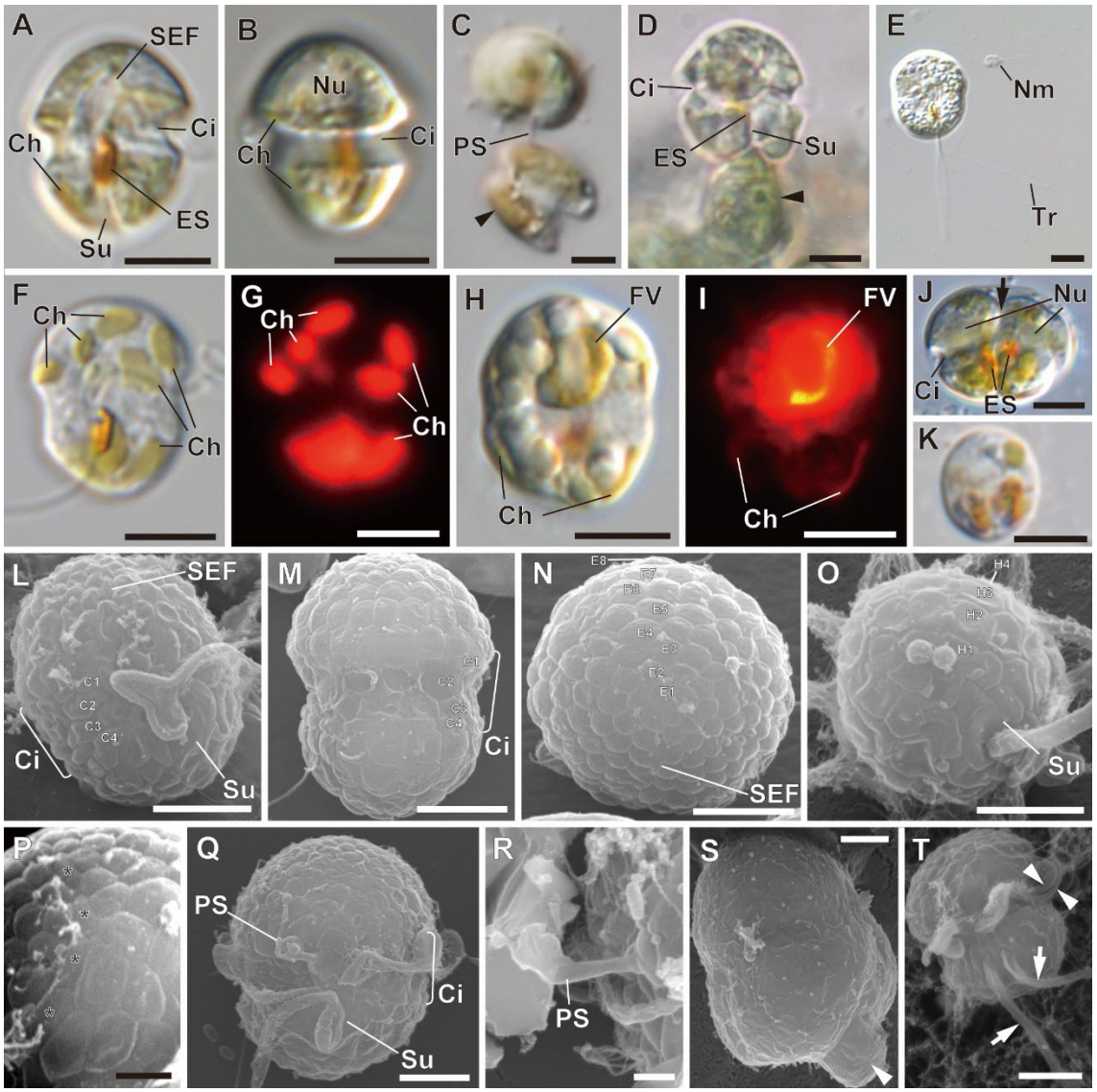
A
SEF
Ci
Ch
ES
Su
B
Nu
Ch
Ci
C
PS
D
Ci
ES
Su
E
Nm
Tr
F
Ch
Ch
G
Ch
Ch
H
FV
Ch
I
FV
Ch
J
Nu
Ci
ES
K
L
SEF
C1
C2
C3
C4
Ci
Su
M
C1
C2
C3
C4
Ci
N
E8
E7
E6
E5
E4
E3
E2
E1
SEF
O
H4
H3
H2
H1
Su
P
Q
PS
Ci
Su
R
PS
S
T

Fig. 2.1. (A–K) Differential interference contrast (DIC) and fluorescence light micrographs of *Paragymnodinium stigmaticum* sp. nov. (A) Ventral view. (B) Dorsal view. (C) A cell capturing a prey (arrowhead) with a peduncle-like structure. (D) A cell ingesting a prey (arrowhead) by engulfment. (E) A cell with discharged trichocysts and a nematocyst. (F, G) The same cell without a food vacuole. Note the fluorescence of the elongate chloroplasts of the dinoflagellate. (H, I) The same cell with a food vacuole. Note the fluorescence of the ingested prey in a food vacuole and of the dinoflagellate chloroplasts. (J) A dividing cell (division cyst). The plane of cell division is indicated by an arrow. (K) An encysted cell following starvation.

(L–T) Scanning electron micrographs of *Paragymnodinium stigmaticum sp. nov.* showing arrangement of the polygonal amphiesmal vesicles (AVs) on cell surface. (L) Ventral view. Vesicles in cingulum arranged in four rows (C1–C4). (M) Dorsal view. Vesicles in cingulum arranged in four rows (C1–C4). (N) Apical view. Vesicles in episome arranged in eight rows (E1–E8). (O) Antapical view. Vesicles in hyposome arranged in four rows (H1–H4). (F) Detail of SEF comprising some elongate AVs (asterisks). (Q) A cell with a peduncle-like structure at ventral area. (R) Detail of peduncle-like structure. (S) A cell ingesting its prey (arrowhead) through antapical area. (T) A cell with double longitudinal (arrows) and transverse (arrowheads) flagella. Scale bars; A–K = 5 μm, L–O, Q, S–T = 3 μm, P, R = 1 μm. Ch, chloroplast; Ci, cingulum; ES, eyespot; FV, food vacuole; Nu, nucleus; Nm, nematocyst; PS; peduncle-like structure; SEF, sulcal extension-like furrow; Su, sulcus; Tr, trichocyst.

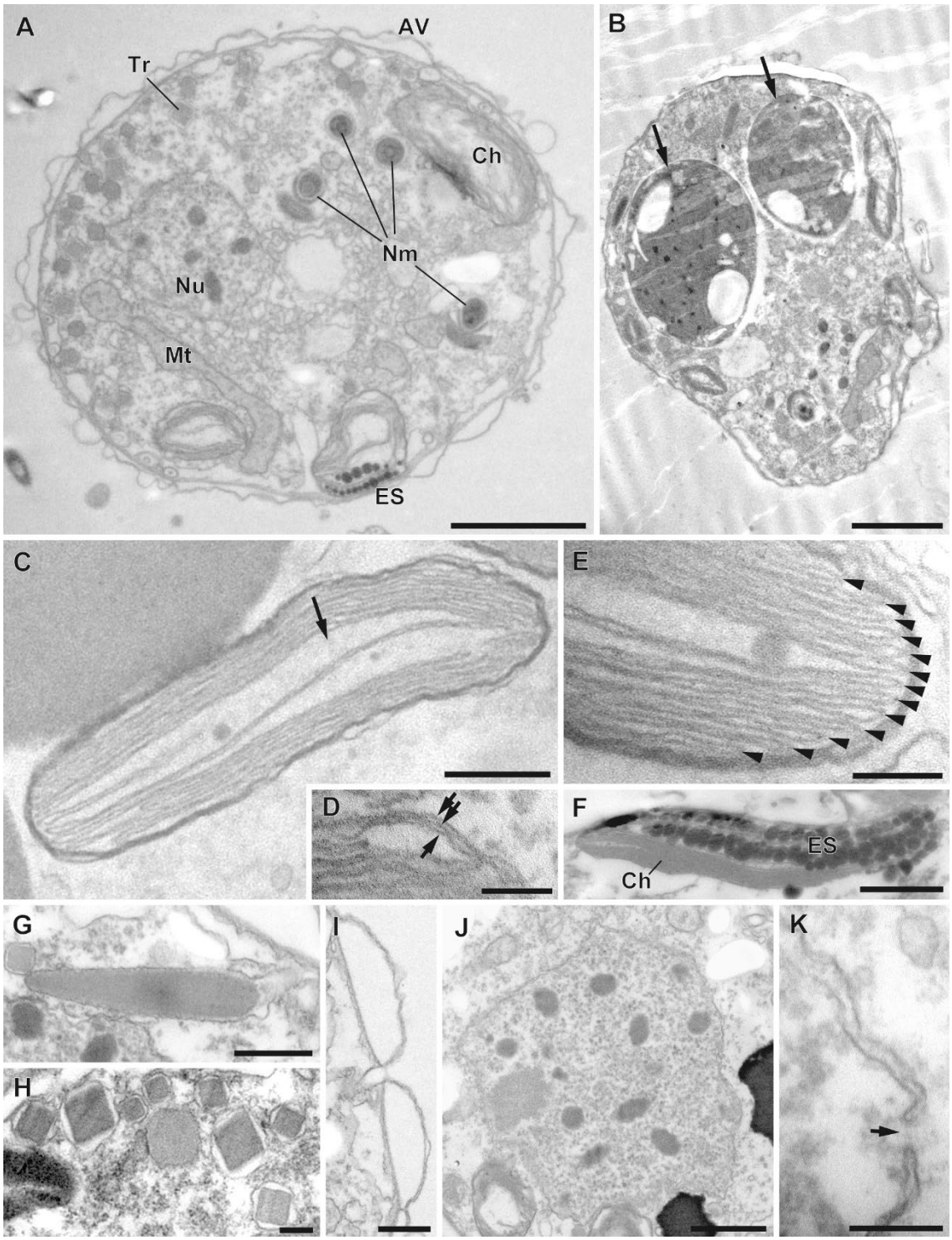
A
AV
Tr
Ch
Nm
Nu
Mt
ES
B
C
E
D
F
ES
Ch
G
I
J
K
H

Fig. 2.2. Transmission electron micrographs (TEMs) of *Paragymnodinium stigmaticum* sp. nov. Note: Figs 2B, C, E, F are from the first fixation protocol, while others are from the second fixation protocol (see Material and Methods). (A) Transverse section of cell. Eyespot is on ventral side. Scale bar = 2 µm. (B) Longitudinal section of cell with ingested prey cells (arrows). Scale bar = 2 µm. (C) Chloroplast with central thylakoid-free region (arrow). Scale bar = 200 nm. (D) Detail of chloroplast bounded by three membranes (arrows). Scale bar = 100 nm. (E) Detail of chloroplast with thylakoid bands (arrowheads). Scale bar = 100 nm. (F) Detail of eyespot. Scale bar = 1 µm. Scale bar = 100 nm. (G) Longitudinal section of a trichocyst. Scale bars = 200 nm. (H) Transverse section of trichocysts. Scale bars = 200 nm. (I) Detail of amphiesmal vesicles. No plate-like structure observed. Scale bar = 500 nm. (J) Nucleus containing condensed chromosomes. Scale bar = 1 µm. (K) Detail of nuclear envelope comprising two membranes and nucleopore (arrow). Scale bar = 100 nm. AV, amphiesmal vesicles; Ch, chloroplast; ES, eyespot; Mt, mitochondrion; N, nucleus; Nm, nematocyst; Tr, trichocyst.

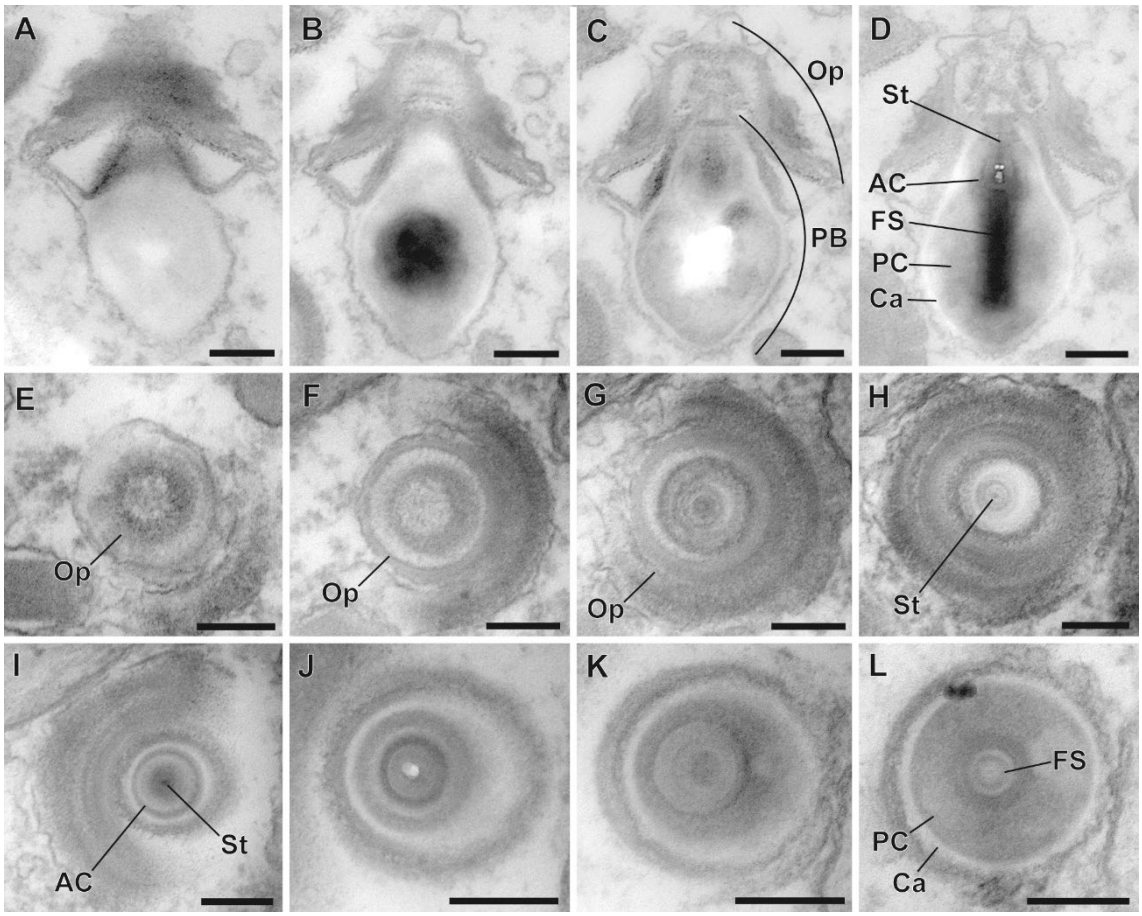

Fig. 2.3. Adjacent serial TEM sections of nematocysts of *Paragymnodinium stigmaticum sp. nov*. Scale bars = 200 nm. (A–D) Longitudinal sections from outside (A) to inside (D). (E–L) Transverse sections from anterior part (E) to central part (L). AC, anterior chamber; Ca, capsule; FS, fibrous strand; Op, operculum; PB, posterior body; PC, posterior chamber; St, stylet.

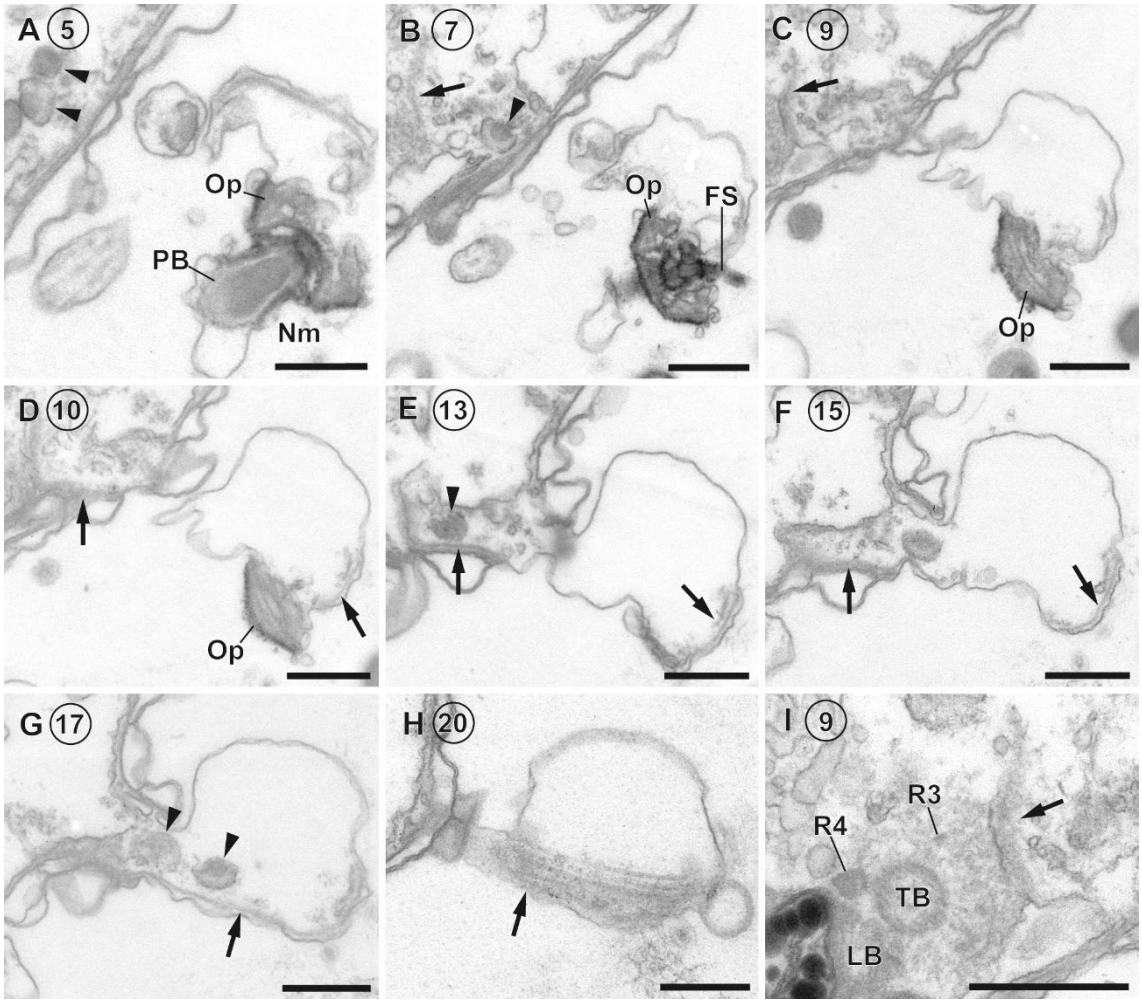

Fig. 2.4. (A–H) Serial TEM sections of extended peduncle-like structure with discharged nematocyst of *Paragymnodinium stigmaticum sp. nov*. Microtubular strand of a peduncle-like structure (MSP, arrows) with the electron-opaque vesicles (arrowheads) indicated. Section numbers circled with direction of sectioning from antapical to apical. (I) Detail of MSP in (C) and its positional relation to flagellar apparatus. Nm, nematocyst; Op, operculum; PB, posterior body; FS, fibrous strand; LB, longitudinal basal body; TB, transverse basal body; R3, root 3; R4, root 4. Scale bars = 500 nm.

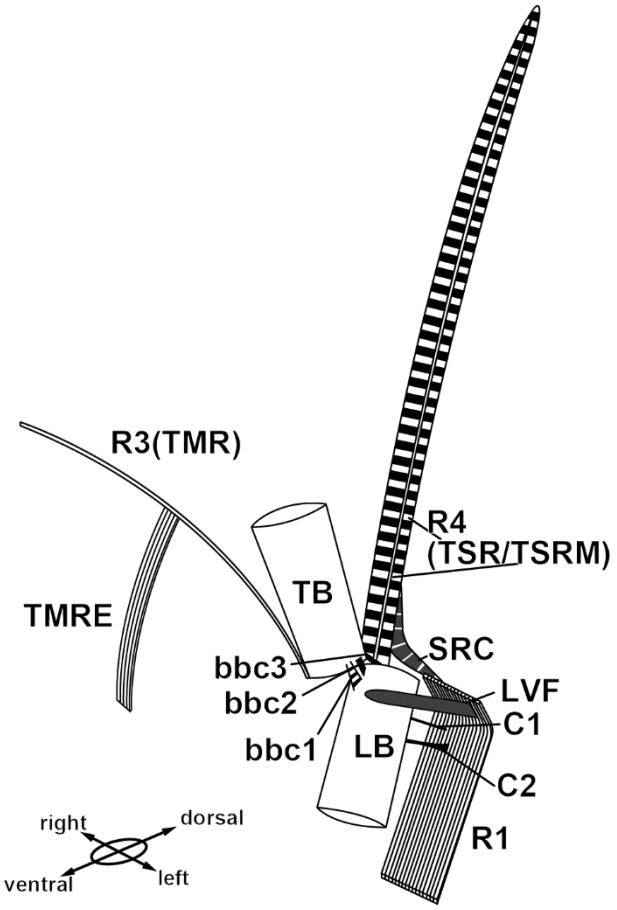

Fig. 2.5. Reconstruction of flagellar apparatus of *Paragymnodinium stigmaticum sp. nov.* bbc1, basal body connective 1; bbc2, basal body connective 2; bbc3, basal body connective 3; C1, connective 1 linking LB and R1; C2, connective 2 linking LB and R1; LB, longitudinal basal body; LVF, left-ventral fiber; R1, root 1; R3, root 3; R4, root 4; SRC, striated root connectives; TB, transverse basal body; TMR, transverse microtubular root; TMRE, transverse microtubular root extension; TSR, transverse striated root; TSRM, transverse striated root microtubule.

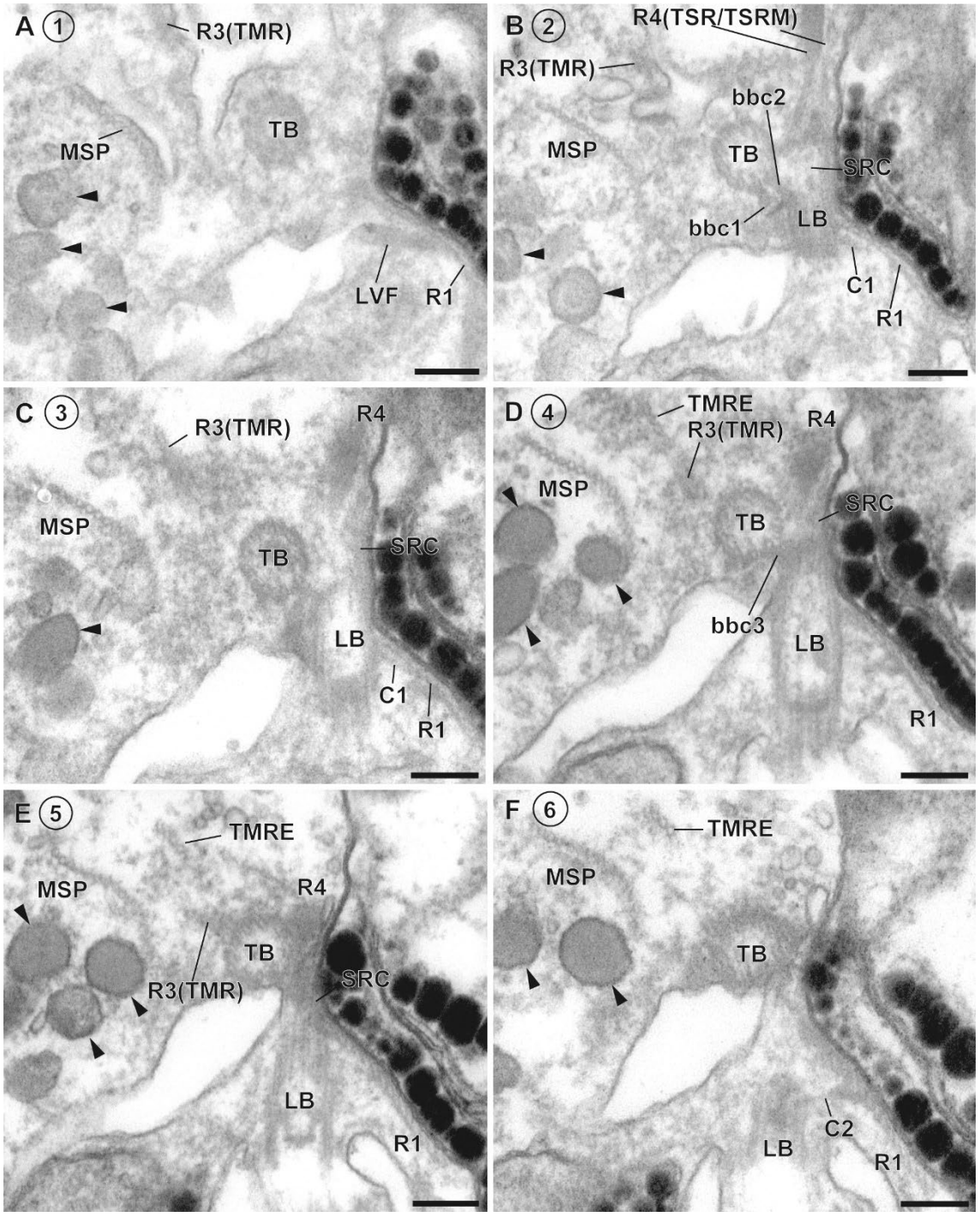
A 1
R3(TMR)
MSP
TB
LVF
R1
B 2
R4(TSR/TSRM)
R3(TMR)
bbc2
MSP
TB
SRC
bbc1
LB
C1
R1
C 3
R3(TMR)
R4
MSP
TB
SRC
LB
C1
R1
D 4
TMRE
R3(TMR)
R4
MSP
SRC
TB
bbc3
LB
R1
E 5
TMRE
MSP
R4
TB
SRC
R3(TMR)
LB
R1
F 6
TMRE
MSP
TB
C2
LB
R1

Fig. 2.6. Serial TEM sections of flagellar apparatus of *Paragymnodinium stigmaticum sp. nov.* Section numbers indicated in circles. Microtubular strand of a peduncle-like structure (MSP) with electron-opaque vesicles (arrowheads) are also shown. Direction of sectioning is from the ventral to the dorsal. bbc1, basal body connective 1; bbc2, basal body connective 2; bbc3, basal body connective 3; C1, connective 1 linking LB and R1; C2, connective 2 linking LB and R1; LB, longitudinal basal body; LVF, left-ventral fiber; R1, root 1; R3, root 3; R4, root 4; SRC, striated root connectives; TB, transverse basal body; TMR, transverse microtubular root; TMRE, transverse microtubular root extension; TSR, transverse striated root; TSRM, transverse striated root microtubule. Scale bars = 200 nm.

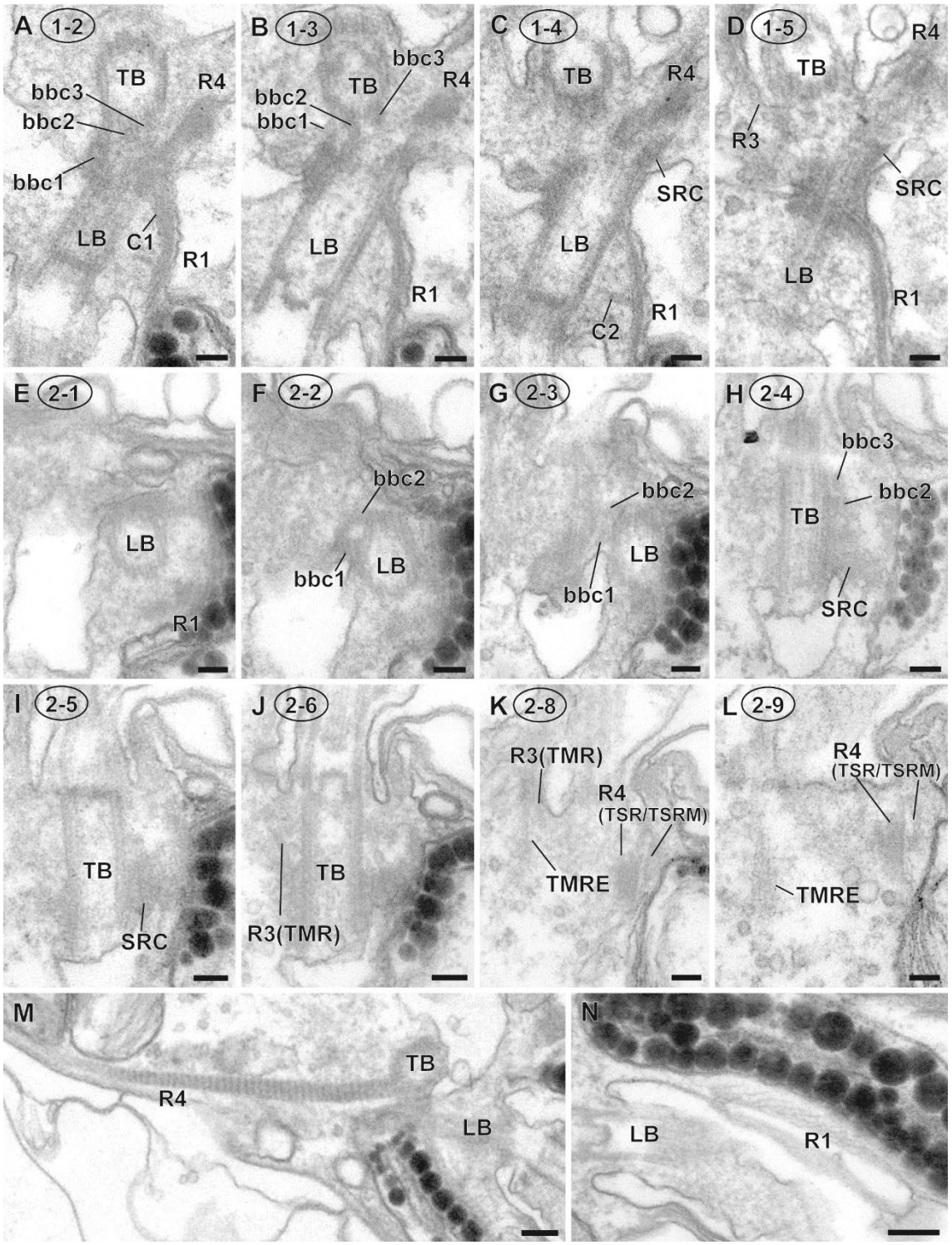
A 1-2
TB
R4
bbc3
bbc2
bbc1
LB
C1
R1
B 1-3
bbc3
TB
R4
bbc2
bbc1
LB
R1
C 1-4
TB
R4
SRC
LB
C2
R1
D 1-5
R4
TB
R3
SRC
LB
R1
E 2-1
LB
R1
F 2-2
bbc2
bbc1
LB
G 2-3
bbc2
LB
bbc1
H 2-4
bbc3
bbc2
TB
SRC
I 2-5
TB
SRC
J 2-6
TB
R3(TMR)
K 2-8
R3(TMR)
R4
(TSR/TSRM)
TMRE
L 2-9
R4
(TSR/TSRM)
TMRE
M
TB
R4
LB
N
LB
R1

Fig. 2.7. Serial TEM sections of flagellar apparatus of *Paragymnodinium stigmaticum sp. nov.* (A–D) Serial sections from dorsal to ventral with section numbers circled. Scale bars = 100 nm. (E–L) Serial sections from antapex to apex with section numbers circled. Scale bars = 100 nm. (M) Entire R4. Scale bar = 200 nm. (N) Detail of R1. Scale bar = 200 nm. bbc1, basal body connective 1; bbc2, basal body connective 2; bbc3, basal body connective 3; C1, connective 1 linking LB and R1; C2, connective 2 linking LB and R1; LB, longitudinal basal body; R1, root 1; R3, root 3; R4, root 4; SRC, striated root connectives; TB, transverse basal body; TMR, transverse microtubular root; TMRE, transverse microtubular root extension; TSR, transverse striated root; TSRM, transverse striated root microtubule.

***Paragymnodinium verecundum* Yokouchi et Horiguchi sp. nov.**

Light and scanning electron microscopy: Cells were 9.4–17.1 μm (13.2 ± 1.9 μm, n = 26) long and 5.7–13.6 μm (9.8 ± 1.7 μm, n = 26) wide. The episome and hyposome were almost equal in size (Fig. 2.8A, B). The episome ranged from conical to hemispherical, while the hyposome was hemispherical (Fig. 2.8A, B). The cingulum was wide and well excavated and descended by a distance equal to one quarter to a half of its own width (Fig. 2.8A, B). The sulcus was straight and widened slightly before reaching the antapex (Fig. 2.8A). A red, rod-shaped eyespot with a hook-like anterior extension was located in the upper part of the sulcal area (Fig. 2.8A). A slightly curved SEF ran from the right end of the cingulum toward the apex (Fig. 2.8A). The nucleus was located in the central area of the cell (Fig. 2.8B). Ingestion of prey cells was achieved in the antapical area (Fig. 2.8C). It took about 1 min to engulf an entire cell of *Rhodomonas* sp. (strain Mr06). The yellowish-brown chloroplasts were small and elongate ovate (Fig. 2.8D). Chloroplast autofluorescence indicated the presence of six to 12 chloroplasts per cell (Fig. 2.8E). Ingested prey cells in food vacuoles (Fig. 2.8F) were also autofluorescent (Fig. 2.8G) but were clearly distinguished from chloroplasts of *P. verecundum* by their round, nonelongated shape and a heightened intensity of fluorescence. The motile cell swam near the bottom of the culture dish during most of the light period. Cells encysted and attached to the bottom during the dark period, but well-fed cells with sufficient prey cells encysted before it became dark. Cell division took place during the cyst stage (Fig. 2.8H). Cells of *P. verecundum* did not form any other type of cyst even when they were starved.

When the motile cells were illuminated by a point source of strong light (> approximately 100 μmol photons m^{-2} s^{-1}), they swam in the opposite direction (Video 2.1). The cells did not show any obvious response to weak light (< approximately 100 μmol photonsm^{-2} s^{-1}). The cells were negatively phototactic when exposed to blue light, irrespective of the time of day, but showed no response to red light. When cells of *Paragymnodinium verecundum* were grown in the culture room, they tended to encyst on the opposite side of the culture vessel to the light source.

SEM observations showed that the cells were covered by small polygonal amphiesmal vesicles (Avs) (Fig. 2.8I–L). Avs were arranged in 15 lateral rows, with six rows on the episome, four rows in the cingulum and five rows on the hyposome (Fig.

2.8I–L). The SEF was obvious and contained some small AVs (Fig. 2.8I, K, M), but the boundary between the Avs of the SEF and the episome was indistinct (Fig. 2.8M). Similarly, the boundary between the sulcal Avs and those of the hyposome was not clear (Fig. 2.8L). Some cells possessed a rod-shaped peduncle-like structure, which protruded from the cell near the upper border of the cingulum on the ventral side (Fig. 2.8N).

Transmission electron microscopy: Figures 9B, H, J, K, 10E were obtained from cells fixed using the first fixation protocol, while the remainder were from individuals fixed using the second protocol (see Material and Methods). A longitudinal section of a motile cell showed a dinokaryon, Avs, mitochondria, chloroplasts, an eyespot, nematocysts and trichocysts (Fig. 2.9A). The food vacuoles of some cells contained recognizable prey cells (Fig. 2.9B), but in most cases digestion was too far advanced to allow identification of the prey. Each chloroplast contained a thylakoid-free region in its central area traversed by one or two thylakoid bands (Fig. 2.9C). Each chloroplast was surrounded by three membranes (Fig. 2.9D) and contained approximately 20 separated thylakoid bands rather than the expected triple stacked lamellae of dinoflagellates (Fig. 2.9E, F). The distance between adjacent thylakoid bands was less than 18 nm, but was influenced by the fixation protocol. The eyespot was located in one of the chloroplasts near the sulcus and consisted of two rows of osmiophilic globules (Fig. 2.9G). The trichocysts were typical for dinoflagellates and were peripheral (Fig. 2.9H, I). Cells were covered by a typical naked amphiesma (Fig. 2.9J), that is the outer plasma membrane underlain by vesicles lacking thecal plates or other plate-like structures (Fig. 2.9J). The nucleus was a typical dinokaryon with condensed chromosomes (Fig. 2.9K) and was central or on the dorsal side of the cell. The nuclear envelope possessed nuclear pores but lacked nuclear envelope chambers (Fig. 2.9K). Cells possessed a pusule in the ventral area of the hyposome (Fig. 2.9M). The pusule comprised a central collecting tubule and peripheral dented vesicles (sensu Dodge 1972).

The cell contained several nematocysts (Fig. 2.10). Each nematocyst was composed of a pyriform posterior body (PB) and an anterior operculum (Op). The PB was covered with a capsule (Ca) and a posterior chamber (PC) and contained a fibrous strand (FS) with a filament (Fi) in its central area. The anterior region of the PB was occupied by an anterior chamber (AC) and an anteriorly directed stylet (St) (terms after

Westfall et al. 1983). The length and width of nematocysts were approximately 1.2 and 0.8 μm, respectively. Taeniocysts and posterior vacuoles were not observed.

A microtubular strand of a peduncle-like structure (MSP) ran from the right side of the flagellar apparatus (Fig. 2.11). The MSP consisted of over 18 microtubules. There were some electron-opaque vesicles near the MSP (Fig. 2.11A–D). The extruded peduncle-like structure contained a nematocyst in its bulb-shaped distal end (Fig. 2.11B–G), the latter of which was capable of discharging an FS from the anterior area (Fig. 2.11F).

The flagellar apparatus of *Paragymnodinium verecundum* was reconstructed from serial sections (Figs 2.12–14). The transverse basal body (TB) and the longitudinal basal body (LB) were connected at an angle of about 130° to one another by three basal body connectives (bbc1–3) (Fig. 2.14F, G). Root1 (R1) consisted of 19 microtubules and was inserted on the dorsal side of LB (Figs 2.13A–F and 14E–L), and they were further linked by two connectives, C1 and C2 (Figs 2.13A and 14J). A left ventral fiber (LVF) linked R1, the left side of LB and a membrane near the end of basal bodies (Figs 2.13A–G and 14F–I). R3 was comprised of a transverse microtubular root (TMR) and a TMR extension (TMRE) (Figs 2.13I–K and 14A–D). The TMR only had a single microtubule and was inserted on the right side of the TB (Figs 2.13I–K and 14A–D). The TMRE consisted of four microtubules nucleated on the TMR (Figs 2.13J, K and 14A). R4, comprised of a transverse striated root (TSR) and a TSR microtubule (TSRM), was inserted on the left side of the TB (Figs 2.13G, H and 14A–E). R1 and R4 were linked by a striated root connective (SRC) (Figs 2.13E, F and 14C–E). Careful scrutiny of three different sets of serial sections through the flagellar apparatus failed to reveal the presence of either R2 or a nuclear fibrous connective.

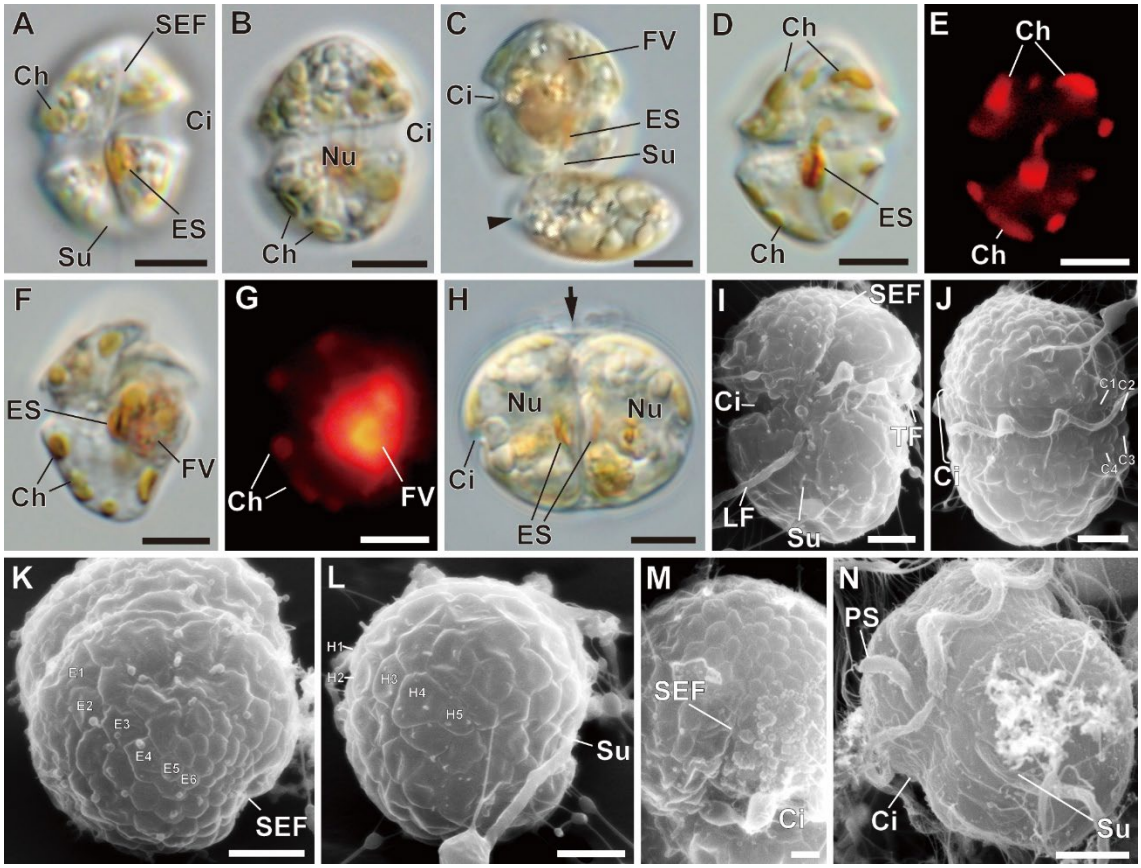

Fig. 2.8. (A–H) Differential interference contrast (DIC) and fluorescence light micrographs of *Paragymnodinium verecundum* sp. nov. (A) Ventral view. (B) Dorsal view. (C) A cell ingesting prey (arrowhead). (D, E) The same cell without a food vacuole. Note the fluorescence of the elongate chloroplasts of the dinoflagellate. (F, G) The same cell with a food vacuole. Note the fluorescence of the ingested prey and of the dinoflagellate chloroplasts. (H) A dividing cell (division cyst). The plane of cell division is indicated by an arrow.

(I–N) Scanning electron micrographs of *P. verecundum* showing arrangement of the polygonal amphiesmal vesicles (AVs) on cell surface. (I) Ventral view. (J) Right lateral view. Vesicles in cingulum arranged in four rows (C1–C4). (K) Apical view. Vesicles in episome arranged in six rows (E1-E6). (L) Antapical view. Vesicles in hyposome arranged in five rows (H1-H5). (M) Detail of SEF. (N) Cell with a peduncle-like structure at ventral area. Scale bars; A–H = 5 µm, I–L, N = 3 µm, M = 1 µm. Ch, chloroplast; Ci, cingulum; ES, eyespot; FV, food vacuole; N, nucleus; PS, peduncle-like structure; SEF, sulcal extension-like furrow; Su, sulcus.

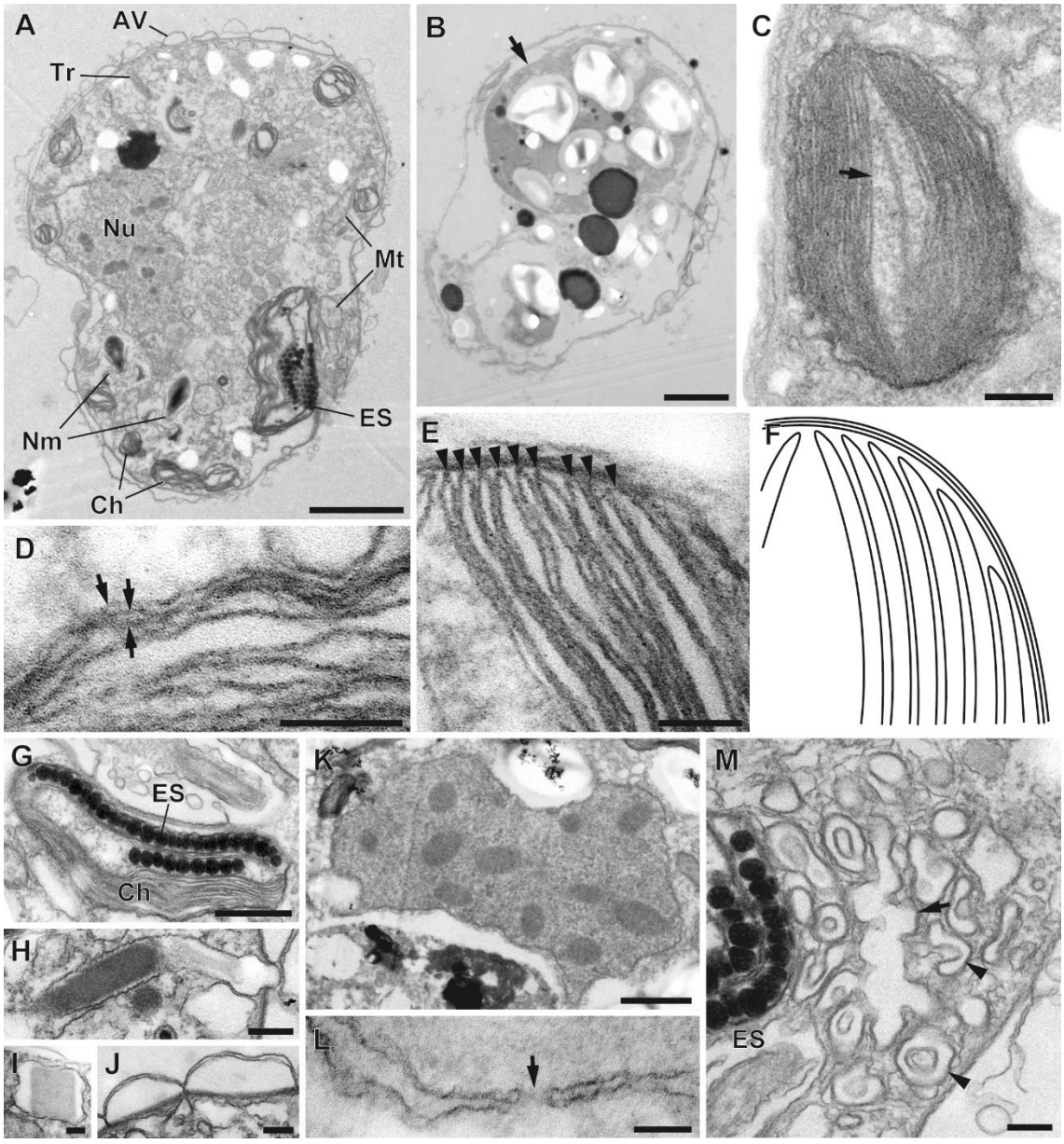
A
AV
Tr
Nu
Mt
Nm
ES
Ch
B
C
D
E
F
G
ES
Ch
H
I
J
K
L
M
ES

Fig. 2.9. Transmission electron micrographs (TEMs) of *Paragymnodinium verecundum* sp. nov. Note: Figs 9B, H, J, K are from the first fixation protocol, while others are from the second fixation protocol (see Material and Methods). (A) Longitudinal section of cell. Eyespot is on ventral side. Scale bar = 2 µm. (B) Cell with ingested prey cells (arrow). Scale bar = 2 µm. (C) Chloroplast with central thylakoid-free region (arrow). Scale bar = 200 nm. (D) Detail of chloroplast bounded by three membranes (arrows). Scale bar = 100 nm. (E) Detail of chloroplast and (F) its schematic illustration with thylakoid bands (arrowheads). Scale bar = 100 nm. (G) Detail of eyespot. Scale bar = 500 nm. (H) Longitudinal section of a trichocyst. Scale bars = 200 nm. (I) Transverse section of trichocysts. Scale bars = 100 nm. (J) Detail of amphiesmal vesicles. No plate-like structure observed. Scale bar = 200 nm. (K) Nucleus containing condensed chromosomes. Scale bar = 1 µm. (L) Detail of nuclear envelope comprising two membranes and nucleopore (arrow). Scale bar = 100 nm. (M) Pusule comprising a collecting tubule (arrow) and pusule vesicles (arrowheads). Scale bar = 200 nm. AV, amphiesmal vesicles; Ch, chloroplast; ES, eyespot; Mt, mitochondrion; N, nucleus; Nm, nematocyst.

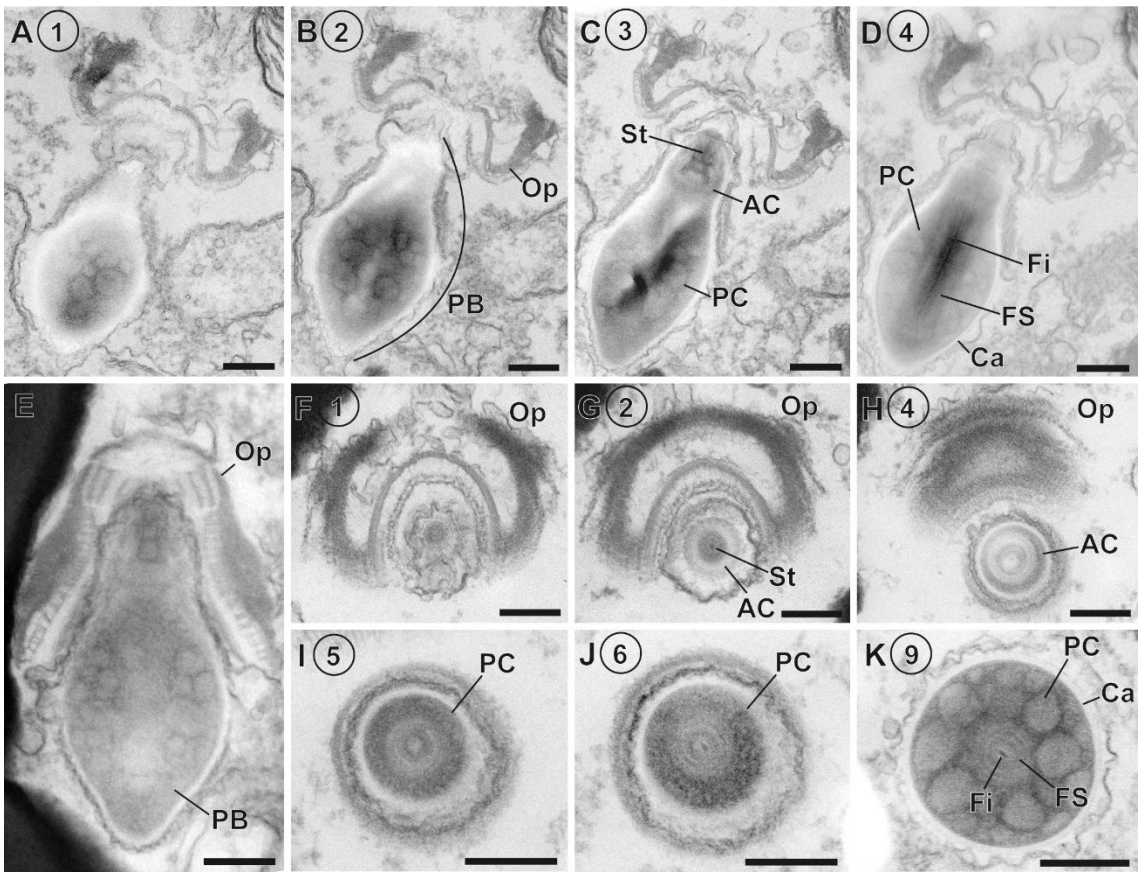

Fig. 2.10. Serial TEM sections of nematocysts of *Paragymnodinium verecundum* sp. nov. Section numbers indicated in circles. Note: Fig. 2.10E is from the first fixation, while the others are from the second fixation (see Material and Methods). (A–D) Longitudinal sections from outside (A) to inside (D). (E) Longitudinal section showing the posterior body and the operculum. (F–K) Transverse sections from anterior part (F) to posterior part (K). AC, anterior chamber; Ca, capsule; Fi, Filament; FS, fibrous strand; Op, operculum; PB, posterior body; PC, posterior chamber. Scale bars = 200 nm.

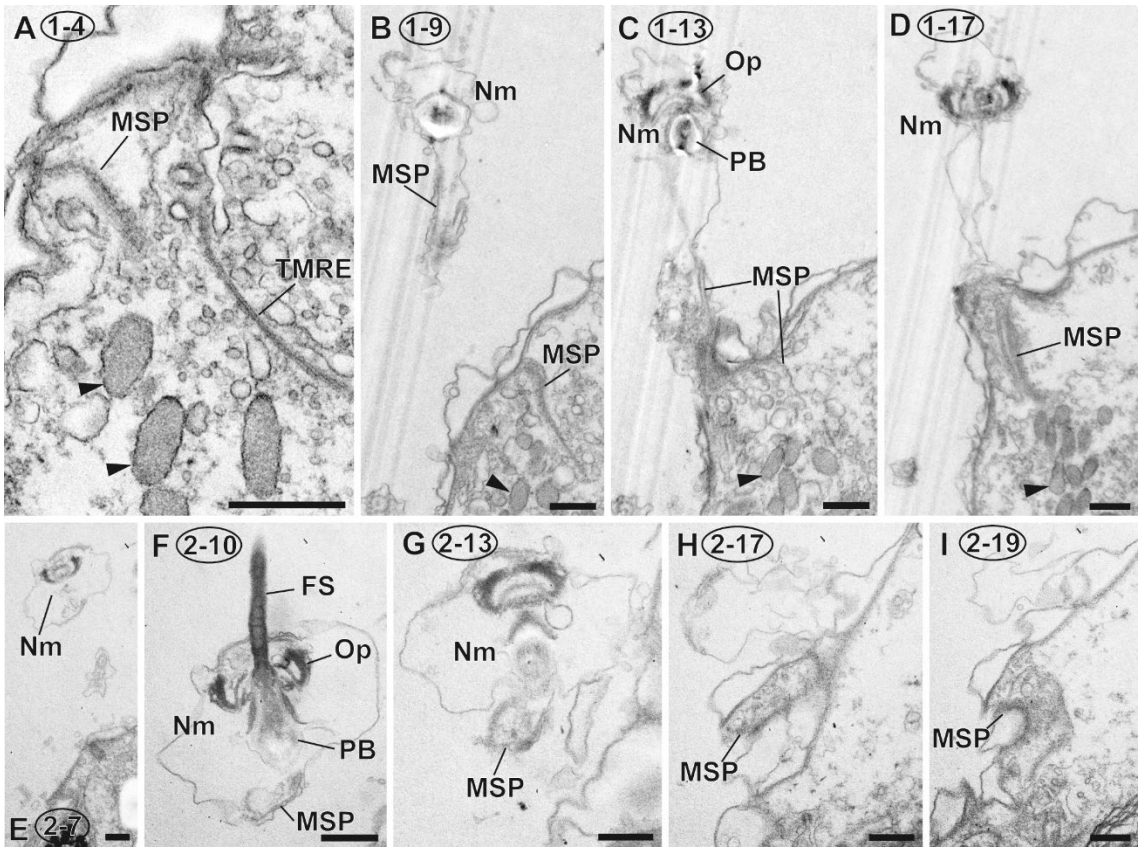

Fig. 2.11. Serial TEM sections of extended peduncle-like structure with discharged nematocyst of *Paragymnodinium verecundum* sp. nov. Microtubular strand of a peduncle-like structure (arrows) with the electron-opaque vesicles (arrowheads) indicated. Section numbers circled with direction of sectioning from left to right. Nm, nematocyst; Op, operculum; PB, posterior body; TMRE; transverse microtubular root extension. Scale bars = 500 nm.

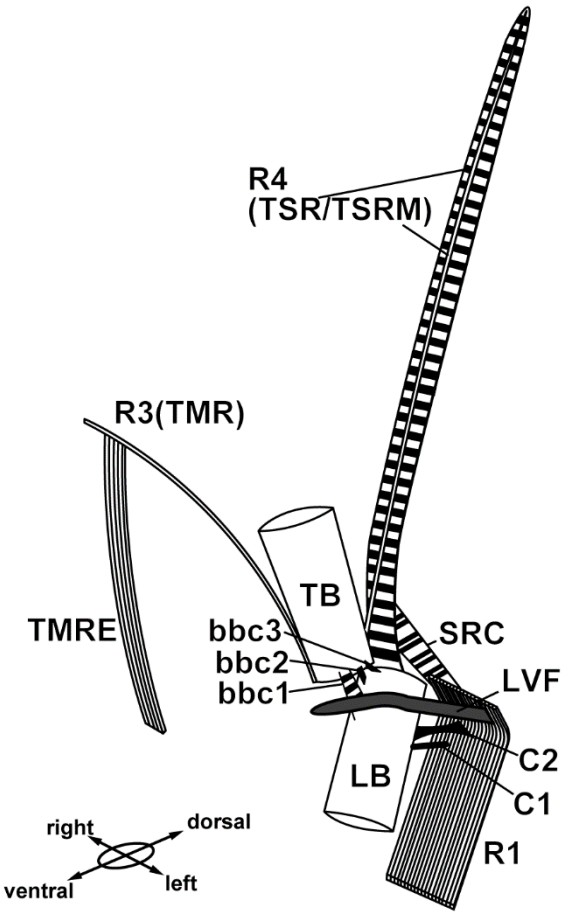

Fig. 2.12. Reconstruction of flagellar apparatus of *Paragymnodinium verecundum* sp. nov. bbc1, basal body connective 1; bbc2, basal body connective 2; bbc3, basal body connective 3; C1, connective 1 linking LB and R1; C2, connective 2 linking LB and R1; LB, longitudinal basal body; LVF, left-ventral fiber; R1, root 1; R3, root 3; R4, root 4; SRC, striated root connectives; TB, transverse basal body; TMR, transverse microtubular root; TMRE, transverse microtubular root extension; TSR, transverse striated root; TSRM, transverse striated root microtubule.

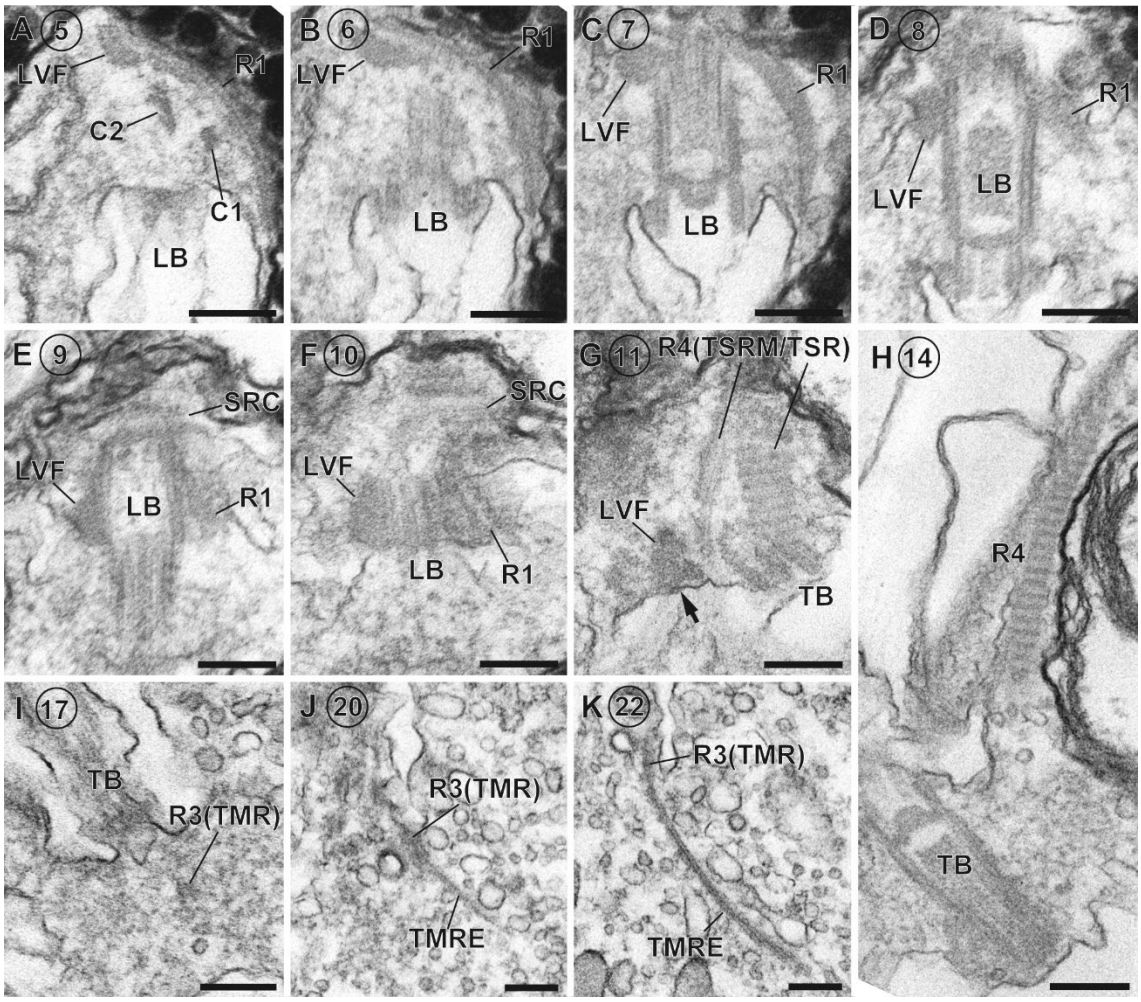

Fig. 2.13. Serial TEM sections of flagellar apparatus of *Paragymnodinium verecundum* sp. nov. Section numbers indicated in circles. Direction of sectioning is from left to right. C1, connective 1 linking LB and R1; C2, connective 2 linking LB and R1; LB, longitudinal basal body; LVF, left-ventral fiber; R1, root 1; R3, root 3; R4, root 4; SRC, striated root connectives; TB, transverse basal body; TMR, transverse microtubular root; TMRE, transverse microtubular root extension; TSR, transverse striated root; TSRM, transverse striated root microtubule. Scale bars = 200 nm.

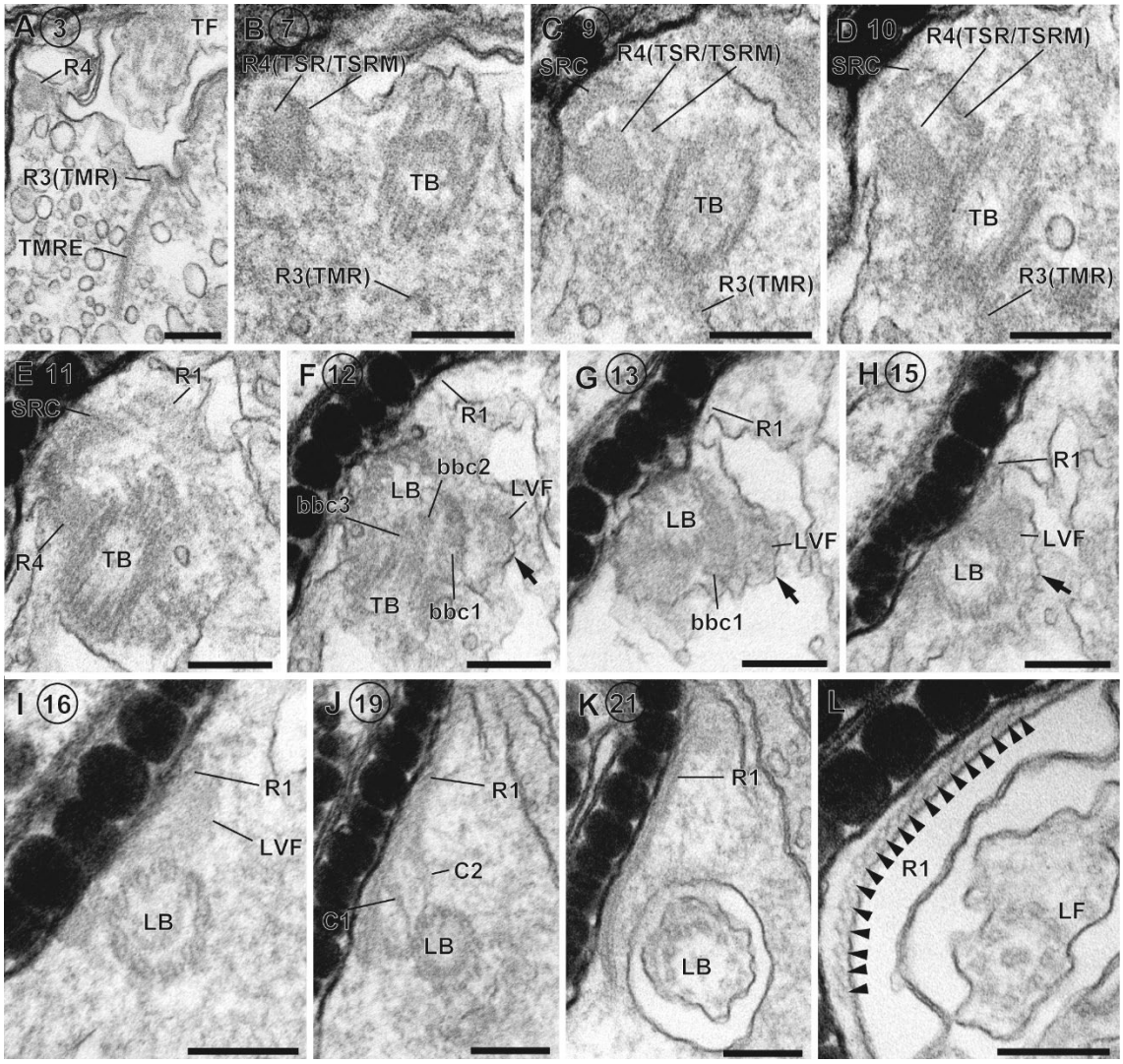

Fig. 2.14. Serial TEM sections of flagellar apparatus of *Paragymnodinium verecundum* sp. nov. (A–K) Serial sections with section numbers circled. Direction of sectioning from antapical to apical. (L) Detail of R1. bbc1, basal body connective 1; bbc2, basal body connective 2; bbc3, basal body connective 3; C1, connective 1 linking LB and R1; C2, connective 2 linking LB and R1; LB, longitudinal basal body; LF, longitudinal flagellum; LVF, left-ventral fiber; R1, root 1; R3, root 3; R4, root 4; SRC, striated root connectives; TB, transverse basal body; TF, transverse flagellum; TMR, transverse microtubular root; TMRE, transverse microtubular root extension; TSR, transverse striated root; TSRM, transverse striated root microtubule. Scale bars = 200 nm.

Paragymnodinium asymmetricum **Yokouchi, Takahashi, Nguyen, Iwataki et Horiguchi sp. nov.**

Light and scanning electron microscopy: Cells small, 7.9–12.6 µm (9.6 ± 1.0 µm, mean ± SD, n = 55) long and 4.7–9.0 µm (6.9 ± 1.0 µm, n = 55) wide. Episome and hyposome were almost equal in size (Fig. 2.15A, B). Episome was conical (Fig. 2.15A, B); hyposome was asymmetric; right side larger than left side (Fig. 2.15A, B). Cingulum was wide, well excavated and descended by a distance one quarter to a half of its own width (Fig. 2.15A, B). Sulcus was straight and widened slightly before reaching the antapex (Fig. 2.15A). Eyespot was not observed. A straight sulcal extension-like furrow (SEF, sensu Kang et al. 2010) ran from the right end of the cingulum toward the apex (Fig. 2.15A). Chloroplast was single and yellow brown (Fig. 2.15C), mainly occupying posterior area of hyposome, but with lateral lobes extending anteriorly into episome but not reaching the apex (Fig. 2.15C, D). Nucleus was located in the central area of episome (Fig. 2.15B, C, E). DAPI staining confirmed the single nucleus occupied almost the entire episome (Fig. 2.15C, E). The motile cell was planktonic and free swimming. Cells encysted during the dark period. Cysts were spherical and covered with a wall (Fig. 2.15F). The organism grew in complete isolation from other eukaryotes and did not show feeding behavior when cocultured with potential prey organisms.

SEM observations showed cells were covered by small polygonal amphiesmal vesicles (AVs; Fig. 2.15G–O). These AVs in the episome were arranged in anything from 5 to 7 lateral rows (Fig. 2.15G–L). Such variation was not observed in the cingulum and the sulcus. The AVs in the cingulum were arranged in five rows (Fig. 2.15J). The sulcus was deeply incised but the exact boundary of sulcus with the remainder of the cell was not sharply defined (Fig. 2.15G, J, M). The SEF was less incised than the sulcus and consisted of nine elongate AVs (Fig. 2.15G, H, K, L, N, O). The hyposome was also covered with AVs arranged in approximately four lateral rows, but the exact number was difficult to ascertain because of its asymmetric shape (Fig. 2.15M).

Transmission electron microscopy: Figures 2.16A–D and 2.17 are cell fixed using the first fixation protocol, while others were fixed using the second protocol (see material and methods). The positioning and morphology of the nucleus and chloroplast in motile cells were confirmed in thin-sectioned material (Fig. 2.16A). The nucleus was

a typical dinokaryon with condensed chromosomes, and occupied most of the episome (Fig. 2.16B). It was surrounded by numerous mitochondria (Fig. 2.16B). The nuclear envelope possessed nuclear pores but lacked nuclear envelope chambers (Fig. 2.16C). Trichocysts were typical for dinoflagellates and were peripherally arranged (Fig. 2.16D, E). Cells were covered by a typical amphiesma, the vesicles of which had no thecal plates or other plate-like structures (Fig. 2.16F). A microtubular strand of a peduncle (MSP) ran from the right side of the flagellar apparatus (Fig. 2.16G–J). There were some electron-opaque vesicles near the MSP (Fig. 2.16G–J).

Chloroplast was surrounded by three membranes. The posterior mass contained condensed thylakoids (Fig. 2.17A); most of which were double stacked, and the distance between adjacent thylakoid bands was approximately 6–10 nm (Fig. 2.17B). On the other hand, the lateral lobes contained double or triple stacked thylakoid bands, and the distance between bands was relatively greater and more variable (Fig. 2.17C, D). The boundary between the more condensed thylakoids of the posterior mass and the less condensed thylakoids of the lateral lobes was obvious (Fig. 2.17E).

Cells each contained at most four nematocysts (Fig. 2.18). Each nematocyst was composed of an oval posterior body and an anterior operculum. The posterior body was covered by a capsule and a posterior chamber, and contained a fibrous strand. The anterior region of the posterior body was occupied by an anterior chamber with a stylet (sensu Westfall et al. 1983). A central filament-like structure was observed in the central axis of the fibrous strand (Fig. 2.18B), but could not be resolved in the transverse serial sections (Fig. 2.18J–L). The length and width of nematocysts were approximately 0.8 μm and 0.5 μm, respectively. Taeniocysts and posterior vacuoles were not observed.

The flagellar apparatus of *Paragymnodinium asymmetricum* was reconstructed (Fig. 2.19) from serial sections (Figs 2.20, 21). The transverse basal body (TB) and the longitudinal basal body (LB) were connected at an oblique angle of about 150° to one another, by a basal body connective (bbc; Figs 2.20F–H, 21C). Root 1 (R1) consisted of 12 microtubules and was inserted on the dorsal side of LB (Figs 2.20A–I, 21D–H). R1 and LB were linked by the connective C1 (Figs 2.20E, 21D). Root 3 (R3) was comprised of a transverse microtubular root (TMR) and a transverse microtubular root extension (TMRE; Figs 2.20C–J, 21A, B, K, L). TMR was a single microtubular root and inserted

on the right side of TB (Figs 2.20D–F, 21A, K). The TMRE consisted of six microtubules nucleated by the TMR (Figs 2.20C–J, 21A, B, K, L). Root 4 (R4), comprising a transverse striated root (TSR) and TSR microtubule (TSRM), was inserted on the left side of the TB (Figs 2.20G–L, 21D–J). R1 and R4 were linked by a striated root connective (SRC; Figs 2.20H, I, 21E–G, J). Despite our observations of the flagellar apparatus being made from five different cells, the expected root 2 and a nuclear fibrous connective were not observed.

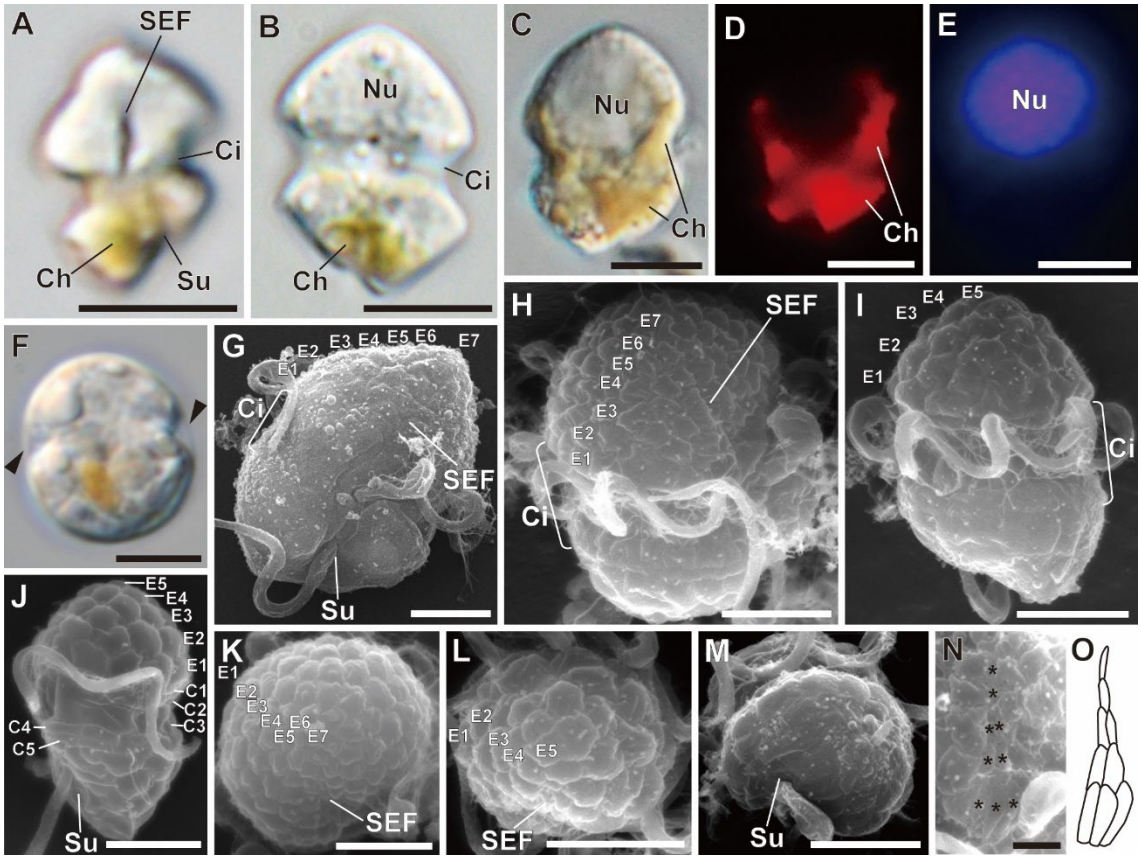

Fig. 2.15. (A–F) Differential interference contrast (DIC) and fluorescence light micrographs of *Paragymnodinium asymmetricum* sp. nov. (A) Ventral view. (B) Dorsal view. (C–E) The same cell showing the fluorescence of (D) the chloroplasts and (E) the nucleus stained by DAPI. (F) Cyst with outer membrane (arrowhead).

(G–O) Scanning electron micrographs of *Paragymnodinium asymmetricum* sp. nov., showing arrangement of polygonal amphiesmal vesicles (AVs) on cell surface. (G, H) Ventral view. Vesicles in episome arranged in seven rows (E1–E7). (I) Dorsal view. Vesicles in episome arranged in five rows (E1–E5). (J) Left lateral view. Vesicles in cingulum arranged in five rows (C1–C5); those in episome arranged in five rows (E1–E5). (K and L) Apical view, showing episome and its vesicles arranged in seven (K) or five (L) rows. (M) Antapical view, showing hyposome, its vesicles and sulcus. (N) Detail of SEF comprising some elongate AVs (asterisks). (O) Schematic illustration of SEF showing arrangement of AVs. Ch, chloroplast; Ci, cingulum; Nu, nucleus; SEF, sulcal extension-like furrow; Su, sulcus. Scale bars; A–F = 5 µm, G–M = 3 µm, N = 1 µm

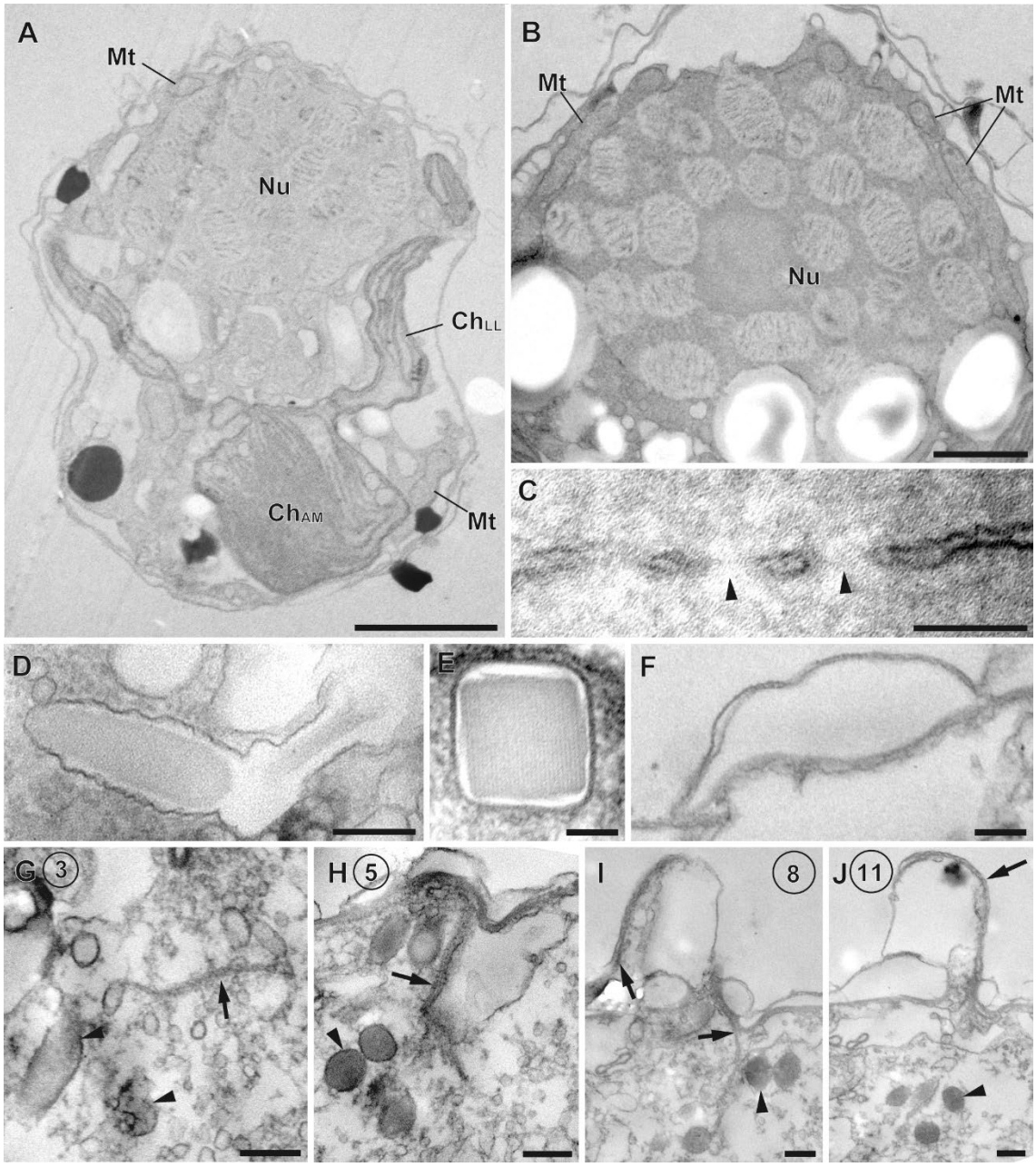
A
Mt
Nu
Ch_LL
Ch_AM
Mt
B
Mt
Mt
Nu
C
D
E
F
G 3
H 5
I 8
J 11

Fig. 2.16. Transmission electron micrographs (TEMs) of *Paragymnodinium asymmetricum* sp. nov. (A) Longitudinal section of cell. Scale bar = 2 μm. (B) Nucleus containing condensed chromosomes and surrounded by numerous mitochondria. Scale bar = 1 μm. (C) Detail of nuclear envelope comprising two membranes and nucleopore (arrowheads). Scale bar = 100 nm. (D) Longitudinal section of trichocyst. Scale bar = 200 nm. (E) Transverse section of trichocyst. Scale bar = 100 nm. (F) Detail of amphiesmal vesicle. No plate-like structure observed. Scale bar = 200 nm. (G–J) Serial, nonconsecutive sections of extended peduncle. Microtubular strand of peduncle (arrows); electron-opaque vesicles (arrowheads) indicated. Numbers of selected serial sections indicated in circles. Scale bars = 200 nm. Ch_{LL}, lateral lobe of chloroplast; Ch_{AM}, antapical mass of chloroplast; Mt, mitochondrion; Nu, nucleus.

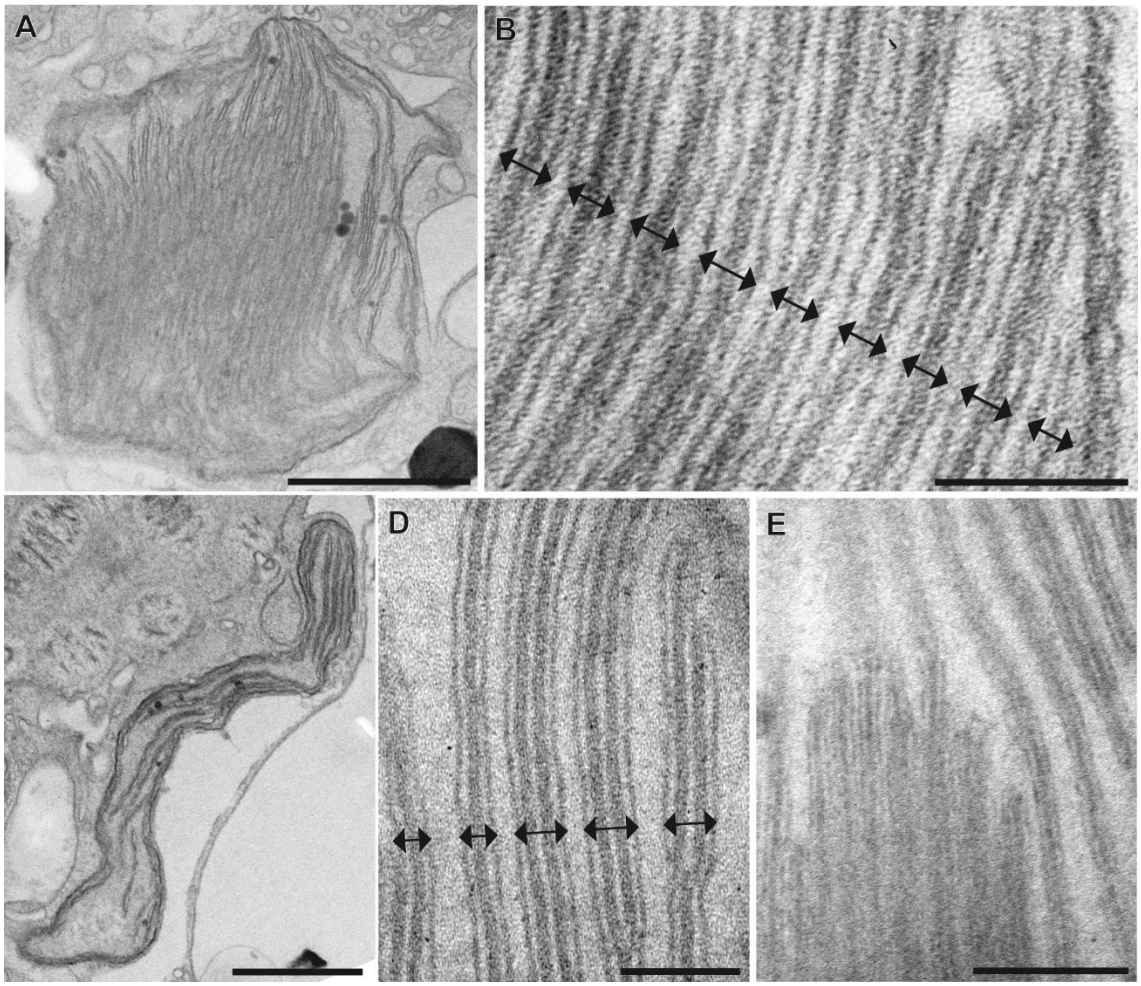

Fig. 2.17. TEM micrographs of chloroplast of *Paragymnodinium asymmetricum* sp. nov. (A) Antapical mass of chloroplast with densely packed thylakoids. Scale bar = 1µm. (B) Detail of antapical mass. Each thylakoid band is double stacked (double-headed arrows). Scale bar = 100 nm. (C) Lateral lobe of chloroplast with less-dense packing of thylakoids. Scale bar = 1 µm. (D) Detail of lateral lobe, showing each thylakoid band as double or triple stacked (double-headed arrows). Scale bar = 100 nm. (E) Boundary between antapical mass and lateral lobe, demonstrating difference in stacking density of thylakoids. Scale bar = 200 nm.

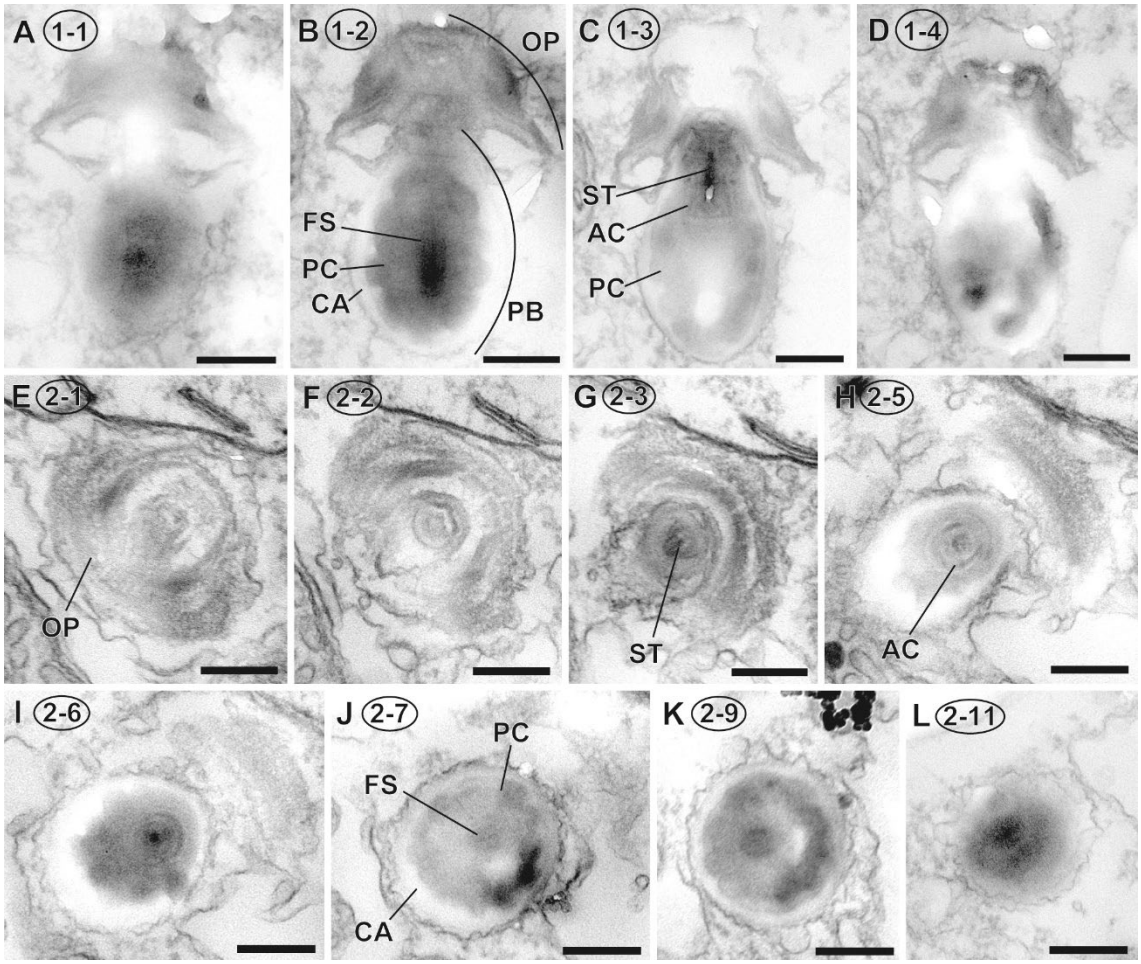

Fig. 2.18. Serial TEM sections of nematocysts of *Paragymnodinium asymmetricum* sp. nov. Section numbers are indicated by circled numbers. (A–D) Longitudinal sections of entire nematocyst. (E–L) Selected transverse sections from anterior (E) to posterior extremes (L). AC, anterior chamber; CA, capsule; FS, fibrous strand; OP, operculum; PB, posterior body; PC, posterior chamber; ST, stylet. Scale bars = 200 nm.

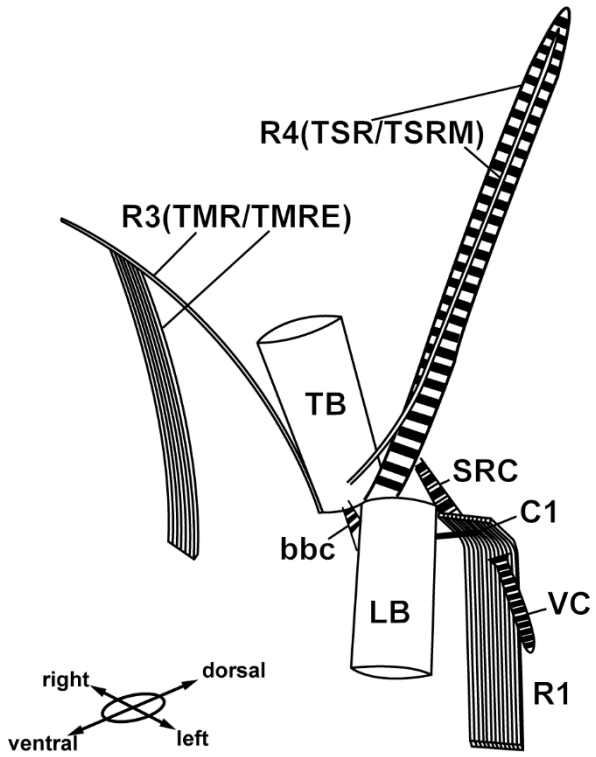

Fig. 2.19. 3D reconstruction of flagellar apparatus of *Paragymnodinium asymmetricum* sp. nov. (not to scale). bbc, basal body connective; C1, connective 1 linking LB and R1; LB, longitudinal basal body; R1, root 1; R3, root 3; R4, root4; SRC, striated root connective; TB, transverse basal body; TMR, transverse microtubular root; TMRE, transverse microtubular root extension; TSR, transverse striated root; TSRM, transverse striated root microtubule; VC, ventral connective.

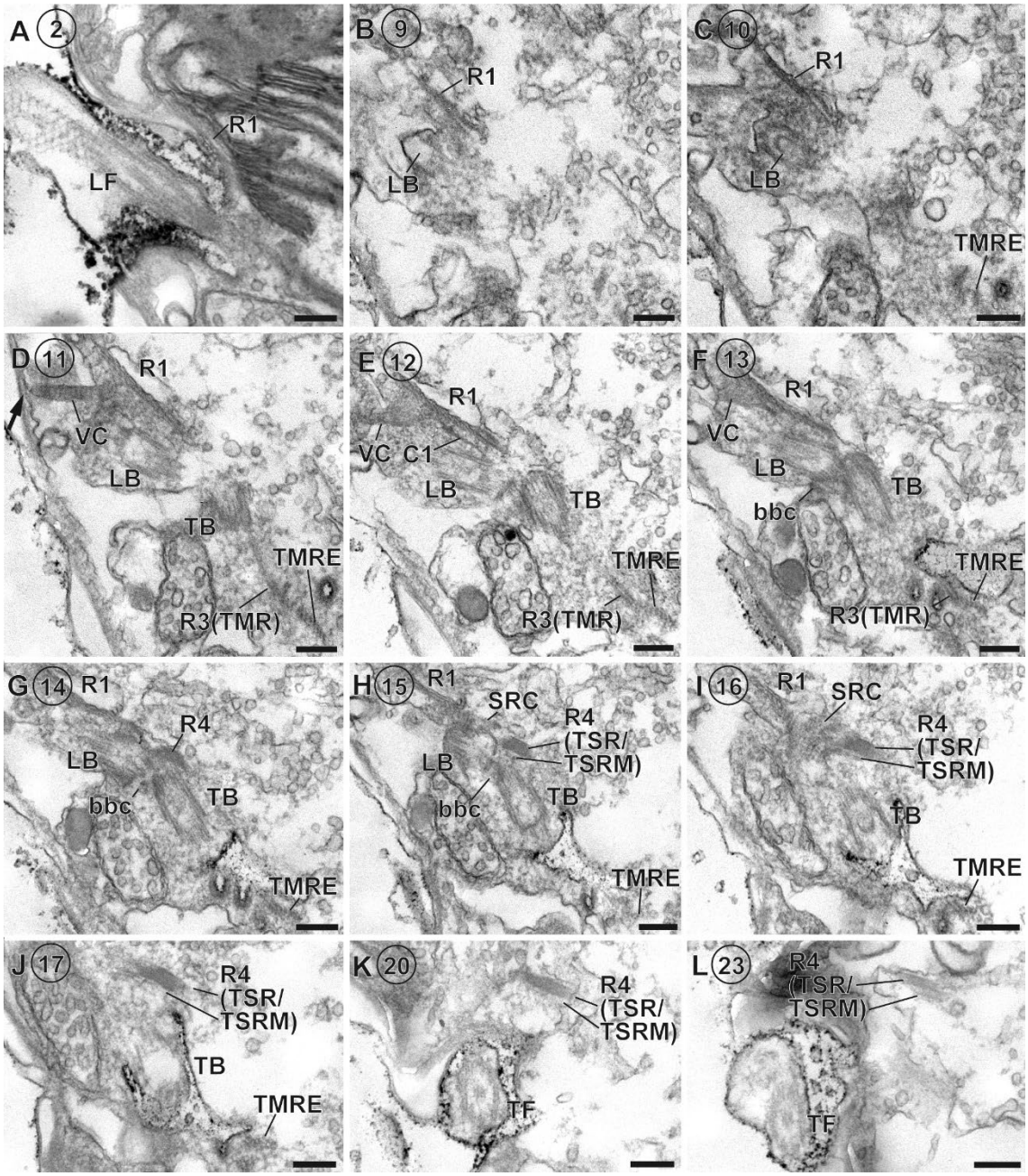

Fig. 2.20. Serial, non-consecutive TEM sections of flagellar apparatus of *Paragymnodinium asymmetricum* sp. nov. Section numbers indicated in circles and direction of sectioning is from right to left. bbc, basal body connective; C1, connective 1 linking LB and R1; LB, longitudinal basal body; LF, longitudinal flagellum; R1, root 1; R3, root 3; R4, root4; SRC, striated root connective; TB, transverse basal body; TF, transverse flagellum; TMR, transverse microtubular root; TMRE, transverse microtubular root extension; TSR, transverse striated root; TSRM, transverse striated root microtubule; VC, ventral connective linking R1 and ventral plasma membrane (arrow). Scale bars = 200 nm.

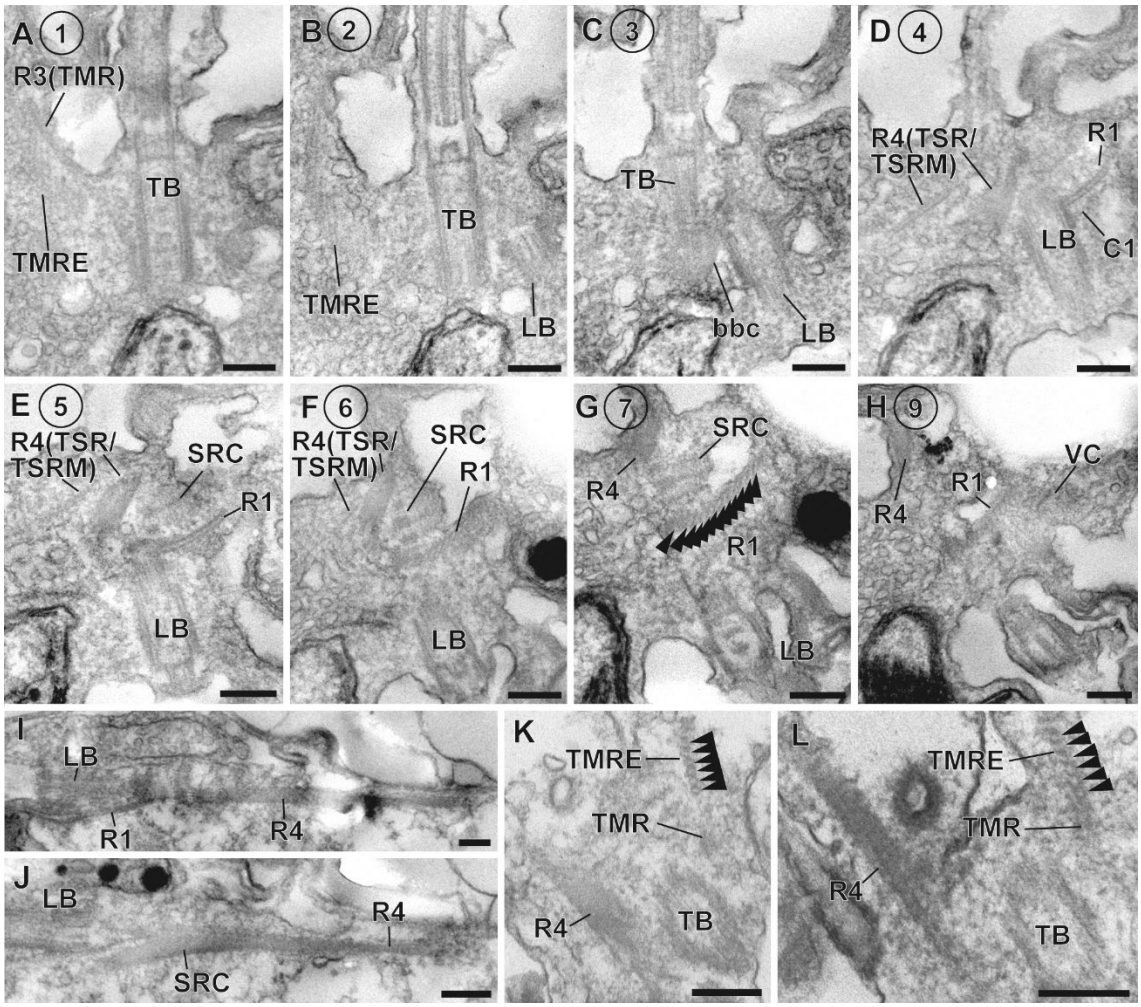

Fig. 2.21. Serial TEM sections of flagellar apparatus of *Paragymnodinium asymmetricum* sp. nov. (A–H) Mostly consecutive serial sections with section numbers circled. The 12 microtubules of R1 indicated by arrowheads. Direction of sectioning is from dorsal to ventral side. (I, J) Serial sections showing detail of R4. (K, L) Adjacent serial sections showing detail of TMRE comprised of six microtubules (arrow heads). bbc, basal body connective; C1, connective 1 linking LB and R1; LB, longitudinal basal body; R1, root 1; R3, root 3; R4, root4; SRC, striated root connective; TB, transverse basal body; TMR, transverse microtubular root; TMRE, transverse microtubular root extension; TSR, transverse striated root; TSRM, transverse striated root microtubule; VC, ventral connective. Scale bars = 200 nm.

***Paragymnodinium inerme* Yokouchi, Takahashi, Nguyen, Iwataki et Horiguchi sp. nov.**

Light and scanning electron microscopy: Cells were 15.3–23.7 µm (19.4 ± 2.0 µm, mean ± SD, n = 28) long and 10.9–19.6 µm (14.9 ± 2.1 µm, n = 28) wide. Episome and hyposome were almost equal in size (Fig. 2.22A, B). Episome was conical to hemispherical, and the hyposome was hemispherical (Fig. 2.22A, B). Cingulum was wide, well excavated, and descended by a distance half to equal of its own width (Fig. 2.22A, B). Sulcus was straight and widened slightly before reaching the antapex (Fig. 2.22A). No eyespot was observed. A slightly curved sulcal extension-like furrow (SEF) ran from the right end of the cingulum toward the apex (Fig. 2.22A). Chloroplasts were yellow brown and distributed throughout the cell (Fig. 2.22A–D). Analysis of autofluorescence images demonstrated the presence of multiple chloroplasts in each cell (Fig. 2.22C, D). The nucleus was central on the dorsal side of the cell (Fig. 2.22B, E, F). DAPI staining showed a single nucleus in the central or dorsal of cell (Fig. 2.22E, F). The motile cell was planktonic and free swimming. Cells encysted during the dark period. Shape of the cysts was similar to that of motile cells but each was covered with a wall. Cell division took place during the walled cyst stage (Fig. 2.22G). Some motile daughters released from germinating cells remained connected at their ventral surfaces (Fig. 2.22H). Cultures of this species grew in the absence of other eukaryotes and did not show feeding behavior when grown together with selected strains of other organisms.

SEM observations showed cells covered by small polygonal amphiesmal vesicles (AVs; Fig. 2.22I–M). AVs were arranged in 19 or 20 lateral rows, i.e., eight or nine rows to the episome, five rows to the cingulum, and six rows to the hyposome (Fig. 2.22J–M). The SEF was slightly incised and consisted of nine AVs (Fig. 2.22N, O). The sulcal AVs can be distinguished from surrounding ones, but the absolute number could not be determined (Fig. 2.22I–K, M). Cells with doubled flagella were common in culture (Fig. 2.22L, M).

Transmission electron microscopy: Figures 2.23B, C and 2.24C are cell fixed using the first fixation protocol, while others were fixed using the second protocol (see material and methods). Positioning and morphology of the organelles in motile cells were confirmed in thin-sectioned material (Fig. 2.23A). The nucleus was a typical dinokaryon

with condensed chromosomes (Fig. 2.23B) and a nuclear envelope interrupted by nuclear pores but lacking nuclear envelope chambers (Fig. 2.23C). Trichocysts were typical for dinoflagellates and were peripheral (Fig. 2.23D, E). Cells were covered by a typical amphiesma (Fig. 2.23F), the vesicles of which had no thecal plates or other plate-like structures (Fig. 2.23F). A microtubular strand of the peduncle ran from the right side of the flagellar apparatus (Fig. 2.23G–J), but electron opaque vesicles in its vicinity were not observed (Fig. 2.23G–J).

The cell contained approximately 20–30 oval chloroplast masses (Fig. 2.24A). Chloroplasts were surrounded by three membranes (Fig. 2.24B) and contained multiple thylakoids forming double or triple-stacked thylakoid lamellae (Fig. 2.24C) that were evenly distributed throughout all chloroplast masses. Some of these masses were inter connected by narrow bridges (Fig. 2.24D–F), making the actual number of chloroplasts fewer than apparent. Serial sections through two whole cells of *Paragymnodinium inerme* revealed that one had only three chloroplasts while the other had 15 (Video 2.2).

Cells rarely contained nematocysts (Fig. 2.25): only 3 of 15 entire cells investigated by serial sectioning were found to have them. Where present, the anterior operculum was almost completely collapsed, leaving the organelles composed solely of the oval posterior bodies. Each posterior body consisted of an anterior chamber and a capsule-covered, posterior chamber, containing multiple (approximately three) fibrous strands. A stylet was not observed.

The flagellar apparatus of *Paragymnodinium inerme* was reconstructed (Fig. 2.26) from serial sections (Figs 2.27, 28). The transverse basal body (TB) and the longitudinal basal body (LB) were held at an oblique angle of about 150° relative to one another by three basal body connectives (bbc1–3; Fig. 2.28E–H). Root 1 (R1) consisted of 18 microtubules and was inserted on the dorsal side of the LB (Figs 2.27A–F, 28A–D). R1 and the LB were linked by two connectives, C1 and C2 (Fig. 27C, D). Root 3 (R3) was comprised of a transverse microtubular root (TMR) and a transverse microtubular root extension (TMRE; Figs 2.27H–L, 28I–K). The TMR was comprised of a single microtubule inserted on the right side of the TB (Figs 2.27H–L, 28I–K). The TMRE consisted of several (presumably less than 10) microtubules nucleated by the TMR, but the precise number could not be determined (Figs 2.27K, L, 28J, K). Root 4 (R4),

comprising a transverse striated root (TSR) and a TSR microtubule (TSRM), was inserted on the left side of the TB (Figs 2.27H–L, 28E–H). R1 and R4 were linked by a striated root connective (SRC; Figs 2.27G, H, 28D, E). Root 2 and a nuclear fibrous connective were not observed in any serial sections through the flagellar apparatus of eight different cells.

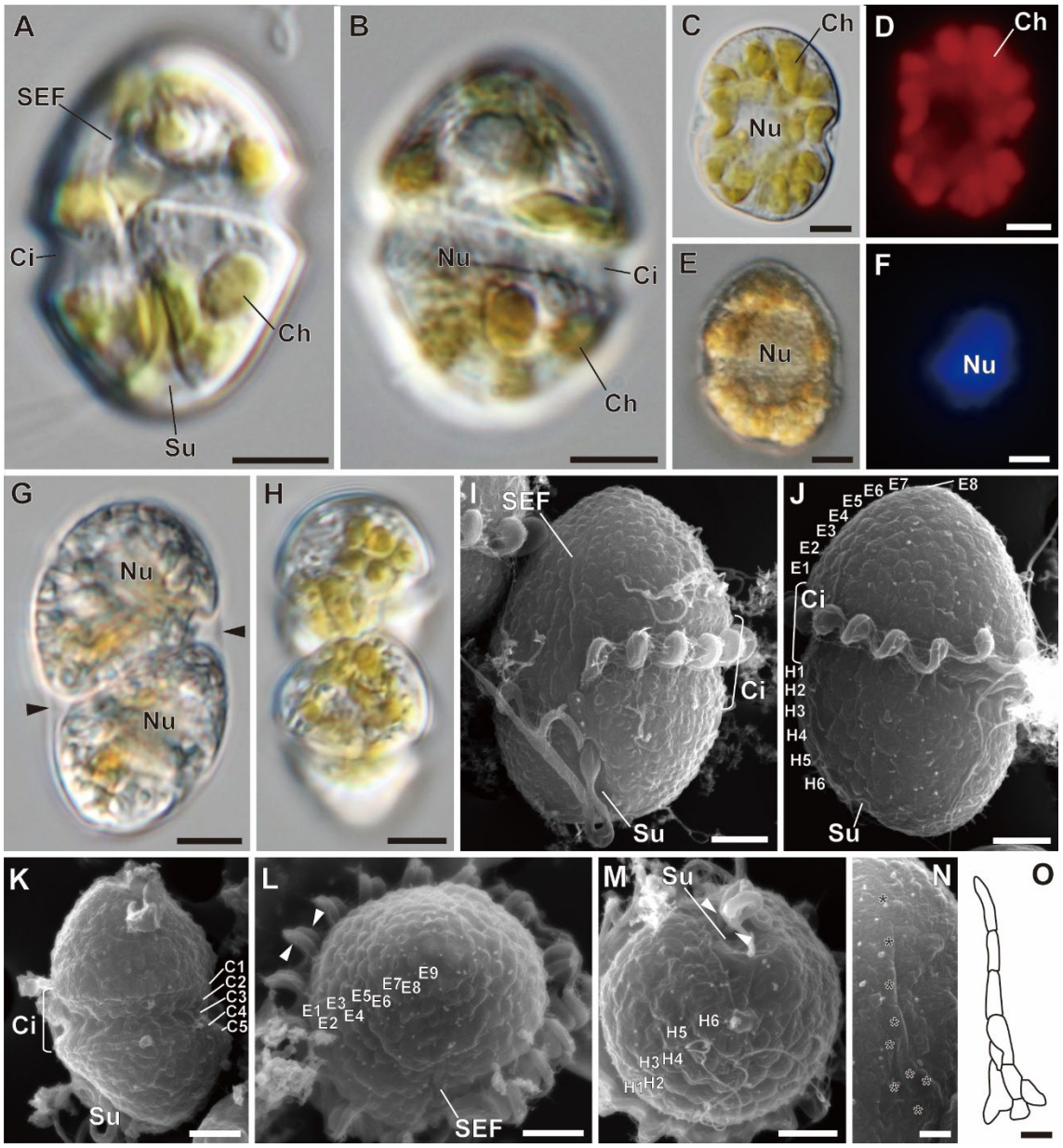
A
SEF
Ci
Ch
Su
B
Nu
Ci
Ch
C
Ch
Nu
D
Ch
E
Nu
F
Nu
G
Nu
Nu
H
I
SEF
Ci
Su
J
E1
E2
E3
E4
E5
E6
E7
E8
Ci
H1
H2
H3
H4
H5
H6
Su
K
C1
C2
C3
C4
C5
Ci
Su
L
E1
E2
E3
E4
E5
E6
E7
E8
E9
SEF
M
Su
H1
H2
H3
H4
H5
H6
N
O

Fig. 2.22. (A–H) Differential interference contrast (DIC) and fluorescence light micrographs of *Paragymnodinium inerme* sp. nov. (A) Ventral view. (B) Dorsal view. (C, D) The same cell showing autofluorescence of chloroplasts. (E, F) The same cell showing fluorescence of nucleus stained by DAPI. (G) Division cyst with outer wall (arrowheads). (H) Two motile cells connected to each other.

(I–O) Scanning electron micrographs of *Paragymnodinium inerme* sp. nov., showing arrangement of numerous polygonal amphiesmal vesicles (AVs) on cell surface. (I) Ventral view. (J) Dorsal view, showing episome and its vesicles arranged in eight rows (E1–E8), hyposome and its vesicles arranged in six rows (H1–H6). (K) Left lateral view, showing cingulum and its vesicles arranged in five rows (C1–C5). (L) Apical view, showing episome and its vesicles arranged in nine rows (E1–E9). Cell possesses double transverse flagella (arrowheads). (M) Antapical view, showing hyposome and its vesicles arranged in six rows (H1–H6) and sulcus. Note double longitudinal flagella (arrow-heads). (N) Detail of SEF comprising nine elongate AVs (asterisks). (O) Schematic illustration of SEF showing arrangement of AVs. Ch, chloroplast; Ci, cingulum; Nu, nucleus; SEF, sulcal extension-like furrow; Su, sulcus. Scale bars; A–H = 5 μm, I–M = 3 μm, N, O = 1 μm.

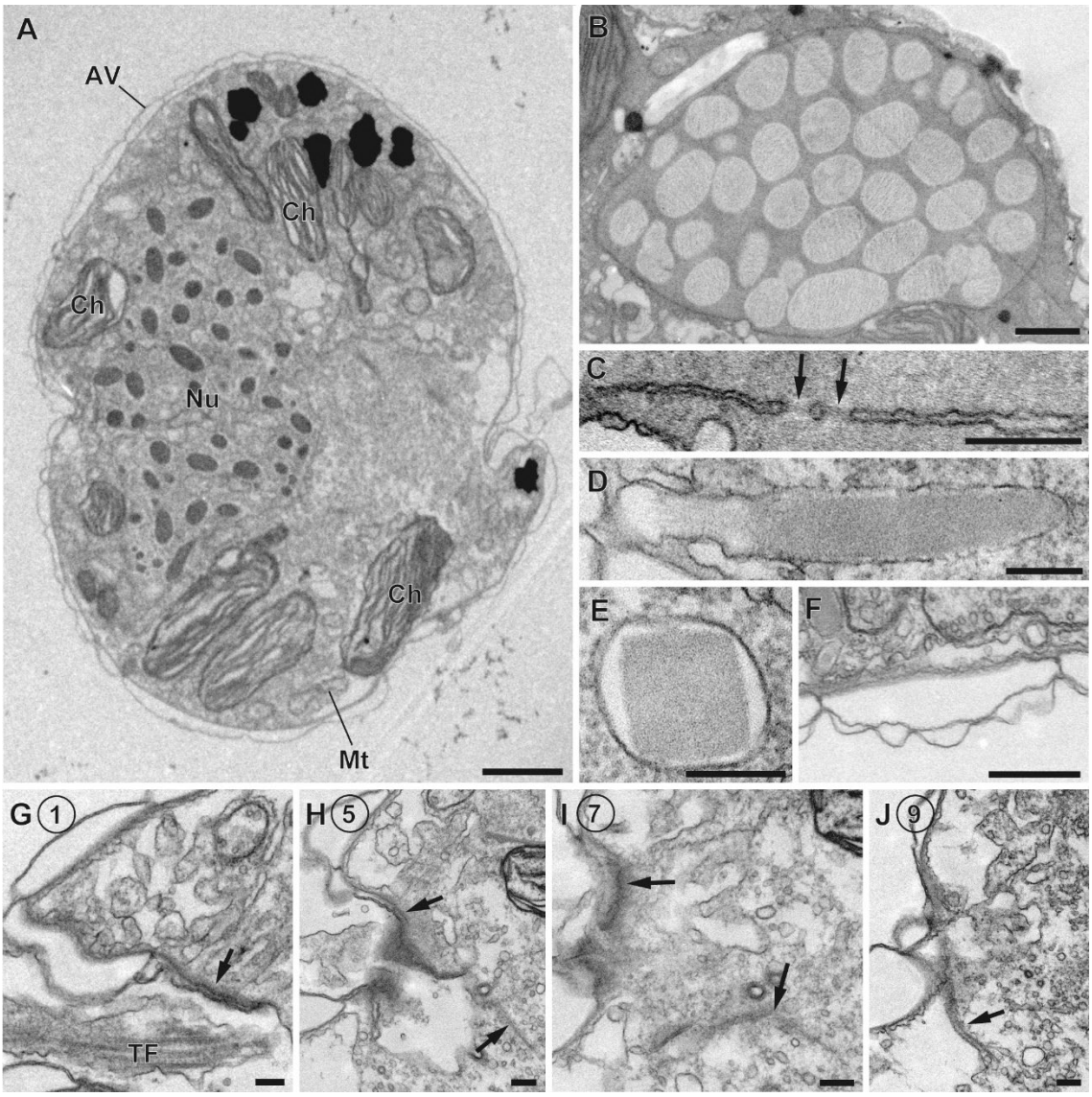

Fig. 2.23. Transmission electron micrographs (TEMs) of *Paragymnodinium inerme* sp. nov. (A) Longitudinal section of cell. AV, amphiesmal vesicle; Ch, chloroplast; Mt, mitochondrion; Nu, nucleus. Scale bar = 2 µm. (B) Nucleus containing condensed chromosomes. Scale bar = 2 µm. (C) Detail of nuclear envelope comprising two membranes and nucleopore (arrows). Scale bar = 200 nm. (D) Longitudinal section of trichocyst. Scale bars = 200 nm. (E) Transverse section of trichocyst. Scale bars = 100 nm. (F) Detail of amphiesmal vesicle. Scale bar = 500 nm. (GJ) Serial, nonconsecutive sections of peduncle. Microtubular strand of peduncle (arrows) indicated. Section numbers circled with direction of sectioning from left to right. Scale bars = 200 nm.

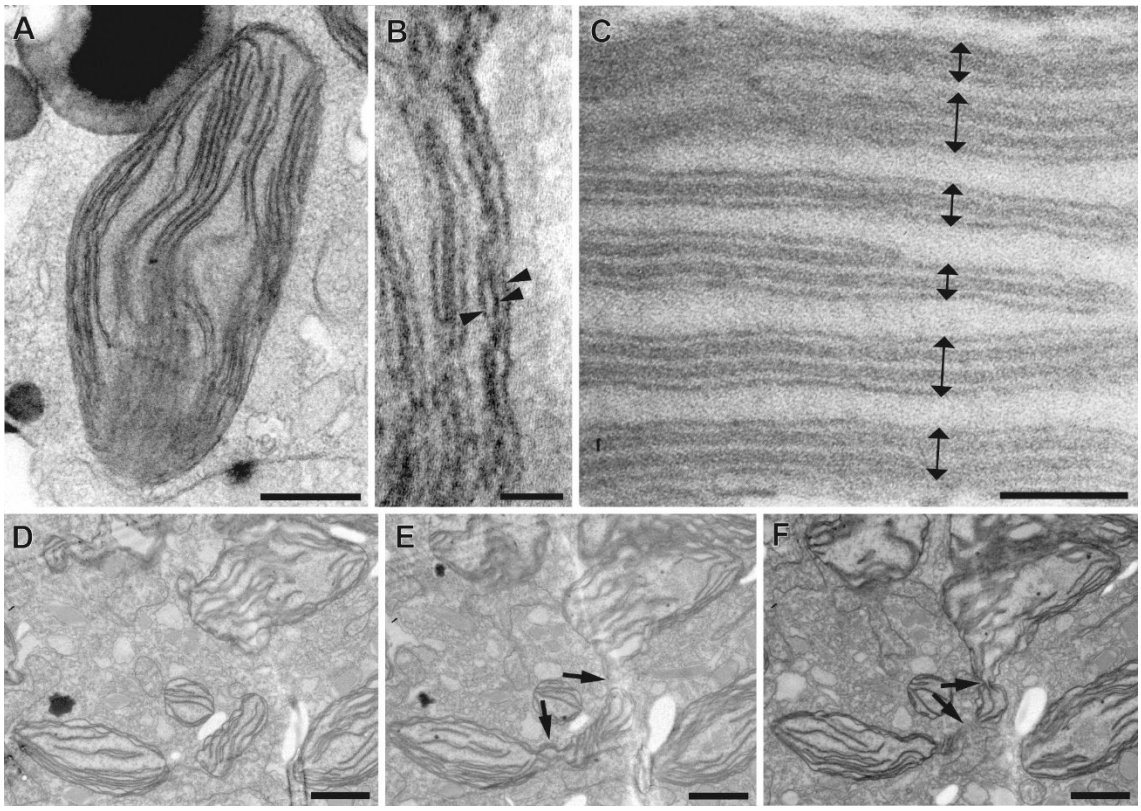

Fig. 2.24. TEM micrographs of the chloroplast of *Paragymnodinium inerme* sp. nov. (A) A mass of chloroplast. Scale bar = 2μm. (B) Detail of chloroplast envelope comprised of three membranes (arrowheads). Scale bar = 50 nm. (C) Detail of chloroplast with double- or triple-stacked thylakoid bands, indicated by the double-headed arrows. Scale bar = 100 nm. (D–F) Many masses of chloroplast are connected by narrow bridges (arrows). Scalebars = 1 μm.

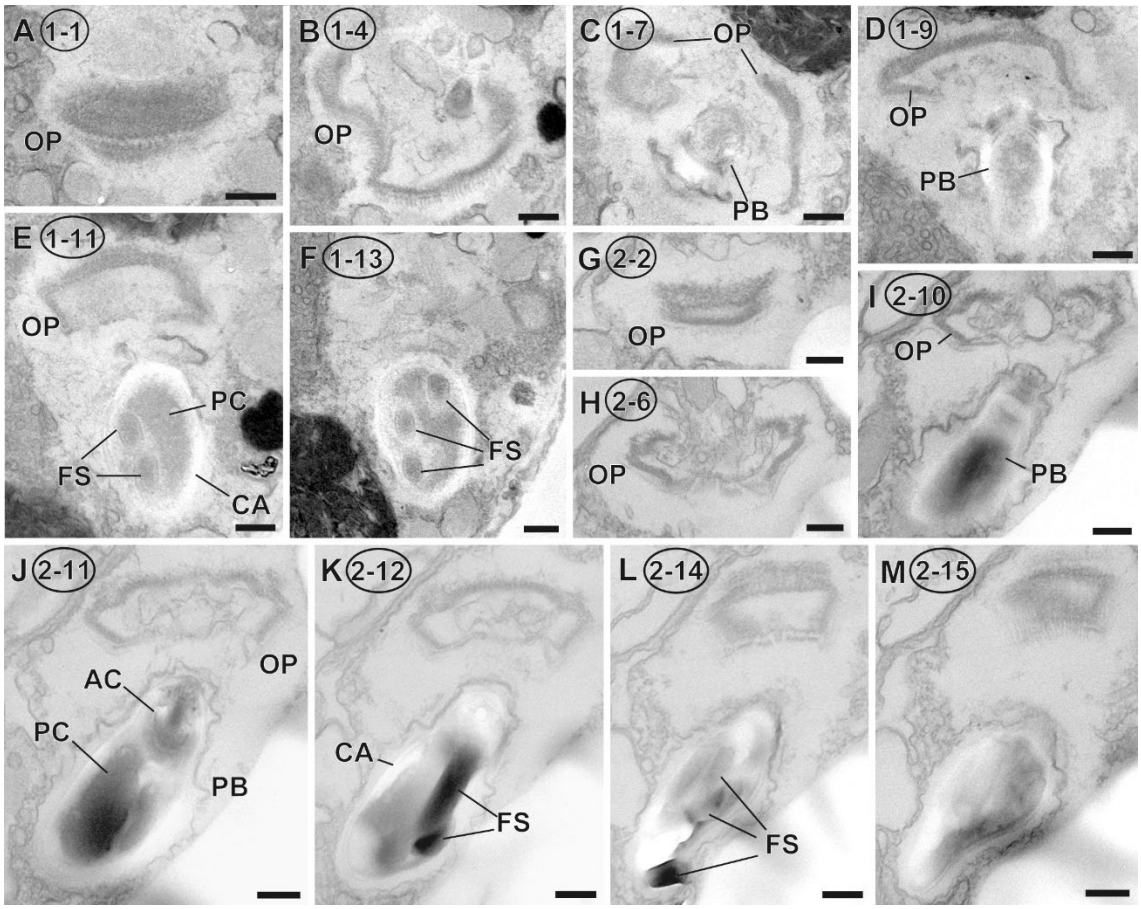

Fig. 2.25. Serial TEM sections of nematocysts of *Paragymnodinium inerme* sp. nov. Section numbers indicated in circles. (A–F) Transverse sections from anterior part (A) to posterior part (F). (G–M) Longitudinal sections. AC, anterior chamber; CA, capsule; FS, fibrous strand; OP, operculum; PB, posterior body; PC, posterior chamber. Scale bars = 200 nm.

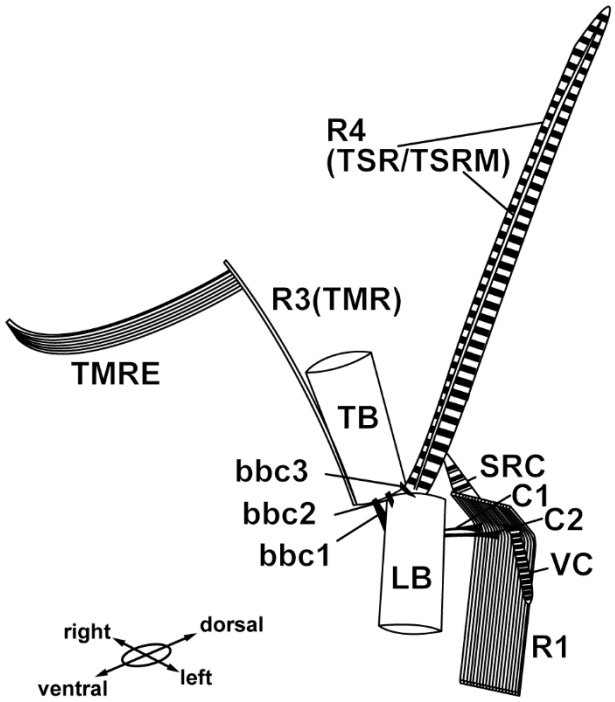

Fig. 2.26. Reconstruction of flagellar apparatus of *Paragymnodinium inerme* sp. nov. bbc1, basal body connective 1; bbc2, basal body connective 2; bbc3, basal body connective 3; C1, connective 1 linking LB and R1; C2, connective 2 linking LB and R1; LB, longitudinal basal body; R1, root 1; R3, root 3; R4, root4; SRC, striated root connective; TB, transverse basal body; TMR, transverse microtubular root; TMRE, transverse microtubular root extension; TSR, transverse striated root; TSRM, transverse striated root microtubule; VC, ventral connective.

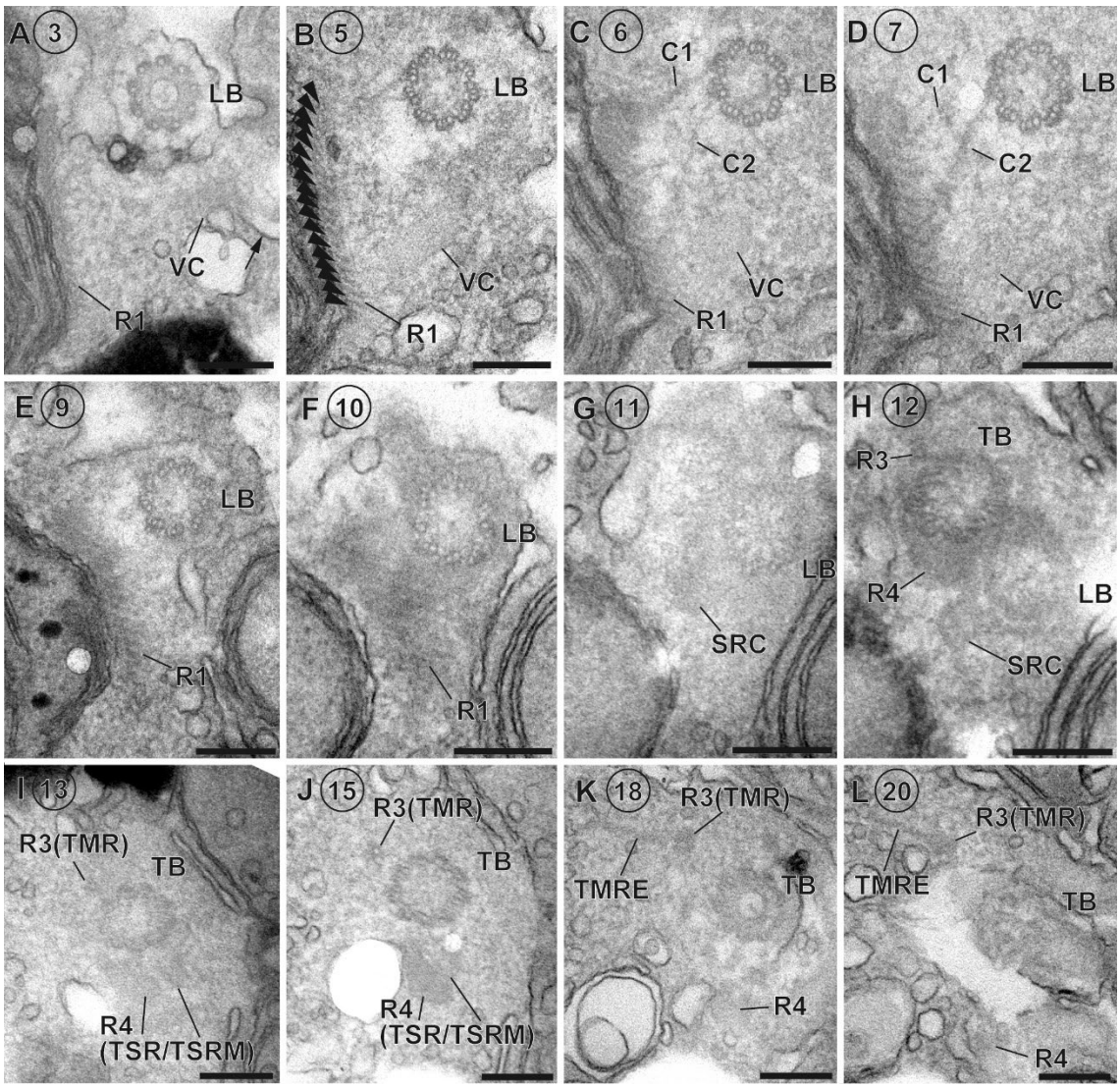

Fig. 2.27. Serial, non-consecutive TEM sections of flagellar apparatus of *Paragymnodinium inerme* sp. nov. Section numbers indicated in circles. Direction of sectioning is from antapical to apical side. The 18 microtubules of R1 indicated by arrowheads. C1, connective 1 linking LB and R1; C2, connective 2 linking LB and R1; LB, longitudinal basal body; R1, root 1; R3, root 3; R4, root 4; SRC, striated root connective; TB, transverse basal body; TMR, transverse microtubular root; TMRE, transverse microtubular root extension; TSR, transverse striated root; TSRM, transverse striated root microtubule; VC, ventral connective. Scale bars = 200 nm.

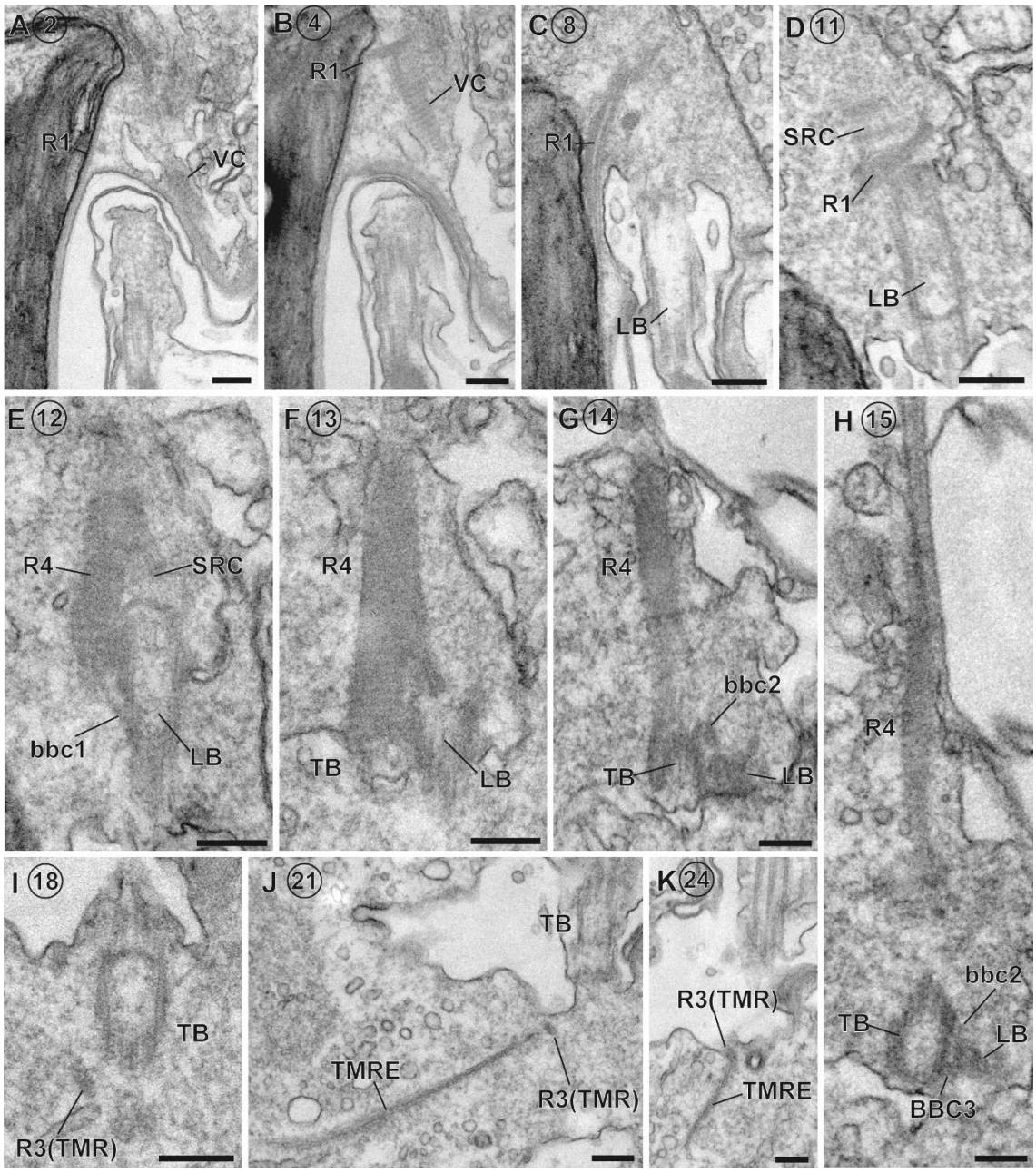

Fig. 2.28. Serial, non-consecutive TEM sections of flagellar apparatus of *Paragymnodinium inerme* sp. nov. Section numbers circled. Direction of sectioning from left to right side. bbc1, basal body connective 1; bbc2, basal body connective 2; bbc3, basal body connective 3; LB, longitudinal basal body; R1, root 1; R3, root 3; R4, root 4; SRC, striated root connective; TB, transverse basal body; TMR, transverse microtubular root; TMRE, transverse microtubular root extension; VC, ventral connective. Scale bars = 200 nm.

Phylogenetic analysis

The phylogenetic tree inferred by ML based on concatenated SSU rDNA and LSU rDNA sequences is shown in Fig. 2.29. The topology resulting from Bayesian analysis was only slightly different. In the phylogenetic tree, all four species studied here were included in the clade *Gymnodinium sensu stricto*, and formed a robust clade with *Paragymnodinium shiwhaense*. Within the *Paragymnodinium* clade, *P. inerme* was shown to be phylogenetically very close to *P. shiwhaense* (Table 2.1). *Paragymnodinium asymmetricum* came to sister position to *P. shiwhaense*/*P. inerme* clade with high support. *Paragymnodinium stigmaticum* and the *P. verecundum* formed highly supported clade and came to the sister position with *P. shiwhaense*/*P. inerme*/*P. asymmetricum* clade. Although the *Paragymnodinium* clade rooted at the base of the clade *Gymnodinium sensu stricto* in both analyses, neither had convincing support. Species with nematocysts were restricted to some members of the clade *Gymnodinium sensu stricto*, notably *Polykrikos*, *Nematodinium*, *Gyrodiniellum* and *Paragymnodinium* (denoted by stars in Fig. 2.29), but they were not monophyletic.

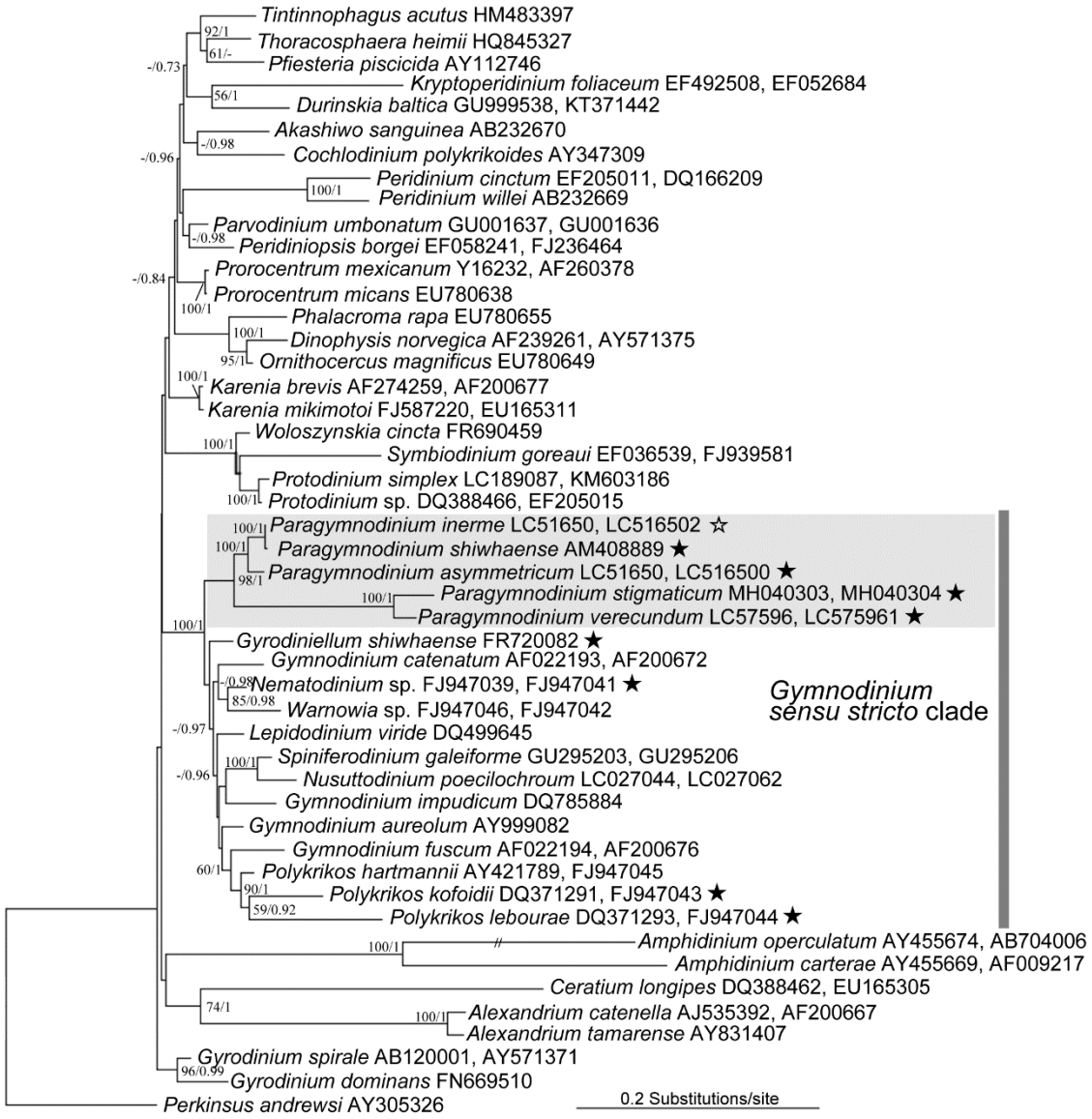

Fig. 2.29. Maximum-likelihood phylogenetic tree of selected dinoflagellates, including *Paragymnodinium stigmaticum* sp. nov., *P. verecundum* sp. nov., *P. asymmetricum* sp. nov. and *P. inerme* sp. nov., based on concatenated SSU rDNA and partial LSU rDNA sequences. Each species name is followed by accession numbers in order of SSU rDNA and partial LSU rDNA sequences. Only one accession number indicates that the sequence assigned by the number includes both of SSU rDNA and partial LSU rDNA sequences. Numbers at each node are ML bootstrap values and Bayesian posterior probabilities. Only values > 50% (bootstrap) and > 0.7 (PP) are indicated. Stars indicate dinoflagellates with nematocysts. *P. inerme* is marked by white star because of abnormality of nematocysts.

Table 2.1. Pairwise distance matrix of the 18S (lower left) and 28S (upper right) rDNA sequences of *Paragymnodinium* spp. calculated using p-distance model.

Species	1	2	3	4
1. *P. shiwhaense*		0.1338	0.0405	0.0075
2. *P. stigmaticum*	0.0919		0.0905	0.0985
3. *P. asymmetricum*	0.0151	0.0901		0.0254
4. *P. inerme*	0.0006	0.0914	0.0145	

DISCUSSION

Taxonomic consideration

Paragymnodinium stigmaticum shares many morphological and nutrition-related features with *P. shiwhaense*. These include the presence of nematocysts and a peduncle or peduncle-like structure, the possession of small polygonal amphiesmal vesicles, the possession of a sulcal extension-like furrow (SEF) in the episome, and mixotrophic nutrition (Kang et al. 2010, Yoo et al. 2010). However, *P. stigmaticum* is clearly different from *P. shiwhaense. Paragymnodinium stigmaticum* ingests prey cells by engulfing them through an antapical area of hyposome, whereas *P. shiwhaense* uses a peduncle in the ventral area for ingestion (Kang et al. 2010, Yoo et al. 2010). Chloroplast morphology is also markedly different between the two taxa, with *P. stigmaticum* containing a thylakoid-free region in the central area and possessing separated thylakoid bands, unlike the triple-stacked thylakoid lamellae seen in most other dinoflagellates (Dodge 1987), whereas *P. shiwhaense* seems to contain a thylakoid-free region in the periphery rather than centrally, with each lamella consisting of 2–3 appressed thylakoids (Kang et al. 2010). Although *P. stigmaticum* possesses a distinct eyespot, no eyespot was reported for *P. shiwhaense*. Their habitats are also different, with *P. stigmaticum* having a benthic lifestyle, whereas *P. shiwhaense* is planktonic (Kang et al. 2010). Furthermore, Kang et al. (2010) suggested the presence of thin plates in amphiesmal vesicles of *P. shiwhaense*, while I found no evidence of such plate-like structures in the amphiesmal vesicles of *P. stigmaticum* (Fig. 2.2I). Although both species essentially share the same structure of their flagellar apparatus (Kang et al. 2010), a transverse microtubular root extension (TMRE) of R3 and a left-ventral fiber (LVF) have not been reported in *P. shiwhaense*.

Paragymnodinium verecundum also shares many morphological features with other members of the genus, such as the possession of nematocysts, polygonal small AVs and an SEF (Kang et al. 2010). This dinoflagellate has some notable shared structures with *P. stigmaticum*. They both have chloroplasts with a thylakoid-free central region and separated thylakoids. They also both have a peduncle-like structure with a terminal nematocyst, potentially capable of being ejected from the cell. These characters are unique to these two species. Furthermore, cells of *P. verecundum* are similar to those of *P. stigmaticum* in size and shape and with respect to their possession of an eyespot and

their benthic lifestyle. Both species ingest prey cells by engulfment at the antapical area of the hyposome without using a peduncle and show a mixotrophic nutritional mode. Therefore, *P. verecundum* and *P. stigmaticum* are difficult to distinguish morphologically or behaviorally. However, some differences do exist between the two species. First, *P. verecundum* shows negative phototaxis while *P. stigmaticum* shows no phototactic behavior, although its encystment was found to be restricted to the dark period, which indicates a capability of differentiating between the presence and absence of light. The absence of phototaxisim in *P. stigmaticum* was confirmed by subjecting it to the same conditions used to demonstrate its presence in *P. verecundum*, where it failed to respond to the light regardless of intensity, color and/or time under the conditions used in this experiment (data not shown). It is possible that a stronger light (1000 μmol photons m^{-2} s^{-1}) may lead a phototactic response in *P. stigmaticum*. However, even so, the sensitivity to light is significantly different between *P. verecundum* and *P. stigmaticum*. Second, nematocysts of *P. verecundum* contain a long filament in the central area of the posterior body (PB) that has not been observed in the nematocysts of other *Paragymnodinium* species (Kang et al. 2010). The structure of this filament is similar to that of *Gyrodiniellum shiwhaense* (Kang et al. 2011). Third, *P. verecundum* contains a pusule in the ventral area of the hyposome. A pusule has not been observed in any other *Paragymnodinium* sp. (Kang et al. 2010). The molecular tree also indicated that, despite being closely related, *P. stigmaticum* and *P. verecundum* are clearly differentiated. Therefore, it is reasonable to conclude that *P. stigmaticum* and *P. verecundum* are different species.

To confirm whether *Paragymnodinium stigmaticum* and *P. inerme* are novel taxa or not, they should also be compared with previously described morphologically similar species. *Gyrodiniellum shiwhaense* also possesses nematocysts. However, it lacks chloroplasts and possesses a loop-shaped apical row of amphiesmal vesicles (LAV) in its episome (Kang et al. 2011), features not shared by *Paragymnodinium* spp. *Protodinium simplex* (or *Gymnodinium simplex*) is similar to *P. stigmaticum* and *P. verecundum* in size, shape and possession of chloroplasts and an eyespot, but the arrangement of amphiesmal vesicles is clearly different, especially with regard to the elongate apical vesicles (EAV) found only in *Pr. simplex* (Luo et al. 2015). Phylogenetic analysis also indicated *Pr.*

simplex as distantly related to *Paragymnodinium* spp. The cells of *Gymnodinium danicans* similarly possesses a red eyespot near the sulcus, but its size is larger than that of *Paragymnodinium* spp., and it lacks a SEF or any similar structures (Hoppenrath 2000, Murray 2003, Hoppenrath et al. 2014). Therefore, *P. stigmaticum* and *P. verecundum* can be distinguished from any other morphologically-similar species described to date, and I conclude that these dinoflagellates are new species in the genus *Paragymodinium*.

Paragymnodinium asymmetricum has characteristics shared by other species of the genus *Paragymnodinium*, such as the possession of nematocysts, polygonal amphiesmal vesicles, and a SEF (Kang et al. 2010). It is more affiliated with *P. shiwhaense* than with *P. stigmaticum* and *P. verecundum* in that it lacks an eyespot, has double- or triple-stacked thylakoid lamellae, and a planktonic lifestyle. This relationship is supported by the topology of the molecular tree. On the other hand, *P. asymmetricum* is clearly distinguished from *P. shiwhaense* by the cell size, the asymmetric shape of hyposome (larger right than left side), and the anterior position of the nucleus rather than central or dorsal position seen in *P. shiwhaense* (Kang et al. 2010). The SEF of *P. asymmetricum* is straight as opposed to the curved equivalent in other members of the genus (Kang et al. 2010). It also shows variation in the number of AV rows of its episome. Intraspecific variation in AVs is seen in some other dinoflagellates (e.g., Pandeirada et al. 2014), but has not been reported in the genus *Paragymnodinium*. If the number of AVs is mutable, this morphological character is not appropriate as a taxonomic criterion. In addition, *P. asymmetricum* can be distinguished from the mixotrophic *P. shiwhaense* (Yoo et al. 2010) because it shows no evidence of feeding behavior and can sustain itself phototrophically. DAPI staining shows that DNA is focused in one area (the nucleus) without subsidiary satellite fluorescence as would be expected had ingested bacteria. In addition to this, no intracellular bacteria were ever observed by TEM. It is conceded that *P. asymmetricum* has the potential to be mixotrophic because it retains structures related to feeding behavior, such as a peduncle and nematocysts. However, it is clearly not an obligate mixotroph that requires both feeding and photosynthesis as is the case for *P. shiwhaense* (Yoo et al. 2010).

Asymmetricity of the hyposome, as seen in *Paragymnodinium asymmetricum*, is rare in athecate dinoflagellates. The hyposome of some species of the genus *Gyrodinium*,

such as *G. dominans*, is similarly asymmetric, but *P. asymmetricum* is clearly not a member of this genus because it does not have longitudinal striations, and it is not heterotrophic (Hoppenrath et al. 2014). The phylogenetic analysis also recovered *Gyrodinium* spp. in a distantly related clade to that of *Paragymnodinium* spp. Therefore, *P. asymmetricum* can be distinguished from any other dinoflagellates described to date, and I conclude that this dinoflagellate is a new species.

Paragymnodinium inerme is similar to *P. shiwhaense* in shape, and in the possession of polygonal AVs, a slightly curved SEF, a planktonic lifestyle, and the absence of an eyespot (Kang et al. 2010). Although the number of AVs of the two species is different, the arrangement of AVs within the SEF is the same (Kang et al. 2010). The genetic distance between these two species is also small. However, the nutritional strategy of *P. inerme* differs from that of *P. shiwhaense*: *P. inerme* can grow without any supplementation to phototrophy and does not feed when provided with cells of *Amphidinium* aff. *carterae* despite the fact that *A. carterae* was identified as the most appropriate prey for *P. shiwhaense* (Yoo et al. 2010). In addition, although we also provided unicellular algae belonging to different classes as possible prey, *P. inerme* did not feed any of these algal cells. DAPI staining and TEM observations showed no evidence of ingested bacteria in *P. inerme*. The abnormality or degeneration of nematocysts in *P. inerme* is also a clear difference from *P. shiwhaense*. In *P. inerme*, there is no evidence of the platelike structures that found in the amphiesmal vesicles of *P. shiwhaense* (Kang et al. 2010). The presence of a transverse microtubular root extension (TMRE) of R3 and of the ventral connective (VC) in the flagellar apparatus of *P. inerme* also represents differences from *P. shiwhaense* (Kang et al. 2010). While it is conceded that the TMRE and VC might have been overlooked in *P. shiwhaense* (see below), there are a suite of clear morphological differences between *P. inerme* and *P. shiwhaense*, despite their close phylogenetic relationship, and the two organisms can be regarded as different species.

There are some dinoflagellates which morphologically resemble *Paragymnodinium inerme*. *Aureodinium pigmentosum* is similar in size and shape to *P. inerme*, but has pyrenoids (Dodge 1967, 1982), which are lacking in *P. inerme*. *Gymnodinium incertum* is also similar, but the SEF or apical groove-like structure has not

been described in this species (Dodge 1982). *Gymnodinium pygmaeum* is also similar in size and has a furrow in its episome, but this species is rounder than *P. inerme*, and both the apex and antapex are notched, so it is distinguishable from *P. inerme* (Dodge 1982, Hansen and Larsen 1992). Therefore, *P. inerme* can be distinguished from any other morphologically similar species described to date, and I conclude that this dinoflagellate is a new species.

Phylogenetic position

The recovery of *Paragymnodinium stigmaticum, P. verecundum*, *P. asymmetricum* and *P. inerme* in a clade with *P. shiwhaense* in the phylogenetic analyses concurs with shared morphological features. Therefore, it is reasonable to conclude that four dinoflagellates studied here represent new species in the genus *Paragymnodinium*. The *Paragymnodinium* clade can be split into two subclades, reflecting some morphological or behavioral distinctions. One clade, comprising *P. shiwhaense*, *P. asymmetricum* and *P. inerme*, shares the absence of an eyespot, double- or triple-stacked thylakoids and a planktonic lifestyle. The remaining clade, comprising *P. stigmaticum* and *P. verecundum*, is characterized by the possession of an eyespot, segregated thylakoids and a benthic lifestyle. Although the number of rows of AVs are mutable from species to species, that in the cingulum reflects their phylogeny; five rows exist in the former clade while four rows define the latter clade. While mixotrophic species are recognized in both clades (Yoo et al. 2010), solely phototrophic species are restricted to the subclade of *Paragymnodinium* lacking an eyespot. All known species of *Paragymnodinium* possess nematocysts that are presumably used to capture prey for ingestion. Thus, the common ancestor of the genus must have had nematocysts and a mixotrophic form of nutrition. The two known solely phototrophic species presumably became secondarily independent of phagotrophy. Interestingly, *P. inerme* and *P. shiwhaense* represent almost same phylogenetic position, despite there are differences in nutritional strategy and nematocyst as discussed above. This result indicates the evolution of nutritional mode and nematocyst has occurred quite recently.

Current phylogenetic analysis indicates that *Paragymnodinium* is included in the clade *Gymnodinium sensu stricto*, even though its species lack a horseshoe-shaped apical

groove, nuclear envelope chambers and nuclear fibrous connectives, all of which are characters of *Gymnodinium* spp. (Daugbjerg et al. 2000, Kang et al. 2010). In this regard, it is notable that *Gyrodiniellum shiwhaense*, another member of the clade *Gymnodinium sensu stricto*, lacks nuclear envelope chambers and a nuclear fibrous connective (Kang et al. 2011). Thus, these characters are not shared by all dinoflagellates in the clade *Gymnodinium sensu stricto*.

Nutritional strategies

In the genus *Paragymnodinium*, *P. shiwhaense*, *P. stigmaticum* and *P. verecundum* ingest prey cells in spite of possessing chloroplasts, indicating a mixotrophic mode of nutrition (Yoo et al. 2010). Some mixotrophic species are regarded as 'kleptochloroplastidic' (i.e., they display 'non-constitutive mixotrophy'), ingesting other photosynthetic protists and maintaining functional plastids in the short-term to obtain photosynthates (Hansen 2011, Mitra et al. 2016, Stoecker et al. 2017). In the clade *Gymnodinium sensu stricto*, kleptochloroplastidic species are restricted to members of the genus *Nusuttodinium* (Takano et al. 2014). In such dinoflagellates, no original dinoflagellate chloroplasts exist and the chloroplasts, together with some other organelles of ingested alga, are retained for some time and not immediately digested (Onuma and Horiguchi 2015). The nutritional strategy of *Paragymnodinium* species is, however, obviously not kleptochloroplastidic, because they have their own chloroplasts and the ingested prey cells are swiftly digested.

Yoo et al. (2010) analyzed the mixotrophic mode of *Paragymnodinium shiwhaense* based on growth experiments. They showed that this species was incapable of growth if it was denied either prey or light. This obligate mixotrophic growth is rarely demonstrated among dinoflagellates and thus far has been demonstrated in the non-kleptochloroplastidic dinoflagellates, *Esoptrodinium* sp. (Fawcett and Parrow 2014), *Polykrikos lebourae* (Kim et al. 2015) and *P. shiwhaense*. *Paragymnodinium stigmaticum* and *P. verecundum* also ingest the prey in spite of the possession of the chloroplasts, indicating the mixotrophic nutrition. On the other hand, *P. asymmetricum* and *P. inerme* grow without prey and do not show feeding behavior, indicating phototrophic nutritional mode rather than mixotrophic. There is still some possibility that these strains have a

potential to be mixotrophic because they contain some structures related to feeding behavior such as peduncle and, for *P. asymmetricum*, nematocyst. Nevertheless, these strains are clearly not obligate mixotrophic requiring both feeding and photosynthesis seen in *P. shiwhaense*. The physiological properties in relation to nutritional strategies in *P. asymmetrucum*, *P. inerme* and *P. stigmaticum* are investigated in chapter 3.

The phototrophic strains are restricted in one of the subclades of *Paragymnodinium* lacking eyespot, and *P. shiwhaense* is the only one obligate mixotrophic species in this clade. Interestingly, the close phylogenetic relationship between *P. shiwhaense* and *P. inerme*, is not reflected in their nutritional mode and thus, the diversification of nutritional mode is thought to have occurred quite recently. Considering that all *Paragymnodinium* species including the phototrophs possess some structures related to feeding, such as nematocysts and a peduncle, the evolution pattern of nutritional mode can be explained by following hypothesis: The common ancestor of this clade had a mixotrophic nutrition, and *P. asymmetricum* and *P. inerme* lost phagotrophic capability independently. Based on this hypothesis, the abnormal nematocyst in *P. inerme* (discussed below) is thought to represent a degeneration of the organelle as a result of the loss of the requirement for phagotrophy. To confirm this hypothesis, the nutritional mode of the common ancestor of the genus *Paragymnodinium* needs to be estimated, and thus, the symplesiomorphic character among these species and the closest related taxa should be confirmed. However, this requires improved statistical support of the entire topology of the phylogenetic tree for the clade *Gymnodinium sensu stricto*.

Chloroplast

The chloroplasts of *Paragymnodinium stigmaticum* and *P. verecundum* are surrounded by three membranes as is typical in dinoflagellates (Dodge 1987). The eyespot in *P. stigmaticum* and *P. verecundum* is type I according to the classification of Hoppenrath (2017), and carotenoid globules are located inside the chloroplast, as is typical in peridinin containing dinoflagellates. However, there are some unusual characters in the morphology of chloroplasts. Firstly, a thylakoid-free region which is transversed by a few thylakoid bands exists in the central part of each chloroplast. Some dinoflagellates

possess a similar region in their chloroplasts (e.g., Hansen et al. 2000, Craveiro et al. 2010), but that of *P. stigmaticum* and *P. verecundum* is relatively large and characterized by an invasion of one or two thylakoid bands. This configuration is similar to the chloroplasts of some 'dinotoms,' which contain diatom-derived chloroplasts (e.g., Yamada et al. 2017). These dinotoms generally possess a distinct lenticular pyrenoid which is often penetrated by thylakoids in this region, and they resemble those of *P. stigmaticum* and *P. verecundum*. However, the TEM observation of *P. stigmaticum* and *P. verecundum* did not show any strong evidence to indicate the presence of a pyrenoid (the texture of this region is unlike typical pyrenoids). Therefore, I describe this structure as a thylakoid-free region in the center of the chloroplast. Secondly, whereas typical dinoflagellate chloroplasts contain lamellae consisting of three appressed thylakoid bands (Dodge 1987), *P. stigmaticum* and *P. verecundum* do not. Each of its chloroplasts contains separated thylakoid bands in the peripheral area. A similar thylakoid arrangement has not been observed previously in dinoflagellates. The chloroplasts of the other *Paragymnodinium* species, *P. shiwhaense*, *P. asymmetricum* and *P. inerme* are similar to 'typical' dinoflagellate (peridinin-containing) chloroplasts, in that they are surrounded by three membranes and contain double or triple thylakoid lamellae (Kang et al. 2010, this study). Some thylakoid-free areas can be seen in the micrographs of chloroplasts in the original description of *P. shiwhaense*, although they are located on the periphery rather than in the center of chloroplasts (Kang et al. 2010). Thus, the thylakoid structure and location of *P. stigmaticum* and *P. verecundum* represent unique characters, which I interpret as autapomorphies.

The chloroplast of *Paragymnodinium asymmetricum* is a single, unlike the multiple chloroplasts seen in other *Paragymnodinium* spp. (Kang et al. 2010). In addition, it is composed of two distinctive parts: an 'antapical mass' and anterior 'lateral lobes.' The antapical mass in the hyposome contains densely stacked, double thylakoids resembling the grana-like thylakoids seen in some dinoflagellates such as *Ansanella granifera* (Jeong et al. 2014) or *Dactylodinium pterobelotum* (Takahashi et al. 2017). However, the double-stacked thylakoids of this region of the chloroplast of *P. asymmetricum* are not attached to each other. Thus, the thylakoids cannot be likened to a true granum, but are rather a tighter packing of the thylakoid lamellae relative to the

lateral lobes, which are an extension of the antapical mass. The variability in the numbers (two or three) of thylakoids stacked together, and in the packing density of these stacks, in different regions of a chloroplast has not been reported in any other dinoflagellates. *Paragymnodinium inerme* also has double- or triple-stacked thylakoids but there is no difference in its packing density or stacking thylakoid number by region of the chloroplast. In addition, *P. inerme* contains numerous oval masses of chloroplasts, which is similar to the condition in *P. shiwhaense* (Kang et al. 2010). However, some of these masses are directly connected to each other by thin bridges.

Nematocyst and peduncle or peduncle-like structure

Within dinoflagellates, nematocysts have been found only in some genera of polykrikoids and warnowiids, and in *Gyrodiniellum* and *Paragymnodinium* (Marshall 1925, Westfall et al. 1983, Greuet 1987, Hoppenrath and Leander 2007a, b, Hoppenrath et al. 2009, 2010, Kang et al. 2010, 2011). *Polykrikos* and *Nematodinium* use their nematocysts to capture prey cells for ingestion (Matsuoka et al. 2000, Gavelis et al. 2017). Although the use of nematocysts by *P. shiwhaense* has not been witnessed directly, the observation of feeding behavior in this species suggests that they (or trichocysts) are involved in prey capture (Jeong et al. 2017). Gavelis et al. (2017) reported a detailed 3D reconstruction of nematocysts in the genera *Polykrikos* (polykrikoid) and *Nematodinium* (warnowiid). The nematocyst in *Paragymnodinium* spp. lacks the taeniocysts, coiled ballistic tubules and posterior vacuoles of *Polykrikos* and the bundle of projectiles reminiscent of a Gatling gun seen in *Nematodinium* (Gavelis et al. 2017). The nematocysts of *Paragymnodinium* spp. and *Gyrodiniellum shiwhaense* are somewhat similar to each other, but *P. shiwhaense, P. stigmaticum* and *P. asymmetricum* do not show the filaments seen in *Gyrodiniellum* (Kang et al. 2011). The make-up of the nematocysts of *Paragymnodinium* spp. are basically the same, but that in *P. shiwhaense* is reported to lack a stylet (Kang et al. 2010).

I observed a peduncle-like structure with a microtubular strand (MSP) in *Paragymnodinium stigmaticum* and *P. verecundum*. The ultrastructure of the MSP of these species is basically similar to the true peduncles of other species, except for the number of comprising microtubules (e.g., Hansen 2001). The electron-opaque vesicles

near the MSP were also observed in other species (e.g., Hansen 2001). Many heterotrophic or mixotrophic dinoflagellates, including *P. shiwhaense*, use a peduncle for ingestion of a prey cell (Hansen 1991, Yoo et al. 2010). However, *P. stigmaticum* and *P. verecundum* ingest a prey cell by engulfment through the antapical area of the hyposome without using their peduncle-like structure. Moreover, the TEM observations showed a discharged nematocyst was contained in the bulb-shaped body of the extended peduncle-like structure; this suggests it is used to locate the nematocyst outside the cell and to let it discharge its fibrous strand. The detailed observation of feeding behavior of *P. stigmaticum* showed a use of peduncle-like structure linking to a prey cell, indicating that the peduncle-like structure and the nematocyst work together to capture the prey before the engulfment. Although the peduncle has been indicated to have various functions other than feeding (Gaines and Elbrächter 1987), no functional relation to a nematocyst has been reported.

In contrast to above, *Paragymnodinium asymmetrucum* and *P. inerme* did not demonstrate phagotrophy. Thus, the function of nematocysts and peduncle remains elusive. In addition, the ultrastructure of the nematocysts of *P. inerme* is notably abnormal and has never been observed before in any other dinoflagellates. The nematocyst is rare in this species (only found in 3 out of 15 cells that were serially sectioned entire cells and in none of the other random sections observed). It is possible that the abnormality of nematocyst shows its developing stage seen in other nematocyst-bearing dinoflagellates (Gavelis et al. 2017), or is a result of external factors, such as poor fixation, but the larger number of fibrous strands relative to the single fibrous strand of nematocysts in other *Paragymnodinium* spp. could be incurred by such factors (Kang et al. 2010). A paucity of nematocysts is also unique to the genus *Paragymnodinium*. The original description of *P. shiwhaense* by Kang et al. (2010) does not mention the number of nematocysts per cell, but at least six nematocysts can be identified in a single TEM image (figs. 73–75 in Kang et al. 2010). While the degree of nematocyst production may be influenced by nutrition, especially the presence/absence of prey, this is unlikely because a cell of *P. asymmetricum* contains numerous nematocysts under the same culture conditions as *P. inerme*. If nematocysts are commonly used by *Paragymnodinium* spp. to capture prey cells, it is

reasonable to assume that there is some link between the reduction in nematocysts and the loss of phagotrophy in *P. inerme*.

Flagellar apparatus

The 3D structures of flagellar apparatuses of *Paragymnodinium stigmaticum*, *P. verecundum*, *P. asymmetricum* and *P. inerme* were reconstructed based on the TEM observations. The flagellar apparatuses of these species share basic features with the related species *P. shiwhaense* (Kang et al. 2010). The absence of the nuclear fibrous connective (NFC), one of the key characters of the genus *Gymnodinium* and also seen in some genus in the clade *Gymnodinium sensu stricto* such as *Polykrikos* (Bradbury et al. 1983, Daugbjerg et al. 2000), is also common to all the species of *Paragymnodinium*.

However, investigated species of *Paragymnodinium* appeared to have the TMRE nucleating from the R3 (TMR), which have not been reported in *P. shiwhaense*. TMRE has been observed in many dinoflagellate species, and some species possess an enormous number of microtubules as the TMRE, e.g., *Gymnodinium fuscum* (Hansen et al. 2000). The TMRE of *Paragymnodinium* spp. contains only four microtubules, which is relatively small number compared to other dinoflagellates. It is very difficult to analyze R3 because of its small size and/or few number of consisted microtubules, especially in these species. R3 of *P. shiwhaense* is shown in only one TEM micrograph in its original description (Kang et al. 2010), so it is possible that the TMRE of *P. shiwhaense* was overlooked.

Paragymnodinium asymmetricum and *P. inerme* have a ventral connective (VC) linking R1 to the plasma membrane, which is often observed in other dinoflagellates (e.g., Iwataki et al. 2010). In the original description of *P. shiwhaense*, an elongate object can be seen near the R1 (fig. 32 in Kang et al. 2010). It is possible that the presence of a VC has been overlooked in *P. shiwhaense*. For *P. stigmaticum* and *P. verecundum*, a connective structure termed left-ventral fiber (LVF) connecting the R1, LB and a membrane near the end of basal bodies was observed, which is similar to the VC in its position. The VC is commonly long and striated, while the LVF in the two *Paragymnodinium* species is relatively short and unstriated. The direction of the LVF is also different from that of the VC of *Paragymnodinium* spp., in that VC runs further from

the LB and connects to the ventral plasma membrane. The LVF is also similar in structure to the ventral fiber of *Baldinia anauniensis*, but the ventral fiber runs from the right rather than the left side of the LB, and does not link to the R1 (Hansen et al. 2007). Therefore, the LVF in *P. stigmaticum* and *P. verecundum* does not correspond to any known structure. The possession of either a VC or an LVF appears to additionally reflect the two subclades; *P. asymmetricum* and *P. inerme* with a common VC, but *P. verecundum* and *P. stigmaticum* with an LVF. Because the VC is found elsewhere in the clade *Gymnodinium sensu stricto*, such as in *Gymnodinium aureolum* (Hansen 2001) and in *Lepidodinium chlorophorum* (as *G. chlorophorum*, Hansen and Moestrup 2005), the common ancestor of *Paragymnodinium* spp. most likely had the VC and it was subsequently lost in the *P. stigmaticum*/*P. verecundum* clade.

Phototaxis

Generally, the photoreceptive tasks of eyespot-bearing organisms are expected to be directional (Colley and Nilsson 2016), because the eyespot is thought to be responsible for recognizing the direction of the light source by either shading, or reflecting, the light from/to the photoreceptor (Kreimer 1994). However, there is a difference in the phototactic behavior of *Paragymnodinium verecundum* and *P. stigmaticum*, both of which possess a distinctive eyespot. Although *P. stigmaticum* recognizes light, it responds with nondirectional photoresponses, that is, its circadian rhythm-related cell cycle, and not with phototaxis. On the other hand, *P. verecundum* shows a directional response, negative phototaxis. The distinction between directional and nondirectional photoreception should be made because the former requires the detection of further information, viz. the ability to locate the source of the light (Nilsson 2013, Colley and Nilsson 2016). Moldrup et al. (2013) reported the loss of phototaxis due to the degeneration of an eyespot in a clone of *Kryptoperidinium foliaceum* caused by its cultivation for more than 25 years. The eyespots of both species of *Paragymnodinium* are robust and identical in shape (rod-shaped with anterior hook). Thus, *P. verecundum* is thought to have functional photoreceptors or photo-pigments for the response to light, which are poor or inactive in *P. stigmaticum*.

Notably, *Paragymnodinium verecundum* shows negative rather than positive phototaxis. Such a response is also seen in some photosynthetic dinoflagellates. For example, Horiguchi et al. (1999) reported negative phototaxis in both *Scrippsiella hexapraecingula* and *Kryptoperidinium foliaceum* (as *Peridinium foliaceum*), despite their different types of eyespots. Further, they found that neither responded to red light but they did to blue light, all of which coincides with the finding for *P. verecundum*. *Prorocentrum micans* has also been reported to show negative phototaxis to high irradiances, but additionally shows positive phototaxis to low irradiances (Eggersdorfer and Häder 1991). Some dinoflagellates including *Pr. micans* may also change their phototactic response depending on the time of day (Sweeney 1984, Eggersdorfer and Häder 1991). However, such a phototactic circadian rhythm was not currently observed in *P. verecundum*, at least over the times investigated (9:30, 15:00, 18:00 and 21:00). The adaptive significance of the negative phototaxis is difficult to explain but we can provide some hypotheses. For example, the negative response of the cells to relatively strong (> approximately 100 μmol photons m^{-2} s^{-1}) light (note that cells cultured with an illumination of 50 μmol photons m^{-2} s^{-1} tended to encyst on the opposite side of the light source, which indicates an ability to respond to a low irradiance as well) might be a strategy to avoid exposure of harmful UV irradiation or other risks of photodamage (Häder 1988, Colley and Nilsson 2016). In addition, the chloroplasts of ingested prey in food vacuoles seem to remain active for some time following ingestion. Negative phototaxis would therefore seem to be an appropriate strategy to suppress the generation of toxic substances such as reactive oxygen species (Lesser 2006) in the food vacuoles. On the other hand, the fact that *P. verecundum* does not show positive phototaxis to the light even with low or medium irradiance might indicate that this dinoflagellate has developed a stronger reliance on the heterotrophic component of its mixotrophic lifestyle for nutrition. Such hypotheses about the adaptive significance of negative phototaxis should be confirmed by performing feeding experiments coupled with various light/dark conditions.

TAXIONOMIC SUMMARY

***Paragymnodinium stigmaticum* Yokouchi, Onuma & Horiguchi sp. nov.**

(see also Yokouchi et al. 2018)

Description: Cells consisted of episome and hyposome of almost equal size, 8.5–15.2 μm long, 6.3–12.4 μm wide. Episome hemispherical or conical and hyposome hemispherical. Cingulum wide and well excavated, descending 1/4 to 1/2 of its own width. Sulcus straight, reaching and widening slightly at the antapex, Eyespot rod-shaped, red, with anterior hook-like extension and located at upper part of sulcus. Nucleus spherical, located in center or dorsal side of cell. Five to 10 elongate oval chloroplasts with central thylakoid-free region distributed on cell periphery. Amphiesmal vesicles arranged in 16lateral rows (eight rows on the episome, four rows in the cingulum and four rows on the hyposome). Peduncle-like structure in ventral area with bulb-shaped body containing a nematocyst. Pusule not observed. Marine, sand-dwelling. GenBank accession numbers are MH040303 for the 18S rDNA sequence and MH040304 for the 28S rDNA sequence.

Holotype: The SEM stub was deposited in the herbarium of the Faculty of Science, Hokkaido University as SAP 115400.

Collection date: August 15, 2011.

Type locality: Sumiyoshi beach, Sado Island, Niigata Prefecture, Japan (38°04.40′N, 138°27.36′E).

Etymology: Greek stigma, refers to the presence of an eyespot.

***Paragymnodinium verecundum* Yokouchi & Horiguchi sp. nov.**

(see also Yokouchi and Horiguchi 2021)

Description: Episome and hyposome of almost equal size, 9.4–17.1 μm long, 5.7–13.6 μm wide. Episome hemispherical to conical and hyposome hemispherical Cingulum wide and well excavated, descending 1/4 to 1/2 its own width Sulcus straight, reaching and widening slightly at the antapex Eyespot rod-shaped, red, with anterior hook-like extension and located in the anterior part of sulcus. Nucleus spherical, located in center of cell. Six to 12 peripheral, elongate, oval chloroplasts, with central thylakoid-free region. AVs arranged in six rows in the episome, four rows in the cingulum and five rows on the hyposome. Peduncle-like structure, ventral with bulb-shaped body containing a

nematocyst. Pusule apical, in region of the eyespot. Several nematocysts scattered through-out cell, negatively phototactic. Marine, sand-dwelling. GenBank accession numbers are LC575960 for the 18S rDNA sequence and LC575961 for the 28S rDNA sequence.

Holotype: An SEM stub has been deposited in the herbarium of the Faculty of Science, Hokkaido University as SAP 115585.

Collection date: March 26, 2018.

Type locality: At a depth of 5 m on Kitsunezaki beach, Miyagi Prefecture, Japan (38°21.21′N, 141°25.26′E).

Etymology: Latin verecundus (= shy) refers to the evasive swimming behavior when exposed to unidirectional light.

Paragymnodinium asymmetricum **Yokouchi, K. Takahashi, Nguyen, Iwataki et Horiguchi sp. nov.**

(see also Yokouchi et al. 2020)

Description: Marine, athecate dinoflagellate. Cells with almost equal-sized episomes and hyposomes, 7.9–12.6 µm long and 4.7–9.0 µm wide. Episome hemispherical or conical. Hyposome asymmetric with larger right side. Cingulum wide and well excavated, descending 1/4 to 1/2 of its own width. Sulcus straight, reaching to, and widening slightly at, the antapex. Sulcal extension-like furrow straight. Eyespot absent. Nucleus spherical, in center of episome. Chloroplast single, mainly in hyposome and with lateral lobes extending into episome. Amphiesmal vesicles arranged in five to seven rows on the episome, in five rows in the cingulum. Nematocysts present. Pyrenoid and pusule not observed. Phototrophic. GenBank accession numbers are LC516501 for 18S rDNA sequence and LC516500 for 28S rDNA sequence.

Holotype: SEM stub was deposited in the herbarium of the Faculty of Science, Hokkaido University as SAP 115483.

Collection date: April 26, 2014.

Type locality: Nha Trang beach, Nha Trang, Vietnam (12°14.56′N, 109°11.49′E).

Etymology: Latin asymmetricum refers to the asymmetric shape of hyposome.

Paragymnodinium inerme **Yokouchi, K. Takahashi, Nguyen, Iwataki et Horiguchi sp. nov.**

(see also Yokouchi et al. 2020)

Description: Marine, athecate dinoflagellate. Cells with almost equally sized episomes and hyposomes, 15.3–23.7 µm long and 10.9–19.6 µm wide. Episome hemispherical or conical and hyposome hemispherical. Cingulum wide and well excavated, descending 1/2 to once its own width. Sulcus straight, reaching to, and widening slightly at the antapex. Sulcal extension-like furrow slightly curved. Eyespot absent. Nucleus spherical, in the center of the dorsal side of cell. A total of 20–30 chloroplasts, some of which are connected by narrow bridges. Amphiesmal vesicles arranged in 19 or 20 lateral rows (eight or nine rows to the episome, five rows to the cingulum, and six rows to the hyposome). Nematocysts rare and, if present, abnormal. Pyrenoid and pusule not observed. Phototrophic. GenBank accession numbers are LC516503 for 18S rDNA sequence and LC516502 for 28S rDNA sequence.

Holotype: SEM stub was deposited in the herbarium of the Faculty of Science, Hokkaido University as SAP 115484.

Collection date: November 19, 2017.

Type locality: Jogashima, Kanagawa, Japan (35°08.02′N, 139°36.41′E).

Etymology: Latin inermis, (= unarmed) refers to absence of nematocyst.

Chapter 3. Comparative analysis of nutritional strategies within the genus *Paragymnodinium*

INTRODUCTION

Many photosynthetic eukaryotes including dinoflagellates are also capable of phagocytotic carbon uptake, exhibiting a mixotrophic nutritional mode. Mixotrophic organisms are important components of aquatic ecosystems (Mitra et al. 2016, Stoecker et al. 2017, Wilken et al. 2019). Some mixotrophic organisms are recognized as representatives exhibiting transitional phase from phototrophy to heterotrophy, or vice versa (e.g., Yamaguchi et al. 2012, Kim et al. 2015). The strategies for, and dependence on, nutrient acquisition through photosynthesis or ingestion in mixotrophic organisms are diverse, and these properties are progressively investigated by various approaches (Stoecker 1999, Mitra et al. 2016, Stoecker et al. 2017, Wilken et al. 2019).

As discussed in chapter 2, all species within the genus *Paragymnodinium* contain pigmented chloroplasts, but they display a significant variety of nutritional strategies; *P. shiwhaense*, *P. stigmaticum* and *P. verecundum* are capable of ingesting other unicellular algae, indicating mixotrophic nutrition (Kang et al. 2010, Yoo et al. 2010, Chapter 2). *Paragymnodinium stigmaticum* and *P. verecundum* have a few notable characters specific to mixotrophy. First, they have an abnormal chloroplast ultrastructure, where the thylakoids are separated rather than stacked in threes as in typical peridinin-type chloroplasts. Secondly, their feeding behavior involving a complex feeding apparatus is indicative of an enhanced heterotrophic nutritional strategy. On the other hand, *P. asymmetricum* and *P. inerme* have never been observed to show feeding behavior and can be cultured in isolation, indicating the dependence of phototrophic nutrition. The functional trait differences within a single genus provides an opportunity to better understand the evolution of nutritional strategies within dinoflagellates as a whole.

To our knowledge, physiological approaches to evaluating the contribution of photosynthesis to the nutrition of *Paragymnodinium* spp. have not been conducted. In this chapter, the nutritional strategies of *P. asymmetricum*, *P. inerme* and *P. stigmaticum* are aligned with their respective photosynthetic properties including growth with or without

prey and monolinuron as an inhibitor of photosystem II (Arnaud et al. 1994, Christa et al. 2013), pigment, absorption spectrum, variable chlorophyll *a* fluorescence, and carbon fixation capabilities of the three species. The results demonstrate distinct differences in nutritional strategies between members of the genus *Paragymnodinium*, providing a platform for the hypothetical loss of photosynthetic function leading to colorless dinoflagellates.

MATERIALS AND METHODS

Preparation of culture strains

Cultures of *Paragymnodinium stigmaticum* (strain SD01), *P. inerme* (strain JGD) and *P. asymmetricum* (strain vnd299) were maintained in Daigo's IMK Medium for Marine Microalgae (Nihon Pharmaceutical Co., Tokyo, Japan) at 20°C with an illumination of 100 μmol photons m^{-2} s^{-1} by a LED lump (LDL40T N/17/25-S, TOSHIBA, Tokyo, Japan) under 16:8 h light:dark cycle. Cells of *Rhodomonas* sp. (strain Mr06, Cryptophyceae) were added as prey for *P. stigmaticum*, and the co-cultivated culture was maintained for over two months. *Paragymnodinium inerme* and *P. asymmetricum* were cultured without adding any prey. Cells in the exponential growth phase were used.

Preliminary experiments (data not shown) revealed that the cells of the *Paragymnodinium stigmaticum* could be in any of the following three life stages: (1) attached to the vessel bottom as immotile cysts during the dark phase, (2) gradually becoming motile after the transition from the dark to the light phase, consequently almost all *P. stigmaticum* cells became motile five to six hours after the onset of light, and (3) encysting again after they ingest sufficient prey or after the return of the dark phase. The immotile cyst cells were strongly attached to the vessel bottom. Cells in the stages of (2) and (3) can be observed simultaneously in the mixotrophic cultures that are well-fed. Taking into account these features, to obtain an unialgal culture of *P. stigmaticum*, cells were co-cultivated with *Rhodomonas* sp. in 50 mL tube, and the culture medium was strongly agitated and replaced to fresh medium to remove *Rhodomonas* cells, immediately before the onset of the light phase. Non-contamination with *Rhodomonas* sp. in the *P. stigmaticum* unialgal culture was confirmed using light microscopy. This unialgal sample was used for the experiments below.

Growth experiment

Growth rates of *Paragymnodinium asymmetricum*, *P. inerme* and *P. stigmaticum* under different prey/light conditions (Table 3.1) were determined by counting the cells at each time point. The initial cell concentrations were adjusted to 2,000 cells mL^{-1} for *P. asymmetricum* and *P. stigmaticum* and 500 cells mL^{-1} for *P. inerme*, because the maximum cell concentration of *P. inerme* tended to be lower than that of other two species.

The initial concentration of *Rhodomonas* sp. as a prey for *P. stigmaticum* was adjusted to 4,000–32,000 cells mL^{-1} (Table 3.1). The growth of *Rhodomonas* sp. in isolation (initial concentration = 4000 cells mL^{-1}) was also measured for estimating the ingestion rate (see below). After the adjustment of cell concentrations, 350 µL aliquots of the culture were transferred into wells of a 96-well plate and incubated under each condition. The cultures were incubated for 11 days, and cells were counted at five to six hours after the onset of light period on days 1–5, 7, 9, 11 or days 1–6, 8, 10 after inoculation. To count the cells, after collecting the culture in each well, the well was rinsed with 350 µL of fresh IMK medium two times through pipetting. The total 1,050 µL of culture + supernatant was collected in a 1.5 mL tube, and then it was immediately fixed with Lugol's Iodine solution (final concentration = 1 %; v/v). When the cells of *P. stigmaticum* and *Rhodomonas* sp. were collected from co-culture, *Rhodomonas* sp. was separated before the onset of the light phase, and *P. stigmaticum* was kept in 350 µL of fresh IMK medium and collected after the transition to motile phase (the stage (2), see above). The fixed cells were counted manually using a Sedgewick-Rafter Counting Chamber and an inverted microscope (Olympus CX40, Tokyo, Japan), and each cell concentration was estimated. After the sample was transferred to the counting chamber, it had been left for 10 minutes for the settlement of cells. Cells were summed until 300 squares were examined, or until over 200 cells were counted. When the cell concentration showed a decreasing trend, counting was stopped on the day whose cell concentration became lower than 100 cells mL^{-1}. All treatments were conducted in triplicate.

For *Paragymnodinium stigmaticum*, the cell division occurred during the stage (1) (see above). However, the growth rates of *P. stigmaticum* under dark conditions were not be estimated, because they were firmly attached to the well floor, therefore the enumeration was infeasible. To compare the growth performance between mixotrophy and phototrophy, monolinuron diluted in DMSO (final concentration = 0.2 %; w/v) was added to certain replicate wells to inhibit photosynthesis, and DMSO without monolinuron was added to others as controls. The growth of *P. asymmetricum* and *P. inerme* was also measured in the same way.

The specific growth rate, µ (d^{-1}), was calculated as follows:

$$\mu = \frac{\mathrm{Ln}\left(\frac{X_t}{X_0}\right)}{t} \quad (1)$$

where X_0 is the initial cell concentration and X_t is the final concentration after time t. The time period for estimating μ ranged between 1 to 3 days, considering that the first day (day 0 to 1) was possibly in a lag phase. Cellular ingestion rates were calculated based on the disappearance of prey in the mixed cultures compared with the levels found in the prey monocultures, using the equations described by Skovgaard et al. (2000):

$$\frac{dX}{dt} = \mu_X \times X \quad (2)$$

$$\frac{dY}{dt} = \mu_Y \times Y - \mathrm{IR} \times X \quad (3)$$

where Y is the prey concentration, μ_Y is the prey growth rate in monoculture, X is the predator concentration (cells mL^{-1}), μ_X is the exponential growth rate of the predator during the incubation period, and IR is the ingestion rate (cells $cell^{-1}$ d^{-1}). Ingestion rates were averaged over a period of 3 d.

Pigment analysis

Samples with known volume and cell concentrations were filtered onto 25 mm Whatman GF/F filters by gentle vacuum (< 0.013 MPa). The resultant filters were cut into small pieces with clean scissors and soaked in 1 mL of HPLC-grade DMF (Fujifilm Wako Pure Chemical Corp.) containing a known amount of trans-β-apo-8'-carotenal (Sigma-Aldrich) as an internal standard. Pigments were extracted using the bead-beating technique described by Suzuki et al. (2015). A Shimadzu UHPLC Nexera X2 SR system (Suzuki et al. 2015) was used to analyze the chlorophylls and carotenoids. Concentrations of each pigment were calculated on the basis of peak areas in the chromatogram and the equation for the standard curve for each pigment (n = 4) (Suzuki et al. 2015). Specific chlorophyll *a* content (fg μm^{-3}) was calculated by dividing the chlorophyll *a* content per cell (fg $cell^{-1}$) by the averaged cell volume (μm^3) of each dinoflagellate under the same conditions. The cell volume was estimated assuming the cell shape is prolate spheroid for *P. inerme* (n = 28) and *P. stigmaticum* (n = 10) and double cone for *P. asymmetricum* (n = 55) (Hillebrand et al. 1999).

Absorption spectra

The absorption spectrum and the chlorophyll *a* specific absorption coefficient (a^*_{ph} (λ), m^2 [mg chlorophyll *a*]$^{-1}$) of each species were measured with the quantitative filter technique (QTF) (n = 4) following Yoshida et al. (2018). Before measurements, cells were concentrated using 47 mm, 1.2 μm MF-Millipore membrane by gentle vacuum, and resuspended in a small amount of the culture medium IMK. The optical density of suspended particles (OD_{sp}) from the membrane for each species was measured in 1 nm steps between 350–750 nm using a dual-beam spectrophotometer (MPS-2450, Shimadzu) with 1-cm pathlength quartz cuvettes. The medium IMK was used for reference during measurement. All spectra were set to zero at 750 nm to minimize differences between sample and reference, assuming the lack of absorption at 750 nm. Also, the samples were filtered onto 25 mm Whatman GF/F filters with gentle vacuum (< 0.013 MPa), and the optical density of particles on the filter (OD_{fp}) was measured using the Shimadzu spectrophotometer with an end-on type photomultiplier tube plus a solid sample holder. A blank filter, wetted with IMK medium, was used as reference. After the pigments on the filter were extracted with methanol, the optical density of detritus (OD_{fd}) on the filter was measured with the same manner. In the case that the absorption from chlorophyll *a* at 675 nm remained after methanol extraction, the filter was boiled in Milli-Q water for denaturing the chlorophyll-protein complexes.

The relationship between OD_s and OD_f reflecting the optical path length amplification factor β was represented as the following equation (Mitchell 1990):

$$OD_s = a \times OD_f + b \times OD_f^2 \quad (4)$$

The coefficients *a* and *b* were derived based on the values of OD_{sp} and OD_{fp} resulted by the first replicate for each species (see RESULTS for these coefficients).

Light absorption coefficient a_{ph} was determined by the following equations (Kishino et al. 1985);

$$a_{ph}(\lambda) = a_p(\lambda) - a_d(\lambda) \quad (5)$$

where a_p and a_d are light absorption coefficients of particles and detritus, respectively, determined by following equations:

$$a_p(\lambda) = 2.3OD_{sp}(\lambda)/l_g \quad (6)$$

$$a_d(\lambda) = 2.3OD_{sd}(\lambda)/l_g \quad (7)$$

where l_g is geometric pathlength obtained from filtered amount (V_f) / filtration area (S). Chlorophyll *a* concentration-standardized specific light absorption coefficients a^*_{ph} was determined referring the chlorophyll *a* concentration of each species. Mean a^*_{ph} within 400–700 nm ($\bar{a}^*_{ph}$, m^2 [mg chlorophyll *a*]$^{-1}$) was weighted with the spectral irradiance of the incubator lamp to correct for the spectral characteristics of the incubator lamp source (Cota et al. 1994):

$$\bar{a}^*_{\mathrm{ph}} = \frac{\int_{\lambda=400}^{700} a^*_{ph}(\lambda) \times E_{\mathrm{NL}}(\lambda)\mathrm{d}\lambda}{\int_{\lambda=400}^{700} E_{\mathrm{NL}}(\lambda)\mathrm{d}\lambda} \quad (8)$$

where $E_{NL}(\lambda)$ is the normalized spectral irradiance of the incubator lamp, estimated as follows:

$$E_{NL} = \frac{E_{\mathrm{L}}(\lambda)}{\int_{\lambda} E_{\mathrm{L}}(\lambda)\mathrm{d}\lambda} \quad (9)$$

where $E_L(\lambda)$ is the incubator lamp spectrum.

Variable chlorophyll *a* fluorescence

Variable fluorescence of chlorophyll *a* was measured for triplicate samples using the two active fluorometers: Satlantic FIRe (Fluorescence Induction and Relaxation) system and pulse-amplitude modulated fluorimeter (WATER-PAM; Walz GmbH, Germany) with red light-emitting diodes (LEDs). For *Paragymnodinium stigmaticum*, the fluorescence was measured at days 1 (n = 3) and 4 (n = 1) after starvation to investigate the changes in photosynthetic activity of photosystem II (PSII). Before measuring, cells were concentrated using a 47 mm, 1.2 μm MF-Millipore membrane under gentle vacuum, resuspended in the medium, and were dark-acclimated for approximately 20 min to open the reaction centers.

For FIRe measurement, a strong short pulse with a duration of 300 μs induced transient changes in chlorophyll *a* fluorescence emission at 680 nm. The duration of a pulse of 300 μs was set to ensure a curve-fitting by the following process. Triplicate samples were measured with 50 iterations per sample. Raw data were collected following the manufacturer's protocol and processed with the MATLAB-based program fireworx,

developed by Dr. Audrey B. Barnett (Dalhousie Univ.) to obtain the maximum quantum yield of photosystem II in a dark-acclimated state (F_v/F_m), the functional absorption cross-section of the photosystem II (σ_{PSII}, $Å^2$ photon^{-1}), and the time constant for the electron transport on the acceptor side of photosystem II (τQ_A, μs) indicating the time of Q_A re-oxidation (Kolber et al. 1998). F_v/F_m in a dark-adapted state was calculated according to Genty et al. (1989):

$$F_v/F_m = (F_m - F_0)/F_m \quad (10)$$

where F_m is the maximum chlorophyll fluorescence yield when photosystem II reaction centers are closed by a strong light pulse and F_0 is basic fluorescence yield recorded with low measuring light intensities.

WATER-PAM with multiple-turnover flashes was also used to measure F_v/F_m and the effective quantum yield of photosystem II for photochemistry in different light levels from 0 to 1,710 μmol photons m^{-2} s^{-1} (Y_{PSII}), according to Genty et al. (1989):

$$Y_{PSII} = (F'_m - F)/F'_m \quad (11)$$

where F'_m is the maximum fluorescence emitted by the light-acclimated sample after a saturating pulse and F is the fluorescence level of the light-acclimated sample measured just prior to the saturating pulse. The relative electron transport rate of photosystem II (rETR_{PSII}, μmol electrons m^{-2} s^{-1}) was calculated using the following equation:

$$rETR_{PSII} = Y_{PSII} \times PAR \times 0.5 \quad (12)$$

where Y_{PSII} is the effective quantum yield of photosystem II, PAR (μmol photons m^{-2} s^{-1}) is the actinic irradiance, 0.5 is a multiplication factor assuming that the electrons are equally distributed to two photosystems (Gilbert et al. 2000, Kromkamp and Forster 2003).

Photosynthetic carbon fixation rate

Each culture was diluted with IMK medium to adjust the chlorophyll *a* concentration to 1–3 μg L^{-1} (final volume of 1.2 L). The culture was dispensed into 11 transparent 70 mL cell culture flasks. Known amount of $NaH^{13}CO_3$ was added to 10 flasks, and the remaining one was kept to determine total carbonic acid concentration before the treatment. Just after the addition of $NaH^{13}CO_3$, the flasks were set on an incubator designed by Marcel et al. (1994) keeping the temperature at 20°C. Samples were exposed

to a gradient of light, from 10 to 900 µmol photons m^{-2} s^{-1}, using a PCS-UMX250 (Nippon PI, Japan) light source. All experiments were done in triplicate for each species. After treatment, the cultures were filtered through 25 mm Whatman GF/F filters (pretreated by heat (450°C, 5 h) to remove extraneous organic matter) by gentle vacuum (< 0.013 MPa). The filters were put in cryovials and stored at −80°C for further analyses. Defrosted filters were exposed to the vapor of concentrated hydrochloric acid, to remove inorganic carbon, and vacuum dried in a desiccator. The dried filters were wrapped with tin foil capsules, and the carbon contents and the stable isotope ratio were analyzed with an isotope mass spectrometer (Flash EA, Thermo Fisher Scientific, Inc. USA). Chlorophyll *a* normalized carbon fixation rate (µmol C [mg chlorophyll *a*]$^{-1}$ h^{-1}) was estimated following Hama et al. (1983). Then dissolved inorganic carbon concentration in IMK medium was assumed to be 24 mg C L^{-1}.

Curve fitting

Electron transport / carbon fixation rate versus light curves were fitted using two models. The first (Jassby and Platt 1976) does not consider photoinhibition:

$$P = P_{\max} \times \tanh(\alpha / P_{\max}) \tag{13}$$

where P is the electron transport or chlorophyll specific carbon fixation rate at each light intensity, $P_{\max}$ is the maximum rate and α is the maximal light utilization efficiency which correspond to the initial slope of the curve. The second (Platt et al. 1980) considers photoinhibition:

$$P = P_s \times \left(1 - e^{-\frac{\alpha \times PAR}{P_s}}\right) \times e^{-\frac{\beta \times PAR}{P_s}} \tag{14}$$

$$P_{\max} = P_s \times \left(\frac{\alpha}{\alpha + \beta}\right) \times \left(\frac{\beta}{\alpha + \beta}\right)^{\frac{\beta}{\alpha}} \tag{15}$$

where P is the electron transport or chlorophyll normalized carbon fixation rate, P_s is the maximum potential light-saturated rate, $P_{\max}$ is the maximum rate, PAR is the actinic irradiance, α is the maximal light utilization efficiency and β is the photoinhibition parameter. The data sets of electron transport and carbon fixation rate were fitted using both models with R version 3.6.3, and the model which recovered the higher R^2 value

was adopted. The minimum saturating irradiance (E_k) were calculated using the following equation:

$$E_k = \frac{P_{max}}{\alpha} \quad (16)$$

where P_{max} is the maximum rate and α is the maximal light utilization efficiency.

Based on α derived from carbon fixation rate versus light curves, the maximum quantum yield of carbon fixation (Φ_{cmax}, mol C mol photon^{-1}) was calculated from the following equation:

$$\Phi_{cmax} = \frac{\alpha}{3600\bar{a}^*_{ph}} \quad (17)$$

where 3600 converts seconds to hours.

Statistics

To test for significant differences of chlorophyll *a* content, molar pigment ratios to chlorophyll *a* and the parameters of the chlorophyll *a* variable fluorescence in *Paragymnodinium asymmetricum*, *P. inerme* and *P. stigmaticum*, one-way ANOVA and Turkey's honestly significant difference *post hoc* test was used at the 99% significance level ($p < 0.01$) with R version 3.6.3.

RESULTS

Growth experiment

The experimental settings with or without prey, DMSO, or monolinuron in each species are provided in Table 3.1. Unialgal cultures of *Paragymnodinium asymmetricum* and *P. inerme* showed positive growth (Fig. 3.1, Table 3.2). The addition of monolinuron resulted in a decrease in cell concentration of *P. asymmetricum* and *P. inerme* soon after the onset of the experiments (As+D+M and In+D+M, Fig. 3.1). A comparison of the growth of *P. stigmaticum* between different prey concentrations (St, St+R4–32) revealed that *P. stigmaticum* grew well only when prey concentrations were initially high (Fig. 3.1, Table 3.2). The specific growth rates (μ) of *P. stigmaticum* under prey-saturated conditions (St+R16, St+R24 and St+R32; μ = 1.06–1.15) were higher than those of *P. asymmetricum* (As; μ = 0.44) and *P. inerme* (In; μ = 0.56) (Table 3.2). The growth of *P. stigmaticum* was suppressed under prey-limited conditions (St+R4, St+R8), and the cell density steadily decreased when their prey was unavailable (St) (Fig. 3.1, Table 3.2). Even after monolinuron was added to the culture, *P. stigmaticum* cells increased when their prey was initially abundant (St+R32+D+M) (Fig. 3.1). However, the specific growth and ingestion rates (IR) under photo-inhibited condition (St+R32+D+M; μ = 0.40, IR = 0.70) were decreased relative to those in the control (St+R32+D; μ = 1.12, IR = 9.70) (Table 3.2).

Pigment analysis

The chlorophyll *a* content (fmol cell^{-1}) and the molar ratio of major other pigments to chlorophyll *a* are summarized in Tables 3.3 and 3.4, respectively. Only low levels of alloxanthin, a specific carotenoid in cryptophytes, were detected in the co-cultivated *Paragymnodinium stigmaticum* and *Rhodomonas* sp. samples (Table 3.3), representing that viable remnants of *Rhodomonas* sp. would be negligible. Specific chlorophyll *a* content (fg μm^{-3}) tended to be higher in *P. inerme* (1.63) than in either *P. asymmetricum* (1.10) or *P. stigmaticum* (0.99), although the differences were not statistically significant ($p > 0.01$, one-way ANOVA, Table 3.3). All species contained peridinin with a molar ratio to chlorophyll *a* of approximately 1 in *P. asymmetricum* and *P. inerme*, but 0.24 in *P. stigmaticum* (Table 3.4). In addition, the molar ratios of chlorophyll c_2 and *β*-carotene

to chlorophyll *a* of *P. stigmaticum* were lower (0.13) and higher (0.41), respectively, from those of the other two species (Table 3.4).

Absorption spectra

The coefficients of the equation (4) representing the relationship between OD_s and OD_f were derived based on the values of OD_{sp} and OD_{fp} for each species. The resultant equations were as follows:

$$OD_s = 0.3612 \times OD_f + 0.2685 \times OD_f^2 \quad (\textit{Paragymnodinium asymmetricum})$$

$$OD_s = 0.4177 \times OD_f - 0.2561 \times OD_f^2 \quad (\textit{P. inerme})$$

$$OD_s = 0.4625 \times OD_f - 0.0560 \times OD_f^2 \quad (\textit{P. stigmaticum})$$

The chlorophyll *a* concentration-normalized light absorption coefficient (a^*_{ph}) is shown in Fig. 3.2. The mean a^*_{ph} ($\bar{a}^*_{ph}$) values between 400–700 nm in *Paragymnodinium asymmetricum*, *P. inerme* and *P. stigmaticum* were 0.035, 0.021 and 0.025, respectively. In *P. inerme*, the values of a^*_{ph} in shorter wavelengths (350–400 nm) tended to be higher, but this was not true for those of *P. asymmetricum* and *P. stigmaticum* (Fig. 3.2). In *P. stigmaticum*, the Q_y band of chlorophyll *a* around 675 nm was red-shifted by approximately 10 nm relative to those observed in *P. asymmetricum* and *P. inerme* (Fig. 3.2).

Variable chlorophyll *a* fluorescence

The results of variable chlorophyll *a* fluorescence parameters measured by FIRe and WATER-PAM fluorometry are summarized in Table 3.5. *Paragymnodinium asymmetricum* and *P. inerme* showed similar values in F_v/F_m, σ_{PSII} and, τQ_A, but F_v/F_m in *P. stigmaticum* was significantly lower than that in the other two species ($p < 0.01$, One-way ANOVA, Fig. 3.5). The F_m values in *P. stigmaticum* were generally quite low even in the dark-adapted condition (data not shown). In addition, σ_{PSII} was approximately three times as high and τQ_A was approximately two thirds as low in *P. stigmaticum* as those in *P. asymmetricum* and *P. inerme* on days 1 and 4 (Table 3.5).

The relationship of the electron transport rate of photosystem II ($rETR_{PSII}$) to light intensity and its originated photosynthetic parameters are shown in Fig. 3.3 and Table 3.6, respectively. Both *Paragymnodinium asymmetricum* and *P. inerme* showed a

typical rETR_{PSII}-light curve response (Fig. 3.3). By using the first model (Eq. 13) that excludes consideration of photoinhibition, *Paragymnodinium asymmetricum* showed much higher values of rETR_{PSII} and of the parameters rETR_{PSII}-max, α and E_k than those of *P. inerme* (Table 3.6). The rETR_{PSII} values of *P. stigmaticum*, however, were too low to read off the curve, therefore the PAM fluorometry-derived parameters were unavailable for this species (Fig. 3.3, Table 3.6).

Photosynthetic carbon fixation rate

The chlorophyll *a* normalized carbon fixation rates as a function of light intensity and its related parameters are shown in Fig. 3.4 and Table 3.6, respectively. By using the second model (Eq. 14–15) taking photoinhibition into account, *Paragymnodinium asymmetricum* and *P. inerme*. *Paragymnodinium asymmetricum* showed higher carbon fixation rates, and α, β and $\Phi_{c\,max}$ values than *P. inerme* (Fig. 3.4, Table 3.6). The E_k value was slightly higher in *P. inerme*. The chlorophyll *a* normalized carbon fixation rates in *P. stigmaticum* were consistently quite low regardless of a verity of light availability. As a result, the photosynthetic parameters were not estimated for this species (Fig. 3.4, Table 3.6).

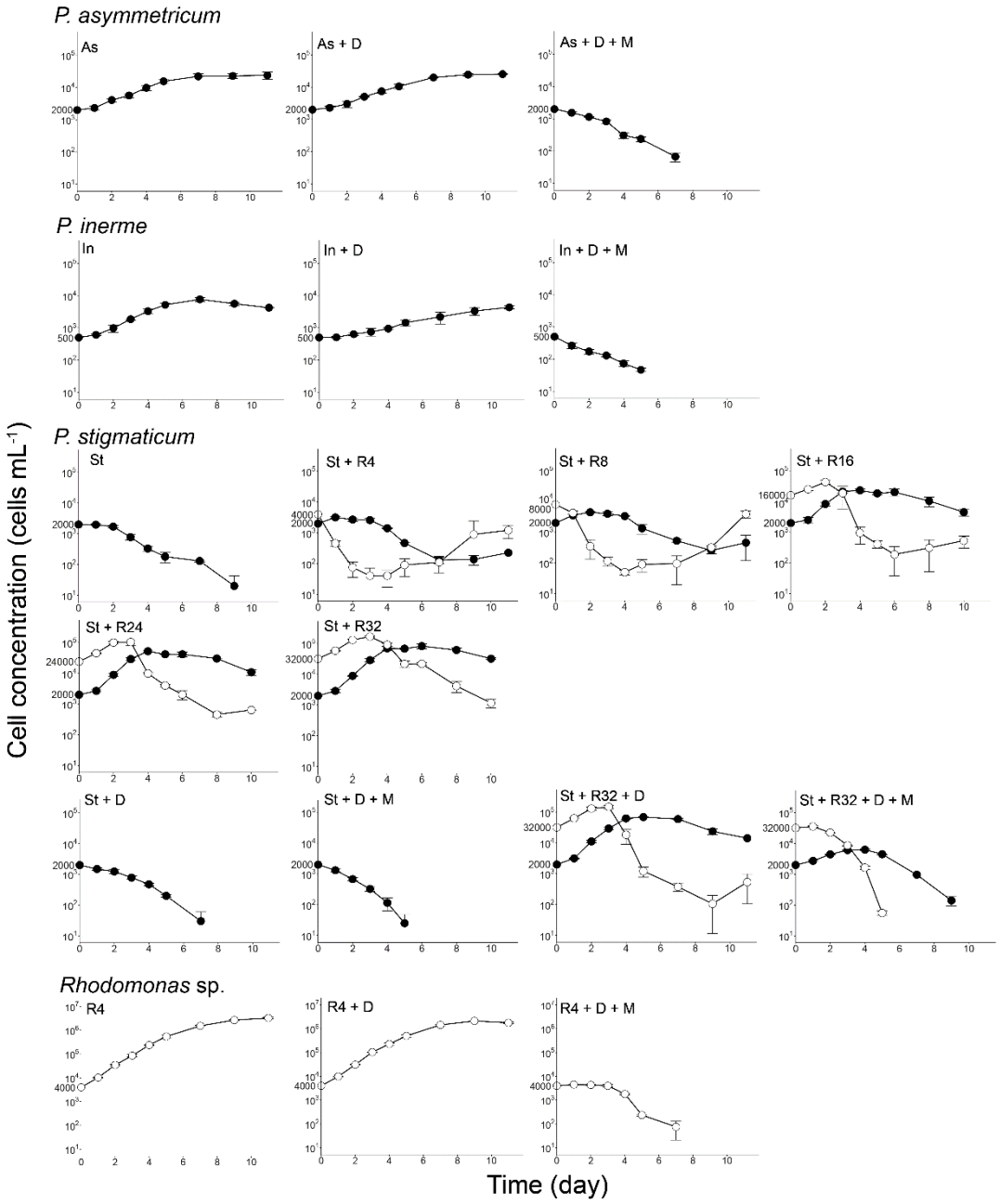

Fig. 3.1. Time course of cell concentration of *Paragymnodinium stigmaticum*, *P. asymmetricum*, *P. inerme* (black) and *Rhodomonas* sp. (white) in different conditions. See Table 1 for the interpretation of the shorthand notation. Data points are means ± SD (n = 3).

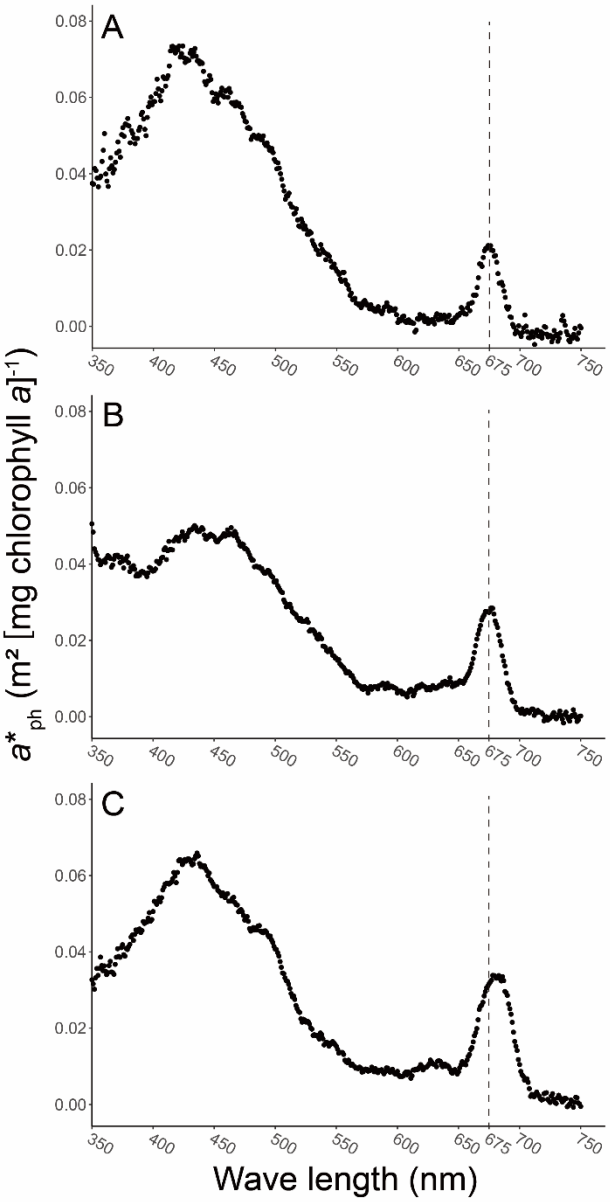

Fig. 3.2. Chlorophyll *a* concentration-normalized light absorption coefficients a^*_{ph} within the photosynthetically active radiation (350–750 nm) (μmol photons m^{-2} s^{-1}) for (A) *Paragymnodinium asymmetricum*, (B) *P. inerme* and (C) *P. stigmaticum*. Dashed lines indicate 675 nm, which is the center wavelength of the Q_y absorption band of chlorophyll *a*.

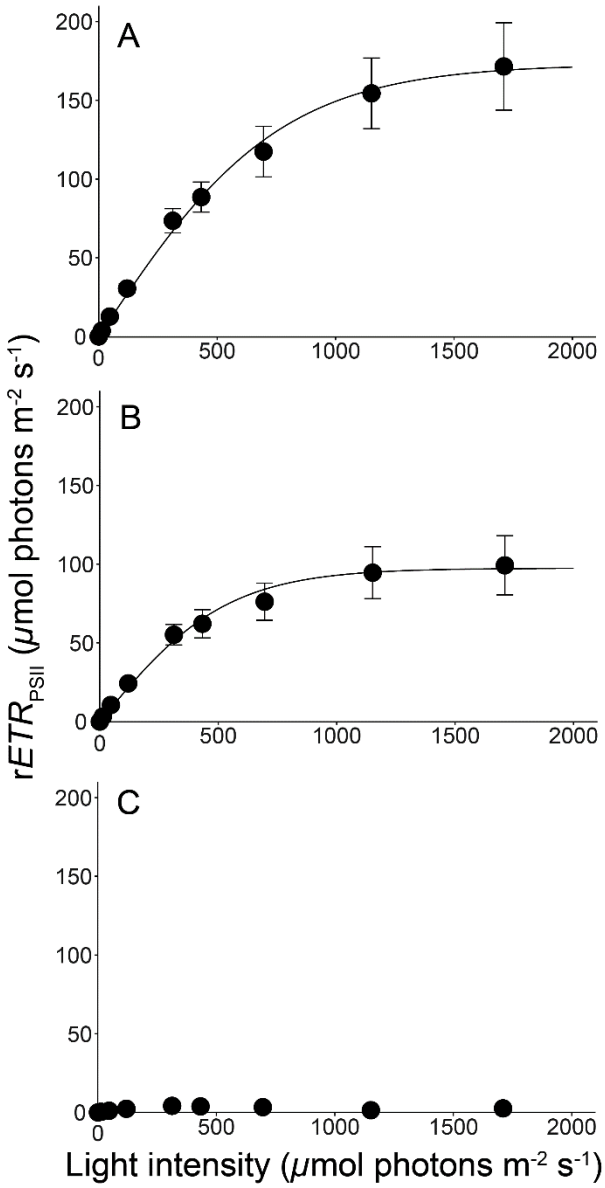

Fig. 3.3. Relative electron transport rate of photosystem II (rETR_{PSII}, µmol photons m^{-2} m^{-1}) against the photosynthetically active light intensity (µmol photons m^{-2} s^{-1}) for (A) *Paragymnodinium asymmetricum*, (B) *P. inerme* and (C) *P. stigmaticum*. Data points are means ± SD (n = 3).

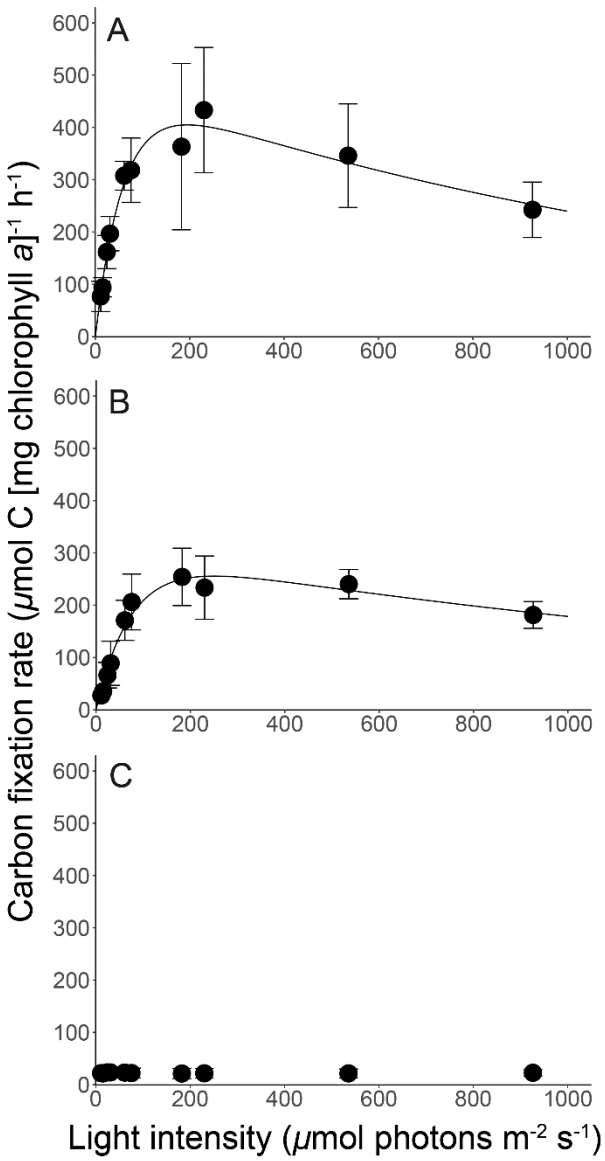

Fig. 3.4. Carbon fixation rate (µmol C [mg chlorophyll *a*]$^{-1}$ h^{-1}) against the photosynthetically active radiation (µmol photons m^{-2} s^{-1}) for (A) *Paragymnodinium asymmetricum*, (B) *P. inerme* and (C) *P. stigmaticum*. Data points are means ± SD (n = 3).

Table 3.1. Shorthand notation of combinations of organisms and conditions used in growth experiments.

Notation	Initial prey concentration (cells mL^{-1})	DMSO	Monolinuron	Examined day
P. asymmetricum				
As	-	-	-	1-5, 7, 9, 11
As+D	-	+	-	1-5, 7, 9, 11
As+D+M	-	+	+	1-5, 7
P. inerme				
In	-	-	-	1-5, 7, 9, 11
In+D	-	+	-	1-5, 7, 9, 11
In+D+M	-	+	+	1-5
P. stigmaticum				
St	-	-	-	1-5, 7, 9
St+R4	+ (4000)	-	-	1-5, 7, 9, 11
St+R8	+ (8000)	-	-	1-5, 7, 9, 11
St+R16	+ (16000)	-	-	1-6, 8, 10
St+R24	+ (24000)	-	-	1-6, 8, 10
St+R32	+ (32000)	-	-	1-6, 8, 10
St+D	-	+	-	1-5, 7
St+D+M	-	+	+	1-5
St+R32+D	+ (32000)	+	-	1-5, 7, 9, 11
St+R32+D+M	+ (32000)	+	+	1-5, 7, 9
Rhodomonas sp.				
R4	-	-	-	1-5, 7, 9, 11
R4+D	-	+	-	1-5, 7, 9, 11
R4+D+M	-	+	+	1-5, 7

Table 3.2. Summary of specific growth rates (μ) and ingestion rates (IR) estimated from the growth experiments. See Table 1 for the sample notations.

Sample notation	μ (d^{-1})	IR (cells $cell^{-1}$ d^{-1})
P. asymmetricum		
As	0.44	-
As+D	0.40	-
As+D+M	−0.31	-
P. inerme		
In	0.56	-
In+D	0.20	-
In+D+M	−0.35	-
P. stigmaticum		
St	−0.47	-
St+R4	−0.10	2.31
St+R8	0.06	3.74
St+R16	1.06	6.70
St+R24	1.19	7.11
St+R32	1.15	8.24
St+D	−0.32	-
St+D+M	−0.70	-
St+R32+D	1.12	9.70
St+R32+D+M	0.40	0.70
Rhodomonas sp.		
R4	1.07	-
R4+D	1.18	-
R4+D+M	−0.06	-

Table 3.3. Chlorophyll *a* content per cell (fg cell^{-1}) and specific chlorophyll *a* content (fg µm^{-3}) in *Paragymnodinium asymmetricum*, *P. inerme* and *P. stigmaticum* (means ± SD, n = 4). Significantly different values ($p < 0.01$, one-way ANOVA) are indicated by letters.

Species	Chl. *a* content per cell (fg cell^{-1})	Specific Chl. *a* content (fg µm^{-3})
P. asymmetricum	275 ± 102 [a]	1.10 ± 0.41 [a]
P. inerme	3821 ± 1008 [b]	1.63 ± 0.43 [a]
P. stigmaticum	611 ± 114 [a]	0.99 ± 0.19 [a]

Table 3.4. Molar ratios of pigment to chlorophyll *a* of the major pigments detected in *Paragymnodinium asymmetricum*, *P. inerme* and *P. stigmaticum* (means ± SD, n = 4). Significantly different values ($p < 0.01$, one-way ANOVA) are indicated by letters.

Species	Chl. c_2	Peridinin	Diadinoxanthin	Dinoxanthin	Alloxanthin	Diatoxanthin	Zeaxanthin	β-carotene
P. asymmetricum	0.31 ± 0.04^{a}	0.95 ± 0.11^{a}	0.50 ± 0.02^{a}	0.11 ± 0.01^{ab}	0^{a}	0.01 ± 0.01^{a}	0.09 ± 0.11^{a}	0.03 ± 0.02^{a}
P. inerme	0.44 ± 0.01^{b}	1.04 ± 0.03^{a}	0.50 ± 0.04^{a}	0.09 ± 0.01^{a}	0^{a}	0^{a}	0.03 ± 0.03^{a}	0.04 ± 0.01^{a}
P. stigmaticum	0.13 ± 0.01^{c}	0.24 ± 0.01^{b}	0.45 ± 0.02^{a}	0.14 ± 0.00^{b}	0.01 ± 0.01^{a}	0.01 ± 0.00^{a}	0^{a}	0.41 ± 0.05^{b}

Table 3.5. Summary of the values of the parameters of the chlorophyll *a* variable fluorescence in *Paragymnodinium asymmetricum*, *P. inerme* and *P. stigmaticum* measured by WATER-PAM and FIRe (means ± SD, n = 3, except for *P. stigmaticum* at day 4 with n = 1). Significantly different values ($p < 0.01$, one-way ANOVA) are indicated by letters.

Parameter	*P. asymmetricum*	*P. inerme*	*P. stigmaticum*	
			day 1	day 4
WATER-PAM				
F_v/F_m	0.620 ± 0.040 [a]	0.647 ± 0.029 [a]	0.049 ± 0.007 [b]	0.023
FIRe				
F_v/F_m	0.360 ± 0.040 [a]	0.394 ± 0.028 [a]	0.040 ± 0.007 [b]	0.042
σ_{PSII} (Å^2 photon^{-1})	48.38 ± 2.16 [a]	53.80 ± 3.06 [a]	146.49 ± 3.91 [b]	288.26
τQ_A (µs)	3335.1 ± 128.9 [a]	3022.7 ± 204.1 [a]	1933.6 ± 330.9 [b]	1881.8

Table 3.6. Summary of the parameter values obtained from the photosynthesis–irradiance curve experiments on the relative electron transport rate in photosystem II (r*ETR*) and carbon fixation rate (C) in *Paragymnodinium asymmetricum* and *P. inerme*.

Parameter	*P. asymmetricum*	*P. inerme*
Relative electron transport rate		
rETR_{PSII}-max (µmol electrons m^{-2} s^{-1})	172.4	96.8
rETR_{PSII}-α (electrons $photons^{-1}$)	0.23	0.18
rETR_{PSII}-E_k (µmol photons m^{-2} s^{-1})	765	544
R^2 of fitting curve	1.00	1.00
Carbon fixation rate		
C-max (µmol C [mg chlorophyll *a*]$^{-1}$ h^{-1})	401	253
C-α ((µmol C [mg chlorophyll *a*]$^{-1}$ h^{-1}) (µmol photons m^{-2} s^{-1}))	7.9	3.9
C-β ((µmol C [mg chlorophyll *a*]$^{-1}$ h^{-1}) (µmol photons m^{-2} s^{-1}))	0.34	0.16
C- E_k (µmol photons m^{-2} s^{-1})	51.0	65.3
R^2 of fitting curve	0.99	0.99
Φ_{cmax} (mol C mol $photon^{-1}$)	0.062	0.051

DISCUSSION

Paragymnodinium asymmetricum and *P. inerme* were clearly autotrophic as they grew in the absence of prey cells, whereas the growth and ingestion rates of *P. stigmaticum* were dependent on the prey concentration, indicating their heterotrophy. *Paragymnodinium stigmaticum* can grow even under the photo-inhibited conditions induced by the addition of monolinuron as an inhibitor of photosystem II (Arnaud et al. 1994, Christa et al. 2013), unlike the other two phototrophic species. However, the growth rate of *P. stigmaticum* with monolinuron was suppressed relative to that of the cells grown without monolinuron. Interestingly, the ingestion rate of *P. stigmaticum* also decreased under photo-inhibited conditions. For the low ingestion rate of *P. stigmaticum* with monolinuron, there are some possibilities; the presence of monolinuron might inhibit directly the feeding behavior by *P. stigmaticum*, or the inhibition of photosynthesis in the *Rhodomonas* cells might suppress their ingestion by *P. stigmaticum*. The decreased growth rate of *P. stigmaticum* under photo-inhibited conditions may be caused by their suppressed ingestion. Although the inhibition of photosynthesis in *P. stigmaticum* cells might contribute to a decline in their growth rate, this is thought to play a minor role, because the photosynthetic competence (Fig. 3.3C) and carbon fixation capability (Fig. 3.4C) were kept low. A growth pattern of the type species of *Paragymnodinium*, *P. shiwhaense*, has been quantitatively demonstrated by Yoo et al. (2010), and was similar to that of *P. stigmaticum* in terms of that both species cannot grow under starved conditions. The maximum specific growth rate of *P. shiwhaense* fed on the autotrophic dinoflagellate *Amphidinium carterae*, which is the most appropriate prey for *P. shiwhaense*, was reported to be 1.097 d^{-1} (Yoo et al. 2010). This value is close to the growth rates of *P. stigmaticum* under prey-saturated conditions (μ = 1.06–1.15 d^{-1}), and significantly higher than the phototrophic growth rate of *P. asymmetricum* and *P. inerme* (μ = 0.44 and 0.56 d^{-1}, respectively). A similar pattern of growth limited to periods of co-cultivation with prey organisms has also been reported in a chloroplast-bearing mixotrophic dinoflagellate, *Polykrikos lebourae* (Kim et al. 2015), indicating that *P. stigmaticum* and *Po. lebourae* have adopted the same nutritional strategy. Kim et al. (2015) also concluded that *Po. lebourae* is an obligate mixotroph because this species cannot grow in isolation under dim light conditions. Additionally, Kim et al. (2015) presumed the obligate mixotrophy

to be due to a shortage of the required materials by prey and/or its own photosynthetic capability. However, the ingestion rate under dim light conditions seems to have been reduced (Figs. 6A and 6D in Kim et al. 2015) just like that witnessed in *P. stigmaticum* under the presence of monolinuron inhibiting the photosynthesis.

The specific chlorophyll *a* content in each *Paragymnodinium* species tend to be lower than those of other mixotrophic dinoflagellates including *P. shiwhaense* (from 1.7 to 4.0 fg μm^{-3}; Yoo et al. 2010). The chlorophyll *a* content in *P. asymmetricum* and *P. stigmaticum* (1.10 and 0.99 fg μm^{-3}, respectively) tend to be lower than that in *P. inerme* (1.63 fg μm^{-3}). This condition in *P. stigmaticum* can be expected because of its reduced photosynthetic activity relative to other two autotrophic species and therefore its concomitant reduction in cellular chlorophyll *a*. However, *P. asymmetricum* is an efficient autotroph despite having a similarly reduced level of chlorophyll *a*. The major pigment compositions of the three *Paragymnodinium* spp. were identical, but the molar ratio of each pigment to chlorophyll *a* in *P. stigmaticum* was significantly different from the two autotrophic species (i.e., the former species showed lower chlorophyll c_2 and peridinin, but higher β-carotene contents to chlorophyll *a*). Considering the lower photosynthetic activity in *P. stigmaticum* than in the other two species, it is expected that the cells contain lessened amounts of accessory photosynthetic pigments like chlorophyll c_2 and peridinin. The relatively elevated content of the non-photosynthetic carotenoid β-carotene can be explained by the presence of the eyespot in *P. stigmaticum* cells (Withers and Haxo 1978), which is absent in two other *Paragymnodinium* spp.

The absorption spectrum analyses showed a shift in the peak of the Q_y band towards longer wavelengths in *Paragymnodinium stigmaticum*. This could be a consequence of a 3D structural change of the porphyrin ring in chlorophyll *a* due to shifts in the accessory proteins as shown in Brassicaceae by Bednarczyk et al. (2016). Further studies are required to investigate the structural changes in chlorophyll-protein complexes of *P. stigmaticum* in relation to the inactivation of their photosynthetic competence observed in this study.

The F_v/F_m values of *Paragymnodinium asymmetricum* and *P. inerme* as measured by PAM fluorometry exceeded 0.6. The theoretical maximum value of F_v/F_m of phytoplankton measured by PAM fluorometry is thought to be from 0.6 to 0.8 (Büchel

and Wilhelm 1993), thus the photosystem II activities of *P. asymmetricum* and *P. inerme* were relatively high. The F_v/F_m values measured by FIRe fluorometry were generally lower than those by PAM fluorometry, and the results were a consequence of different excitation light regimes to reduce electron acceptors in photosystem II (i.e., the former and the latter possess single-turnover and multiple-turnover flashes, respectively; Kromkamp and Forster 2003). Despite the similar F_v/F_m values under the dark-adapted condition, the values for rETR_{PSII} and for the parameters rETR_{PSII}-max, α and E_k tend to be higher in *P. asymmetricum* than in *P. inerme*. The values of these parameters in *P. asymmetricum* are similar to those of other photosynthetic dinoflagellates reported elsewhere (e.g., Jones and Berkelmans 2012, Shen et al. 2019). The carbon fixation rate and the values of its parameters (with the exception of C-E_k) were also higher in *P. asymmetricum*. These show that *P. asymmetricum* is more capable of acclimating to light for photosynthesis than *P. inerme*. The cause of this difference in light utilization efficiency between these two species is unknown, but a difference in their chloroplast morphology might contribute to it: *P. asymmetricum* possesses only one chloroplast composed of two parts, a posterior mass and lateral lobes, whereas *P. inerme* contains multiple oval chloroplasts, some of which are interconnected by narrow bridges (Chapter 2). The complex morphology of the chloroplast in *P. asymmetricum* could increase their photosynthetic capability.

Compared to the two autotrophic dinoflagellates, the values of the F_v/F_m, rETR_{PSII} and carbon fixation rate of *Paragymnodinium stigmaticum* were low, indicating that their photosystem II was compromised and almost no carbon was fixed photosynthetically. In *P. stigmaticum*, the F_m values were kept low regardless of light conditions, indicating that the variable chlorophyll fluorescence was constantly weak. Interestingly, the σ_{PSII} value was higher and the τQ_A value was lower in *P. stigmaticum* than in the corresponding values of the other two species. These results indicated that photosystem II in *P. stigmaticum* possessed higher functional absorption cross-section and faster re-oxidation of the first electron acceptor, and those contracted the inactivation of photosynthetic activity as observed in this species by the other photosynthetic parameters. It is possible that the fluorescence of *P. stigmaticum* was too low to accurately determine σ_{PSII} and τQ_A. The results of the variable chlorophyll *a* fluorescence and carbon

fixation rate analyses clearly reflect the different nutritional strategies within the genus *Paragymnodinium*, and support the hypothesis that *P. stigmaticum* represents an intermediate stage of in the loss of photosynthetic function or chloroplasts. In addition, although the previous results of morphological and behavioral observations have led the assumption that *P. stigmaticum* is mixotrophic (Chapter 2), the current results suggest that the photosynthetic function of *P. stigmaticum* is almost lost, therefore the dinoflagellate species is becoming truly heterotrophic. The non-photosynthetic chloroplast in *P. stigmaticum* might remain some metabolic functions or biosynthetic pathways (Hadariová et al. 2018). The detailed genetic profile of the chloroplast in *P. stigmaticum* is investigated by transcriptome analyses in chapter 4.

A freshwater dinoflagellate, *Esoptrodinium* sp. can be compared to *Paragymnodinium* to understand functional significance of the loss of chloroplasts (Fawcett and Parrow 2014). This dinoflagellate contains either pigmented or non-pigmented strains, and all strains need to ingest prey for their growth (Fawcett and Parrow 2014). It is notable that the decline in variable chlorophyll *a* fluorescence, which was observed in *P. stigmaticum*, was also reported from the pigmented strain of *Esoptrodinium* sp. (Fawcett and Parrow 2014). On the other hand, the pigmented strain of *Esoptrodinium* sp. was also demonstrated to gain at least some nourishment by photosynthesis (Fawcett and Parrow 2014), unlike *P. stigmaticum*. The similarities and differences between *Esoptrodinium* sp. and *P. stigmaticum* suggest that a similar process of loss of chloroplasts is progressing in both dinoflagellates, although showing different steps of the evolution. The findings for *Esoptrodinium* sp. and *P. stigmaticum* indicate that the loss of photosynthetic function, the decline in variable chlorophyll *a* fluorescence and the changes in pigment content ratio are likely to progress simultaneously in a shift from autotrophy to heterotrophy. However, the photosynthetic function seems to disappear before the elimination of photosynthetic pigments, which was demonstrated by this study for *P. stigmaticum*. Considering that the intraspecific strains of *Esoptrodinium* sp. represent the various steps of the loss of chloroplasts (Fawcett and Parrow 2014), the shift from autotrophy to heterotrophy might advance in a relatively short period. For a further comparison, it is needed to investigate *Esoptrodinium* sp. by the physiological approaches which were conducted in our study. In addition, polykrikoid dinoflagellates

might demonstrate the steps of loss of chloroplasts (Hoppenrath and Leander 2007a, Kim et al. 2015), but the photosynthetic properties have little been investigated. Overall, the deficient examples hinder a comparative consideration of loss of chloroplasts and a construction of its hypothetical scenario in dinoflagellates. A foundation and a similar investigation of other species which may be viewed as representing progressive steps in this hypothetical scenario might rapidly advance our knowledge in this area.

Chapter 4. Comparative transcriptomic analysis within the genus *Paragymnodinium*, focusing on the chloroplast-related gene expression

INTRODUCTION

Dinoflagellates are known to have experienced complex evolutionary processes in terms of chloroplasts and nutritional strategy. The last common ancestor of dinoflagellates and the sister group apicomplexans is thought to have acquired chloroplasts through the secondary endosymbiosis with red algae, but the chloroplasts have lost in multiple lineages secondarily, resulting in the presence of non-photosynthetic species in various unrelated dinoflagellate taxa (Keeling 2013, Janouškovec et al. 2017, Waller and Kořený 2017). Some heterotrophic dinoflagellates retain remnants of plastids, and their remaining functions are actively revealed (Sanchez-Puerta et al. 2007, Slamovits and Keeling 2008, Janouškovec et al. 2017). Moreover, some dinoflagellates are known to have replaced their plastids after the loss of original plastids (Keeling 2013, Waller and Kořený 2017) (see Chapter 1).

In spite of the frequent losses of chloroplasts, the whole process of loss of photosynthesis, especially in its early steps, are less investigated by molecular genetic approaches in dinoflagellates than that in other eukaryotic groups. There are two possible causes preventing the progression of this area; first, species presumably representing the early steps of this reductive evolution are less recognizable and/or are unculturable, although the loss of photosynthesis in polykrikoid dinoflagellates, which are thought to be on the way of transition from phototrophy to heterotrophy, has been investigated using single-cell transcriptomics (Gavelis et al. 2015). Second, the large size of dinoflagellate nuclear genome makes the whole-genomic analyses difficult (Lin 2011, Wisecaver and Hackett 2011). Thus far, currently available genomic data of dinoflagellates are restricted to only a few species with relatively small genome size (Stephens et al. 2020).

In the previous chapters, I have demonstrated the variation of the nutritional strategies and photosynthetic properties within the genus *Paragymnodinium*. The results

showed a phagotrophic nutrition and an inactivated photosynthetic capability in *P. stigmaticum*, whereas *P. asymmetricum* and *P. inerme* retain the obligate phototrophic nutrition, robustly supporting the hypothesis that *P. stigmaticum* exhibits the early step of the loss of chloroplasts. This fact leads an idea that a comparative analysis of *Paragymnodinium* spp. will help to solve the former one of the two problems stated above (inadequate exploration of species representing the early steps of this evolution) for understanding the genetic aspect on the process of the loss of photosynthesis in dinoflagellates. In addition, a recent development of transcriptomic technique using next-generation sequencers (NGSs) can partly solve the latter problem (difficulty of genomic-scaled analyses due to the large size of dinoflagellate nucleus). Transcriptomic data provide a comprehensive information of gene expression and is used to evaluate the photosynthetic state and chloroplast function of chloroplast-bearing organisms, without analyzing the whole genome (e.g., Bayer et al. 2012, Gavelis et al. 2015, Kamikawa et al. 2017). In this chapter, a transcriptomic analysis within the genus *Paragymnodinium* is conducted to evaluate the differences of gene expression between photosynthetic/non-photosynthetic species. To further compare the gene expression properties of *Paragymnodinium* spp. with those of another species of photosynthetic dinoflagellate outside of the genus, transcriptome data of *Gymnodinium catenatum* were also utilized. The results illuminate the evolutionary model for early step of loss of photosynthesis and chloroplasts within dinoflagellates.

MATERIAL AND METHODS

Preparation of culture strains

Cultures of *Paragymnodinium asymmetricum* (strain vnd299), *P. inerme* (strain JGD) and *P. stigmaticum* (strain SD01) were maintained in Daigo's IMK Medium for Marine Microalgae (Nihon Pharmaceutical Co., Tokyo, Japan) at 20°C with an illumination of 100 µmol photons m^{-2} s^{-1} under 16:8 h light:dark cycle. Cells of *Rhodomonas* sp. (strain Mr06, Cryptophyceae) were added as prey for *P. stigmaticum*, and the co-cultivated culture was maintained for over two months. In order to remove *Rhodomonas* sp. and obtain a unialgal culture of *P. stigmaticum*, the culture co-cultivated in 50 mL tube was washed by shaking and pipetting during dark phase, where the cysts of *P. stigmaticum* is strongly attached to the vessel (see chapter 3). The obtained unialgal culture was remained one day to wait for digestion of *Rhodomonas* sp. in food vacuoles.

RNA preparation for transcriptomic analyses

Cells in the exponential growth phase were collected at 1 PM (5 hours after the change from dark to light phase) by centrifugation at 10000 × g for 10 min. The cell pellet was immediately frozen in liquid nitrogen. Total RNA was extracted and purified with a combination of phenol / chloroform / isoamyl alcohol method and NucleoSpin RNA XS kit (TaKaRa). The quality of extracted RNA was confirmed by agarose gel electrophoresis and Nanodrop (Thermo Scientific). To construct a cDNA library, 1.484 µg (*Paragymnodinium asymmetricum*), 1.603 µg (*P. inerme*) and 1.517 µg (*P. stigmaticum*) of total RNA were used. Paired-end sequencing was performed using the Illumina sequencing platform (Novaseq 6000).

De novo assembly and annotation

The RNA-seq raw reads were cleaned up using cutadapt ver. 2.8 (Martin 2011) by trimming low-quality ends (< QV30) and adapter sequences, and by discarding reads shorter than 50 bp. The trimmed reads were assembled *de novo* using Trinity ver. 2.9.1 (Grabherr et al. 2011) with the paired-end mode. When splicing variants of a gene were found, the longest transcript was selected as a representative mRNA sequence. The quality of the transcriptome data was confirmed with BUSCO ver. 5.1.2 (Simão et al.

2015, Manni et al. 2021), resulted in the presence of 96.5% (*Paragymnodinium asymmetricum*), 95.9% (*P. inerme*) and 93.6% (*P. stigmaticum*) of a core gene set of Alveolata. Open reading frames (ORFs) were predicted and translated to amino acids by TransDecoder ver. 5.5.0 (Haas et al. 2013). The numbers of raw reads, contigs and ORFs and the average length of contigs and ORFs are summarized in Table 4.1.

The Kyoto Encyclopedia of Genes and Genomes (KEGG) Orthology ID assignment was performed for all ORFs in the KAAS pipeline for annotation (Ogata et al. 1999, Moriya et al. 2007). The sequences were also annotated with BLASTP against UniProt database (Bateman et al. 2021). Expression of 104 transcripts which are strongly predicted to be localized to the plastid or to be involved in the photosynthesis (Fig. 4.1, Table 4.2) were sorted from the KAAS-annotated genes list. In the KAAS pipeline, some mRNAs were not successfully annotated, so the expression of these transcripts was found based on the UniProt annotation. For comparison, a transcriptome data of *Gymnodinium catenatum* (strain GC744, MMETSP0784) from Marine Microbial Eukaryote Transcriptome Sequencing Project was downloaded on June 18, 2021, and annotated as with described above.

Phylogenetic analysis

To distinguish chloroplastidic isoform for Calvin cycle and cytosolic isoform for oxidative pentose phosphate pathway, phylogenetic analyses were conducted for each gene. The datasets of amino acid sequences for the phylogenetic analyses were constructed mainly based on the datasets by Van Vlierberghe et al. (2021) and some cytosolic or mitochondrial eukaryotic and prokaryotic homologues were manually added from databases of UniProt and Clusters of Orthologous Genes (COGs) (Tatusov et al. 2000). The sequences of the annotated transcripts from the four investigated dinoflagelaltes in this study were added to the datasets. Sequences were aligned using MAFFT online service ver. 7.487 (Katoh et al. 2019). Variable and ambiguously aligned sites were removed using Gblocks server ver. 0.91b (Castresana 2000). The numbers of amino acid positions and sequences of organized dataset were summarized in Table 4.3. Each dataset was subjected to maximum likelihood phylogenetic analysis with RAxML (Stamatakis 2006) ver. 8.2.12 under the LG model (Le and Gascuel 2008) incorporating empirical amino acid frequencies and among-site rate variation approximated by a discrete gamma distribution (LG + Γ model). ML bootstrap values were calculated by

summarizing 100 trees. Based on the resulted trees, the transcripts nested in the clades including chloroplast-targeting proteins were estimated to be chloroplastidic.

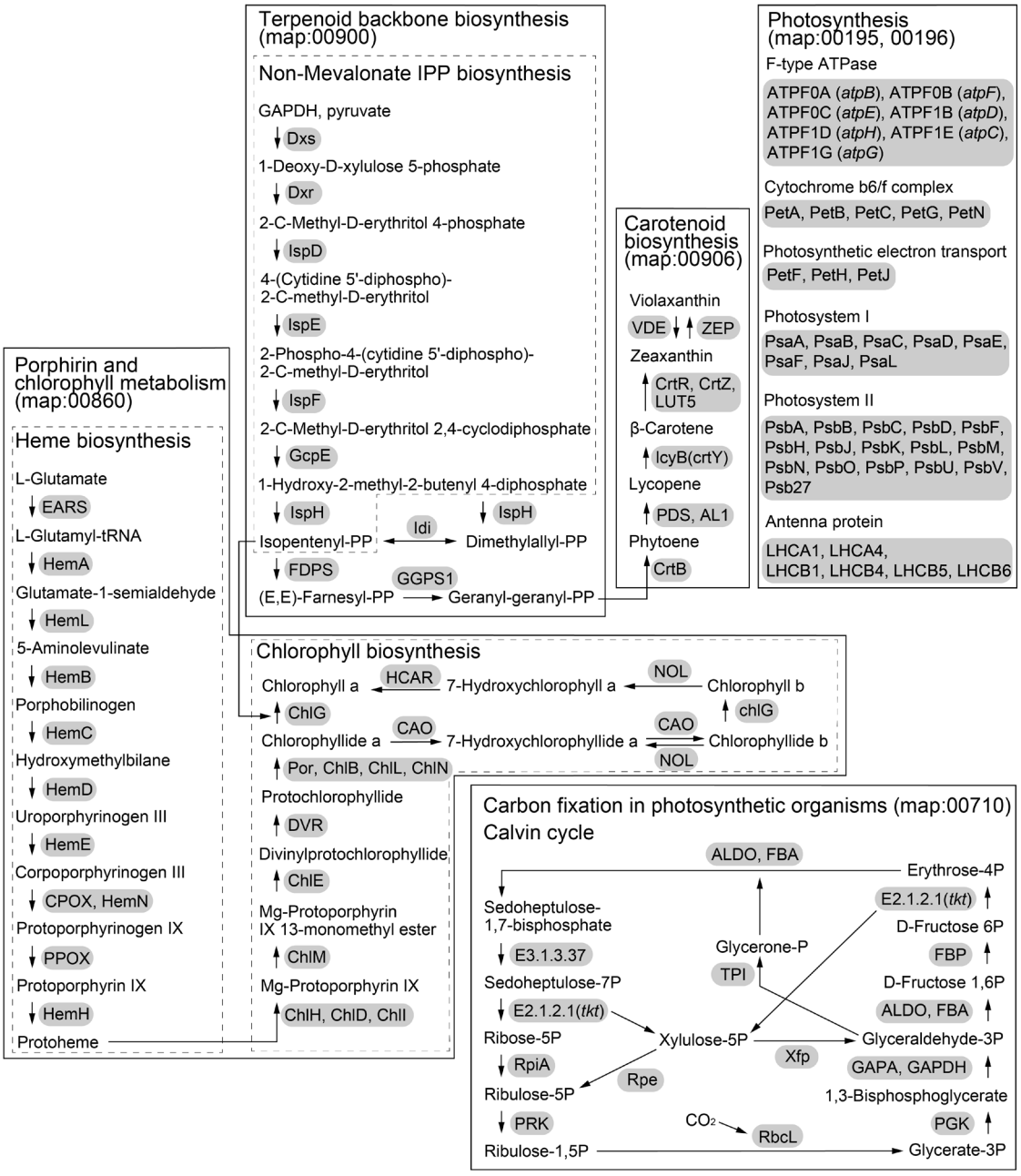

Fig. 4.1. A pathway map showing the investigated transcripts indicated by gray and their reactions and the compounds. Each pathway is organized based on its map IDs described in the KEGG database. Heme, chlorophyll and non-mevalonate isopentenyl diphosphate (IPP) biosynthesis pathways are enclosed by dashed lines. For abbreviations of each transcript, refer to Table 4.1.

Table 4.1. Overview of the sequence data, assembly and open reading frame (ORF) prediction.

	P. asymmetricum	*P. inerme*	*P. stigmaticum*
No. of raw reads	132,203,992	114,844,228	135,904,744
No. of contigs	287,213	256,709	107,768
Average contig length (bases)	1,107	1,078	1,286
No. of ORFs	64,845	68,823	35,214
Average ORF length (amino acids)	468.7	450.8	488.9

Table 4.2. A list of investigated transcripts and their information. The transcripts are sorted by its pathway (map ID) and function.

Transcript abbreviation	KO	Transcript description
Porphyrin and chlorophyll metabolism (map00860); heme biosynthesis		
EARS	K01885	glutamyl-tRNA synthetase [EC:6.1.1.17]
HemA	K02492	glutamyl-tRNA reductase [EC:1.2.1.70]
HemL	K01845	glutamate-1-semialdehyde 2,1-aminomutase [EC:5.4.3.8]
HemB	K01698	porphobilinogen synthase [EC:4.2.1.24]
HemC	K01749	hydroxymethylbilane synthase [EC:2.5.1.61]
HemD	K01719	uroporphyrinogen-III synthase [EC:4.2.1.75]
HemE	K01599	uroporphyrinogen decarboxylase [EC:4.1.1.37]
CPOX	K00228	coproporphyrinogen III oxidase [EC:1.3.3.3]
HemN	K02495	oxygen-independent coproporphyrinogen III oxidase [EC:1.3.98.3]
PPOX	K00231	protoporphyrinogen/coproporphyrinogen III oxidase [EC:1.3.3.4 1.3.3.15]
HemH	K01772	protoporphyrin/coproporphyrin ferrochelatase [EC:4.99.1.1 4.99.1.9]
Porphyrin and chlorophyll metabolism (map00860); chlorophyll biosynthesis		
ChlH	K03403	magnesium chelatase subunit H [EC:6.6.1.1]
ChlD	K03404	magnesium chelatase subunit D [EC:6.6.1.1]
ChlI	K03405	magnesium chelatase subunit I [EC:6.6.1.1]
ChlM	K03428	magnesium-protoporphyrin O-methyltransferase [EC:2.1.1.11]
ChlE	K04035	magnesium-protoporphyrin IX monomethyl ester (oxidative) cyclase [EC:1.14.13.81]
DVR	K19073	divinyl chlorophyllide *a* 8-vinyl-reductase [EC:1.3.1.75]
Por	K00218	protochlorophyllide reductase [EC:1.3.1.33]
ChlL	K04037	light-independent protochlorophyllide reductase subunit L

Table 4.2. (*Continued*)

ChlN	K04038	light-independent protochlorophyllide reductase subunit N [EC:1.3.7.7]
ChlB	K04039	light-independent protochlorophyllide reductase subunit B
ChlG	K04040	chlorophyll/bacteriochlorophyll a synthase [EC:2.5.1.62 2.5.1.133]
CAO	K13600	chlorophyllide a oxygenase [EC:1.14.13.122]
NOL	K13606	chlorophyll(ide) b reductase [EC:1.1.1.294]
HCAR	K18010	7-hydroxymethyl chlorophyll a reductase [EC:1.17.7.2]
Terpenoid backbone biosynthesis (map00900); non-mevalonate IPP biosynthesis		
Dxs	K01662	1-deoxy-D-xylulose-5-phosphate synthase [EC:2.2.1.7]
Dxr	K00099	1-deoxy-D-xylulose-5-phosphate reductoisomerase [EC:1.1.1.267]
IspD	K00991	2-C-methyl-D-erythritol 4-phosphate cytidylyltransferase [EC:2.7.7.60]
IspE	K00919	4-diphosphocytidyl-2-C-methyl-D-erythritol kinase [EC:2.7.1.148]
IspF	K01770	2-C-methyl-D-erythritol 2,4-cyclodiphosphate synthase [EC:4.6.1.12]
GcpE	K03526	(E)-4-hydroxy-3-methylbut-2-enyl-diphosphate synthase [EC:1.17.7.1 1.17.7.3]
IspH	K03527	4-hydroxy-3-methylbut-2-en-1-yl diphosphate reductase [EC:1.17.7.4]
Terpenoid backbone biosynthesis (map00900); others		
Idi	K01823	isopentenyl-diphosphate Delta-isomerase [EC:5.3.3.2]
FDPS	K00787	farnesyl diphosphate synthase [EC:2.5.1.1 2.5.1.10]
GGPS1	K00804	geranylgeranyl diphosphate synthase, type III [EC:2.5.1.1 2.5.1.10 2.5.1.29]
Caroteroid biosynthesis (map00906)		
CrtB	K02291	15-cis-phytoene synthase [EC:2.5.1.32]
PDS	K02293	15-cis-phytoene desaturase [EC:1.3.5.5]
AL1	K15745	phytoene desaturase (3,4-didehydrolycopene-forming) [EC:1.3.99.30]

Table 4.2. (*Continued*)

LcyB	K06443	lycopene beta-cyclase [EC:5.5.1.19]
CrtR	K02294	beta-carotene hydroxylase [EC:1.14.13.-]
CrtZ	K15746	beta-carotene 3-hydroxylase [EC:1.14.15.24]
LUT5	K15747	beta-ring hydroxylase [EC:1.14.-.-]
ZEP	K09838	zeaxanthin epoxidase [EC:1.14.15.21]
VDE	K09839	violaxanthin de-epoxidase [EC:1.23.5.1]
Photosynthesis (map00195); F-type ATPase		
ATPF0A (*atpB*)	K02108	F-type H+-transporting ATPase subunit a
ATPF0B (*atpF*)	K02109	F-type H+-transporting ATPase subunit b
ATPF0C (*atpE*)	K02110	F-type H+-transporting ATPase subunit c
ATPF1B (*atpD*)	K02112	F-type H+/Na+-transporting ATPase subunit beta [EC:7.1.2.2 7.2.2.1]
ATPF1D (*atpH*)	K02113	F-type H+-transporting ATPase subunit delta
ATPF1E (*atpC*)	K02114	F-type H+-transporting ATPase subunit epsilon
ATPF1G (*atpG*)	K02115	F-type H+-transporting ATPase subunit gamma
Photosynthesis (map00195); Cytochrome b6/f complex		
PetA	K02634	apocytochrome f
PetB	K02635	cytochrome b6
PetC	K02636	cytochrome b6-f complex iron-sulfur subunit [EC:7.1.1.6]
PetG	K02640	cytochrome b6-f complex subunit 5
PetN	K03689	cytochrome b6-f complex subunit 8
Photosynthesis (map00195); Photosynthetic electron transport		
PetF	K02639	Ferredoxin

Table 4.2. (*Continued*)

PetH	K02641	ferredoxin-NADP+ reductase [EC:1.18.1.2]
PetJ	K08906	cytochrome c6
Photosynthesis (map00195); Photosystem I		
PsaA	K02689	photosystem I P700 chlorophyll a apoprotein A1
PsaB	K02690	photosystem I P700 chlorophyll a apoprotein A2
PsaC	K02691	photosystem I subunit VII
PsaD	K02692	photosystem I subunit II
PsaE	K02693	photosystem I subunit IV
PsaF	K02694	photosystem I subunit III
PsaJ	K02697	photosystem I subunit IX
PsaL	K02699	photosystem I subunit XI
Photosynthesis (map00195); Photosystem II		
PsbA	K02703	photosystem II P680 reaction center D1 protein [EC:1.10.3.9]
PsbB	K02704	photosystem II CP47 chlorophyll apoprotein
PsbC	K02705	photosystem II CP43 chlorophyll apoprotein
PsbD	K02706	photosystem II P680 reaction center D2 protein [EC:1.10.3.9]
PsbF	K02708	photosystem II cytochrome b559 subunit beta
PsbH	K02709	photosystem II PsbH protein
PsbJ	K02711	photosystem II PsbJ protein
PsbK	K02712	photosystem II PsbK protein
PsbL	K02713	photosystem II PsbL protein
PsbM	K02714	photosystem II PsbM protein

Table 4.2. (*Continued*)

PsbN	K02715	PsbN protein
PsbO	K02716	photosystem II oxygen-evolving enhancer protein 1
PsbP	K02717	photosystem II oxygen-evolving enhancer protein 2
PsbU	K02719	photosystem II PsbU protein
PsbV	K02720	photosystem II cytochrome c550
PsbY	K02723	photosystem II PsbY protein
Psb27	K08902	photosystem II Psb27 protein
Photosynthesis - antenna proteins (map00196)		
LHCA1	K08907	light-harvesting complex I chlorophyll a/b binding protein 1
LHCA4	K08910	light-harvesting complex I chlorophyll a/b binding protein 4
LHCB1	K08912	light-harvesting complex II chlorophyll a/b binding protein 1
LHCB4	K08915	light-harvesting complex II chlorophyll a/b binding protein 4
LHCB5	K08916	light-harvesting complex II chlorophyll a/b binding protein 5
LHCB6	K08917	light-harvesting complex II chlorophyll a/b binding protein 6
Carbon fixation in photosynthetic organisms (map00710); Calvin cycle		
RbcL	K01601	ribulose-bisphosphate carboxylase large chain [EC:4.1.1.39]
PGK	K00927	phosphoglycerate kinase [EC:2.7.2.3]
GAPA	K05298	glyceraldehyde-3-phosphate dehydrogenase (NADP+) (phosphorylating) [EC:1.2.1.13]
GAPDH	K00134	glyceraldehyde 3-phosphate dehydrogenase [EC:1.2.1.12]
ALDO	K01623	fructose-bisphosphate aldolase, class I [EC:4.1.2.13]
FBA	K01624	fructose-bisphosphate aldolase, class II [EC:4.1.2.13]
FBP	K03841	fructose-1,6-bisphosphatase I [EC:3.1.3.11]

Table 4.2. (*Continued*)

E2.2.1.1 (*tkt*)	K00615	transketolase [EC:2.2.1.1]
E3.1.3.37	K01100	sedoheptulose-bisphosphatase [EC:3.1.3.37]
RpiA	K01807	ribose 5-phosphate isomerase A [EC:5.3.1.6]
PRK	K00855	phosphoribulokinase [EC:2.7.1.19]
TPI	K01803	triosephosphate isomerase (TIM) [EC:5.3.1.1]
Rpe	K01783	ribulose-phosphate 3-epimerase [EC:5.1.3.1]
Xfp	K01621	xylulose-5-phosphate/fructose-6-phosphate phosphoketolase [EC:4.1.2.9 4.1.2.22]

Table 4.3. The numbers of amino acid positions and sequences of Calvin cycle proteins used for phylogenetic analyses.

Transcript	Amino acid positions	Number of sequences
RbcL	190	111
PGK	200	167
GAPA	212	145
GAPDH	192	247
ALDO	222	156
FBA	230	145
FBP	141	218
E2.2.1.1 (*tkt*)	345	143
E3.1.3.37	115	217
RpiA	126	89
PRK	37	98
TPI	142	158
Rpe	134	104

RESULTS

In the four analyzed dinoflagellates, *Paragymnodinium asymmetricum*, *P. inerme*, *P. stigmaticum* and *Gymnodinium catenatum*, most of the transcripts required for the heme, chlorophyll and non-mevalonate isopentenyl pathway for diphosphate (IPP) biosynthesis were identified (Fig. 4.2). On the other hand, magnesium-protoporphyrin IX monomethyl ester cyclase (ChlE) and chlorophyllide *a* oxygenase (CAO) were detected from neither species. Oxygen-independent coproporphyrinogen III oxidase (HemN) was found only from *P. asymmetricum* and *G. catenatum* (Fig. 4.2). In *P. stigmaticum*, magnesium-protoporphyrin O-methyltransferase (ChlM) and chlorophyll/bacteriochlorophyll *a* synthase (ChlG), which were expressed in other three species, were not detected (Fig. 4.2).

All mRNAs involved in the non-mevalonate IPP biosynthesis were detected from all four analyzed dinoflagellates. Of the transcripts for the pathway after the generation of IPP, isopentenyl-diphosphate Delta-isomerase (Idi) was detected only in *Paragymnodinium asymmetricum* and *Gymnodinium catenatum*, and geranylgeranyl diphosphate synthase, type III (GGPS1) was not detected from the investigated dinoflagelaltes (Fig. 4.2).

Paragymnodinium asymmetricum showed expressions of most investigated mRNAs involved in the carotenoid biosynthesis including beta-carotene biosynthesis and xanthophyll cycle, except for beta-carotene 3-hydroxylase (CrtZ) (Fig. 4.2). In *P. inerme* and *P. stigmaticum*, beta-carotene hydroxylase (CrtR) and beta-ring hydroxylase (LUT5), which are required for synthesis of zeaxanthin, were not detected, although CrtZ was detected only by the annotation with BLASTP to the UniProt database (Fig. 4.2). In addition, *P. stigmaticum* did not show the expression of 15-cis-phytoene synthase (CrtB) (Fig. 4.2). CrtR, CrtZ and LUT5 were not detected from *Gymnodinium catenatum* (Fig. 4.2).

Most of transcripts of Calvin cycle were annotated by KAAS pipeline, while ribulose-bisphosphate carboxylase large chain (RbcL) was detected only by the annotation with BLASTP to the UniProt database (Fig. 4.2). In *Paragymnodinium stigmaticum*, rbcL was not detected by both annotation procedures (Fig. 4.2). In addition, glyceraldehyde-3-phosphate dehydrogenase (NADP+) (phosphorylating) (GAPA) was

not detected in *Gymnodinium catenatum*, and xylulose-5-phosphate/fructose-6-phosphate phosphoketolase (Xfp) was not found in any dinoflagellates by both annotations (Fig. 4.2). The presence of chloroplast-targeted isoform in the detected transcripts was estimated based on the phylogenetic analyses (Fig. 4.2, 4.3). As a result, fructose-bisphosphate aldolase class I (ALDO), ribose 5-phosphate isomerase A (RpiA) and phosphoribulokinase (PRK) were not estimated to be chloroplastidic in all four dinoflagellates (Fig. 4.2, 4.3). Ribulose-phosphate 3-epimerase (Rpe) was found to be chloroplastidic except for *P. stigmaticum*, and remained transcripts were shown to be chloroplastidic in all four dinoflagelaltes (Fig. 4.2, 4.3). All detected RbcL sequences from three species were nested in the clade of the form II RuBisCO typical for dinoflagelaltes (Fig. 4.3). Sedoheptulose-bisphosphatase (E3.1.3.37) was not determined to be class I or II by the result of annotation, but the phylogenetic analysis including the sequences of both classes revealed that all detected sequences were accommodated to class I (Fig. 4.3).

Of the transcripts for photosynthesis (F-type ATPase, cytochrome b6/f complex, photosynthetic electron transport, photosystem I and II and their antenna proteins), total 32 transcripts for the proteins which have been reported to be nucleus-encoded in *Symbiodinium minutum* (Mungpakdee et al. 2014) were searched from expressed transcripts (Fig. 4.2, Table 4.2). In addition, eight transcripts which are chloroplast-encoded in *S. minutum* were detected from at least one of the four investigated dinoflagellates in this study (Fig. 4.2, Table 4.2). For F-type ATPase, cytochrome b6/f complex, photosynthetic electron transport and photosystem I (PSI), all dinoflagellates showed similar patterns of gene expression with minor exceptions seen in cytochrome b6 (PetB) and cytochrome b6-f complex subunit 5 (PetG); PetB was detected from *Paragymnodinium stigmaticum*, while PetG was detected from *P. asymmetricum*, *P. inerme* and *Gymnodinium catenatum* (Fig. 4.2). Expression of antenna protein of the PSI showed a variation in its repertoire, and *G. catenatum* solely expressed two types of proteins (light-harvesting complex I chlorophyll a/b binding protein 1 and 4, LHCA1 and LHCA4), while other three species expressed either one (Fig. 4.2). On the other hand of these slightly variated transcripts, a significant reduction of expression of the photosystem II (PSII) and its antenna proteins in *P. stigmaticum* was observed; any transcripts were

not detected except for PSII oxygen-evolving enhancer protein 1 (PsbO) and light-harvesting complex II chlorophyll a/b binding protein 5 (LHCB5) (Fig. 4.2). In the other three species, *P. asymmetricum*, *P. inerme* and *G. catenatum*, a major part of transcripts involved in the PSII and its antenna proteins were shown to be expressed, while the transcripts for presumably nuclear-encoded PsbJ and PsbM proteins were not detected (Fig. 4.2). Although the three species showed similar patterns of gene expression for PSII, P680 reaction center D1 and D2 proteins (PsbA and PsbD) were not detected only in *G. catenatum*, and photosystem II PsbH protein (PsbH) was not detected only in *P. asymmetricum*. Light-harvesting complex II chlorophyll a/b binding protein 4 (LHCB4) was detected only in *P. asymmetricum* (Fig. 4.2).

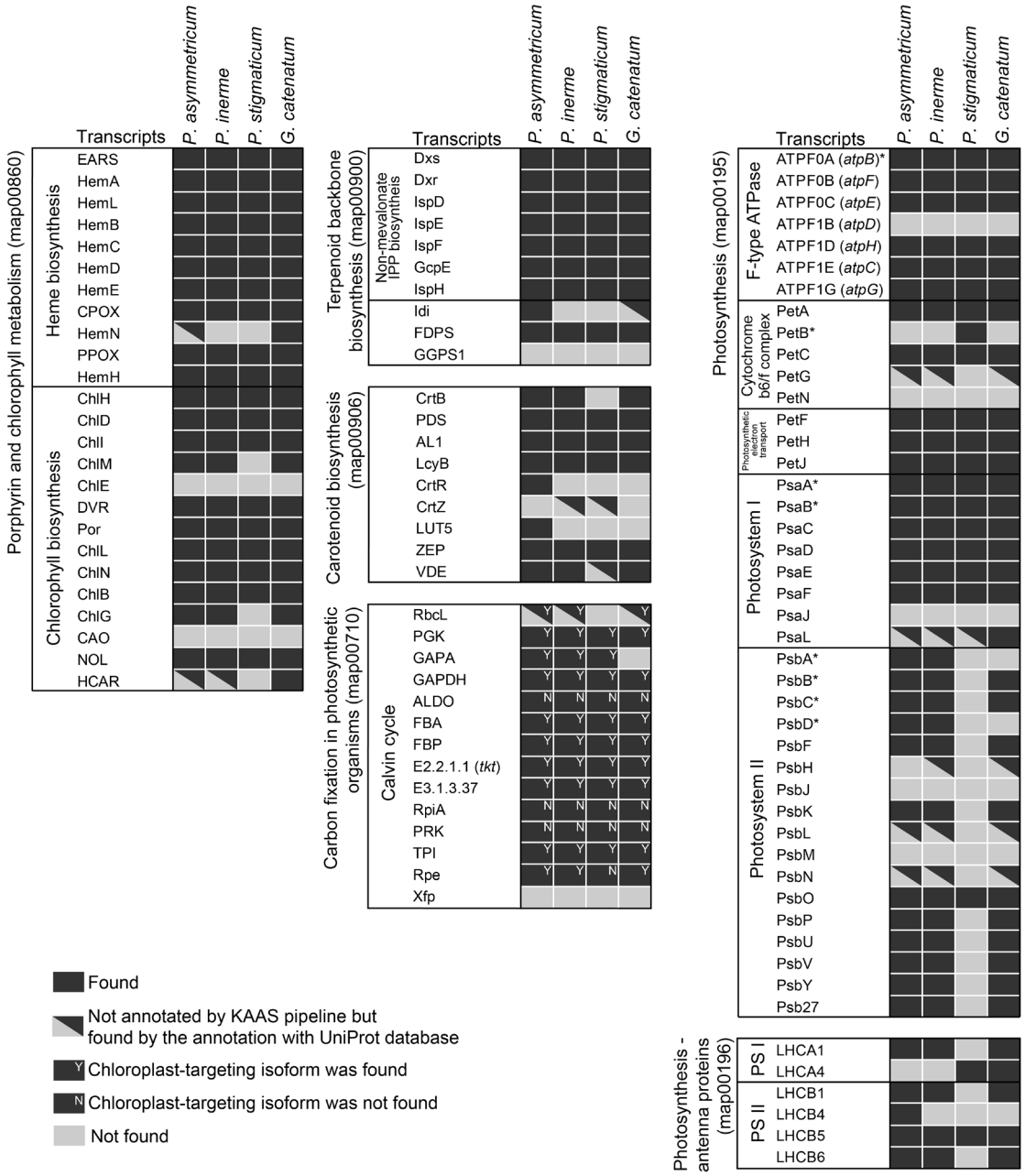

Fig. 4.2. Comparisons of the transcripts of four investigated dinoflagellates, *Paragymnodinium asymmetricum*, *P. inerme*, *P. stigmaticum* and *Gymnodinium catenatum* strain GC744. Transcripts are sorted based on its pathways and functions. Transcripts which were successfully found by the annotation with KAAS pipeline are indicated by black, and others are white. Transcripts which were not annotated by KAAS pipeline but found by the annotation with UniProt database are also indicated. For Calvin cycle, the transcripts which were determined to contain chloroplast-targeting isoform are indicated by Y and others are by N. For abbreviations of each transcript, refer to Table 4.1. *Predicted to be chloroplast-encoded according to Mungpakdee et al. (2014).

Fig. 4.3. Maximum-likelihood phylogenetic trees of the transcripts for proteins involved in Calvin cycle. Sequences of *Paragymnodinium asymmetricum*, *P. inerme*, *P. stigmaticum* and *G. catenatum* are shown in red. Nuclear-encoded or chloroplast-encoded chloroplast-targeting proteins are shown in green and tagged by nucpt# and cpcpt#, respectively. Nuclear-encoded proteins which are not targeted to chloroplast (cytosol- or mitochondria-targeting) are shown in blue and tagged by cyto# and mito#, respectively. Other proteins whose localization are not determined are shown in black. Proteins of prokaryotes are shown in gray and tagged by prok#. The detected transcripts which are nested in the clade including chloroplast-targeted proteins are estimated to be chloroplastidic and enclosed by red boxes. Taxon IDs are shown after the taxon name, and Accession numbers are shown after @. Numbers at each node are ML bootstrap values (≧50).

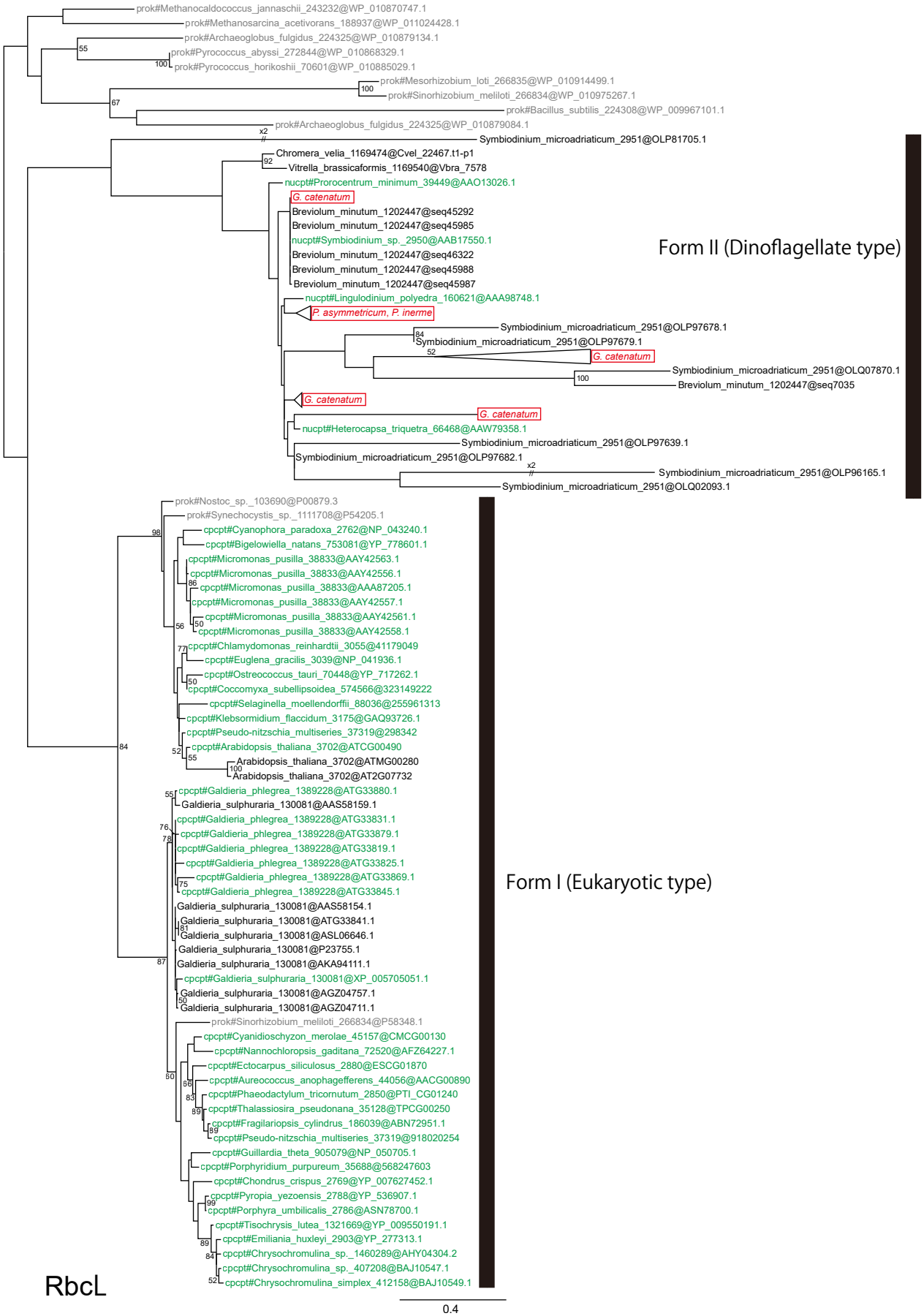
prok#Methanocaldococcus_jannaschii_243232@WP_010870747.1
prok#Methanosarcina_acetivorans_188937@WP_011024428.1
prok#Archaeoglobus_fulgidus_224325@WP_010879134.1
prok#Pyrococcus_abyssi_272844@WP_010868329.1
prok#Pyrococcus_horikoshii_70601@WP_010885029.1
prok#Mesorhizobium_loti_266835@WP_010914499.1
prok#Sinorhizobium_meliloti_266834@WP_010975267.1
prok#Bacillus_subtilis_224308@WP_009967101.1
prok#Archaeoglobus_fulgidus_224325@WP_010879084.1
Symbiodinium_microadriaticum_2951@OLP81705.1
Chromera_velia_1169474@Cvel_22467.t1-p1
Vitrella_brassicaformis_1169540@Vbra_7578
nucpt#Prorocentrum_minimum_39449@AAO13026.1
G. catenatum
Breviolum_minutum_1202447@seq45292
Breviolum_minutum_1202447@seq45985
nucpt#Symbiodinium_sp._2950@AAB17550.1
Breviolum_minutum_1202447@seq46322
Breviolum_minutum_1202447@seq45988
Breviolum_minutum_1202447@seq45987
nucpt#Lingulodinium_polyedra_160621@AAA98748.1
P. asymmetricum, P. inerme
Symbiodinium_microadriaticum_2951@OLP97678.1
Symbiodinium_microadriaticum_2951@OLP97679.1
G. catenatum
Symbiodinium_microadriaticum_2951@OLQ07870.1
Breviolum_minutum_1202447@seq7035
G. catenatum
G. catenatum
nucpt#Heterocapsa_triquetra_66468@AAW79358.1
Symbiodinium_microadriaticum_2951@OLP97639.1
Symbiodinium_microadriaticum_2951@OLP97682.1
Symbiodinium_microadriaticum_2951@OLP96165.1
Symbiodinium_microadriaticum_2951@OLQ02093.1
Form II (Dinoflagellate type)
prok#Nostoc_sp._103690@P00879.3
prok#Synechocystis_sp._1111708@P54205.1
cpcpt#Cyanophora_paradoxa_2762@NP_043240.1
cpcpt#Bigelowiella_natans_753081@YP_778601.1
cpcpt#Micromonas_pusilla_38833@AAY42563.1
cpcpt#Micromonas_pusilla_38833@AAY42556.1
cpcpt#Micromonas_pusilla_38833@AAA87205.1
cpcpt#Micromonas_pusilla_38833@AAY42557.1
cpcpt#Micromonas_pusilla_38833@AAY42561.1
cpcpt#Micromonas_pusilla_38833@AAY42558.1
cpcpt#Chlamydomonas_reinhardtii_3055@41179049
cpcpt#Euglena_gracilis_3039@NP_041936.1
cpcpt#Ostreococcus_tauri_70448@YP_717262.1
cpcpt#Coccomyxa_subellipsoidea_574566@323149222
cpcpt#Selaginella_moellendorffii_88036@255961313
cpcpt#Klebsormidium_flaccidum_3175@GAQ93726.1
cpcpt#Pseudo-nitzschia_multiseries_37319@298342
cpcpt#Arabidopsis_thaliana_3702@ATCG00490
Arabidopsis_thaliana_3702@ATMG00280
Arabidopsis_thaliana_3702@AT2G07732
cpcpt#Galdieria_phlegrea_1389228@ATG33880.1
Galdieria_sulphuraria_130081@AAS58159.1
cpcpt#Galdieria_phlegrea_1389228@ATG33831.1
cpcpt#Galdieria_phlegrea_1389228@ATG33879.1
cpcpt#Galdieria_phlegrea_1389228@ATG33819.1
cpcpt#Galdieria_phlegrea_1389228@ATG33825.1
cpcpt#Galdieria_phlegrea_1389228@ATG33869.1
cpcpt#Galdieria_phlegrea_1389228@ATG33845.1
Galdieria_sulphuraria_130081@AAS58154.1
Galdieria_sulphuraria_130081@ATG33841.1
Galdieria_sulphuraria_130081@ASL06646.1
Galdieria_sulphuraria_130081@P23755.1
Galdieria_sulphuraria_130081@AKA94111.1
cpcpt#Galdieria_sulphuraria_130081@XP_005705051.1
Galdieria_sulphuraria_130081@AGZ04757.1
Galdieria_sulphuraria_130081@AGZ04711.1
prok#Sinorhizobium_meliloti_266834@P58348.1
cpcpt#Cyanidioschyzon_merolae_45157@CMCG00130
cpcpt#Nannochloropsis_gaditana_72520@AFZ64227.1
cpcpt#Ectocarpus_siliculosus_2880@ESCG01870
cpcpt#Aureococcus_anophagefferens_44056@AACG00890
cpcpt#Phaeodactylum_tricornutum_2850@PTI_CG01240
cpcpt#Thalassiosira_pseudonana_35128@TPCG00250
cpcpt#Fragilariopsis_cylindrus_186039@ABN72951.1
cpcpt#Pseudo-nitzschia_multiseries_37319@918020254
cpcpt#Guillardia_theta_905079@NP_050705.1
cpcpt#Porphyridium_purpureum_35688@568247603
cpcpt#Chondrus_crispus_2769@YP_007627452.1
cpcpt#Pyropia_yezoensis_2788@YP_536907.1
cpcpt#Porphyra_umbilicalis_2786@ASN78700.1
cpcpt#Tisochrysis_lutea_1321669@YP_009550191.1
cpcpt#Emiliania_huxleyi_2903@YP_277313.1
cpcpt#Chrysochromulina_sp._1460289@AHY04304.2
cpcpt#Chrysochromulina_sp._407208@BAJ10547.1
cpcpt#Chrysochromulina_simplex_412158@BAJ10549.1
Form I (Eukaryotic type)
RbcL
0.4

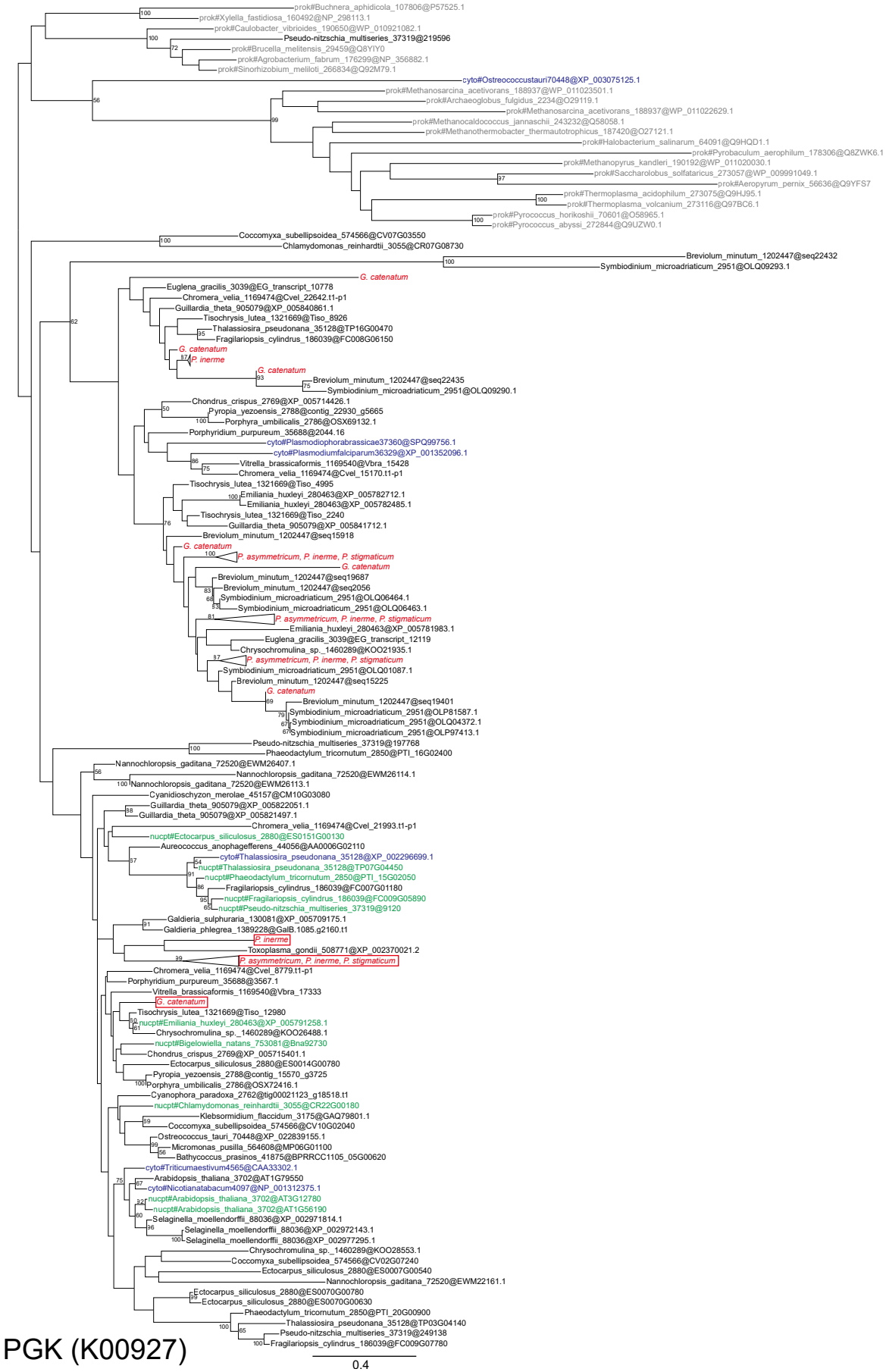
prok#Buchnera_aphidicola_107806@P57525.1
prok#Xylella_fastidiosa_160492@NP_298113.1
prok#Caulobacter_vibrioides_190650@WP_010921082.1
Pseudo-nitzschia_multiseries_37319@219596
prok#Brucella_melitensis_29459@Q8YIY0
prok#Agrobacterium_fabrum_176299@NP_356882.1
prok#Sinorhizobium_meliloti_266834@Q92M79.1
cyto#Ostreococcustauri70448@XP_003075125.1
prok#Methanosarcina_acetivorans_188937@WP_011023501.1
prok#Archaeoglobus_fulgidus_2234@O29119.1
prok#Methanosarcina_acetivorans_188937@WP_011022629.1
prok#Methanocaldococcus_jannaschii_243232@Q58058.1
prok#Methanothermobacter_thermautotrophicus_187420@O27121.1
prok#Halobacterium_salinarum_64091@Q9HQD1.1
prok#Pyrobaculum_aerophilum_178306@Q8ZWK6.1
prok#Methanopyrus_kandleri_190192@WP_011020030.1
prok#Saccharolobus_solfataricus_273057@WP_009991049.1
prok#Aeropyrum_pernix_56636@Q9YFS7
prok#Thermoplasma_acidophilum_273075@Q9HJ95.1
prok#Thermoplasma_volcanium_273116@Q97BC6.1
prok#Pyrococcus_horikoshii_70601@O58965.1
prok#Pyrococcus_abyssi_272844@Q9UZW0.1
Coccomyxa_subellipsoidea_574566@CV07G03550
Chlamydomonas_reinhardtii_3055@CR07G08730
Breviolum_minutum_1202447@seq22432
Symbiodinium_microadriaticum_2951@OLQ09293.1
G. catenatum
Euglena_gracilis_3039@EG_transcript_10778
Chromera_velia_1169474@Cvel_22642.t1-p1
Guillardia_theta_905079@XP_005840861.1
Tisochrysis_lutea_1321669@Tiso_8926
Thalassiosira_pseudonana_35128@TP16G00470
Fragilariopsis_cylindrus_186039@FC008G06150
G. catenatum
P. inerme
G. catenatum
Breviolum_minutum_1202447@seq22435
Symbiodinium_microadriaticum_2951@OLQ09290.1
Chondrus_crispus_2769@XP_005714426.1
Pyropia_yezoensis_2788@contig_22930_g5665
Porphyra_umbilicalis_2786@OSX69132.1
Porphyridium_purpureum_35688@2044.16
cyto#Plasmodiophorabrassicae37360@SPQ99756.1
cyto#Plasmodiumfalciparum36329@XP_001352096.1
Vitrella_brassicaformis_1169540@Vbra_15428
Chromera_velia_1169474@Cvel_15170.t1-p1
Tisochrysis_lutea_1321669@Tiso_4995
Emiliania_huxleyi_280463@XP_005782712.1
Emiliania_huxleyi_280463@XP_005782485.1
Tisochrysis_lutea_1321669@Tiso_2240
Guillardia_theta_905079@XP_005841712.1
Breviolum_minutum_1202447@seq15918
G. catenatum
P. asymmetricum, P. inerme, P. stigmaticum
G. catenatum
Breviolum_minutum_1202447@seq19687
Breviolum_minutum_1202447@seq2056
Symbiodinium_microadriaticum_2951@OLQ06464.1
Symbiodinium_microadriaticum_2951@OLQ06463.1
P. asymmetricum, P. inerme, P. stigmaticum
Emiliania_huxleyi_280463@XP_005781983.1
Euglena_gracilis_3039@EG_transcript_12119
Chrysochromulina_sp._1460289@KOO21935.1
P. asymmetricum, P. inerme, P. stigmaticum
Symbiodinium_microadriaticum_2951@OLQ01087.1
Breviolum_minutum_1202447@seq15225
G. catenatum
Breviolum_minutum_1202447@seq19401
Symbiodinium_microadriaticum_2951@OLP81587.1
Symbiodinium_microadriaticum_2951@OLQ04372.1
Symbiodinium_microadriaticum_2951@OLP97413.1
Pseudo-nitzschia_multiseries_37319@197768
Phaeodactylum_tricornutum_2850@PTI_16G02400
Nannochloropsis_gaditana_72520@EWM26407.1
Nannochloropsis_gaditana_72520@EWM26114.1
Nannochloropsis_gaditana_72520@EWM26113.1
Cyanidioschyzon_merolae_45157@CM10G03080
Guillardia_theta_905079@XP_005822051.1
Guillardia_theta_905079@XP_005821497.1
Chromera_velia_1169474@Cvel_21993.t1-p1
nucpt#Ectocarpus_siliculosus_2880@ES0151G00130
Aureococcus_anophagefferens_44056@AA0006G02110
cyto#Thalassiosira_pseudonana_35128@XP_002296699.1
nucpt#Thalassiosira_pseudonana_35128@TP07G04450
nucpt#Phaeodactylum_tricornutum_2850@PTI_15G02050
Fragilariopsis_cylindrus_186039@FC007G01180
nucpt#Fragilariopsis_cylindrus_186039@FC009G05890
nucpt#Pseudo-nitzschia_multiseries_37319@9120
Galdieria_sulphuraria_130081@XP_005709175.1
Galdieria_phlegrea_1389228@GalB.1085.g2160.t1
P. inerme
Toxoplasma_gondii_508771@XP_002370021.2
P. asymmetricum, P. inerme, P. stigmaticum
Chromera_velia_1169474@Cvel_8779.t1-p1
Porphyridium_purpureum_35688@3567.1
Vitrella_brassicaformis_1169540@Vbra_17333
G. catenatum
Tisochrysis_lutea_1321669@Tiso_12980
nucpt#Emiliania_huxleyi_280463@XP_005791258.1
Chrysochromulina_sp._1460289@KOO26488.1
nucpt#Bigelowiella_natans_753081@Bna92730
Chondrus_crispus_2769@XP_005715401.1
Ectocarpus_siliculosus_2880@ES0014G00780
Pyropia_yezoensis_2788@contig_15570_g3725
Porphyra_umbilicalis_2786@OSX72416.1
Cyanophora_paradoxa_2762@tig00021123_g18518.t1
nucpt#Chlamydomonas_reinhardtii_3055@CR22G00180
Klebsormidium_flaccidum_3175@GAQ79801.1
Coccomyxa_subellipsoidea_574566@CV10G02040
Ostreococcus_tauri_70448@XP_022839155.1
Micromonas_pusilla_564608@MP06G01100
Bathycoccus_prasinos_41875@BPRRCC1105_05G00620
cyto#Triticumaestivum4565@CAA33302.1
Arabidopsis_thaliana_3702@AT1G79550
cyto#Nicotianatabacum4097@NP_001312375.1
nucpt#Arabidopsis_thaliana_3702@AT3G12780
nucpt#Arabidopsis_thaliana_3702@AT1G56190
Selaginella_moellendorffii_88036@XP_002971814.1
Selaginella_moellendorffii_88036@XP_002972143.1
Selaginella_moellendorffii_88036@XP_002977295.1
Chrysochromulina_sp._1460289@KOO28553.1
Coccomyxa_subellipsoidea_574566@CV02G07240
Ectocarpus_siliculosus_2880@ES0007G00540
Nannochloropsis_gaditana_72520@EWM22161.1
Ectocarpus_siliculosus_2880@ES0070G00780
Ectocarpus_siliculosus_2880@ES0070G00630
Phaeodactylum_tricornutum_2850@PTI_20G00900
Thalassiosira_pseudonana_35128@TP03G04140
Pseudo-nitzschia_multiseries_37319@249138
Fragilariopsis_cylindrus_186039@FC009G07780
0.4

PGK (K00927)


prok#Archaeoglobus_fulgidus_224325@O28542.1
prok#Halobacterium_salinarum_64091@Q9HSS7.1
prok#Methanosarcina_acetivorans_188937@P58838.1
prok#Methanosarcina_acetivorans_188937@P58837.1
prok#Pyrobaculum_aerophilum_178306@Q8ZWK7.1
prok#Aeropyrum_pernix_272557@WP_010865544.1
prok#Saccharolobus_solfataricus_2287@1B7G_O
prok#Methanopyrus_kandleri_190192@P58839.1
prok#Thermoplasma_volcanium_273116@Q97BJ8.1
prok#Thermoplasma_acidophilum_273075@Q9HJ69.1
prok#Pyrococcus_horikoshii_70601@O59494.1
prok#Pyrococcus_abyssi_272844@Q9V1P1.1
prok#Methanocaldococcus_jannaschii_243232@Q58546.1
prok#Methanothermobacter_thermautotrophicus_187420@O27090.1
Nannochloropsis_gaditana_72520@EWM21008.1
nucpt#Ectocarpus_siliculosus_2880@ES0240G00170
nucpt#Thalassiosira_pseudonana_35128@TP01G05370
nucpt#Fragilariopsis_cylindrus_186039@FC022G02990
Fragilariopsis_cylindrus_186039@FC012G02400
Phaeodactylum_tricornutum_2850@PTI_15G02910
nucpt#Pseudo-nitzschia_multiseries_37319@192435
Guillardia_theta_905079@XP_005840507.1
nucpt#Guillardia_theta_905079@XP_005839199.1
nucpt#Aureococcus_anophagefferens_44056@AA0004G05450
Symbiodinium_microadriaticum_2951@OLP76128.1
Symbiodinium_microadriaticum_2951@OLP94817.1
Breviolum_minutum_1202447@seq36594
Breviolum_minutum_1202447@seq38253
Breviolum_minutum_1202447@seq36596
Toxoplasma_gondii_508771@XP_002365612.2
Chromera_velia_1169474@Cvel_5775.t1-p1
Vitrella_brassicaformis_1169540@Vbra_15241
Tisochrysis_lutea_1321669@Tiso_16519
Emiliania_huxleyi_280463@XP_005782410.1
Chrysochromulina_sp._1460289@KOO46000.1
Euglena_gracilis_3039@EG_transcript_12332
Euglena_gracilis_3039@EG_transcript_16406
Symbiodinium_microadriaticum_2951@OLP80677.1
Symbiodinium_microadriaticum_2951@OLQ09366.1
Symbiodinium_microadriaticum_2951@OLP80679.1
Breviolum_minutum_1202447@seq6681
Breviolum_minutum_1202447@seq16709
Breviolum_minutum_1202447@seq12421
Breviolum_minutum_1202447@seq16710
Breviolum_minutum_1202447@seq16714
Breviolum_minutum_1202447@seq16713
cyto#Coelastrellavacuolata77546@CAC81014.1
cyto#Zeamays4577@AAA03202.1
prok#Pseudomonas_aeruginosa_208964@NP_249242.1
prok#Vibrio_cholerae_243277@WP_000946626.1
prok#Yersinia_pestis_214092@NP_404540.1
prok#Salmonella_enterica_99287@NP_461986.1
prok#Escherichia_coli_83334@P0A9B8.2
nucpt#Euglena_gracilis_3039@EG_transcript_8042
P. asymmetricum, P. inerme, P. stigmaticum
Cyanidioschyzon_merolae_45157@CM10G00420
Porphyridium_purpureum_35688@4494.2
Galdieria_sulphuraria_130081@XP_005704189.1
Galdieria_phlegrea_1389228@GalB.5544.g6991.t1
Chondrus_crispus_2769@XP_005715477.1
Porphyra_umbilicalis_2786@OSX77143.1
Pyropia_yezoensis_2788@contig_8807_g2079
Cyanophora_paradoxa_2762@tig00000157_g9626.t1
Bathycoccus_prasinos_41875@BPRRCC1105_01G01370
Micromonas_pusilla_564608@MP02G07590
Ostreococcus_tauri_70448@XP_022838170.1
Coccomyxa_subellipsoidea_574566@CV18G02910
nucpt#Chlamydomonas_reinhardtii_3055@CR01G02240
Micromonas_pusilla_564608@MP01G07350
Ostreococcus_tauri_70448@XP_022839867.1
Bathycoccus_prasinos_41875@BPRRCC1105_11G03630
Klebsormidium_flaccidum_3175@GAQ83271.1
Selaginella_moellendorffii_88036@XP_002981126.1
nucpt#Arabidopsis_thaliana_3702@AT1G42970
Selaginella_moellendorffii_88036@XP_002970103.1
Klebsormidium_flaccidum_3175@GAQ82109.1
nucpt#Arabidopsis_thaliana_3702@AT3G26650
nucpt#Arabidopsis_thaliana_3702@AT1G12900
Porphyridium_purpureum_35688@2393.1
Cyanidioschyzon_merolae_45157@CM10G02520
Cyanidioschyzon_merolae_45157@CM13G01670
Galdieria_sulphuraria_130081@XP_005708895.1
Galdieria_phlegrea_1389228@GalB.1115.g2218.t1
Porphyra_umbilicalis_2786@OSX79791.1
Pyropia_yezoensis_2788@contig_22208_g5493
cyto#Gracilariagracilis2777@AAB01379.1
Chondrus_crispus_2769@XP_005715932.1
cyto#Chondruscrispus2769@CAA51515.1
Klebsormidium_flaccidum_3175@GAQ84340.1
Plasmodium_falciparum_36329@PF3D7_1462800.1
Thalassiosira_pseudonana_35128@TP05G05020
Phaeodactylum_tricornutum_2850@PTI_16G02760
Fragilariopsis_cylindrus_186039@FC009G03910
Pseudo-nitzschia_multiseries_37319@187507
Vitrella_brassicaformis_1169540@Vbra_3476
Chromera_velia_1169474@Cvel_9419.t1-p1
Chromera_velia_1169474@Cvel_9420.t1-p1
Cryptosporidium_parvum_353152@cgd6_3790
Toxoplasma_gondii_508771@XP_018636414.1
Symbiodinium_microadriaticum_2951@OLP91391.1
Symbiodinium_microadriaticum_2951@OLP99701.1
Breviolum_minutum_1202447@seq19955
Breviolum_minutum_1202447@seq19957
Selaginella_moellendorffii_88036@XP_002975979.1
Selaginella_moellendorffii_88036@XP_002968506.1
cyto#Nicotiana_tabacum4097@AAA34077.1
Arabidopsis_thaliana_3702@AT3G04120
Arabidopsis_thaliana_3702@AT1G13440
Nannochloropsis_gaditana_72520@EWM26684.1
Nannochloropsis_gaditana_72520@EWM27464.1
cyto#Phytophthorainfestans4787@CAA45835.1
Aureococcus_anophagefferens_44056@AA0026G00080
Thalassiosira_pseudonana_35128@TP05G01950
Thalassiosira_pseudonana_35128@TP05G01960
Phaeodactylum_tricornutum_2850@PTI_02G02770
Phaeodactylum_tricornutum_2850@PTI_02G02760
Fragilariopsis_cylindrus_186039@FC007G03580
Pseudo-nitzschia_multiseries_37319@8993
Fragilariopsis_cylindrus_186039@FC007G03590
Pseudo-nitzschia_multiseries_37319@253151
Selaginella_moellendorffii_88036@XP_002965494.1
Selaginella_moellendorffii_88036@XP_002982970.1
nucpt#Arabidopsis_thaliana_3702@AT1G16300
nucpt#Arabidopsis_thaliana_3702@AT1G79530
Guillardia_theta_905079@XP_005834101.1
Klebsormidium_flaccidum_3175@GAQ87890.1
Chrysochromulina_sp._1460289@KOO26187.1
Tisochrysis_lutea_1321669@Tiso_10819
Emiliania_huxleyi_280463@XP_005763158.1
Tisochrysis_lutea_1321669@Tiso_691
Goniomonas_avonlea_1255295@comp64756_c0_seq1_6_ORF22_361
Goniomonas_avonlea_1255295@comp39437_c0_seq1_6_ORF35_343
Cyanophora_paradoxa_2762@tig00001424_g8706.t1
Bathycoccus_prasinos_41875@BPRRCC1105_12G01480
Chlamydomonas_reinhardtii_3055@AAA86856.1
cyto#Coelastrellavacuolata77546@CAC81012.1
Coccomyxa_subellipsoidea_574566@CV26G00130
Coccomyxa_subellipsoidea_574566@CV07G03540
0.8

GAPA (K05298)

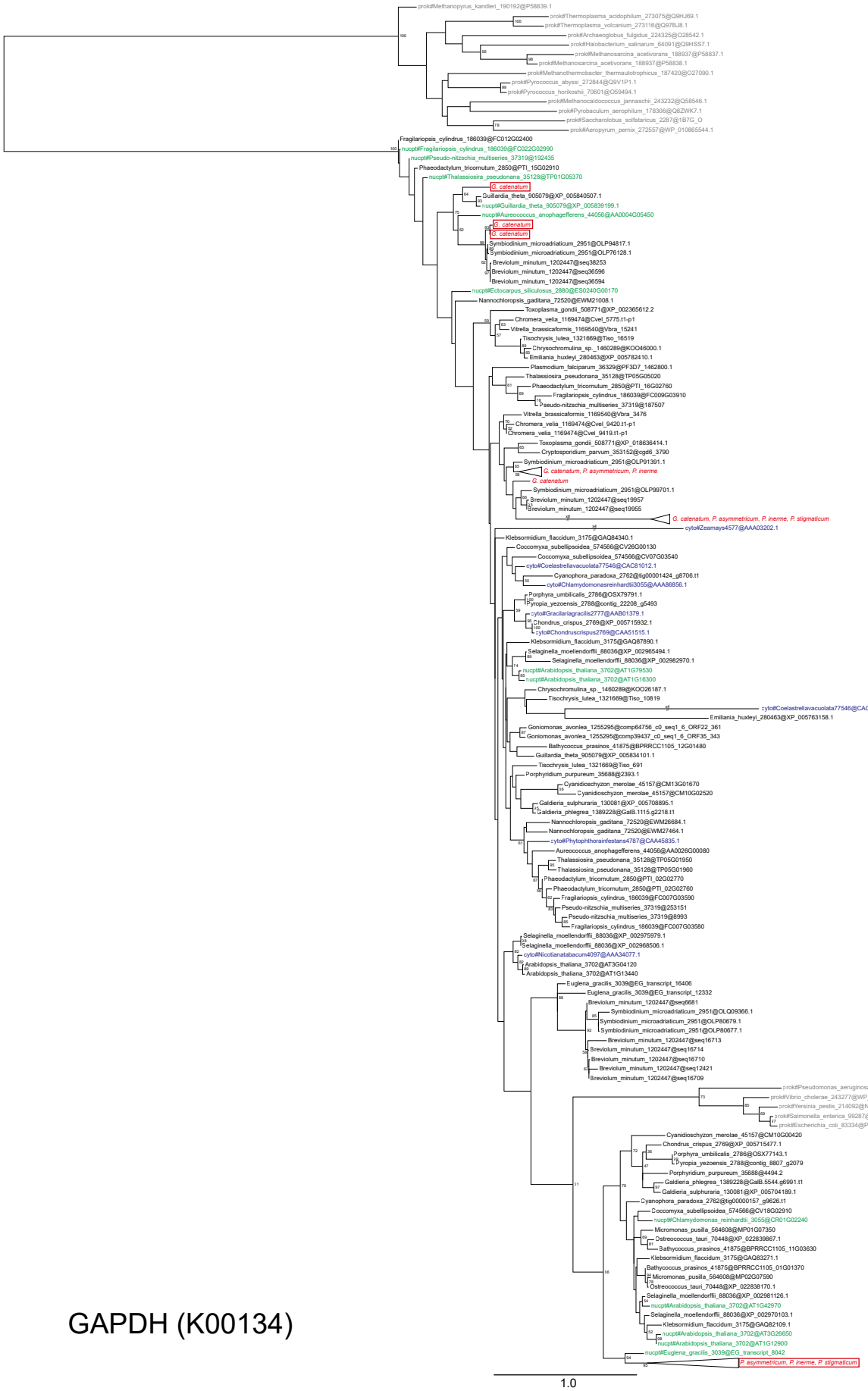

GAPDH (K00134)

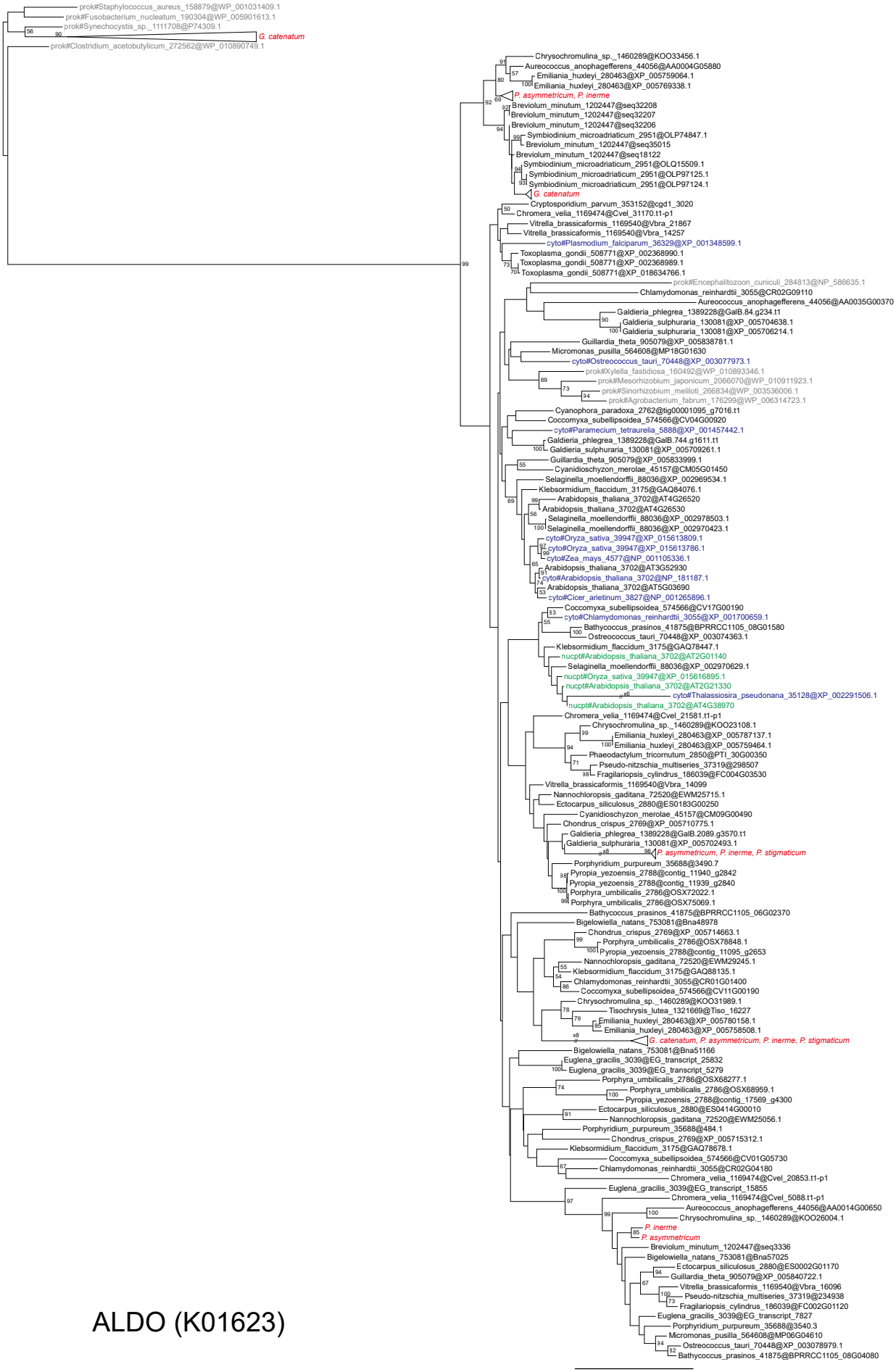
prok#Staphylococcus_aureus_158879@WP_001031409.1
prok#Fusobacterium_nucleatum_190304@WP_005901613.1
prok#Synechocystis_sp._1111708@P74309.1
G. catenatum
prok#Clostridium_acetobutylicum_272562@WP_010890749.1
Chrysochromulina_sp._1460289@KOO33456.1
Aureococcus_anophagefferens_44056@AA0004G05880
Emiliania_huxleyi_280463@XP_005759064.1
Emiliania_huxleyi_280463@XP_005769338.1
P. asymmetricum, P. inerme
Breviolum_minutum_1202447@seq32208
Breviolum_minutum_1202447@seq32207
Breviolum_minutum_1202447@seq32206
Symbiodinium_microadriaticum_2951@OLP74847.1
Breviolum_minutum_1202447@seq35015
Breviolum_minutum_1202447@seq18122
Symbiodinium_microadriaticum_2951@OLQ15509.1
Symbiodinium_microadriaticum_2951@OLP97125.1
Symbiodinium_microadriaticum_2951@OLP97124.1
G. catenatum
Cryptosporidium_parvum_353152@cgd1_3020
Chromera_velia_1169474@Cvel_31170.t1-p1
Vitrella_brassicaformis_1169540@Vbra_21867
Vitrella_brassicaformis_1169540@Vbra_14257
cyto#Plasmodium_falciparum_36329@XP_001348599.1
Toxoplasma_gondii_508771@XP_002368990.1
Toxoplasma_gondii_508771@XP_002368989.1
Toxoplasma_gondii_508771@XP_018634766.1
prok#Encephalitozoon_cuniculi_284813@NP_586635.1
Chlamydomonas_reinhardtii_3055@CR02G09110
Aureococcus_anophagefferens_44056@AA0035G00370
Galdieria_phlegrea_1389228@GalB.84.g234.t1
Galdieria_sulphuraria_130081@XP_005704638.1
Galdieria_sulphuraria_130081@XP_005706214.1
Guillardia_theta_905079@XP_005838781.1
Micromonas_pusilla_564608@MP18G01630
cyto#Ostreococcus_tauri_70448@XP_003077973.1
prok#Xylella_fastidiosa_160492@WP_010893346.1
prok#Mesorhizobium_japonicum_2066070@WP_010911923.1
prok#Sinorhizobium_meliloti_266834@WP_003536006.1
prok#Agrobacterium_fabrum_176299@WP_006314723.1
Cyanophora_paradoxa_2762@tig00001095_g7016.t1
Coccomyxa_subellipsoidea_574566@CV04G00920
cyto#Paramecium_tetraurelia_5888@XP_001457442.1
Galdieria_phlegrea_1389228@GalB.744.g1611.t1
Galdieria_sulphuraria_130081@XP_005709261.1
Guillardia_theta_905079@XP_005833999.1
Cyanidioschyzon_merolae_45157@CM05G01450
Selaginella_moellendorffii_88036@XP_002969534.1
Klebsormidium_flaccidum_3175@GAQ84076.1
Arabidopsis_thaliana_3702@AT4G26520
Arabidopsis_thaliana_3702@AT4G26530
Selaginella_moellendorffii_88036@XP_002978503.1
Selaginella_moellendorffii_88036@XP_002970423.1
cyto#Oryza_sativa_39947@XP_015613809.1
cyto#Oryza_sativa_39947@XP_015613786.1
cyto#Zea_mays_4577@NP_001105336.1
Arabidopsis_thaliana_3702@AT3G52930
cyto#Arabidopsis_thaliana_3702@NP_181187.1
Arabidopsis_thaliana_3702@AT5G03690
cyto#Cicer_arietinum_3827@NP_001265896.1
Coccomyxa_subellipsoidea_574566@CV17G00190
cyto#Chlamydomonas_reinhardtii_3055@XP_001700659.1
Bathycoccus_prasinos_41875@BPRRCC1105_08G01580
Ostreococcus_tauri_70448@XP_003074363.1
Klebsormidium_flaccidum_3175@GAQ78447.1
nucpt#Arabidopsis_thaliana_3702@AT2G01140
Selaginella_moellendorffii_88036@XP_002970629.1
nucpt#Oryza_sativa_39947@XP_015616895.1
nucpt#Arabidopsis_thaliana_3702@AT2G21330
cyto#Thalassiosira_pseudonana_35128@XP_002291506.1
nucpt#Arabidopsis_thaliana_3702@AT4G38970
Chromera_velia_1169474@Cvel_21581.t1-p1
Chrysochromulina_sp._1460289@KOO23108.1
Emiliania_huxleyi_280463@XP_005787137.1
Emiliania_huxleyi_280463@XP_005759464.1
Phaeodactylum_tricornutum_2850@PTI_30G00350
Pseudo-nitzschia_multiseries_37319@298507
Fragilariopsis_cylindrus_186039@FC004G03530
Vitrella_brassicaformis_1169540@Vbra_14099
Nannochloropsis_gaditana_72520@EWM25715.1
Ectocarpus_siliculosus_2880@ES0183G00250
Cyanidioschyzon_merolae_45157@CM09G00490
Chondrus_crispus_2769@XP_005710775.1
Galdieria_phlegrea_1389228@GalB.2089.g3570.t1
Galdieria_sulphuraria_130081@XP_005702493.1
P. asymmetricum, P. inerme, P. stigmaticum
Porphyridium_purpureum_35688@3490.7
Pyropia_yezoensis_2788@contig_11940_g2842
Pyropia_yezoensis_2788@contig_11939_g2840
Porphyra_umbilicalis_2786@OSX72022.1
Porphyra_umbilicalis_2786@OSX75069.1
Bathycoccus_prasinos_41875@BPRRCC1105_06G02370
Bigelowiella_natans_753081@Bna48978
Chondrus_crispus_2769@XP_005714663.1
Porphyra_umbilicalis_2786@OSX78848.1
Pyropia_yezoensis_2788@contig_11095_g2653
Nannochloropsis_gaditana_72520@EWM29245.1
Klebsormidium_flaccidum_3175@GAQ88135.1
Chlamydomonas_reinhardtii_3055@CR01G01400
Coccomyxa_subellipsoidea_574566@CV11G00190
Chrysochromulina_sp._1460289@KOO31989.1
Tisochrysis_lutea_1321669@Tiso_16227
Emiliania_huxleyi_280463@XP_005780158.1
Emiliania_huxleyi_280463@XP_005758508.1
G. catenatum, P. asymmetricum, P. inerme, P. stigmaticum
Bigelowiella_natans_753081@Bna51166
Euglena_gracilis_3039@EG_transcript_25832
Euglena_gracilis_3039@EG_transcript_5279
Porphyra_umbilicalis_2786@OSX68277.1
Porphyra_umbilicalis_2786@OSX68959.1
Pyropia_yezoensis_2788@contig_17569_g4300
Ectocarpus_siliculosus_2880@ES0414G00010
Nannochloropsis_gaditana_72520@EWM25056.1
Porphyridium_purpureum_35688@484.1
Chondrus_crispus_2769@XP_005715312.1
Klebsormidium_flaccidum_3175@GAQ78678.1
Coccomyxa_subellipsoidea_574566@CV01G05730
Chlamydomonas_reinhardtii_3055@CR02G04180
Chromera_velia_1169474@Cvel_20853.t1-p1
Euglena_gracilis_3039@EG_transcript_15855
Chromera_velia_1169474@Cvel_5088.t1-p1
Aureococcus_anophagefferens_44056@AA0014G00650
Chrysochromulina_sp._1460289@KOO26004.1
P. inerme
P. asymmetricum
Breviolum_minutum_1202447@seq3336
Bigelowiella_natans_753081@Bna57025
Ectocarpus_siliculosus_2880@ES0002G01170
Guillardia_theta_905079@XP_005840722.1
Vitrella_brassicaformis_1169540@Vbra_16096
Pseudo-nitzschia_multiseries_37319@234938
Fragilariopsis_cylindrus_186039@FC002G01120
Euglena_gracilis_3039@EG_transcript_7827
Porphyridium_purpureum_35688@3540.3
Micromonas_pusilla_564608@MP06G04610
Ostreococcus_tauri_70448@XP_003078979.1
Bathycoccus_prasinos_41875@BPRRCC1105_08G04080
1.0

ALDO (K01623)

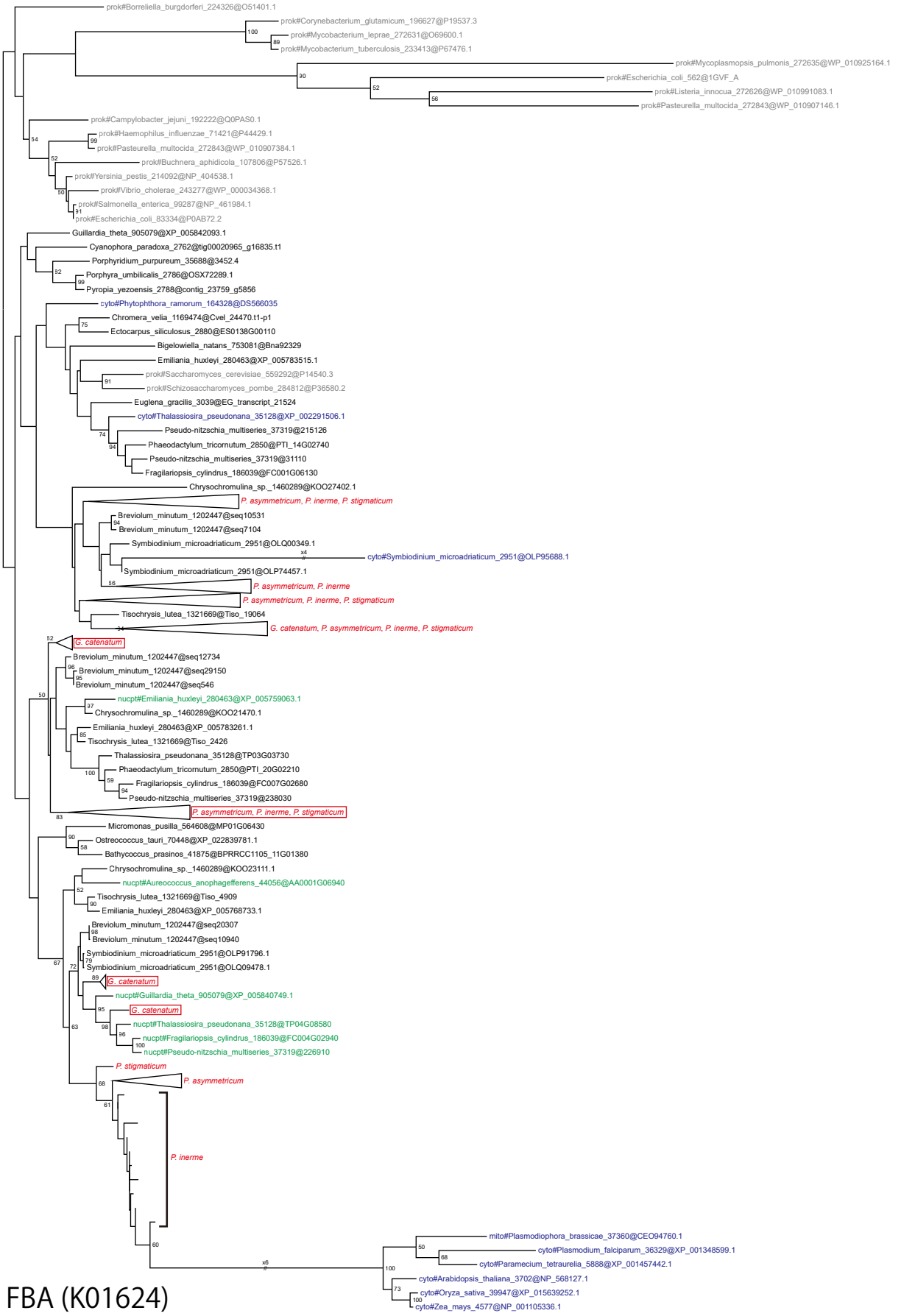
prok#Borreliella_burgdorferi_224326@O51401.1
prok#Corynebacterium_glutamicum_196627@P19537.3
prok#Mycobacterium_leprae_272631@O69600.1
prok#Mycobacterium_tuberculosis_233413@P67476.1
prok#Mycoplasmopsis_pulmonis_272635@WP_010925164.1
prok#Escherichia_coli_562@1GVF_A
prok#Listeria_innocua_272626@WP_010991083.1
prok#Pasteurella_multocida_272843@WP_010907146.1
prok#Campylobacter_jejuni_192222@Q0PAS0.1
prok#Haemophilus_influenzae_71421@P44429.1
prok#Pasteurella_multocida_272843@WP_010907384.1
prok#Buchnera_aphidicola_107806@P57526.1
prok#Yersinia_pestis_214092@NP_404538.1
prok#Vibrio_cholerae_243277@WP_000034368.1
prok#Salmonella_enterica_99287@NP_461984.1
prok#Escherichia_coli_83334@P0AB72.2
Guillardia_theta_905079@XP_005842093.1
Cyanophora_paradoxa_2762@tig00020965_g16835.t1
Porphyridium_purpureum_35688@3452.4
Porphyra_umbilicalis_2786@OSX72289.1
Pyropia_yezoensis_2788@contig_23759_g5856
cyto#Phytophthora_ramorum_164328@DS566035
Chromera_velia_1169474@Cvel_24470.t1-p1
Ectocarpus_siliculosus_2880@ES0138G00110
Bigelowiella_natans_753081@Bna92329
Emiliania_huxleyi_280463@XP_005783515.1
prok#Saccharomyces_cerevisiae_559292@P14540.3
prok#Schizosaccharomyces_pombe_284812@P36580.2
Euglena_gracilis_3039@EG_transcript_21524
cyto#Thalassiosira_pseudonana_35128@XP_002291506.1
Pseudo-nitzschia_multiseries_37319@215126
Phaeodactylum_tricornutum_2850@PTI_14G02740
Pseudo-nitzschia_multiseries_37319@31110
Fragilariopsis_cylindrus_186039@FC001G06130
Chrysochromulina_sp._1460289@KOO27402.1
P. asymmetricum, P. inerme, P. stigmaticum
Breviolum_minutum_1202447@seq10531
Breviolum_minutum_1202447@seq7104
Symbiodinium_microadriaticum_2951@OLQ00349.1
cyto#Symbiodinium_microadriaticum_2951@OLP95688.1
Symbiodinium_microadriaticum_2951@OLP74457.1
P. asymmetricum, P. inerme
P. asymmetricum, P. inerme, P. stigmaticum
Tisochrysis_lutea_1321669@Tiso_19064
G. catenatum, P. asymmetricum, P. inerme, P. stigmaticum
G. catenatum
Breviolum_minutum_1202447@seq12734
Breviolum_minutum_1202447@seq29150
Breviolum_minutum_1202447@seq546
nucpt#Emiliania_huxleyi_280463@XP_005759063.1
Chrysochromulina_sp._1460289@KOO21470.1
Emiliania_huxleyi_280463@XP_005783261.1
Tisochrysis_lutea_1321669@Tiso_2426
Thalassiosira_pseudonana_35128@TP03G03730
Phaeodactylum_tricornutum_2850@PTI_20G02210
Fragilariopsis_cylindrus_186039@FC007G02680
Pseudo-nitzschia_multiseries_37319@238030
P. asymmetricum, P. inerme, P. stigmaticum
Micromonas_pusilla_564608@MP01G06430
Ostreococcus_tauri_70448@XP_022839781.1
Bathycoccus_prasinos_41875@BPRRCC1105_11G01380
Chrysochromulina_sp._1460289@KOO23111.1
nucpt#Aureococcus_anophagefferens_44056@AA0001G06940
Tisochrysis_lutea_1321669@Tiso_4909
Emiliania_huxleyi_280463@XP_005768733.1
Breviolum_minutum_1202447@seq20307
Breviolum_minutum_1202447@seq10940
Symbiodinium_microadriaticum_2951@OLP91796.1
Symbiodinium_microadriaticum_2951@OLQ09478.1
G. catenatum
nucpt#Guillardia_theta_905079@XP_005840749.1
G. catenatum
nucpt#Thalassiosira_pseudonana_35128@TP04G08580
nucpt#Fragilariopsis_cylindrus_186039@FC004G02940
nucpt#Pseudo-nitzschia_multiseries_37319@226910
P. stigmaticum
P. asymmetricum
P. inerme
mito#Plasmodiophora_brassicae_37360@CEO94760.1
cyto#Plasmodium_falciparum_36329@XP_001348599.1
cyto#Paramecium_tetraurelia_5888@XP_001457442.1
cyto#Arabidopsis_thaliana_3702@NP_568127.1
cyto#Oryza_sativa_39947@XP_015639252.1
cyto#Zea_mays_4577@NP_001105336.1
0.9

FBA (K01624)

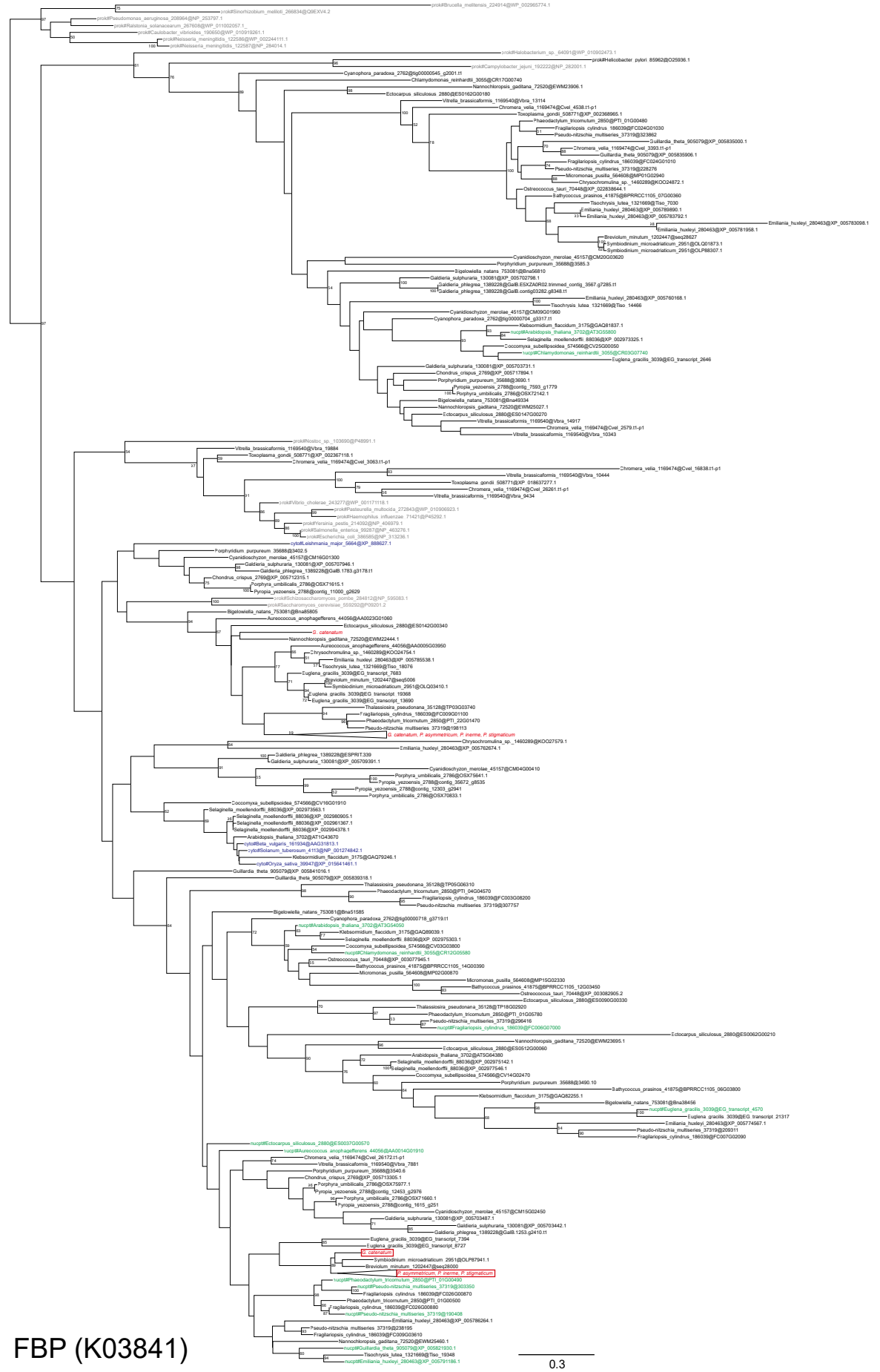
prokl#Brucella_melitensis_224914@WP_002965774.1
prokl#Sinorhizobium_meliloti_266834@Q9EXV4.2
prokl#Pseudomonas_aeruginosa_208964@NP_253797.1
prokl#Ralstonia_solanacearum_267608@WP_011002057.1_
prokl#Caulobacter_vibrioides_190650@WP_010919261.1
prokl#Neisseria_meningitidis_122586@WP_002244111.1
prokl#Neisseria_meningitidis_122587@NP_284014.1
prokl#Halobacterium_sp._64091@WP_010993473.1
prokl#Helicobacter_pylori_85962@O25936.1
prokl#Campylobacter_jejuni_192222@NP_282001.1
Cyanophora_paradoxa_2762@tig00000545_g2001.t1
Chlamydomonas_reinhardtii_3055@CR17G00740
Nannochloropsis_gaditana_72520@EWM23906.1
Ectocarpus_siliculosus_2880@ES0162G00180
Vitrella_brassicaformis_1169540@Vbra_13114
Chromera_velia_1169474@Cvel_4538.t1-p1
Toxoplasma_gondii_508771@XP_002368965.1
Phaeodactylum_tricornutum_2850@PTI_01G00480
Fragilariopsis_cylindrus_186039@FC024G01030
Pseudo-nitzschia_multiseries_37319@323862
Guillardia_theta_905079@XP_005835000.1
Chromera_velia_1169474@Cvel_3393.t1-p1
Guillardia_theta_905079@XP_005835906.1
Fragilariopsis_cylindrus_186039@FC024G01010
Pseudo-nitzschia_multiseries_37319@228276
Micromonas_pusilla_564608@MP01G02940
Chrysochromulina_sp._1460289@KOO24872.1
Ostreococcus_tauri_70448@XP_022838644.1
Bathycoccus_prasinos_41875@BPRRCC1105_07G00360
Tisochrysis_lutea_1321669@Tiso_7030
Emiliania_huxleyi_280463@XP_005789890.1
Emiliania_huxleyi_280463@XP_005783792.1
Emiliania_huxleyi_280463@XP_005783098.1
Emiliania_huxleyi_280463@XP_005781958.1
Braviolum_minutum_1202447@seq28627
Symbiodinium_microadriaticum_2951@OLQ01873.1
Symbiodinium_microadriaticum_2951@OLP88307.1
Cyanidioschyzon_merolae_45157@CM2G03620
Porphyridium_purpureum_35688@3585.3
Bigelowiella_natans_753081@Bna56810
Galdieria_sulphuraria_130081@XP_005702798.1
Galdieria_phlegrea_1389228@GalB.E5XZA0R02.trimmed_contig_3567.g7285.t1
Galdieria_phlegrea_1389228@GalB.contig03282.g8348.t1
Emiliania_huxleyi_280463@XP_005760168.1
Tisochrysis_lutea_1321669@Tiso_14466
Cyanidioschyzon_merolae_45157@CM09G01960
Cyanophora_paradoxa_2762@tig00000704_g3317.t1
Klebsormidium_flaccidum_3175@GAQ81837.1
nucp#Arabidopsis_thaliana_3702@AT3G55800
Selaginella_moellendorffii_88036@XP_002973325.1
Coccomyxa_subellipsoidea_574566@CV25G00050
nucp#Chlamydomonas_reinhardtii_3055@CR03G07740
Euglena_gracilis_3039@EG_transcript_2646
Galdieria_sulphuraria_130081@XP_005703731.1
Chondrus_crispus_2769@XP_005717894.1
Porphyridium_purpureum_35688@3690.1
Pyropia_yezoensis_2788@contig_7593_g1779
Porphyra_umbilicalis_2786@OSX72142.1
Bigelowiella_natans_753081@Bna49334
Nannochloropsis_gaditana_72520@EWM25027.1
Ectocarpus_siliculosus_2880@ES0147G00370
Vitrella_brassicaformis_1169540@Vbra_14917
Chromera_velia_1169474@Cvel_2579.t1-p1
Vitrella_brassicaformis_1169540@Vbra_10343
prokl#Nostoc_sp._103690@P48991.1
Vitrella_brassicaformis_1169540@Vbra_19884
Toxoplasma_gondii_508771@XP_002367118.1
Chromera_velia_1169474@Cvel_3083.t1-p1
Chromera_velia_1169474@Cvel_16838.t1-p1
Vitrella_brassicaformis_1169540@Vbra_10444
Toxoplasma_gondii_508771@XP_018637277.1
Chromera_velia_1169474@Cvel_26261.t1-p1
Vitrella_brassicaformis_1169540@Vbra_9434
prokl#Vibrio_cholerae_243277@WP_001171118.1
prokl#Pasteurella_multocida_272843@WP_010906923.1
prokl#Haemophilus_influenzae_71421@P45292.1
prokl#Yersinia_pestis_214092@NP_406979.1
prokl#Salmonella_enterica_99287@NP_463276.1
prokl#Escherichia_coli_386585@NP_313236.1
cytol#Leishmania_major_5664@XP_888627.1
Porphyridium_purpureum_35688@3402.5
Cyanidioschyzon_merolae_45157@CM16G01300
Galdieria_sulphuraria_130081@XP_005707946.1
Galdieria_phlegrea_1389228@GalB.1783.g3178.t1
Chondrus_crispus_2769@XP_005712315.1
Porphyra_umbilicalis_2786@OSX71615.1
Pyropia_yezoensis_2788@contig_11000_g2629
prokl#Schizosaccharomyces_pombe_284812@NP_595083.1
prokl#Saccharomyces_cerevisiae_559292@P09201.2
Bigelowiella_natans_753081@Bna85805
Aureococcus_anophagefferens_44056@AA0023G01060
Ectocarpus_siliculosus_2880@ES0142G00340
G. catenatum
Nannochloropsis_gaditana_72520@EWM22444.1
Aureococcus_anophagefferens_44056@AA0005G03950
Chrysochromulina_sp._1460289@KOO24754.1
Emiliania_huxleyi_280463@XP_005785538.1
Tisochrysis_lutea_1321669@Tiso_18076
Euglena_gracilis_3039@EG_transcript_7683
Braviolum_minutum_1202447@seq5006
Symbiodinium_microadriaticum_2951@OLQ03410.1
Euglena_gracilis_3039@EG_transcript_19368
Euglena_gracilis_3039@EG_transcript_13690
Thalassiosira_pseudonana_35128@TP03G03740
Fragilariopsis_cylindrus_186039@FC009G01100
Phaeodactylum_tricornutum_2850@PTI_22G01470
Pseudo-nitzschia_multiseries_37319@198113
G. catenatum, P. asymmetricum, P. inerme, P. stigmaticum
Chrysochromulina_sp._1460289@KOO27579.1
Emiliania_huxleyi_280463@XP_005762674.1
Galdieria_phlegrea_1389228@ESPRIT.339
Galdieria_sulphuraria_130081@XP_005709391.1
Cyanidioschyzon_merolae_45157@CM04G00410
Porphyra_umbilicalis_2786@OSX75641.1
Pyropia_yezoensis_2788@contig_35672_g8535
Pyropia_yezoensis_2788@contig_12303_g2941
Porphyra_umbilicalis_2786@OSX70833.1
Coccomyxa_subellipsoidea_574566@CV16G01910
Selaginella_moellendorffii_88036@XP_002973563.1
Selaginella_moellendorffii_88036@XP_002980905.1
Selaginella_moellendorffii_88036@XP_002961367.1
Selaginella_moellendorffii_88036@XP_002994378.1
Arabidopsis_thaliana_3702@AT1G43670
cytol#Beta_vulgaris_161934@AAG31813.1
cytol#Solanum_tuberosum_4113@NP_001274842.1
Klebsormidium_flaccidum_3175@GAQ79246.1
cytol#Oryza_sativa_39947@XP_015641461.1
Guillardia_theta_905079@XP_005841916.1
Guillardia_theta_905079@XP_005839318.1
Thalassiosira_pseudonana_35128@TP05G06310
Phaeodactylum_tricornutum_2850@PTI_04G04570
Fragilariopsis_cylindrus_186039@FC003G08200
Pseudo-nitzschia_multiseries_37319@307757
Bigelowiella_natans_753081@Bna51585
Cyanophora_paradoxa_2762@tig00000718_g3719.t1
nucp#Arabidopsis_thaliana_3702@AT3G54050
Klebsormidium_flaccidum_3175@GAQ89039.1
Selaginella_moellendorffii_88036@XP_002975303.1
Coccomyxa_subellipsoidea_574566@CV03G03800
nucp#Chlamydomonas_reinhardtii_3055@CR12G00580
Ostreococcus_tauri_70448@XP_003077945.1
Bathycoccus_prasinos_41875@BPRRCC1105_14G00390
Micromonas_pusilla_564608@MP02G00870
Micromonas_pusilla_564608@MP15G02330
Bathycoccus_prasinos_41875@BPRRCC1105_12G03450
Ostreococcus_tauri_70448@XP_003082905.2
Ectocarpus_siliculosus_2880@ES0090G00330
Thalassiosira_pseudonana_35128@TP18G02920
Phaeodactylum_tricornutum_2850@PTI_01G05780
Pseudo-nitzschia_multiseries_37319@296416
nucp#Fragilariopsis_cylindrus_186039@FC006G07000
Ectocarpus_siliculosus_2880@ES0062G00210
Nannochloropsis_gaditana_72520@EWM23695.1
Ectocarpus_siliculosus_2880@ES0512G00060
Arabidopsis_thaliana_3702@AT5G64380
Selaginella_moellendorffii_88036@XP_002975142.1
Selaginella_moellendorffii_88036@XP_002977546.1
Coccomyxa_subellipsoidea_574566@CV14G02470
Porphyridium_purpureum_35688@3490.10
Bathycoccus_prasinos_41875@BPRRCC1105_06G03800
Klebsormidium_flaccidum_3175@GAQ82255.1
Bigelowiella_natans_753081@Bna38456
nucp#Euglena_gracilis_3039@EG_transcript_4570
Euglena_gracilis_3039@EG_transcript_21317
Emiliania_huxleyi_280463@XP_005774567.1
Pseudo-nitzschia_multiseries_37319@209311
Fragilariopsis_cylindrus_186039@FC007G02090
nucp#Ectocarpus_siliculosus_2880@ES0037G00570
nucp#Aureococcus_anophagefferens_44056@AA0014G01910
Chromera_velia_1169474@Cvel_26172.t1-p1
Vitrella_brassicaformis_1169540@Vbra_7881
Porphyridium_purpureum_35688@3540.6
Chondrus_crispus_2769@XP_005713305.1
Porphyra_umbilicalis_2786@OSX75977.1
Pyropia_yezoensis_2788@contig_12453_g2976
Porphyra_umbilicalis_2786@OSX71660.1
Pyropia_yezoensis_2788@contig_1615_g251
Cyanidioschyzon_merolae_45157@CM15G02450
Galdieria_sulphuraria_130081@XP_005703487.1
Galdieria_sulphuraria_130081@XP_005703442.1
Galdieria_phlegrea_1389228@GalB.1253.g2410.t1
Euglena_gracilis_3039@EG_transcript_7394
Euglena_gracilis_3039@EG_transcript_8727
G. catenatum
Symbiodinium_microadriaticum_2951@OLP87941.1
Braviolum_minutum_1202447@seq28000
P. asymmetricum, P. inerme, P. stigmaticum
nucp#Phaeodactylum_tricornutum_2850@PTI_01G00490
nucp#Pseudo-nitzschia_multiseries_37319@303350
Fragilariopsis_cylindrus_186039@FC026G00870
Phaeodactylum_tricornutum_2850@PTI_01G00500
Fragilariopsis_cylindrus_186039@FC026G00880
nucp#Pseudo-nitzschia_multiseries_37319@190408
Emiliania_huxleyi_280463@XP_005786264.1
Pseudo-nitzschia_multiseries_37319@238195
Fragilariopsis_cylindrus_186039@FC009G03610
Nannochloropsis_gaditana_72520@EWM25460.1
nucp#Guillardia_theta_905079@XP_005821930.1
Tisochrysis_lutea_1321669@Tiso_19348
nucp#Emiliania_huxleyi_280463@XP_005791186.1
0.3

FBP (K03841)

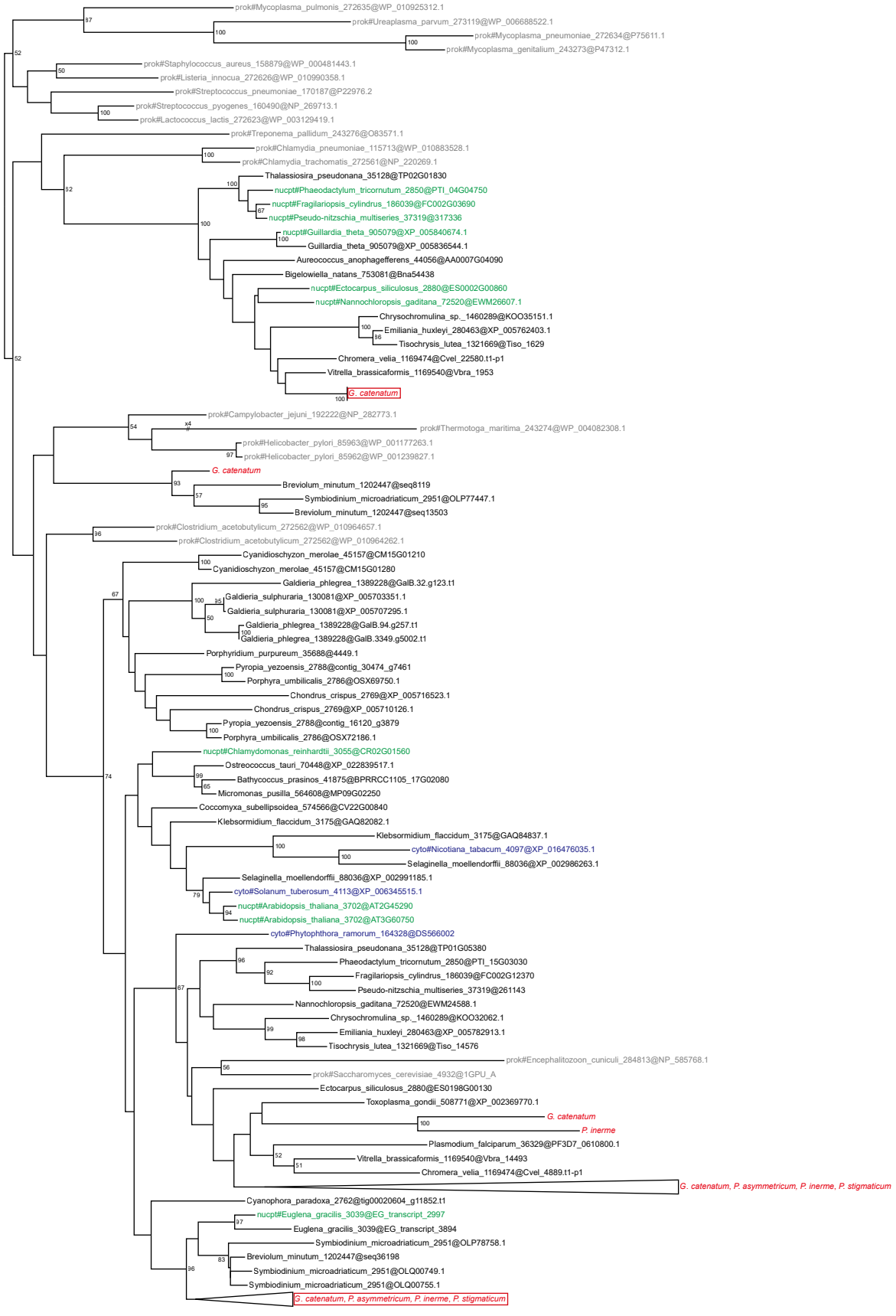

E2.2.1.1 (K00615)

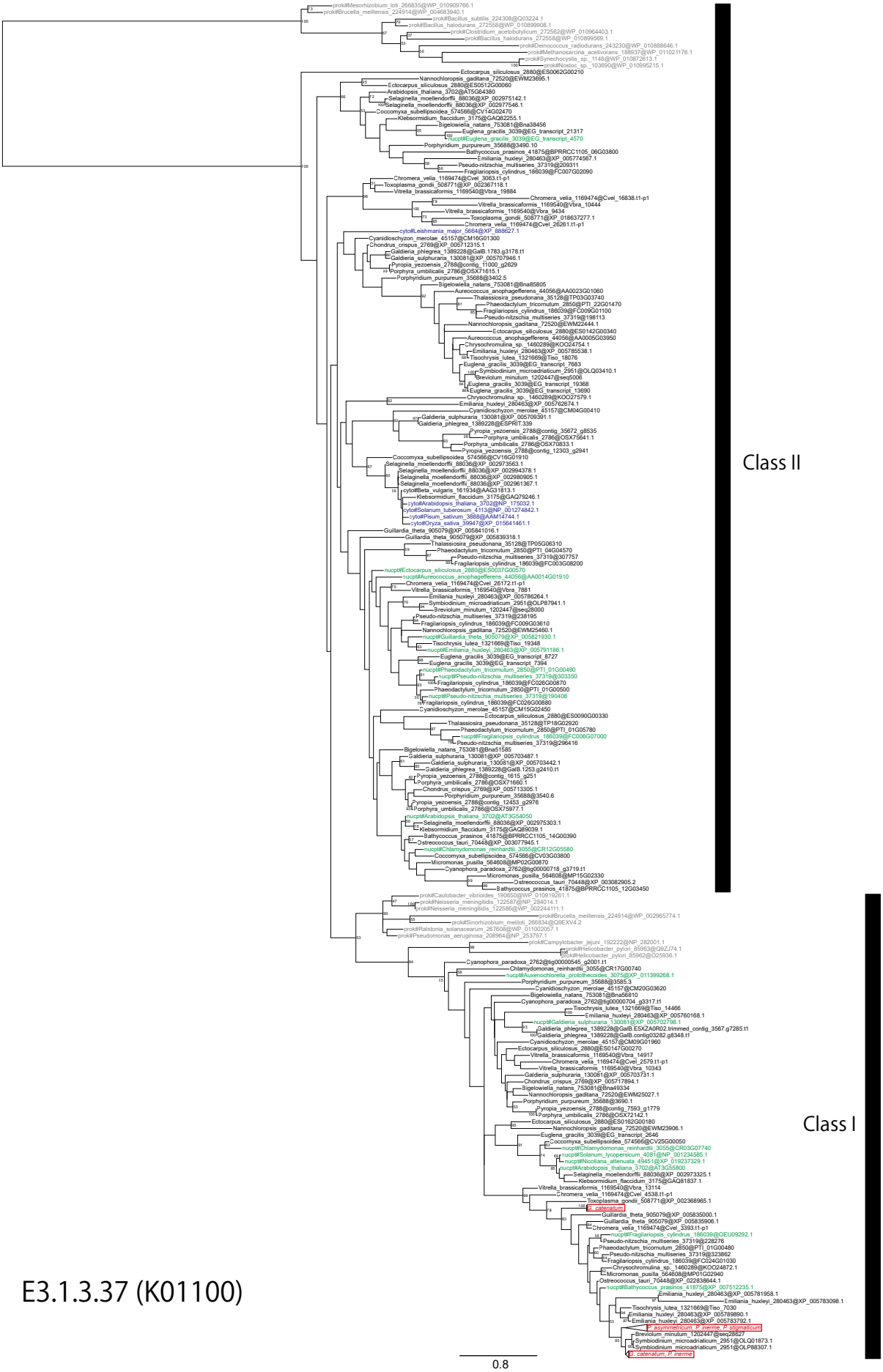
Class II
Class I
E3.1.3.37 (K01100)
0.8

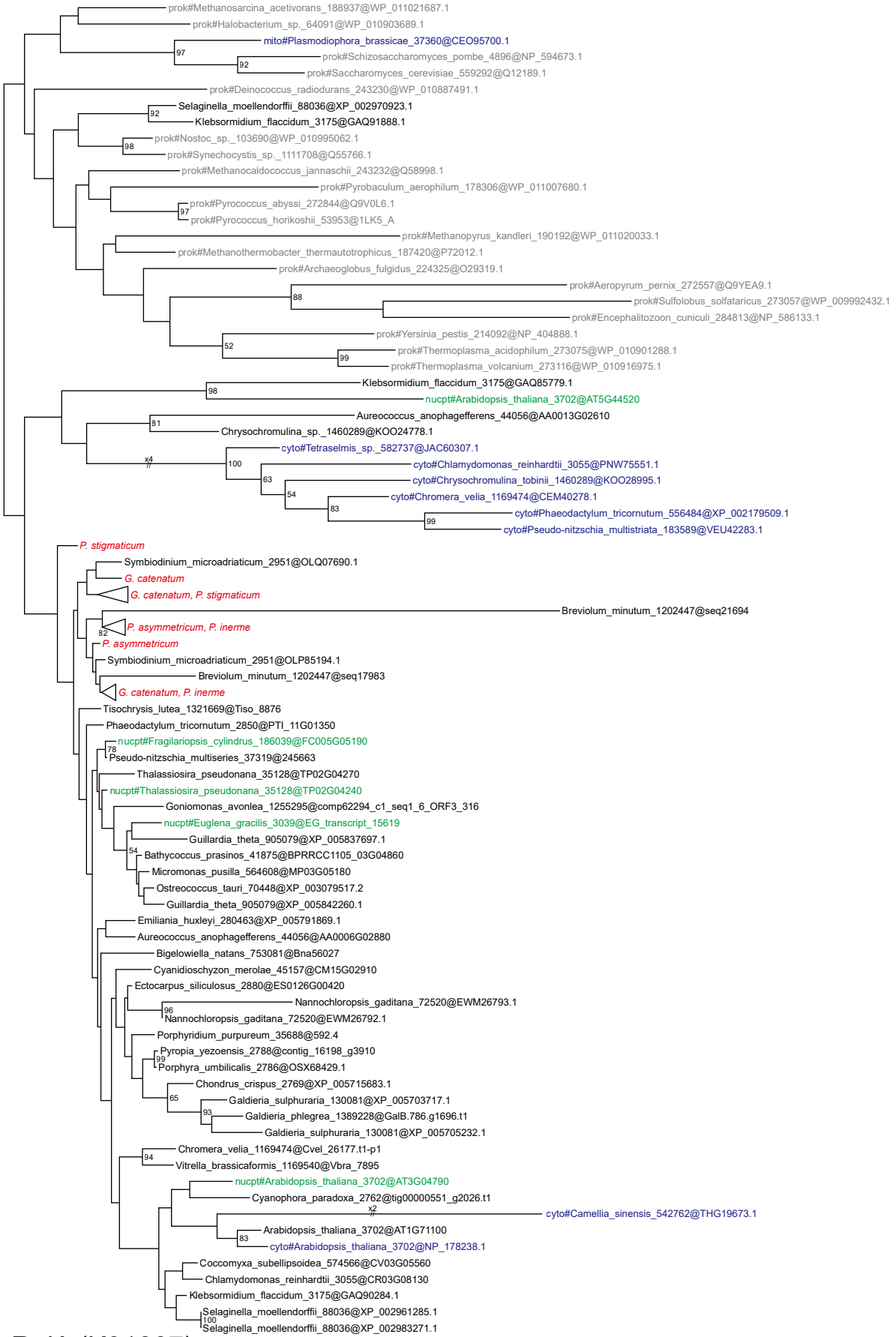
prok#Methanosarcina_acetivorans_188937@WP_011021687.1
prok#Halobacterium_sp._64091@WP_010903689.1
mito#Plasmodiophora_brassicae_37360@CEO95700.1
97
prok#Schizosaccharomyces_pombe_4896@NP_594673.1
92
prok#Saccharomyces_cerevisiae_559292@Q12189.1
prok#Deinococcus_radiodurans_243230@WP_010887491.1
Selaginella_moellendorffii_88036@XP_002970923.1
92
Klebsormidium_flaccidum_3175@GAQ91888.1
prok#Nostoc_sp._103690@WP_010995062.1
98
prok#Synechocystis_sp._1111708@Q55766.1
prok#Methanocaldococcus_jannaschii_243232@Q58998.1
prok#Pyrobaculum_aerophilum_178306@WP_011007680.1
prok#Pyrococcus_abyssi_272844@Q9V0L6.1
97
prok#Pyrococcus_horikoshii_53953@1LK5_A
prok#Methanopyrus_kandleri_190192@WP_011020033.1
prok#Methanothermobacter_thermautotrophicus_187420@P72012.1
prok#Archaeoglobus_fulgidus_224325@O29319.1
prok#Aeropyrum_pernix_272557@Q9YEA9.1
88
prok#Sulfolobus_solfataricus_273057@WP_009992432.1
prok#Encephalitozoon_cuniculi_284813@NP_586133.1
prok#Yersinia_pestis_214092@NP_404888.1
52
prok#Thermoplasma_acidophilum_273075@WP_010901288.1
99
prok#Thermoplasma_volcanium_273116@WP_010916975.1
Klebsormidium_flaccidum_3175@GAQ85779.1
98
nucpt#Arabidopsis_thaliana_3702@AT5G44520
Aureococcus_anophagefferens_44056@AA0013G02610
81
Chrysochromulina_sp._1460289@KOO24778.1
cyto#Tetraselmis_sp._582737@JAC60307.1
x4
100
cyto#Chlamydomonas_reinhardtii_3055@PNW75551.1
63
cyto#Chrysochromulina_tobinii_1460289@KOO28995.1
54
cyto#Chromera_velia_1169474@CEM40278.1
83
cyto#Phaeodactylum_tricornutum_556484@XP_002179509.1
99
cyto#Pseudo-nitzschia_multistriata_183589@VEU42283.1
P. stigmaticum
Symbiodinium_microadriaticum_2951@OLQ07690.1
G. catenatum
G. catenatum, P. stigmaticum
Breviolum_minutum_1202447@seq21694
92
P. asymmetricum, P. inerme
P. asymmetricum
Symbiodinium_microadriaticum_2951@OLP85194.1
Breviolum_minutum_1202447@seq17983
G. catenatum, P. inerme
Tisochrysis_lutea_1321669@Tiso_8876
Phaeodactylum_tricornutum_2850@PTI_11G01350
nucpt#Fragilariopsis_cylindrus_186039@FC005G05190
78
Pseudo-nitzschia_multiseries_37319@245663
Thalassiosira_pseudonana_35128@TP02G04270
nucpt#Thalassiosira_pseudonana_35128@TP02G04240
Goniomonas_avonlea_1255295@comp62294_c1_seq1_6_ORF3_316
nucpt#Euglena_gracilis_3039@EG_transcript_15619
Guillardia_theta_905079@XP_005837697.1
54
Bathycoccus_prasinos_41875@BPRRCC1105_03G04860
Micromonas_pusilla_564608@MP03G05180
Ostreococcus_tauri_70448@XP_003079517.2
Guillardia_theta_905079@XP_005842260.1
Emiliania_huxleyi_280463@XP_005791869.1
Aureococcus_anophagefferens_44056@AA0006G02880
Bigelowiella_natans_753081@Bna56027
Cyanidioschyzon_merolae_45157@CM15G02910
Ectocarpus_siliculosus_2880@ES0126G00420
Nannochloropsis_gaditana_72520@EWM26793.1
96
Nannochloropsis_gaditana_72520@EWM26792.1
Porphyridium_purpureum_35688@592.4
Pyropia_yezoensis_2788@contig_16198_g3910
99
Porphyra_umbilicalis_2786@OSX68429.1
Chondrus_crispus_2769@XP_005715683.1
65
Galdieria_sulphuraria_130081@XP_005703717.1
93
Galdieria_phlegrea_1389228@GalB.786.g1696.t1
Galdieria_sulphuraria_130081@XP_005705232.1
Chromera_velia_1169474@Cvel_26177.t1-p1
94
Vitrella_brassicaformis_1169540@Vbra_7895
nucpt#Arabidopsis_thaliana_3702@AT3G04790
Cyanophora_paradoxa_2762@tig00000551_g2026.t1
x2
cyto#Camellia_sinensis_542762@THG19673.1
Arabidopsis_thaliana_3702@AT1G71100
83
cyto#Arabidopsis_thaliana_3702@NP_178238.1
Coccomyxa_subellipsoidea_574566@CV03G05560
Chlamydomonas_reinhardtii_3055@CR03G08130
Klebsormidium_flaccidum_3175@GAQ90284.1
Selaginella_moellendorffii_88036@XP_002961285.1
100
Selaginella_moellendorffii_88036@XP_002983271.1
RpiA (K01807)
0.6

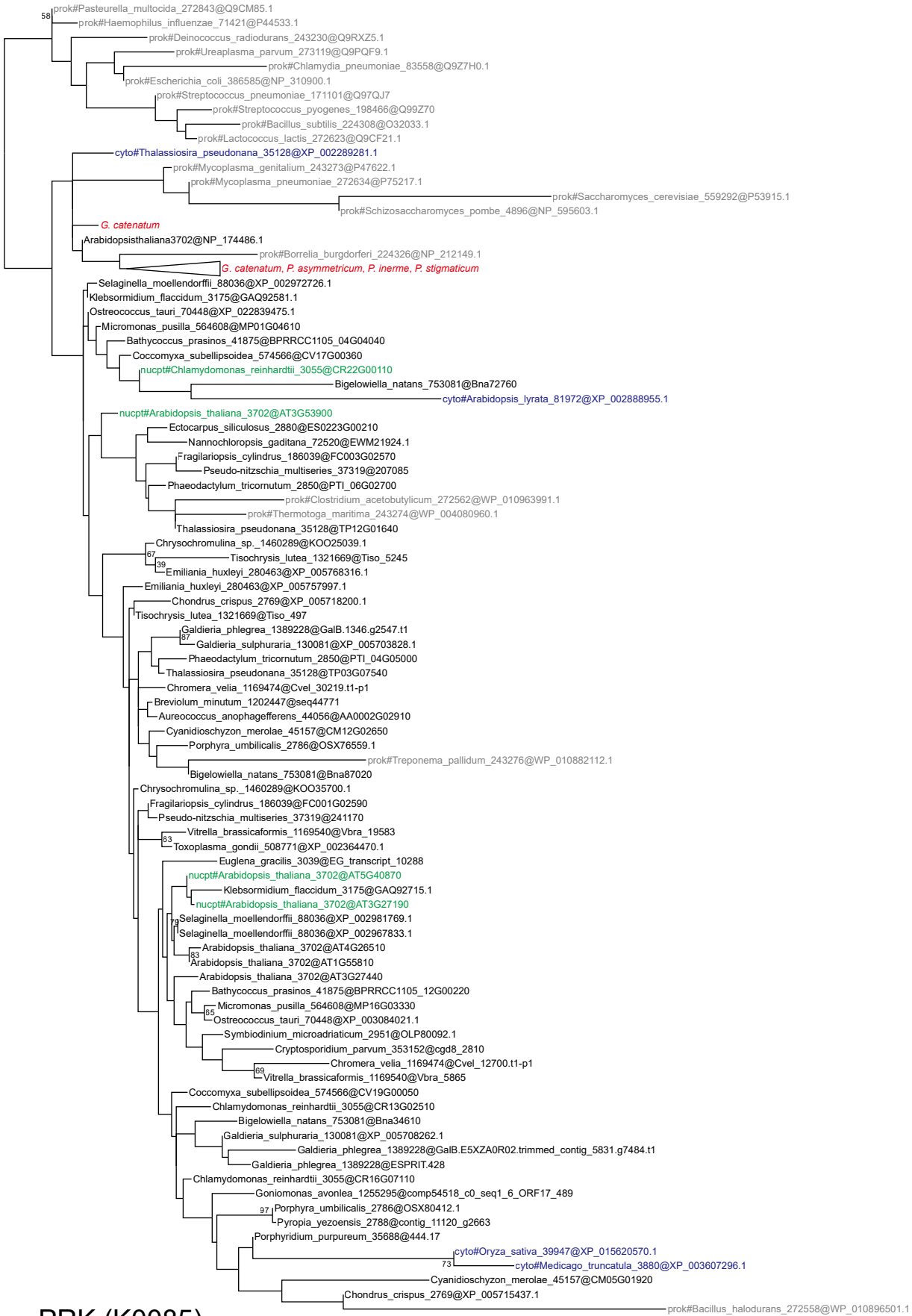
prok#Pasteurella_multocida_272843@Q9CM85.1
58
prok#Haemophilus_influenzae_71421@P44533.1
prok#Deinococcus_radiodurans_243230@Q9RXZ5.1
prok#Ureaplasma_parvum_273119@Q9PQF9.1
prok#Chlamydia_pneumoniae_83558@Q9Z7H0.1
prok#Escherichia_coli_386585@NP_310900.1
prok#Streptococcus_pneumoniae_171101@Q97QJ7
prok#Streptococcus_pyogenes_198466@Q99Z70
prok#Bacillus_subtilis_224308@O32033.1
prok#Lactococcus_lactis_272623@Q9CF21.1
cyto#Thalassiosira_pseudonana_35128@XP_002289281.1
prok#Mycoplasma_genitalium_243273@P47622.1
prok#Mycoplasma_pneumoniae_272634@P75217.1
prok#Saccharomyces_cerevisiae_559292@P53915.1
prok#Schizosaccharomyces_pombe_4896@NP_595603.1
G. catenatum
Arabidopsisthaliana3702@NP_174486.1
prok#Borrelia_burgdorferi_224326@NP_212149.1
G. catenatum, P. asymmetricum, P. inerme, P. stigmaticum
Selaginella_moellendorffii_88036@XP_002972726.1
Klebsormidium_flaccidum_3175@GAQ92581.1
Ostreococcus_tauri_70448@XP_022839475.1
Micromonas_pusilla_564608@MP01G04610
Bathycoccus_prasinos_41875@BPRRCC1105_04G04040
Coccomyxa_subellipsoidea_574566@CV17G00360
nucpt#Chlamydomonas_reinhardtii_3055@CR22G00110
Bigelowiella_natans_753081@Bna72760
cyto#Arabidopsis_lyrata_81972@XP_002888955.1
nucpt#Arabidopsis_thaliana_3702@AT3G53900
Ectocarpus_siliculosus_2880@ES0223G00210
Nannochloropsis_gaditana_72520@EWM21924.1
Fragilariopsis_cylindrus_186039@FC003G02570
Pseudo-nitzschia_multiseries_37319@207085
Phaeodactylum_tricornutum_2850@PTI_06G02700
prok#Clostridium_acetobutylicum_272562@WP_010963991.1
prok#Thermotoga_maritima_243274@WP_004080960.1
Thalassiosira_pseudonana_35128@TP12G01640
Chrysochromulina_sp._1460289@KOO25039.1
67
Tisochrysis_lutea_1321669@Tiso_5245
39
Emiliania_huxleyi_280463@XP_005768316.1
Emiliania_huxleyi_280463@XP_005757997.1
Chondrus_crispus_2769@XP_005718200.1
Tisochrysis_lutea_1321669@Tiso_497
Galdieria_phlegrea_1389228@GalB.1346.g2547.t1
87
Galdieria_sulphuraria_130081@XP_005703828.1
Phaeodactylum_tricornutum_2850@PTI_04G05000
Thalassiosira_pseudonana_35128@TP03G07540
Chromera_velia_1169474@Cvel_30219.t1-p1
Breviolum_minutum_1202447@seq44771
Aureococcus_anophagefferens_44056@AA0002G02910
Cyanidioschyzon_merolae_45157@CM12G02650
Porphyra_umbilicalis_2786@OSX76559.1
prok#Treponema_pallidum_243276@WP_010882112.1
Bigelowiella_natans_753081@Bna87020
Chrysochromulina_sp._1460289@KOO35700.1
Fragilariopsis_cylindrus_186039@FC001G02590
Pseudo-nitzschia_multiseries_37319@241170
Vitrella_brassicaformis_1169540@Vbra_19583
83
Toxoplasma_gondii_508771@XP_002364470.1
Euglena_gracilis_3039@EG_transcript_10288
nucpt#Arabidopsis_thaliana_3702@AT5G40870
Klebsormidium_flaccidum_3175@GAQ92715.1
nucpt#Arabidopsis_thaliana_3702@AT3G27190
Selaginella_moellendorffii_88036@XP_002981769.1
78
Selaginella_moellendorffii_88036@XP_002967833.1
Arabidopsis_thaliana_3702@AT4G26510
83
Arabidopsis_thaliana_3702@AT1G55810
Arabidopsis_thaliana_3702@AT3G27440
Bathycoccus_prasinos_41875@BPRRCC1105_12G00220
Micromonas_pusilla_564608@MP16G03330
65
Ostreococcus_tauri_70448@XP_003084021.1
Symbiodinium_microadriaticum_2951@OLP80092.1
Cryptosporidium_parvum_353152@cgd8_2810
Chromera_velia_1169474@Cvel_12700.t1-p1
69
Vitrella_brassicaformis_1169540@Vbra_5865
Coccomyxa_subellipsoidea_574566@CV19G00050
Chlamydomonas_reinhardtii_3055@CR13G02510
Bigelowiella_natans_753081@Bna34610
Galdieria_sulphuraria_130081@XP_005708262.1
Galdieria_phlegrea_1389228@GalB.E5XZA0R02.trimmed_contig_5831.g7484.t1
Galdieria_phlegrea_1389228@ESPRIT.428
Chlamydomonas_reinhardtii_3055@CR16G07110
Goniomonas_avonlea_1255295@comp54518_c0_seq1_6_ORF17_489
97
Porphyra_umbilicalis_2786@OSX80412.1
Pyropia_yezoensis_2788@contig_11120_g2663
Porphyridium_purpureum_35688@444.17
cyto#Oryza_sativa_39947@XP_015620570.1
73
cyto#Medicago_truncatula_3880@XP_003607296.1
Cyanidioschyzon_merolae_45157@CM05G01920
Chondrus_crispus_2769@XP_005715437.1
prok#Bacillus_halodurans_272558@WP_010896501.1
PRK (K0085)
0.6


prok#Campylobacter_jejuni_192222@NP_282542.1
prok#Helicobacter_pylori_85963@Q9ZMN8.1
prok#Helicobacter_pylori_85962@P56076.1
prok#Thermoplasma_volcanium_273116@Q978V5.2
prok#Saccharolobus_solfataricus_273057@Q97VM8.1
prok#Methanopyrus_kandleri_190192@Q8TUT9.1
prok#Aeropyrum_pernix_272557@NP_148008.1
prok#Pyrobaculum_aerophilum_178306@Q8ZXZ8.1
prok#Halobacterium_salinarum_64091@Q9HQS4.1
prok#Pyrococcus_abyssi_272844@Q9UXX2.1
prok#Pyrococcus_horikoshii_53953@O59536.1
prok#Methanocaldococcus_jannaschii_243232@Q58923.1
prok#Archaeoglobus_fulgidus_224325@O28965.1
prok#Methanosarcina_acetivorans_188937@Q8THB0.1
prok#Methanothermobacter_thermautotrophicus_187420@O27120.1
prok#Thermotoga_maritima_2336@1B9B_B
Cyanophora_paradoxa_2762@tig00021070_g17938.t1
prok#Sinorhizobium_meliloti_266834@WP_010969784.1
prok#Mesorhizobium_loti_266835@WP_010914724.1
prok#Pasteurella_multocida_272843@WP_005724499.1
prok#Listeria_innocua_272626@WP_010990359.1
Thalassiosira_pseudonana_35128@TP07G06060
Pseudo-nitzschia_multiseries_37319@298789
Pseudo-nitzschia_multiseries_37319@68149
Fragilariopsis_cylindrus_186039@FC013G01160
Bigelowiella_natans_753081@Bna80758
nucpt#Thalassiosira_pseudonana_35128@TP06G02010
Phaeodactylum_tricornutum_2850@PTI_02G05100
Phaeodactylum_tricornutum_2850@PTI_02G03430
Fragilariopsis_cylindrus_186039@FC007G04910
nucpt#Pseudo-nitzschia_multiseries_37319@211159
Micromonas_pusilla_564608@MP03G08710
Ostreococcus_tauri_70448@XP_022840169.1
Bathycoccus_prasinos_41875@BPRRCC1105_02G05760
Emiliania_huxleyi_280463@XP_005759977.1
nucpt#Ectocarpus_siliculosus_2880@ES0238G00220
nucpt#Guillardia_theta_905079@XP_005818343.1
Guillardia_theta_905079@XP_005823710.1
Aureococcus_anophagefferens_44056@AA0001G01280
Aureococcus_anophagefferens_44056@AA0017G00470
Aureococcus_anophagefferens_44056@AA0006G00830
Thalassiosira_pseudonana_35128@TP10G03660
Pseudo-nitzschia_multiseries_37319@199058
Fragilariopsis_cylindrus_186039@FC008G00530
Breviolum_minutum_1202447@seq33461
Symbiodinium_microadriaticum_2951@OLQ00030.1
Chromera_velia_1169474@Cvel_26393.t1-p1
P. inerme
P. asymmetricum
G. catenatum
P. inerme
P. asymmetricum
Fragilariopsis_cylindrus_186039@FC007G09310
G. catenatum, P. inerme
Chromera_velia_1169474@Cvel_17569.t1-p1
Vitrella_brassicaformis_1169540@Vbra_16848
G. catenatum
Breviolum_minutum_1202447@seq21246
Breviolum_minutum_1202447@seq26337
Symbiodinium_microadriaticum_2951@OLP84917.1
Breviolum_minutum_1202447@seq18552
Breviolum_minutum_1202447@seq12471
Nannochloropsis_gaditana_72520@EWM26658.1
Vitrella_brassicaformis_1169540@Vbra_15673
Chromera_velia_1169474@Cvel_11213.t1-p1
Aureococcus_anophagefferens_44056@AA0023G00520
Aureococcus_anophagefferens_44056@AA0097G00010
Thalassiosira_pseudonana_35128@TP18G01290
Phaeodactylum_tricornutum_2850@PTI_13G02410
Pseudo-nitzschia_multiseries_37319@247019
Fragilariopsis_cylindrus_186039@FC002G10470
cyto#Chlorella_variabilis_554065@XP_005845877.1
Coccomyxa_subellipsoidea_574566@CV16G02250
Toxoplasma_gondii_508771@XP_002368209.1
Ectocarpus_siliculosus_2880@ES0398G00040
Guillardia_theta_905079@XP_005836057.1
Breviolum_minutum_1202447@seq31110
Symbiodinium_microadriaticum_2951@OLQ09399.1
Symbiodinium_microadriaticum_2951@OLQ11317.1
Aureococcus_anophagefferens_44056@AA0010G01220
Chrysochromulina_sp._1460289@KOO28550.1
Emiliania_huxleyi_280463@XP_005760841.1
Emiliania_huxleyi_280463@XP_005758706.1
Chrysochromulina_sp._1460289@KOO35577.1
Chrysochromulina_sp._1460289@KOO22251.1
Tisochrysis_lutea_1321669@Tiso_10777
G. catenatum, P. asymmetricum, P. inerme, P. stigmaticum
Porphyra_umbilicalis_2786@OSX70626.1
Porphyridium_purpureum_35688@462.12
Chondrus_crispus_2769@XP_005718997.1
Bigelowiella_natans_753081@Bna87329
Bigelowiella_natans_753081@Bna22258
Galdieria_sulphuraria_130081@XP_005706061.1
Galdieria_phlegrea_1389228@GalB.1823.g3232.t1
Euglena_gracilis_3039@EG_transcript_14120
Euglena_gracilis_3039@EG_transcript_30563
Euglena_gracilis_3039@EG_transcript_30456
Galdieria_phlegrea_1389228@ESPRIT.86
Chondrus_crispus_2769@XP_005716285.1
Porphyra_umbilicalis_2786@OSX73519.1
Pyropia_yezoensis_2788@contig_41843_g9507
Cyanidioschyzon_merolae_45157@CM17G01720
Porphyridium_purpureum_35688@2306.3
Euglena_gracilis_3039@EG_transcript_44253
Euglena_gracilis_3039@EG_transcript_18179
Selaginella_moellendorffii_88036@XP_002986327.1
nucpt#Zea_mays_4577@NP_001131642.2
nucpt#Nicotiana_attenuata_49451@XP_019235731.1
nucpt#Nelumbo_nucifera_4432@XP_010268151.1
nucpt#Juglans_regia_51240@XP_018823791.1
nucpt#Vigna_radiata_3916@XP_014496394.1
nucpt#Cicer_arietinum_3827@XP_004494086.1
nucpt#Arabidopsis_thaliana_3702@AT2G21170
Micromonas_pusilla_564608@MP08G00150
Bathycoccus_prasinos_41875@BPRRCC1105_12G01650
nucpt#Chlorella_variabilis_554065@XP_005846199.1
Coccomyxa_subellipsoidea_574566@CV03G06060
Chlamydomonas_reinhardtii_3055@CR01G06070
P. inerme
Breviolum_minutum_1202447@seq23861
P. asymmetricum, P. inerme, P. stigmaticum
Micromonas_pusilla_564608@MP03G00180
Bathycoccus_prasinos_41875@BPRRCC1105_10G04160
Ostreococcus_tauri_70448@XP_022839536.1
Klebsormidium_flaccidum_3175@GAQ81213.1
Klebsormidium_flaccidum_3175@GAQ81916.1
cyto#Zea_mays_4577@NP_001140424.1
Selaginella_moellendorffii_88036@XP_002960386.1
Arabidopsis_thaliana_3702@AT3G55440
cyto#Cicer_arietinum_3827@XP_004487007.1
cyto#Vigna_radiata_3916@XP_014498236.1
cyto#Nelumbo_nucifera_4432@XP_010256927.1
cyto#Nicotiana_attenuata_49451@XP_019232908.1
cyto#Juglans_regia_51240@XP_018823301.1
0.4

TPI (K01803)

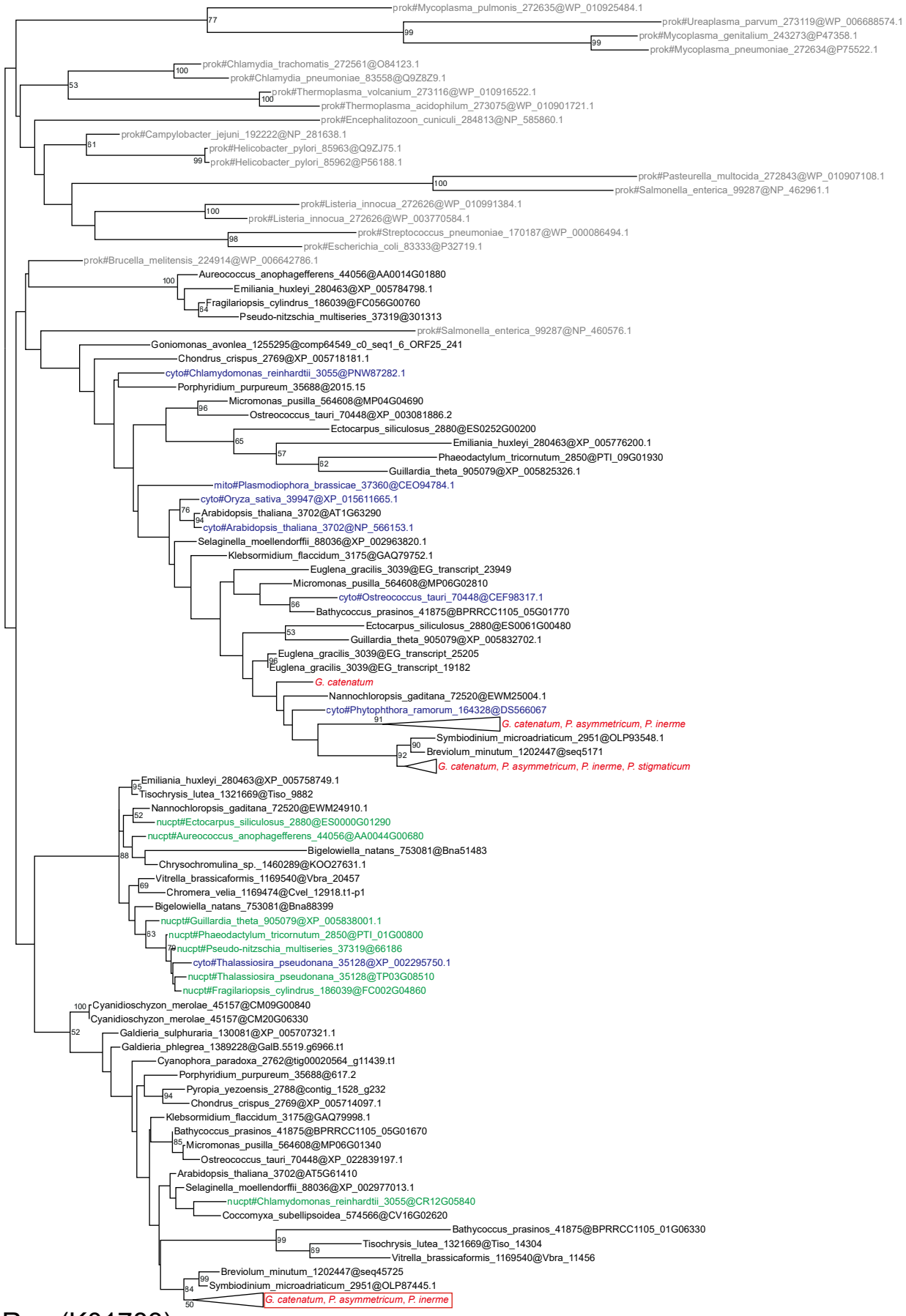
prok#Mycoplasma_pulmonis_272635@WP_010925484.1
prok#Ureaplasma_parvum_273119@WP_006688574.1
prok#Mycoplasma_genitalium_243273@P47358.1
prok#Mycoplasma_pneumoniae_272634@P75522.1
prok#Chlamydia_trachomatis_272561@O84123.1
prok#Chlamydia_pneumoniae_83558@Q9Z8Z9.1
prok#Thermoplasma_volcanium_273116@WP_010916522.1
prok#Thermoplasma_acidophilum_273075@WP_010901721.1
prok#Encephalitozoon_cuniculi_284813@NP_585860.1
prok#Campylobacter_jejuni_192222@NP_281638.1
prok#Helicobacter_pylori_85963@Q9ZJ75.1
prok#Helicobacter_pylori_85962@P56188.1
prok#Pasteurella_multocida_272843@WP_010907108.1
prok#Salmonella_enterica_99287@NP_462961.1
prok#Listeria_innocua_272626@WP_010991384.1
prok#Listeria_innocua_272626@WP_003770584.1
prok#Streptococcus_pneumoniae_170187@WP_000086494.1
prok#Escherichia_coli_83333@P32719.1
prok#Brucella_melitensis_224914@WP_006642786.1
Aureococcus_anophagefferens_44056@AA0014G01880
Emiliania_huxleyi_280463@XP_005784798.1
Fragilariopsis_cylindrus_186039@FC056G00760
Pseudo-nitzschia_multiseries_37319@301313
prok#Salmonella_enterica_99287@NP_460576.1
Goniomonas_avonlea_1255295@comp64549_c0_seq1_6_ORF25_241
Chondrus_crispus_2769@XP_005718181.1
cyto#Chlamydomonas_reinhardtii_3055@PNW87282.1
Porphyridium_purpureum_35688@2015.15
Micromonas_pusilla_564608@MP04G04690
Ostreococcus_tauri_70448@XP_003081886.2
Ectocarpus_siliculosus_2880@ES0252G00200
Emiliania_huxleyi_280463@XP_005776200.1
Phaeodactylum_tricornutum_2850@PTI_09G01930
Guillardia_theta_905079@XP_005825326.1
mito#Plasmodiophora_brassicae_37360@CEO94784.1
cyto#Oryza_sativa_39947@XP_015611665.1
Arabidopsis_thaliana_3702@AT1G63290
cyto#Arabidopsis_thaliana_3702@NP_566153.1
Selaginella_moellendorffii_88036@XP_002963820.1
Klebsormidium_flaccidum_3175@GAQ79752.1
Euglena_gracilis_3039@EG_transcript_23949
Micromonas_pusilla_564608@MP06G02810
cyto#Ostreococcus_tauri_70448@CEF98317.1
Bathycoccus_prasinos_41875@BPRRCC1105_05G01770
Ectocarpus_siliculosus_2880@ES0061G00480
Guillardia_theta_905079@XP_005832702.1
Euglena_gracilis_3039@EG_transcript_25205
Euglena_gracilis_3039@EG_transcript_19182
G. catenatum
Nannochloropsis_gaditana_72520@EWM25004.1
cyto#Phytophthora_ramorum_164328@DS566067
G. catenatum, P. asymmetricum, P. inerme
Symbiodinium_microadriaticum_2951@OLP93548.1
Breviolum_minutum_1202447@seq5171
G. catenatum, P. asymmetricum, P. inerme, P. stigmaticum
Emiliania_huxleyi_280463@XP_005758749.1
Tisochrysis_lutea_1321669@Tiso_9882
Nannochloropsis_gaditana_72520@EWM24910.1
nucpt#Ectocarpus_siliculosus_2880@ES0000G01290
nucpt#Aureococcus_anophagefferens_44056@AA0044G00680
Bigelowiella_natans_753081@Bna51483
Chrysochromulina_sp._1460289@KOO27631.1
Vitrella_brassicaformis_1169540@Vbra_20457
Chromera_velia_1169474@Cvel_12918.t1-p1
Bigelowiella_natans_753081@Bna88399
nucpt#Guillardia_theta_905079@XP_005838001.1
nucpt#Phaeodactylum_tricornutum_2850@PTI_01G00800
nucpt#Pseudo-nitzschia_multiseries_37319@66186
cyto#Thalassiosira_pseudonana_35128@XP_002295750.1
nucpt#Thalassiosira_pseudonana_35128@TP03G08510
nucpt#Fragilariopsis_cylindrus_186039@FC002G04860
Cyanidioschyzon_merolae_45157@CM09G00840
Cyanidioschyzon_merolae_45157@CM20G06330
Galdieria_sulphuraria_130081@XP_005707321.1
Galdieria_phlegrea_1389228@GalB.5519.g6966.t1
Cyanophora_paradoxa_2762@tig00020564_g11439.t1
Porphyridium_purpureum_35688@617.2
Pyropia_yezoensis_2788@contig_1528_g232
Chondrus_crispus_2769@XP_005714097.1
Klebsormidium_flaccidum_3175@GAQ79998.1
Bathycoccus_prasinos_41875@BPRRCC1105_05G01670
Micromonas_pusilla_564608@MP06G01340
Ostreococcus_tauri_70448@XP_022839197.1
Arabidopsis_thaliana_3702@AT5G61410
Selaginella_moellendorffii_88036@XP_002977013.1
nucpt#Chlamydomonas_reinhardtii_3055@CR12G05840
Coccomyxa_subellipsoidea_574566@CV16G02620
Bathycoccus_prasinos_41875@BPRRCC1105_01G06330
Tisochrysis_lutea_1321669@Tiso_14304
Vitrella_brassicaformis_1169540@Vbra_11456
Breviolum_minutum_1202447@seq45725
Symbiodinium_microadriaticum_2951@OLP87445.1
G. catenatum, P. asymmetricum, P. inerme
Rpe (K01783)
0.4

DISCUSSION

Paragymnodinium stigmaticum showed a significant lack of expressions for PSII and its antenna proteins (Psb and LHCB). It has been shown that *P. stigmaticum* gains all or most of part of nutrients by ingestion of prey in spite of the possession of chloroplasts (Chapter 3). The function of PSII and the carbon fixation in *P. stigmaticum* have also been revealed to be inactive (Chapter 3). The content ratio of peridinin, which is an accessory pigment of chlorophyll *a* to support the PSII activity, has also been shown to be lower than that in the other photosynthetic relatives (Chapter 3). These results are consistent to the reduced expression of the proteins of PSII in *P. stigmaticum*. The detection of a mRNA for PsbO protein, which enhances the oxygen evolving function by PSII (Bricker et al. 2012), and for LHCB5 protein indicates a possibility that some genes for the PSII might still remain in the nuclear genome.

Current data is not enough to determine whether the PSII supercomplexes are completely lost or partly remained in *Paragymnodinium stigmaticum*. However, the ultrastructure of chloroplasts in *P. stigmaticum* shown in chapter 2 might indicate an extreme reduction of PSII complexes and its LHC proteins. Whereas typical peridinin-type chloroplasts in dinoflagellates contain triple-stacking thylakoids (Dodge 1987), *P. stigmaticum* and *P. verecundum* represent a rare exception with unstacked (or separated) thylakoids (Chapter 2). It is notable that previous researches of land plants revealed that LHC proteins play an essential role for thylakoid stacking or grana formation (Standfuss et al. 2005, Kim et al. 2009, Tanaka and Tanaka 2011). This fact leads an idea that both of the reduction of photosynthetic nutrition and the collapse of thylakoid stacking might be caused by the mutation or disappearance of the PSII supercomplex. This hypothesis must be evaluated by a confirmation of existence of the PSII supercomplex by further experiments. In addition, if any other novel eukaryotes with separated thylakoids were found, it would help understanding the reductive evolution of photosynthesis, PSII and thylakoid formation.

Interestingly, *Paragymnodinium stigmaticum* was shown to express the mRNAs of F-type ATPase (ATPF), cytochrome b6/f complex, photosynthetic electron transport (Pet) and PSI (Psa and LHCA) at the same level to other three photosynthetic species, *P. asymmetricum*, *P. inerme* and *Gymnodinium catenatum*. Photosynthetic reactions are

driven by a combination of all of the mechanisms; thus, generally, the genes for photosynthesis (especially *psa* and *psb* genes) are supposed to be reduced simultaneously at the early step of loss of autotrophy (Barrett et al. 2014, Graham et al. 2017, Hadariová et al. 2018). An exception has been reported in members of nitrogen-fixing cyanobacterium called UCYN-A, which lack genes for PSII and retains PSI intactly (Zehr et al. 2008) It is hypothesized that UCYN-A might use H_2 and organic carbon, instead of water, as electron donors for PSI (Tripp et al. 2010). Heterocysts of nitrogen-fixing cyanobacterium have also been suggested to lack PSII complexes (Haselkorn 1978). However, no such an example exists in eukaryotes in my knowledge. Therefore, the repertoire of expressed mRNAs in *P. stigmaticum* represents a quite rare case showing the transitional way of loss of photosynthetic capability. It is unclear how the remaining mechanisms for photosynthesis function under the inactivated PSII, although it is possible that they drive in the similar way to that of nitrogen-fixing cyanobacterium stated above. The detailed status of these photosynthetic apparatuses might be revealed by further proteomic or physiological analyses.

There are also some other differences in the expression between *Paragymnodinium stigmaticum* and other three photosynthetic species. One of the most remarkable differences is observed in the expression of RbcL comprising RuBisCO. It is the most essential protein for carbon fixation, combining ribulose 1,5-bisphosphate with CO_2 and resulting in two molecules of 3-phosphoglycerate. It is known that dinoflagellates adopt nuclear-encoding chloroplast-targeting form II RuBisCO, which is basically restricted to certain proteobacteria, unlike the other phototrophic eukaryotes possessing form I (Morse et al. 1995). The result of transcriptomic and phylogenetic analyses supports that *P. asymmetricum*, *P. inerme* and *Gymnodinium catenatum* express RbcL comprising form II RuBisCO as expected. On the other hand, the mRNA of RbcL is shown to be absent in *P. stigmaticum*, in spite of the presence of most of other components for Calvin cycle. This result is not contradicted to the fact that *P. stigmaticum* fixes no carbon (Chapter 3). The reduced carbon fixation might be caused by the down-regulation or disappearance of RbcL expression. Previous studies have reported various patterns of status of the gene of RbcL in non-photosynthetic organisms. For example, some non-photosynthetic taxa including dinoflagellate possess an intact gene of RbcL in

the genome and actively transcribe it (Delavault et al. 1995, Sanchez-Puerta et al. 2007), whereas in other organisms the gene of RbcL is highly divergent or lost (Záhonová et al. 2016, Kamikawa et al. 2017, Kayama et al. 2020). Although the reduced expression of RbcL in *P. stigmaticum* is revealed by this study, it is possible that the gene of RbcL retains in its genome. Further specific analysis based on PCR, for example, is needed to confirm the property of this gene.

Another notable feature of *Paragymnodinium stigmaticum* is seen in the chlorophyll and carotenoid biosynthesis pathways. *P. stigmaticum* does not express ChlM, ChlG, HCAR and CrtB, which are expressed in other three dinoflagellates. Especially, the absence of the chlorophyll *a* synthase (ChlG) and phytoene synthase (CrtB) does not consist to the fact that *P. stigmaticum* contains a significant amount of chlorophyll *a* and other carotenoids under the same condition to that for RNA extraction, revealed by the pigment analysis in chapter 3. Considering that the RNA was extracted from the cells under single unified condition (starved motile cells under light condition), it is still possible that these proteins are expressed in other conditions or situations. To determine the presence and function of each gene, further analyses of transcriptomes from the cells under various conditions or specific PCR analyses are needed.

Paragymnodinium stigmaticum showed the almost same level of mRNA expression to other photosynthetic dinoflagellates for the proteins of heme and non-mevalonate IPP biosynthesis, which are predicted to be chloroplast-targeting (Cornah et al. 2003, Oborník and Green 2005, Bentlage et al. 2016). These pathways tend to be retained even in highly reduced chloroplasts, including colorless chloroplasts in heterotrophic dinoflagellates or apicoplasts in apicomplexan parasites (Foth and McFadden 2003, Sanchez-Puerta et al. 2007, Slamovits and Keeling 2008, Maciszewski and Karnkowska 2019). Currently, many lines of evidence support the hypothesis that *P. stigmaticum* is at the earlier step of loss of chloroplasts than such colorless dinoflagellates and apicomplexans. The completely remained heme and IPP synthesis pathways of *P. stigmaticum* are reasonable considering its predicted evolutionary phase.

Paragymnodinium asymmetricum and *P. inerme* resulted in almost same repertoires of expressed mRNAs to the typical photosynthetic dinoflagellate, *Gymnodinium catenatum*. They are photosynthetic organisms (Chapter 3), so it is

consistent that they express the mRNAs for chloroplast- or photosynthesis-related proteins at the same level. Only one minor difference between the two *Paragymnodinium* spp. and *G. catenatum* is observed in the proteins for PSII. *Paragymnodinium asymmetricum* and *P. inerme* expressed PsbA and PsbD, which were not detected from *G. catenatum*. Within the detected transcripts, PsaA, B, PsbA, B, C, D, PetB and ATPF0A are known to encoded in plastid genome as minicircle genes in other dinoflagellates (Howe et al. 2008b, Barbrook et al. 2014, Mungpakdee et al. 2014). These proteins were not expected to be detected by the procedure used in this study because the nuclear-encoded transcriptome was sorted based on the poly-A sequences, which is not attached to the minicircle-encoded transcripts. It is possible that the massive expression of these genes might cause accidental detections. There are also some proteins which are predicted nuclear-encoded but not detected in this study, that is, ATPF1B, PetN, PsaJ, PsbJ and M proteins (Mungpakdee et al. 2014). It might be able to hypothesized that the repertoires of nuclear- and minicircle-encoded genes for photosynthesis in the investigated species are different from that of others, considering that any dinoflagellates with available minicircle-gene list are not phylogenetically close to *Gymnodinium* or *Paragymnodinium* (Barbrook et al. 2014). However, this idea must carefully be evaluated by further genomic-scaled investigations. Based on the current data, it is more reasonable to think that the low amount or absence of transcripts have affected the successful detection of these proteins.

CONCLUSION

This study described four new dinoflagellates belonging to the genus *Paragymnodinium*, showing various nutritional strategies. The comparative investigation of the phototrophic species (*P. asymmetricum* and *P. inerme*) and phagotrophic species (*P. stigmaticum*) showed that *P. stigmaticum* exhibited a lot of distinctive features in its physiological and genetic properties. The pigment analyses showed that the content ratios of peridinin and chlorophyll c_2 were lower in *P. stigmaticum* than those of other photosynthetic species. The absorption spectrum analysis revealed a red-shift in the peak of the Q_y band of chlorophyll *a* in *P. stigmaticum*, indicating a change in chlorophyll-protein complexes. The variable chlorophyll *a* fluorescence properties and carbon fixation rates indicated significantly lower photosynthetic capability of *P. stigmaticum* than those of the photosynthetic species. The transcriptomic analysis showed a significant reduction of mRNA expressions for PSII and *rbcL* gene, although the other components for photosynthesis including PSI remained. The lack of PSII supercomplex is also indicated by the collapse of triple-stacked thylakoid bands. It is concluded that such characters in *P. stigmaticum* represent the first step of reductive process of chloroplasts in dinoflagellates, which has been unknown thus far. The status of *P. stigmaticum* is consistent to the general model of the early step of chloroplast reduction, proposed by previous studies (Fig. 1.1) (Barrett et al. 2014, Graham et al. 2017, Hadariová et al. 2018, Maciszewski and Karnkowska 2019). It is notable that some features of *P. stigmaticum*, such as the absence of photosynthetic capability under the presence of pigments, and the absence of PSII under the presence of PSI, clarified what is happening at the first step of chloroplast reduction more detailly than the existing model demonstrated by other eukaryotes. These findings provided a lot of noticeable insights into the evolutionary model for the early step of the reductive evolution of chloroplasts not only in dinoflagellates but also in eukaryotes.

REFERENCES

Adl, S.M., Bass, D., Lane, C.E., Lukeš, J., Schoch, C.L., Smirnov, A., Agatha, S. et al. 2019. Revisions to the classification, nomenclature, and diversity of eukaryotes. *J. Eukaryot. Microbiol.* 66:4–119.

Archibald, J.M. 2015. Genomic perspectives on the birth and spread of plastids. *Proc. Natl. Acad. Sci. U. S. A.* 112:10147–53.

Arnaud, L., Taillandier, G., Kaouadji, M., Ravanel, P. & Tissut, M. 1994. Photosynthesis inhibition by phenylureas: A QSAR approach. *Ecotox. Environ. Safe.* 28:121–33.

Barbrook, A.C., Voolstra, C.R. & Howe, C.J. 2014. The chloroplast genome of a *symbiodinium* sp. clade C3 isolate. *Protist*. 165:1–13.

Barrett, C.F., Freudenstein, J. V., Li, J., Mayfield-Jones, D.R., Perez, L., Pires, J.C. & Santos, C. 2014. Investigating the path of plastid genome degradation in an early-transitional clade of heterotrophic orchids, and implications for heterotrophic angiosperms. *Mol. Biol. Evol.* 31:3095–112.

Bateman, A., Martin, M.-J., Orchard, S., Magrane, M., Agivetova, R., Ahmad, S., Alpi, E. et al. 2021. UniProt: the universal protein knowledgebase in 2021. *Nucleic Acids Res.* 49:D480–9.

Bayer, T., Aranda, M., Sunagawa, S., Yum, L.K., DeSalvo, M.K., Lindquist, E., Coffroth, M.A. et al. 2012. *Symbiodinium* transcriptomes: Genome insights into the dinoflagellate symbionts of reef-building corals. *PLoS One*. 7:e35269.

Bednarczyk, D., Dym, O., Prabahar, V., Peleg, Y., Pike, D.H. & Noy, D. 2016. Fine Tuning of Chlorophyll Spectra by Protein-Induced Ring Deformation. *Angew. Chemie - Int. Ed.* 55:6901–5.

Bentlage, B., Rogers, T.S., Bachvaroff, T.R. & Delwiche, C.F. 2016. Complex ancestries of isoprenoid synthesis in dinoflagellates. *J. Eukaryot. Microbiol.* 63:123–37.

Blackburn, S.I., Hallegraeff, G.M. & Bolch, C.J. 1989. Vegetative reproduction and sexual life cycle of the toxic dinoflagellate *Gymnodinium catenatum* from Tasmania, Australia. *J. Phycol.* 25:577–90.

Bradbury, P.C., Westfall, J.A. & Townsend, J.W. 1983. Ultrastructure of the dinoflagellate *Polykrikos*. II. The nucleus and its connections to the flagellar apparatus. *J. Ultrastruct. Res.* 85:24–32.

Bricker, T.M., Roose, J.L., Fagerlund, R.D., Frankel, L.K. & Eaton-Rye, J.J. 2012. The extrinsic proteins of Photosystem II. *Biochim. Biophys. Acta - Bioenerg.* 1817:121–42.

Büchel, C. & Wilhelm, C. 1993. *In vivo* analysis of slow chlorophyll fluorescence induction kinetics in algae: progress, problems and perspectives. *Phytochem. Phytobiol.* 58:137–48.

Burkholder, J.A.M., Glibert, P.M. & Skelton, H.M. 2008. Mixotrophy, a major mode of nutrition for harmful algal species in eutrophic waters. *Harmful Algae*. 8:77–93.

Castresana, J. 2000. Selection of conserved blocks from multiple alignments for their use in phylogenetic analysis. *Mol. Biol. Evol.* 17:540–52.

Christa, G., Zimorski, V., Woehle, C., Tielens, A.G.M., Wägele, H., Martin, W.F. & Gould, S.B. 2013. Plastid-bearing sea slugs fix CO_2 in the light but do not require photosynthesis to survive. *Proc. Biol. Sci. / R. Soc.* 281.

Coats, D.W. 1999. Parasitic life styles of marine dinoflagellates. *J. Eukaryot. Microbiol.* 46:402–9.

Colley, N.J. & Nilsson, D.E. 2016. Photoreception in phytoplankton. *Integr. Comp. Biol.* 56:764–75.

Cornah, J.E., Terry, M.J. & Smith, A.G. 2003. Green or red: What stops the traffic in the tetrapyrrole pathway? *Trends Plant Sci.* 8:224–30.

Cota, G.F., Smith, W.O. & Mitchell, B.G. 1994. Photosynthesis of *Phaeocystis* in the Greenland Sea. *Limnol. Oceanogr.* 39:948–53.

Craveiro, S.C., Moestrup, Ø., Daugbjerg, N. & Calado, A.J. 2010. Ultrastructure and large subunit rDNA-based phylogeny of *Sphaerodinium cracoviense*, an unusual freshwater dinoflagellate with a novel type of eyespot. *J. Eukaryot. Microbiol.* 57:568–85.

Daugbjerg, N., Hansen, G., Larsen, J. & Moestrup, Ø. 2000. Phylogeny of some of the major genera of dinoflagellates based on ultrastructure and partial LSU rDNA sequence data, including the erection of three new genera of unarmoured dinoflagellates. *Phycologia*. 39:302–17.

Delavault, P., Sakanyan, V. & Thalouarn, P. 1995. Divergent evolution of two plastid genes, *rbcL* and *atpB*, in a non-photosynthetic parasitic plant. *Plant Mol. Biol.* 29:1071–9.

Dodge, J.D. 1967. Fine structure of the dinoflagellate *Aureodinium pigmentosum* gen. et sp. nov. *Br. Phycol. Bull.* 3:327–36.

Dodge, J.D. 1972. The ultrastructure of the dinoflagellate pusule: A unique osmo-regulatory organelle. *Protoplasma*. 75:285–302.

Dodge, J.D. 1982. Marine dinoflagellates of the British Isles. Her Majesty's Stationery Office, London. 303 p.

Dodge, J.D. 1987. General ultrastructure. *In* Taylor, F. J. [Ed.] *The Biology of Dinoflagellates*. Blackwell Science, Oxford, pp. 93–119.

Dodge, J.D. & Crawford, R.M. 1971. A fine-structural survey of dinoflagellate pyrenoids and food-reserves. *Bot. J. Linn. Soc.* 64:105–15.

Dorrell, R.G., Azuma, T., Nomura, M., Audren de Kerdrel, G., Paoli, L., Yang, S., Bowler, C. et al. 2019. Principles of plastid reductive evolution illuminated by nonphotosynthetic chrysophytes. *Proc. Natl. Acad. Sci.* 116:201819976.

Edgar, R.C. 2004. MUSCLE: a multiple sequence alignment method with reduced time and space complexity. *BMC Bioinformatics*. 5:113.

Eggersdorfer, B. & Häder, D.P. 1991. Phototaxis, gravitaxis and vertical migrations in the marine dinoflagellate *Prorocentrum micans*. *FEMS Microbiol. Lett.* 85:319–26.

Fawcett, R.C. & Parrow, M.W. 2014. Mixotrophy and loss of phototrophy among geographic isolates of freshwater *Esoptrodinium*/*Bernardinium* sp. (Dinophyceae). *J. Phycol.* 50:55–70.

Foth, B.J. & McFadden, G.I. 2003. The apicoplast: A plastid in *Plasmodium falciparum* and other apicomplexan parasites. *Int. Rev. Cytol.* 224:57–110.

Gaines, G. & Elbrächter, M. 1987. Heterotrophic nutrition. *In* Taylor, F. J. R. [Ed.] *The Biology of Dinoflagellates*. Blackwell Science, Oxford, pp. 224–68.

Gavelis, G.S., Hayakawa, S., White III, R.A., Gojobori, T., Suttle, C.A., Keeling, P.J. & Leander, B.S. 2015. Eye-like ocelloids are built from different endosymbiotically acquired components. *Nature*. 523:204–7.

Gavelis, G.S., Wakeman, K.C., Tillmann, U., Ripken, C., Mitarai, S., Herranz, M., Özbek, S. et al. 2017. Microbial arms race : Ballistic “nematocysts” in dinoflagellates represent a new extreme in organelle complexity. *Sci. Adv.* 3:1–7.

Gavelis, G.S., White, R.A., Suttle, C.A., Keeling, P.J. & Leander, B.S. 2015. Single-cell transcriptomics using spliced leader PCR: Evidence for multiple losses of photosynthesis in polykrikoid dinoflagellates. *BMC Genomics*. 16:528.

Genty, B., Briantais, J.M. & Baker, N.R. 1989. The relationship between the quantum yield of photosynthetic electron transport and quenching of chlorophyll fluorescence. *Biochim. Biophys. Acta - Gen. Subj.* 990:87–92.

Gilbert, M., Domin, A., Becker, A. & Wilhelm, C. 2000. Estimation of primary production by chlorophyll a in vivo fluorescence in freshwater phytoplankton. *Photosynthetica*. 38:111–26.

Gockel, G. & Hachtel, W. 2000. Complete gene map of the plastid genome of the nonphotosynthetic Euglenoid flagellate *Astasia longa*. *Protist*. 151:347–51.

Gómez, F. 2005. A list of free-living dinoflagellate species in the world’s oceans. *Acta Bot. Croat.* 64:129–212.

Gornik, S.G., Febrimarsa, Cassin, A.M., MacRae, J.I., Ramaprasad, A., Rchiad, Z., McConville, M.J. et al. 2015. Endosymbiosis undone by stepwise elimination of the plastid in a parasitic dinoflagellate. *Proc. Natl. Acad. Sci. U. S. A.* 112:5767–72.

Grabherr, M.G., Haas, B.J., Yassour, M., Levin, J.Z., Thompson, D.A., Amit, I., Adiconis, X. et al. 2011. Full-length transcriptome assembly from RNA-Seq data without a reference genome. *Nat. Biotechnol.* 29:644–52.

Graham, S.W., Lam, V.K.Y. & Merckx, V.S.F.T. 2017. Plastomes on the edge: the evolutionary breakdown of mycoheterotroph plastid genomes. *New Phytol.* 214:48–55.

Greuet, C. 1987. Complex organelles. *In* Taylor, F. J. R. [Ed.] *The Biology of Dinoflagellates*. Blackwell Science, Oxford, pp. 119–142.

Haas, B.J., Papanicolaou, A., Yassour, M., Grabherr, M., Blood, P.D., Bowden, J., Couger, M.B. et al. 2013. *De novo* transcript sequence reconstruction from RNA-seq using the Trinity platform for reference generation and analysis. *Nat. Protoc.* 8:1494–512.

Hadariová, L., Vesteg, M., Hampl, V. & Krajčovič, J. 2018. Reductive evolution of chloroplasts in non-photosynthetic plants, algae and protists. *Curr. Genet.* 64:365–87.

Häder, D.P. 1988. New trends in photobiology. Ecological consequences of photomovement in microorganisms. *J. Photochem. Photobiol. B Biol.* 1:385–414.

Hama, T., Miyazaki, T., Ogawa, Y., Iwakuma, T., Takahashi, M., Otsuki, A. & Ichimura, S. 1983. Measurement of photosynthetic production of a marine phytoplankton population using a stable 13C isotope. *Mar. Biol.* 73:31–6.

Hansen, G. 2001. Ultrastructure of *Gymnodinium aureolum* (Dinophyceae): toward a further redefinition of *Gymnodinium sensu stricto*. *J. Phycol.* 37:612–23.

Hansen, G. & Larsen, J. 1992. Dinoflagellater i danske farvande. *In* Thomsen, H. A. [Ed.] *Plankton i de Indre Danske Farvande*. Havforskning fra Miljøstyrelsen, Copenhagen, pp. 45–155.

Hansen, G., Moestrup, Ø. & Roberts, K.R. 2000. Light and electron microscopical observations on the type species of *Gymnodinium*, *G. fuscum* (Dinophyceae). *Phycologia*. 39:365–76.

Hansen, G., Daugbjerg, N. & Henriksen, P. 2007. *Baldinia anauniensis* gen. et sp. nov.: a "new" dinoflagellate from Lake Tovel, N. Italy. *Phycologia*. 46:86–108.

Hansen, G. & Moestrup, Ø. 2005. Flagellar apparatus and nuclear chambers of the green dinoflagellate *Gymnodinium chlorophorum*. *Phycol. Res.* 53:169–81.

Hansen, P.J. 1991. Quantitative importance and trophic role of heterotrophic dinoflagellates in a coastal pelagial food web. *Mar. Ecol. Prog. Ser.* 73:253–61.

Hansen, P.J. 2011. The role of photosynthesis and food uptake for the growth of marine mixotrophic dinoflagellates. *J. Eukaryot. Microbiol.* 58:203–14.

Haselkorn, R. 1978. Heterocysts. *Annu. Rev. Plant Physiol.* 29:319–44.

Hillebrand, H., Dürselen, C.D., Kirschtel, D., Pollingher, U. & Zohary, T. 1999. Biovolume calculation for pelagic and benthic microalgae. *J. Phycol.* 35:403–24.

Hoppenrath, M. 2000. Taxonomische und ökologische Untersuchungen von Flagellaten mariner Sande. PhD thesis, Universität Hamburg, Germany. 311 p.

Hoppenrath, M. 2017. Dinoflagellate taxonomy — a review and proposal of a revised classification. *Mar. Biodivers.* 47:381–403.

Hoppenrath, M., Bachvaroff, T.R., Handy, S.M., Delwiche, C.F. & Leander, B.S. 2009. Molecular phylogeny of ocelloid-bearing dinoflagellates (Warnowiaceae) as inferred from SSU and LSU rDNA sequences. *BMC Evol. Biol.* 9:116.

Hoppenrath, M. & Leander, B.S. 2007a. Character evolution in polykrikoid dinoflagellates. *J. Phycol.* 43:366–77.

Hoppenrath, M. & Leander, B.S. 2007b. Morphology and phylogeny of the pseudocolonial dinoflagellates *Polykrikos lebourae* and *Polykrikos herdmanae* n. sp. *Protist*. 158:209–27.

Hoppenrath, M., Murray, S.A., Chromérat, N. & Horiguchi, T. 2014. Marine benthic dinoflagellates – unveiling their worldwide biodiversity. Schweizerbart, Stuttgart. 276 p.

Hoppenrath, M., Yubuki, N., Bachvaroff, T.R. & Leander, B.S. 2010. Re-classification of *Pheopolykrikos hartmannii* as *Polykrikos* (Dinophyceae) based partly on the ultrastructure of complex extrusomes. *Eur. J. Protistol.* 46:29–37.

Horiguchi, T., Kawai, H., Kubota, M., Takahashi, T. & Watanabe, M. 1999. Phototactic responses of four marine dinoflagellates with different types of eyespot and chloroplast. *Phycol. Res.* 47:101–7.

Howe, C.J., Barbrook, A.C., Nisbet, R.E.R., Lockhart, P.J. & Larkum, A.W.D. 2008a. The origin of plastids. *Philos. Trans. R. Soc. B Biol. Sci.* 363:2675–85.

Howe, C.J., Nisbet, R.E.R. & Barbrook, A.C. 2008b. The remarkable chloroplast genome of dinoflagellates. *J. Exp. Bot.* 59:1035–45.

Huelsenbeck, J.P. & Ronquist, F. 2001. MRBAYES: Bayesian inference of phylogenetic trees. *Bioinformatics*. 17:754–5.

Iritani, D., Horiguchi, T. & Wakeman, K.C. 2018. Molecular phylogenetic positions and ultrastructure of marine gregarines (Apicomplexa) *Cuspisella ishikariensis* n. gen., n. sp. and *Loxomorpha* cf. *harmothoe* from western Pacific scaleworms (Polynoidae). *J. Eukaryot. Microbiol.* 65:637–47.

Iwataki, M., Hansen, G., Moestrup, Ø. & Matsuoka, K. 2010. Ultrastructure of the harmful unarmored dinoflagellate *Cochlodinium polykrikoides* (Dinophyceae) with reference to the apical groove and flagellar apparatus. *J. Eukaryot. Microbiol.* 57:308–21.

Janouškovec, J., Gavelis, G.S., Burki, F., Dinh, D., Bachvaroff, T.R., Gornik, S.G., Bright, K.J. et al. 2017. Major transitions in dinoflagellate evolution unveiled by phylotranscriptomics. *Proc. Natl. Acad. Sci.* 114:E171–80.

Janouškovec, J., Tikhonenkov, D. V., Burki, F., Howe, A.T., Kolísko, M., Mylnikov, A.P. & Keeling, P.J. 2015. Factors mediating plastid dependency and the origins of parasitism in apicomplexans and their close relatives. *Proc. Natl. Acad. Sci.* 112:10200–7.

Jassby, A.D. & Platt, T. 1976. Mathematical formulation of the relationship between photosynthesis and light for phytoplankton. *Limnol. Oceanogr.* 21:540–7.

Jeong, H.J., Jang, S.H., Moestrup, Ø., Kang, N.S., Lee, S.Y., Potvin, É. & Noh, J.H. 2014. *Ansanella granifera* gen. et sp. nov. (Dinophyceae), a new dinoflagellate from the coastal waters of Korea. *Algae*. 29:75–99.

Jeong, H.J., Kim, J.S., Lee, K.H., Seong, K.A., Yoo, Y. Du, Kang, N.S., Kim, T.H. et al. 2017. Differential interactions between the nematocyst-bearing mixotrophic dinoflagellate *Paragymnodinium shiwhaense* and common heterotrophic protists and copepods: Killer or prey. *Harmful Algae*. 62:37–51.

John, U., Lu, Y., Wohlrab, S., Groth, M., Janouškovec, J., Kohli, G.S., Mark, F.C. et al. 2019. An aerobic eukaryotic parasite with functional mitochondria that likely lacks a mitochondrial genome. *Sci. Adv.* 5:eaav1110.

Jones, A. & Berkelmans, R. 2012. The photokinetics of thermo-tolerance in *Symbiodinium*. *Mar. Ecol.* 33:490–8.

Kamikawa, R., Moog, D., Zauner, S., Tanifuji, G., Ishida, K.I., Miyashita, H., Mayama, S. et al. 2017. A non-photosynthetic diatom reveals early steps of reductive evolution in plastids. *Mol. Biol. Evol.* 34:2355–66.

Kang, N.S., Jeong, H.J., Moestrup, Ø. & Park, T.G. 2011. *Gyrodiniellum shiwhaense* n. gen., n. sp., a new planktonic heterotrophic dinoflagellate from the coastal waters of western Korea: Morphology and ribosomal DNA gene sequence. *J. Eukaryot. Microbiol.* 58:284–309.

Kang, N.S., Jeong, H.J., Moestrup, Ø., Shin, W., Nam, S.W., Park, J.Y., De Salas, M.F. et al. 2010. Description of a new planktonic mixotrophic dinoflagellate *Paragymnodinium shiwhaense* n. gen., n. sp. from the coastal waters off western

Korea: Morphology, pigments, and ribosomal DNA gene sequence. *J. Eukaryot. Microbiol.* 57:121–44.

Katoh, K., Rozewicki, J. & Yamada, K.D. 2019. MAFFT online service: Multiple sequence alignment, interactive sequence choice and visualization. *Brief. Bioinform.* 20:1160–6.

Kayama, M., Maciszewski, K., Yabuki, A., Miyashita, H., Karnkowska, A. & Kamikawa, R. 2020. Highly reduced plastid genomes of the non-photosynthetic Dictyochophyceans *Pteridomonas* spp. (Ochrophyta, SAR) are retained for tRNA-Glu-based organellar heme biosynthesis. *Front. Plant Sci.* 11:1–13.

Keeling, P.J. 2013. The number, speed, and impact of plastid endosymbioses in eukaryotic evolution. *Annu. Rev. Plant Biol.* 64:583–607.

Kim, E.H., Li, X.P., Razeghifard, R., Anderson, J.M., Niyogi, K.K., Pogson, B.J. & Chow, W.S. 2009. The multiple roles of light-harvesting chlorophyll *a*/*b*-protein complexes define structure and optimize function of *Arabidopsis* chloroplasts: A study using two chlorophyll *b*-less mutants. *Biochim. Biophys. Acta - Bioenerg.* 1787:973–84.

Kim, S., Yoon, J. & Park, M.G. 2015. Obligate mixotrophy of the pigmented dinoflagellate *Polykrikos lebourae* (Dinophyceae, Dinoflagellata). *Algae*. 30:35–47.

Kishino, M., Takahashi, M., Okami, N. & Ichimura, S. 1985. Estimation of the spectral absorption coefficients of phytoplankton in the sea. *Bull. Mar. Sci.* 37:634–42.

Kogame, K., Horiguchi, T. & Masuda, M. 1999. Phylogeny of the order Scytosiphonales (Phaeophyceae) based on DNA sequences of *rbcL*, partial *rbcS*, and partial LSU nrDNA. *Phycologia*. 38:496–502.

Kolber, Z.S., Prášil, O. & Falkowski, P.G. 1998. Measurements of variable chlorophyll fluorescence using fast repetition rate techniques: Defining methodology and experimental protocols. *Biochim. Biophys. Acta*. 1367:88–106.

Kreimer, G. 1994. Cell biology of phototaxis in flagellate algae. *Int. Rev. Cytol.* 148:229–310.

Kromkamp, J.C. & Forster, R.M. 2003. The use of variable fluorescence measurements in aquatic ecosystems: Differences between multiple and single turnover measuring protocols and suggested terminology. *Eur. J. Phycol.* 38:103–12.

Kumar, S., Stecher, G. & Tamura, K. 2016. MEGA7: Molecular evolutionary genetics analysis version 7.0 for bigger datasets. *Mol. Biol. Evol.* 33:1870–4.

Le, S.Q. & Gascuel, O. 2008. An improved general amino acid replacement matrix. *Mol. Biol. Evol.* 25:1307–20.

Lesser, M.P. 2006. Oxidative stress in marine environments: Biochemistry and Physiological Ecology. *Annu. Rev. Physiol.* 68:253–78.

Lin, S. 2011. Genomic understanding of dinoflagellates. *Res. Microbiol.* 162:551–69.

Lin, S., Zhang, H., Zhuang, Y., Tran, B. & Gill, J. 2010. Spliced leader-based metatranscriptomic analyses lead to recognition of hidden genomic features in dinoflagellates. *Proc. Natl. Acad. Sci. U. S. A.* 107:20033–8.

Luo, Z., Yang, W., Xu, B., Zheng, B., & Gu, H. 2015. Morphology, ultrastructure, and phylogeny of *Protodinium simplex* and *Biecheleriopsis* cf. *adriatica* (Dinophyceae) from the China Sea. *Nova Hedwigia* 101:252–68.

Maciszewski, K. & Karnkowska, A. 2019. Should I stay or should I go? Retention and loss of components in vestigial endosymbiotic organelles. *Curr. Opin. Genet. Dev.* 58–59:33–9.

Manni, M., Berkeley, M.R., Seppey, M., Simão, F.A. & Zdobnov, E.M. 2021. BUSCO update: novel and streamlined workflows along with broader and deeper phylogenetic coverage for scoring of eukaryotic, prokaryotic, and viral genomes. *Mol. Biol. Evol.* 38:4647–54.

Marcel, B., Morel, A. & Gagnon, R. 1994. An incubator designed for extensive and sensitive measurements of phytoplankton photosynthetic parameters. *Limnol. Oceanogr.* 39:694–702.

Marshall, S.M. 1925. On *Proterythropsis vigilans*, n.sp. *Quart. J. Micr. Sci.* 69:177–84.

Martin, M. 2011. Cutadapt removes adapter sequences from high-throughput sequencing reads. *EMBnet.journal*. 17:10.

Martin, W., Stoebe, B., Goremykin, V., Hansmann, S., Hasegawa, M. & Kowallik, K. V. 1998. Gene transfer to the nucleus and the evolution of chloroplasts. *Nature*. 393:162–5.

Martin, W., Rujan, T., Richly, E., Hansen, A., Cornelsen, S., Lins, T., Leister, D. et al. 2002. Evolutionary analysis of *Arabidopsis*, cyanobacterial, and chloroplast

genomes reveals plastid phylogeny and thousands of cyanobacterial genes in the nucleus. *Proc. Natl. Acad. Sci. U. S. A.* 99:12246–51.

Matsumoto, T., Shinozaki, F., Chikuni, T., Yabuki, A., Takishita, K., Kawachi, M., Nakayama, T. et al. 2011. Green-colored plastids in the dinoflagellate genus *Lepidodinium* are of core chlorophyte origin. *Protist*. 162:268–76.

Matsuo, E. & Inagaki, Y. 2018. Patterns in evolutionary origins of heme, chlorophyll *a* and isopentenyl diphosphate biosynthetic pathways suggest non-photosynthetic periods prior to plastid replacements in dinoflagellates. *PeerJ.* 6:e5345.

Matsuoka, K., Cho, H.-J. & Jacobson, D.M. 2000. Observations of the feeding behavior and growth rates of the heterotrophic dinoflagellate *Polykrikos kofoidii* (Polykrikaceae, Dinophyceae). *Phycologia*. 39:82–6.

Mitchell, B.G. 1990. Algorithms for determining the absorption coefficient for aquatic particulates using the quantitative filter technique. *Ocean Opt.* 1302:137–48.

Mitra, A., Flynn, K.J., Tillmann, U., Raven, J.A., Caron, D., Stoecker, D.K., Not, F. et al. 2016. Defining planktonic protist functional groups on mechanisms for energy and nutrient acquisition: Incorporation of diverse mixotrophic strategies. *Protist*. 167:106–20.

Moestrup, Ø. 2000. The flagellate cytoskeleton: introduction of a general terminology for microtubular flagellar roots in protists. *In* Leadbeater, B. S. C. & Green, J. C. [Eds.] *The Flagellates: Unity, Diversity and Evolution*. Taylor & Francis, London, pp. 67–94.

Moestrup, Ø. & Calado, A. 2018. Süßwasserflora von Mitteleuropa, Bd. 6 - Freshwater flora of central Europe, Vol. 6: Dinophyceae. Springer Spektrum. 561 pp.

Moestrup, Ø. & Daugbjerg, N. 2007. On dinoflagellate phylogeny and classification. *In* Brodie, J. & Lewis, J. [Eds.] *Unravelling the Algae: The Past, Present, and Future of Algae Systematics*. CRC Press, Taylor & Francis Group, London, pp. 215–30.

Moldrup, M., Moestrup, Ø. & Hansen, P.J. 2013. Loss of phototaxis and degeneration of an eyespot in long-term algal cultures: Evidence from ultrastructure and behaviour in the dinoflagellate *Kryptoperidinium foliaceum*. *J. Eukaryot. Microbiol.* 60:327–34.

Molina, J., Hazzouri, K.M., Nickrent, D., Geisler, M., Meyer, R.S., Pentony, M.M., Flowers, J.M. et al. 2014. Possible loss of the chloroplast genome in the parasitic flowering plant *Rafflesia lagascae* (Rafflesiaceae). *Mol. Biol. Evol.* 31:793–803.

Moriya, Y., Itoh, M., Okuda, S., Yoshizawa, A.C. & Kanehisa, M. 2007. KAAS: An automatic genome annotation and pathway reconstruction server. *Nucleic Acids Res.* 35:182–5.

Morse, D., Salois, P., Markovic, P. & Hastings, J.W. 1995. A nuclear-encoded form II RuBisCO in dinoflagellates. *Science.* 268:1622–4.

Mungpakdee, S., Shinzato, C., Takeuchi, T., Kawashima, T., Koyanagi, R., Hisata, K., Tanaka, M. et al. 2014. Massive gene transfer and extensive RNA editing of a symbiotic dinoflagellate plastid genome. *Genome Biol. Evol.* 6:1408–22.

Murray, S. 2003. Diversity and phylogenetics of sand-dwelling dinoflagellates from Southern Australia. University of Sydney, Sydney, 202 p.

Nakayama, T., Watanabe, S., Mitsui, K., Uchida, H. & Inouye, I. 1996. The phylogenetic relationship between the Chlamydomonadales and Chlorococcales inferred from 18S rDNA sequence data.

Nilsson, D.E. 2013. Eye evolution and its functional basis. *Vis. Neurosci.* 30:5–20.

Nunn, G.B., Theisen, B.F., Christensen, B. & Arctander, P. 1996. Simplicity-correlated size growth of the nuclear 28S ribosomal RNA D3 expansion segment in the crustacean order Isopoda. *J. Mol. Evol.* 42:211–23.

Oborník, M. & Green, B.R. 2005. Mosaic origin of the heme biosynthesis pathway in photosynthetic eukaryotes. *Mol. Biol. Evol.* 22:2343–53.

Ogata, H., Goto, S., Sato, K., Fujibuchi, W., Bono, H. & Kanehisa, M. 1999. KEGG: Kyoto Encyclopedia of Genes and Genomes. *Nucleic Acids Res.* 27:29–34.

Onuma, R. & Horiguchi, T. 2015. Kleptochloroplast enlargement, karyoklepty and the distribution of the cryptomonad nucleus in *Nusuttodinium* (= *Gymnodinium*) *aeruginosum* (Dinophyceae). *Protist*. 166:177–95.

Pandeirada, M.S., Craveiro, S.C., Daugbjerg, N., Moestrup, Ø. & Calado, A.J. 2014. Studies on woloszynskioid dinoflagellates VI: description of *Tovellia aveirensis* sp. nov. (Dinophyceae), a new species of Tovelliaceae with spiny cysts. *Eur. J. Phycol.* 49:230–43.

Platt, T., Gallegos, C.L. & Harrison, W.G. 1980. Photoinhibition of photosynthesis in natural assemblages of marine phytoplankton. *J. Mar. Res.* 38:687–701.

Ponce-Toledo, R.I., Deschamps, P., López-García, P., Zivanovic, Y., Benzerara, K. & Moreira, D. 2017. An early-branching freshwater cyanobacterium at the origin of plastids. *Curr. Biol.* 27:386–91.

Rockwell, N.C., Lagarias, J.C. & Bhattacharya, D. 2014. Primary endosymbiosis and the evolution of light and oxygen sensing in photosynthetic eukaryotes. *Front. Ecol. Evol.* 2:1–13.

Ruhlman, T.A. & Daniell, H. 2007. Plastid Pathways. *In* Verpoorte R., Alfermann A.W. & Johnson T.S. [Eds.] *Applications of plant metabolic engineering.* Springer, Dordrecht, pp. 79–108.

Saldarriaga, J.F., Taylor, F.J.R., Keeling, P.J. & Cavalier-Smith, T. 2001. Dinoflagellate nuclear SSU rRNA phylogeny suggests multiple plastid losses and replacements. *J. Mol. Evol.* 53:204–13.

Sanchez-Puerta, M.V., Lippmeier, J.C., Apt, K.E. & Delwiche, C.F. 2007. Plastid genes in a non-photosynthetic dinoflagellate. *Protist*. 158:105–17.

Schnepf, E. & Elbrächter, M. 1992. Nutritional strategies in dinoflagellates: A review with emphasis on cell biological aspects. *Eur. J. Protistol.* 28:3–24.

Schnepf, E. & Elbrächter, M. 1999. Dinophyte chloroplasts and phylogeny - A review. *Grana*. 38:81–97.

Scholin, C.A., Herzog, M., Sogin, M. & Anderson, D.M. 1994. Identification of group- and strain-specific genetic markers for globally distributed *Alexandrium* (Dinophyceae), II. Sequence analysis of a fragment of the LSU rRNA gene. *J. Phycol.* 30:999–1011.

Shen, A., Ishizaka, J., Yang, M., Ouyang, L., Yin, Y. & Ma, Z. 2019. Changes in community structure and photosynthetic activities of total phytoplankton species during the growth, maintenance, and dissipation phases of a *Prorocentrum* donghaiense bloom. *Harmful Algae*. 82:35–43.

Simão, F.A., Waterhouse, R.M., Ioannidis, P., Kriventseva, E. V. & Zdobnov, E.M. 2015. BUSCO: Assessing genome assembly and annotation completeness with single-copy orthologs. *Bioinformatics*. 31:3210–2.

Skovgaard, A., Hansen, P.J. & Stoecker, D.K. 2000. Physiology of the mixotrophic dinoflagellate *Fragilidium subglobosum*. I. Effect of phagotrophy and irradiance on photosynthesis and carbon content. *Mar. Ecol. Prog. Ser.* 201:129–36.

Slamovits, C.H. & Keeling, P.J. 2008. Plastid-derived genes in the nonphotosynthetic alveolate *Oxyrrhis marina*. *Mol. Biol. Evol.* 25:1297–306.

Smith, D.R. & Lee, R.W. 2014. A plastid without a genome: Evidence from the nonphotosynthetic green algal genus *Polytomella*. *Plant Physiol.* 164:1812–9.

Stamatakis, A. 2006. RAxML-VI-HPC: Maximum likelihood-based phylogenetic analyses with thousands of taxa and mixed models. *Bioinformatics*. 22:2688–90.

Standfuss, J., Van Scheltinga, A.C.T., Lamborghini, M. & Kühlbrandt, W. 2005. Mechanisms of photoprotection and nonphotochemical quenching in pea light-harvesting complex at 2.5 Å resolution. *EMBO J.* 24:919–28.

Stephens, T.G., González-Pech, R.A., Cheng, Y., Mohamed, A.R., Burt, D.W., Bhattacharya, D., Ragan, M.A. et al. 2020. Genomes of the dinoflagellate *Polarella glacialis* encode tandemly repeated single-exon genes with adaptive functions. *BMC Biol.* 18:1–21.

Stoecker, D.K. 1999. Mixotrophy among dinoflagellates. *J. Eukaryot. Microbiol.* 46:397–401.

Stoecker, D.K. 1998. Conceptual models of mixotrophy in planktonic protists and some ecological and evolutionary implications. *Eur. J. Protistol.* 34:281–90.

Stoecker, D.K., Hansen, P.J., Caron, D.A. & Mitra, A. 2017. Mixotrophy in the marine plankton. *Ann. Rev. Mar. Sci.* 9:311–35.

Suzuki, K., Kamimura, A. & Hooker, S.B. 2015. Rapid and highly sensitive analysis of chlorophylls and carotenoids from marine phytoplankton using ultra-high performance liquid chromatography (UHPLC) with the first derivative spectrum chromatogram (FDSC) technique. *Mar. Chem.* 176:96–109.

Sweeney, B.M. 1984. Circadian rhythmicity in dinoflagellates. *In* Spector, D.L. [Ed.] *Dinoflagellates*. Academic Press, Orlando, pp. 343–64.

Takahashi, K., Moestrup, Ø., Wada, M., Ishimatsu, A., Nguyen, V.N., Fukuyo, Y. & Iwataki, M. 2017. *Dactylodinium pterobelotum* gen. et sp. nov., a new marine

woloszynskioid dinoflagellate positioned between the two families Borghiellaceae and Suessiaceae. *J. Phycol.* 53:1223–40.

Takano, Y. & Horiguchi, T. 2004. Surface ultrastructure and molecular phylogenetics of four unarmored heterotrophic dinoflagellates, including the type species of the genus *Gyrodinium* (Dinophyceae). *Phycol. Res.* 52:107–16.

Takano, Y., Yamaguchi, H., Inouye, I., Moestrup, O. & Horiguchi, T. 2014. Phylogeny of five species of *Nusuttodinium* gen. nov. (Dinophyceae), a genus of unarmoured kleptoplastidic dinoflagellates. *Protist*. 165:759–78.

Tanabe, A.S. 2011. Kakusan4 and Aminosan: Two programs for comparing nonpartitioned, proportional and separate models for combined molecular phylogenetic analyses of multilocus sequence data. *Mol. Ecol. Resour.* 11:914–21.

Tanaka, R. & Tanaka, A. 2011. Chlorophyll cycle regulates the construction and destruction of the light-harvesting complexes. *Biochim. Biophys. Acta - Bioenerg.* 1807:968–76.

Tanifuji, G., Kamikawa, R., Moore, C.E., Mills, T., Onodera, N.T., Kashiyama, Y., Archibald, J.M. et al. 2020. Comparative plastid genomics of cryptomonas species reveals fine-scale genomic responses to loss of photosynthesis. *Genome Biol. Evol.* 12:3926–37.

Tatusov, R.L., Galperin, M.Y., Natale, D.A. & Koonin, E. V. 2000. The COG database: A tool for genome-scale analysis of protein functions and evolution. *Nucleic Acids Res.* 28:33–6.

Tengs, T., Dahlberg, O.J., Shalchian-Tabrizi, K., Klaveness, D., Rudi, K., Delwiche, C.F. & Jakobsen, K.S. 2000. Phylogenetic analyses indicate flint the 19'hexanoyloxy-fucoxanthin-containing dinoflagellates have tertiary plastids of haptophyte origin. *Mol. Biol. Evol.* 17:718–29.

Tripp, H.J., Bench, S.R., Turk, K.A., Foster, R.A., Desany, B.A., Niazi, F., Affourtit, J.P. et al. 2010. Metabolic streamlining in an open-ocean nitrogen-fixing cyanobacterium. *Nature.* 464:90–4.

Van Vlierberghe, M., Philippe, H. & Baurain, D. 2021. Broadly sampled orthologous groups of eukaryotic proteins for the phylogenetic study of plastid-bearing lineages. *BMC Res. Notes*. 14:21–4.

Waller, R.F. & Kořený, L. 2017. Plastid complexity in dinoflagellates: A picture of gains, losses, replacements and revisions. *Adv. Bot. Res.* 84:105–43.

Watanabe, M.M., Suda, S., Inouye, I., Sawaguchi, T. & Chihara, M. 1990. *Lepidodinium viride* gen. et sp. nov. (Gymnodiniales, Dynophyta), a green dinoflagellate with a chlorophyll *a*- and *b*-containing endosymbiont. *J. Phycol.* 26:741–51.

Watanabe, M.M., Takeda, Y., Sasa, T., Inouye, I. & Chihara, M. 1987. A green dinoflagellate with chlorophylls *a* and *b*: morphology, fine structure of the chloroplast and chlorophyll composition. *J. Phycol.* 23:382–9.

Westfall, J.A., Bradbury, P.C. & Townsend, J.W. 1983. Ultrastructure of the dinoflagellate *Polykrikos*. I. Developement of the nematocyst-taeniocyst complex and morphology of the site for extrusion. *J. Cell Sci.* 63:245–61.

Wicke, S., Müller, K.F., DePamphilis, C.W., Quandt, D., Bellot, S. & Schneeweiss, G.M. 2016. Mechanistic model of evolutionary rate variation en route to a nonphotosynthetic lifestyle in plants. *Proc. Natl. Acad. Sci. U. S. A.* 113:9045–50.

Wilken, S., Yung, C.C.M., Hamilton, M., Hoadley, K., Nzongo, J., Eckmann, C., Corrochano-Luque, M., et al. 2019. The need to account for cell biology in characterizing predatory mixotrophs in aquatic environments. *Philos. T. R. Soc. B.* 374:20190090.

Wilson, R.J.M. (Iain), Denny, P.W., Preiser, P.R., Rangachari, K., Roberts, K., Roy, A., Whyte, A. et al. 1996. Complete gene map of the plastid-like DNA of the malaria parasite *Plasmodium falciparum*. *J. Mol. Biol.* 261:155–72.

Wisecaver, J.H. & Hackett, J.D. 2011. Dinoflagellate genome evolution. *Annu. Rev. Microbiol.* 65:369–87.

Withers, N.W. & Haxo, F.T. 1978. Isolation and characterization of carotenoid-rich lipid globules from *Peridinium foliaceum*. *Plant Physiol.* 62:36–9.

Yamada, N., Sym, S.D. & Horiguchi, T. 2017. Identification of highly divergent diatom-derived chloroplasts in dinoflagellates, including a description of *Durinskia kwazulunatalensis* sp. nov. (Peridiniales, Dinophyceae). *Mol. Biol. Evol.* 34:1335–51.

Yamaguchi, A., Yubuki, N. & Leander, B.S. 2012. Morphostasis in a novel eukaryote illuminates the evolutionary transition from phagotrophy to phototrophy: description of *Rapaza viridis* n. gen. et sp. (Euglenozoa, Euglenida). *BMC Evol. Biol.* 12:29.

Yokouchi, K., Onuma, R. & Horiguchi, T. 2018. Ultrastructure and phylogeny of a new species of mixotrophic dinoflagellate, *Paragymnodinium stigmaticum* sp. nov. (Gymnodiniales, Dinophyceae). *Phycologia* 57:539–54.

Yokouchi, K., Takahashi, K., Nguyen, V. N., Iwataki, M. & Horiguchi, T. 2020. Ultrastructure and systematics of two new species of dinoflagellate, *Paragymnodinium asymmetricum* sp. nov. and *Paragymnodinium inerme* sp. nov. (Gymnodiniales, Dinophyceae). *J. Phycol.* 56:730–46.

Yokouchi, K. & Horiguchi, T. 2021. *Paragymnodinium verecundum* sp. nov. (Gymnodiniales, Dinophyceae), a new species of mixotrophic dinoflagellate from Japan. *Phycol. Res.* 69:124–36.

Yoo, Y. Du, Jeong, H.J., Kang, N.S., Song, L.Y., Kim, K.Y., Lee, G. & Kim, J.H. 2010. Feeding by the newly described mixotrophic dinoflagellate *Paragymnodinium shiwhaense*: Feeding mechanism, prey species, and effect of prey concentration. *J. Eukaryot. Microbiol.* 57:145–58.

Yoshida, K., Endo, H., Lawrenz, E., Isada, T., Hooker, S.B., Prášil, O. & Suzuki, K. 2018. Community composition and photophysiology of phytoplankton assemblages in coastal Oyashio waters of the western North Pacific during early spring. *Estuar. Coast. Shelf Sci.* 212:80–94.

Záhonová, K., Füssy, Z., Oborník, M., Eliáš, M. & Yurchenko, V. 2016. RuBisCO in non-photosynthetic alga *Euglena longa*: Divergent features, transcriptomic analysis and regulation of complex formation. *PLoS One*. 11:e0158790.

Zehr, J.P., Bench, S.R., Carter, B.J., Hewson, I., Niazi, F., Shi, T., Tripp, H.J. et al. 2008. Globally distributed uncultivated oceanic N2-Fixing cyanobacteria lack oxygenic photosystem II. *Science.* 322:1110–2.

Zhang, Z., Green, B.R. & Cavalier-Smith, T. 1999. Single gene circles in dinoflagellate chloroplast genomes. *Nature.* 400:155–9.

Zimorski, V., Ku, C., Martin, W.F. & Gould, S.B. 2014. Endosymbiotic theory for organelle origins. *Curr. Opin. Microbiol.* 22:38–48.

SUPPLEMENTARY MATERIALS

Video 2.1. The negative phototaxis of *Paragymnodinium verecundum* sp. nov.

Video 2.2. Serial TEM sections of a whole cell of *Paragymnodinium inerme* sp. nov. showing more than 20 masses of chloroplasts and only some of them are connected to each other by the thin bridges. The total number of discrete chloroplasts in this individual is three (indicated by A–C).